UNIVERSITÀ DEGLI STUDI DI MILANO-BICOCCA

Department: Fisica G. Occhialini
PhD Program: Physics and Astronomy
Curriculum: Astrophysics

X-RAY EMISSION FROM THE MAGNETIC POLAR CAPS OF OLD ROTATION-POWERED PULSARS

Tutors:
Prof. Monica Colpi
Dr. Sandro Mereghetti

Coordinator:
Prof. Marta Calvi

Candidate:
Michela Rigoselli
Registration n. 823544

Cycle XXXII

"The larger one's ignorance,
the stronger the magnetic field."

L. Woltjer, 1967

Contents

Abstract

Neutron stars are the remnants of massive stars whose cores collapse during the supernova explosions. They are among the objects with the most peculiar physical conditions observable in the Universe. The project of this PhD Thesis consisted in the study and the characterization of the X-ray emission from isolated neutron stars older than about 100 000 years. The work was based mainly on data obtained with the *XMM-Newton* satellite of the European Space Agency. To extract the best possible information from the data of these rather faint X-ray sources, I implemented a maximum likelihood (ML) technique and used it to derive the spectra and pulse profiles of several old pulsars, that were then studied with state-of-the-art models of magnetized neutron star atmospheres. The combination of these two factors enabled to solve the puzzling emission of some old neutron stars, and to disfavor the predictions of a family of polar cap accelerator models.

The Thesis is structured as follows: in the first three chapters I outline the main properties of isolated neutron stars, with a major focus on the thermal and nonthermal processes that produce X-rays. The nonthermal X-rays are produced by relativistic particles accelerated by rotation-induced electric fields and moving along the magnetic field lines. A fraction of these particles is accelerated backward and returns on the stellar surface, heating the magnetic polar caps. The thermal component, that can be produced by the whole stellar surface or by small hot spots, can be described, in a first approximation, by a blackbody. However, the presence of intense surface magnetic fields strongly affects the properties of matter, and the emergent radiation is widely anisotropic. Therefore, more realistic models, as those used in my work, are required to properly derive the physical properties of these objects.

In Chapter 4, I describe how I generated synthetic spectra and pulse profiles using thermal emission models that consider polar caps covered by a magnetized hydrogen atmosphere or with a condensed iron surface. I relied on an existing software that, given a set of stellar parameters, evaluates the emerging intensity of the radiation. A second software, which I adapted on the sources I analyzed in the Thesis, collects the contribution of surface elements which are in view at different rotation phases from a stationary observer. Then, in Chapter 5, I describe how I implemented an analysis software that relies on the ML method. It estimates the most probable number of source and background counts by comparing the spatial distribution of the observed counts with the expected distribution for a point source plus an uniform background. I demonstrated that the ML method is particularly effective for dim sources, as most old pulsars are.

Subsequently, I applied the methods described above to some old pulsars. In Chapter 6, I report the analysis of PSR J0726−2612, a radio pulsar that shares some properties with the radio-silent XDINSs, as the long period, the high magnetic field, and the thermal X-ray emission from the cooling surface. Thanks to an in-depth analysis of the combined spectrum and pulse profile, I showed that the presence of radio pulses from PSR J0726−2612, as well as the

absence from the XDINSs, might simply be due to different viewing geometries. In Chapter 7, I present the case of PSR B0943+10, a pulsar with a nonthermal and thermal X-ray spectrum but that, despite being an aligned rotator, has a large pulsed fraction. I could reconcile the two opposite properties analyzing with the ML the spectrum and the pulse profile, and considering the magnetic beaming of a magnetized atmosphere model, that well fits the thermal component. In Chapter 8, I applied the ML method to seven old and dim pulsars, of which four had controversial published results, and three were so far undetected. I found convincing evidence of thermal emission only in the phase-averaged spectrum of two of them, plus a hint for a thermal pulsed spectrum in a third object.

Finally, I considered all the old thermal emitters and I compared their observed temperatures, radii and luminosities to the expectations of the current theoretical models for these objects. In particular, I found that the emitting area are generally in agreement with the polar cap regions evaluated in a dipole approximation, if the combined effects of geometry projections plus realistic thermal models (as the magnetic atmosphere) are taken into account.

List of Figures

List of Tables

List of Publications

Many of the ideas and figures in this Thesis appeared previously in articles I published on peer-reviewed journals during my three year PhD course. Nevertheless, this work is not a simple collection of previously published papers, but rather elaborates on selected works in order to provide a coherent picture of the X-ray emission properties of old isolated pulsars. Here, a complete list of my publications, updated to January 2020:

- F. Pintore, M. Marelli, R. Salvaterra, G. L. Israel, G. A. Rodriguez Castillo, P. Esposito, A. Belfiore, A. De Luca, A. Wolter, S. Mereghetti, L. Stella, M. Rigoselli, H. P. Earnshaw, C. Pinto, T. P. Roberts, D. J. Walton, F. Bernardini, F. Haberl, C. Salvaggio, A. Tiengo, L. Zampieri, M. Bachetti, M. Brightman, P. Casella, D. D'Agostino, S. Dall'Osso, F. Fuerst, F. A. Harrison, M. Mapelli, A. Papitto, and M. Middleton. The Ultraluminous X-ray sources population of the galaxy NGC 7456. *The Astrophysical Journal*, under review, 2020.

- M. Rigoselli, S. Mereghetti, V. Suleimanov, A. Y. Potekhin, R. Turolla, R. Taverna, and F. Pintore. XMM-Newton observations of PSR J0726-2612, a radio-loud XDINS. *Astronomy and Astrophysics*, 627:A69, Jul 2019. doi: 10.1051/0004-6361/201935485.

- M. Rigoselli, S. Mereghetti, R. Turolla, R. Taverna, V. Suleimanov, and A. Y. Potekhin. Thermal Emission and Magnetic Beaming in the Radio and X-Ray Mode-switching PSR B0943+10. *The Astrophysical Journal*, 872(1):15, Feb 2019. doi: 10.3847/1538-4357/aafac7.

- A. P. Igoshev, S. S. Tsygankov, M. Rigoselli, S. Mereghetti, S. B. Popov, J. G. Elfritz, and A. A. Mushtukov. Discovery of X-Rays from the Old and Faint Pulsar J1154-6250. *The Astrophysical Journal*, 865(2):116, Oct 2018. doi: 10.3847/1538-4357/aadd93.

- S. Mereghetti, L. Kuiper, A. Tiengo, J. Hessels, W. Hermsen, K. Stovall, A. Possenti, J. Rankin, P. Esposito, R. Turolla, D. Mitra, G. Wright, B. Stappers, A. Horneffer, S. Oslowski, M. Serylak, J. M. Griessmeier, and M. Rigoselli. X-rays from the mode-switching PSR B0943+10. In P. Weltevrede, B. B. P. Perera, L. L. Preston, and S. Sanidas, editors, *Pulsar Astrophysics the Next Fifty Years*, volume 337 of *IAU Symposium*, pages 62–65, Aug 2018. doi: 10.1017/S1743921317009504.

- S. Mereghetti, A. De Luca, D. Salvetti, A. Belfiore, M. Marelli, A. Paizis, M. Rigoselli, R. Salvaterra, L. Sidoli, and A. Tiengo. EXTraS discovery of a peculiar flaring X-ray source in the Galactic globular cluster NGC 6540. *Astronomy and Astrophysics*, 616:A36, Aug 2018. doi: 10.1051/0004-6361/201833086.

- M. Rigoselli and S. Mereghetti. A new X-ray look into four old pulsars. *Astronomy and Astrophysics*, 615:A73, Jul 2018. doi: 10.1051/0004-6361/201732408.

- F. PINTORE, A. BELFIORE, G. NOVARA, R. SALVATERRA, M. MARELLI, A. DE LUCA, M. RIGOSELLI, G. L. ISRAEL, G. A. RODRIGUEZ CASTILLO, S. MEREGHETTI, A. WOLTER, D. J. WALTON, F. FUERST, E. AMBROSI, L. ZAMPIERI, A. TIENGO, AND C. SALVAGGIO. A new ultraluminous X-ray source in the galaxy NGC 5907. *Monthly Notices of the Royal Astronomical Society*, 477(1):L90–L95, Jun 2018. doi: 10.1093/mnrasl/sly048.

- S. MEREGHETTI, L. KUIPER, A. TIENGO, J. HESSELS, W. HERMSEN, K. STOVALL, A. POSSENTI, J. RANKIN, P. ESPOSITO, R. TUROLLA, D. MITRA, WRIGHT G., B. STAPPERS, A. HORNEFFER, S. OSLOWSKI, M. SERYLAK, J. M. GRIESSMEIER, AND M. RIGOSELLI. X-ray properties of the mode-switching pulsar PSR B0943+10. In *Journal of Physics Conference Series*, volume 932, page 012009, Dec 2017. doi: 10.1088/1742-6596/932/1/012009.

- S. MEREGHETTI AND M. RIGOSELLI. The Radio and X-ray Mode-Switching Pulsar PSR B0943+10. *Journal of Astrophysics and Astronomy*, 38(3):54, Sep 2017. doi: 10.1007/s12036-017-9464-7.

Chapter 1

Introduction

Neutron stars are the remnants of massive stars whose cores collapse during the supernova explosions, at the end of their nuclear fusion lifetimes. They are strongly magnetized, fast rotating compact objects, that are supported against their own gravity by the pressure of degenerate neutrons. In this introductory chapter, I retrace the historical path of how neutron stars were theoretically envisaged and then observationally identified (Section 1.1), and I briefly describe their general properties, as the composition, the intense magnetic field and the fast rotation (Section 1.2). The rotation is exactly the power source of typical neutron stars (Section 1.3), and it sustains their multiwavelength emission, from low-energy radio waves to high-energy X- and γ-rays (Section 1.4). X-ray observations have been crucial to discover other manifestations of isolated neutron stars (i.e. not in a binary system), that originate from other power sources besides the rotation, as the magnetic field decay or the latent heat of the neutron star matter (Section 1.5).

1.1 Historical introduction

The idea of neutron stars can be traced back to the early 1930s when, one year before the discovery of the neutron by James Chadwick in 1932 [59], Lev Landau wrote a remarkable paper [228]. As reported by Yakovlev et al. [438], in that paper Landau calculated the maximum mass of white dwarf stars (independently of, but later than, Chandrasekhar [60]), and predicted the existence of dense stars which look like giant atomic nuclei (a valid description of neutron stars nowadays). He suggested also that the laws of quantum mechanics are violated in these very dense stars.

The first explicit prediction of neutron stars was made in 1933 by Walter Baade and Fritz Zwicky [19], who proposed that neutron stars could be the final outcome of star evolution, formed in supernovae explosions. In 1939, Robert Oppenheimer and George Volkoff [294] studied the internal structure of neutron stars and calculated that, if the star is entirely described by an ideal Fermi gas of neutrons, general relativity imposes an upper limit for the neutron star mass. Any star that exceeds this limit, called Oppenheimer-Volkoff limit, will collapse to form a black hole. Unfortunately, their pioneering work did not predict anything astronomers could actually observe, and the idea of neutron stars was discarded.

In 1942, Baade [18] and Minkowski [275] analyzed the emission from the Crab Nebula, that was the remnant associated with the supernova explosion of 1054 A.D. They observed that most of the optical emission showed a continuous spectrum, and they interpreted it as due to free-free and free-bound transitions of electrons in a highly ionized gas. When in 1953

the Crab Nebula was also observed at radio wavelengths, Shklovsky [53, e.g.] argued that the radio spectrum was caused by synchrotron radiation from relativistic electrons moving through a magnetic field [7]. This mechanism could also explain the highly polarized optical continuous radiation. Oort & Walraven [292] calculated that the relativistic electrons loose their energy within 200 years, which meant a source that continuously supplies the nebula with new electrons must exist. However, X-ray observations [50] revealed that at the center of the Crab Nebula there was an extended source ($\sim$1 amin), and not a point source as a neutron star was expected to be.

In 1967, Jocelyn Bell and Anthony Hewish came across a series of pulsating radio signals from an unknown source, located at R.A. = 19^h20^m, Dec. = $+23^\circ$[1]. The extreme precision of the period was interpreted as artificial, and the source was dubbed as LGM-1, an acronym for Little Green Man 1. However, as a few similar sources were detected at very different sky positions, it became clear that a new kind of celestial object had been discovered [168].

The link between these pulsating radio sources, which were called *pulsars*, and fast spinning neutron stars, was finally provided by Franco Pacini [295, 296] and Thomas Gold [117, 118]. They proposed that the pulsars radiate at expense of their rotational energy because of dipole magnetic braking. Moreover, relativistic particles are accelerated along the magnetic field lines and emit the previously-observed synchrotron radiation. The discovery of the first radio pulsar was followed very soon by the discoveries of the 33 ms pulsar in the Crab Nebula [379] and the 89 ms pulsar in the Vela supernova remnant [229]. The fact that these pulsars were located within supernova remnants provided striking confirmations that neutron stars are born in core-collapse supernovae; moreover, the picture of Pacini and Gold was strengthened when the spin down of the Crab pulsar was measured [355].

While the evidence for the existence of neutron stars came from radio astronomy, the X-rays played an important role in detecting the first accreting neutron star in a binary system. In the first half of the XX century, it was widely believed that the Sun was the only source emitting detectable X-rays: all other stars, much more distant than the Sun, should have been too faint. On the other hand, results from cosmic ray experiments suggested that there were celestial objects which produce high-energy cosmic rays in processes which, in turn, may also produce X-rays and γ-rays [284].

These predictions were confirmed in 1962, when the team led by Bruno Rossi and Riccardo Giacconi detected X-rays from the extra-solar source Sco X$-$1 [312]. Shklovsky [373] proposed that the X-rays from Sco X$-$1 originated from a hot gas flowing onto a neutron star from a close binary companion. It was also noticed that the orbital parameters of such a system could indicate the nature of the compact object, which could also be a black hole [453].

By the end of the 60's, about 20 X-ray sources were located, but the real breakthrough was achieved at the end of 1970 after the launch of *Uhuru*, the first astronomical X-ray satellite. Within just over two years, *Uhuru* detected and localized 339 X-ray sources [108]. The detection of pulsations from the source Cen X$-$3 was the smoking gun for the existence of X-ray binary pulsars [107]. The cyclotron line in the pulsed spectrum of Her X$-$1, instead, was the evidence for the presence of $\sim 10^{12}$ G magnetic field on neutron stars [394, 159].

Today, more than 2500 pulsars are known [249] because of their multiwavelength emission, from the radio band to the more energetic X- and γ-rays (see Section 1.4).

[1] CP 1919+21, where the CP stands for Cambridge Pulsar; the source is now known as PSR B1919+21.

1.2 Neutron star basics

In the following, I briefly explain how a neutron star forms (Section 1.2.1), what is its internal composition (Section 1.2.2) and its observational features (Section 1.2.3). These sections are based on the works of Becker [27], Degenaar & Suleimanov [80], Kaspi et al. [209], Shapiro & Teukolsky [371], Viganó [423] and, especially Section 1.2.1, are intentionally oversimplified.

1.2.1 Evolution

A neutron star (NS) is the ultimate stage of massive star evolution; it is formed in the dense and hot core of the star, while the outer envelopes are expelled with the supernova explosion. The mass of the progenitor determines whether the compact object will be a neutron star, or a black hole: neutron stars are thought to originate from stars with masses from about 9 $M_\odot$ to 25 $M_\odot$ [155].

At the final life stages, a massive star starts to burn heavy elements, and within days an iron core is produced. ^{56}Fe is the most stable nucleus, thus the nuclear fusion processes stop and the core starts to contract, sustained by the pressure of degenerate electrons. As the contraction goes on, the electrons become more and more relativistic. When the core mass exceeds the Chandrasekhar mass (1.4 $M_\odot$), the electron pressure is insufficient to balance the gravitational attraction, and the core collapses in less than one second. The extreme conditions of the core ($T \sim 10^9 - 10^{10}$ K and $\rho \sim 10^9 - 10^{10}$ g cm^{-3}) favorite the photo-disintegration $^{56}_{26}\mathrm{Fe} + \gamma \rightarrow 13\, ^4_2\mathrm{He} + 4n$, $^4_2\mathrm{He} + \gamma \rightarrow 2p + 2n$, and the electronic capture $p + e^- \rightarrow n + \nu_e$.

In this framework, a large amount of neutrinos are produced (via the electronic capture or thermal mechanisms as $e^+ + e^- \rightarrow \nu + \bar{\nu}$), and when the core density reaches the so-called neutrino trapping density, $\rho_{\mathrm{trap}} = 1.4 \times 10^{11}$ g cm^{-3}, they are forced to interact with the other fermions. ρ_{trap} is obtained by equating the timescale of neutrino diffusion out of the core and the free fall collapse time, $t_{\mathrm{ff}} \sim (G\rho)^{1/2} \sim 10^{-3}$ s. Neutrino trapping has deep consequences on the core collapse: gravitational binding energy of the core is released in internal energy of the neutrinos instead of kinetic energy (neutrino heating), and it favors an adiabatical and homologous core collapse (on dynamical timescales).

The core density increases until it reaches the nuclear saturation density $\rho_0 \approx 3 \times 10^{14}$ g cm^{-3}; this density is sufficient to halt the collapse, causing the homologous core to bounce and then rebound, before it eventually settles down to hydrostatic equilibrium. The outer core, in the meantime, continues to fall towards the center at supersonic velocities. As a result, the rebounding inner core, acting as a piston, drives a shock wave into the infalling outer core. Neutrinos, that now can diffuse freely, contribute to the kinetic energy of the shock wave. The typical total energy injected to the shock is a few 10^{51} erg [435, 421], more than adequate to disrupt the outer envelopes of the star. This is the supernova explosion (see Bethe [36] for a review).

The inner core is the newborn neutron star: it is formed at very high temperatures ($\sim 10^{11}$ K) and in about one day it cools down to $\sim 10^9 - 10^{10}$ K through neutrino emission, because their mean free path is much longer than the star radius. The dominating processes at this phase are direct Urca processes[2] ($n \rightarrow p + e^- + \nu_e$, $p + e^- \rightarrow n + \nu_e$) and neutrino bremsstrahlung ($e + e \rightarrow e + e + \nu + \bar{\nu}$).

[2]Urca is the name of a casino in Rio de Janeiro, and was adopted as a name for these reactions by Gamow & Schoenberg [97] who saw a parallel between how quickly money disappears from gamblers' pockets and how quickly energy is lost in these processes.

At temperatures below 10^9 K, the direct Urca processes for nucleons are suppressed, because protons and neutrons become degenerate and energy and momentum can be conserved only if an additional particle is involved in the reaction (modified Urca processes: $n + n \rightarrow n + p + e^- + \bar{\nu}_e$, $n + p + e^- \rightarrow n + n + \nu_e$). Since the modified Urca processes are less efficient than the direct ones, the neutron star cooling proceeds more slowly than before (at least 10^5 yr, *standard cooling*). However, in regions with high proton fraction (reached only in the inner core of high mass neutron stars, see [233]), the fast direct Urca are still allowed, and the temperature drop occurs after tens of years (*rapid cooling*).

When the temperature is lower than 5×10^7 K, the neutrino emissivities become irrelevant, and photons radiated from the surface become the main cooling channel (*photon-cooling era*). The electromagnetic emission can be observed as a thermal component in the X-ray spectra of nearby neutron stars (see Section 1.4.2). Figure 1.1 shows the cooling curves, i.e. the evolution in time of the temperature of the crust (see Section 1.2.2) as a function of the age. The curves have been evaluated by Viganó [423] for different masses and envelope compositions: note also that in the photon-cooling era neutron stars with light-element envelopes (left panel) are much cooler than those with iron envelopes (right panel) [299].

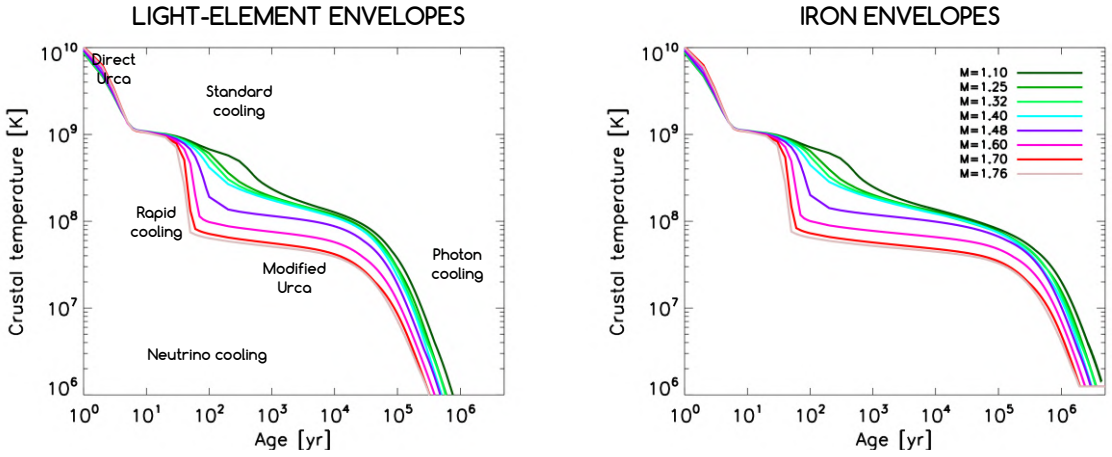

Figure 1.1: Cooling curves (crustal temperature vs. age) for eight stars (masses from 1.10 to 1.76 $M_\odot$) with light-element (left panel) and iron (right panel) envelopes. Different cooling regimes as a function of the age can be observed. Adapted from Viganó [423].

1.2.2 Internal composition and equations of state

Figure 1.2 shows a schematic drawing of the general structure of a neutron star, that is made of several shells with increasing density and pressure as the depth increases.

The outermost layer is the *atmosphere*, that is only a few cm thick and it is composed of H, He or C [62, 63, 282]. It leaves an imprint in the NS spectra, as it shapes the thermal photons emerging from the photosphere (see Section 3.1.2 for further details). The surface of the NS is called *envelope or ocean*, and it extends for ~ 100 m up to $\rho \sim 10^{10}$ g cm^{-3}. It can be liquid or solid (see Section 3.1.3), and it affects the thermal conduction from the (isothermal) star interior to the photosphere (see Section 3.1.1). The *crust* typically covers about one tenth of the NS radius and can be subdivided into an inner and an outer part. The outer crust extends from the surface to the neutron drip density, $\rho_{\rm drip} \approx 4.3 \times 10^{11}$ g cm^{-3}, that is the density at which the neutrons start to drip out of the nuclei. The inner crust extends to ρ_0 and is composed of

electrons, free superfluid neutrons and neutron-rich nuclei. The *core* constitutes the largest part of the neutron star, containing approximately 99% of the total mass, and it is subdivided into an outer and an inner part. The outer core occupies the density range $\rho \sim (1-2)\rho_0$, where matter consists mainly of degenerate neutrons and a few percent of protons and electrons because of the β-decay stability at such large densities. In the inner core of the neutron star, the density may become as high as $\rho \sim (10-15)\rho_0$.

Due to the growing Fermi energies, it may become energetically favorable for more exotic particles, rather than the standard composition of p, e^- and n, to occur at these high densities. For instance, neutrons may be replaced by hyperons, electrons may be replaced by pions or kaons and form a (superfluid) Bose-Einstein condensate. Finally, the density becomes even so high that the attractive force between quarks can be neglected so that the quarks become unconfined. Many authors debate the existence of quark NSs, but the lack of accurate first-principles predictions for the properties of QCD matter at high baryon densities has hindered firm conclusions so far [222].

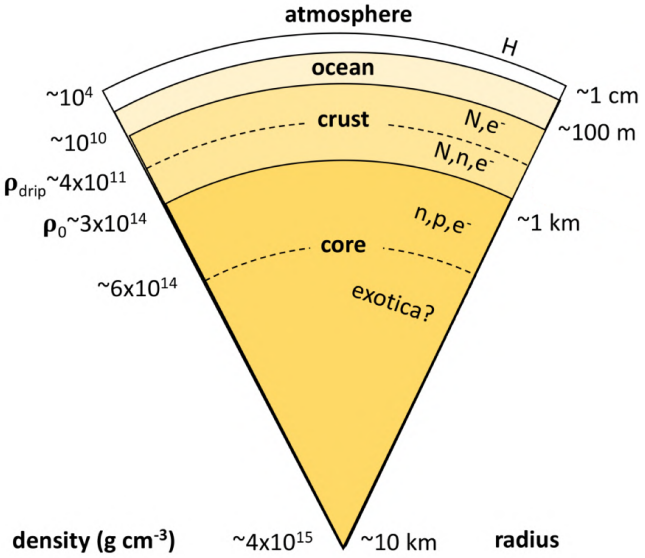

Figure 1.2: Schematic drawing of the structure of a neutron star (not to scale). Some indicative numbers for the size and density are given, and the main particle constituents are indicated: H stands for hydrogen, N for nuclei, n for neutrons, e^- for electrons and p for protons. The dashed lines indicate dividing lines between the inner/outer crust and core. Adapted from Degenaar & Suleimanov [80].

The unknown composition of the inner core adds to the poorly known strong-force interaction between hadrons: as a result, an equation of state (EOS) that describes the bulk matter is currently unknown (see e.g. Lattimer & Prakash [232]). However, the EOS is crucial to determine the NS mass and the radius: for a given EOS, the general relativistic structure equations (the Tolman-Oppenheimer-Volkoff equations) can be solved for an assumed central density, leading to a predicted mass and radius. Using a range of different central densities, the $M-R$ relation can be constructed for any given EOS. Some examples are illustrated in Figure 1.3[3].

Moreover, for each EOS there is a maximum central density beyond which no stable configuration is possible, hence every EOS is characterized by a maximum NS mass. The EOS is

[3]Created by Norbert Wex, http://www3.mpifr-bonn.mpg.de/staff/pfreire/NS_masses.html.

effectively a measure for the compressibility of the matter, which is also referred to as its softness: strong repulsive interactions between particles make the EOS harder, while the presence of hadrons more massive than neutrons and protons makes the EOS softer. Since for soft EOSs the matter is more compressible, these generally predict neutron stars with smaller maximum masses rather than harder EOSs.

Astrophysical observations give the chance to reverse the issue and to use a NS mass measurement to discard those EOSs that predict a maximum mass lower than the observed one. This is the case of the three massive NS ($M \gtrsim 2\ M_\odot$) displayed in Figure 1.3, whose masses have been derived with a technique called Shapiro delay [370]. The other EOSs can be tested through measurements of the mass [318], the radius [234, 81, 380], and the compactness (i.e. the ratio of mass and radius) [143, 144]. For a complete review of the electromagnetic observations used to test the NS EOSs, see Degenaar & Suleimanov [80].

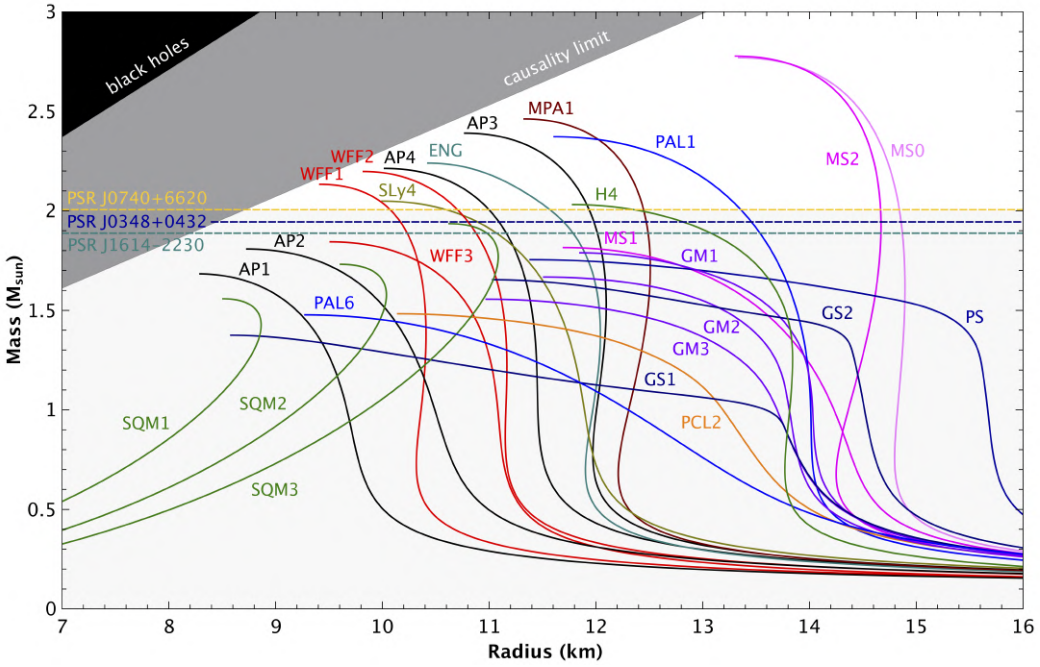

Figure 1.3: EOSs tabulated in Lattimer & Prakash [231] and provided by the authors. The massive NS are PSR J0740+6620 ($M = 2.17^{+0.11}_{-0.10}\ M_\odot$ [74]), PSR J0348+0432 ($M = 2.01 \pm 0.03\ M_\odot$ [10]), and PSR J1614−2230, ($M = 1.928 \pm 0.017\ M_\odot$ [83, 94]).

The ranges for observed masses and radii are $1 - 2\ M_\odot$ and $R = 10 - 15$ km, that lead to a compactness $x = R_S/R = 0.2 - 0.5$ (where $R_S = 2GM/c^2$ is the Schwarzschild radius). As a consequence, the effects of the general relativity theory deeply affect the NS properties; the most relevant ones are the gravitational redshift and the light bending.

Let's define z, called gravitational redshift, as

$$1 + z = \left(1 - \frac{R_S}{R}\right)^{-1/2}; \tag{1.1}$$

for the above quoted values of mass and radius, $z = 0.1 - 0.5$. Let's consider $z = 0.2$ for order of magnitude estimations. According to general relativity, the quantities measured on the NS surface are different from the same quantities measured by a distant observer (labeled with $_\infty$),

and they are related as follow:

$$T_\infty = T(1+z)^{-1} < T \tag{1.2}$$

is the temperature measured by a distant observer, that will appear colder, while

$$R_\infty = R(1+z) > R \tag{1.3}$$

is the radius, that will appear magnified. The bolometric luminosity, that is a function of temperature and radius, will appear weaker than the actual bolometric luminosity:

$$L_\infty = 4\pi R_\infty^2 \sigma T_\infty^4 = L(1+z)^{-2} < L \tag{1.4}$$

In general relativity, light rays do not travel in straight lines but rather along geodesic curves. The shape of these light trajectories depends on the geometry of space-time. In the case of Schwarzschild metric, the light trajectory lies in one plane and only two angles need to be connected to the surface normal: the emitted angle α and the observed angle ψ (see Figure 1.4). The correct connection is given by the so-called elliptic integral [309]

$$\psi = \int_R^\infty \frac{dr}{r^2}\left[\frac{1}{b^2} - \frac{1}{r^2}\left(1 - \frac{R_S}{r}\right)\right]^{-1/2} \tag{1.5}$$

where

$$b = R(1+z)\sin\alpha \tag{1.6}$$

is the impact parameter.

A simple and useful analytical approximation of the elliptic integral was derived by Beloborodov [33]:

$$1 - \cos\psi \approx (1-\cos\alpha)(1+z)^2. \tag{1.7}$$

This relation is applicable for $R > 2R_S$ and sufficiently accurate (error $< 3\%$) for $R > 3R_S$. The maximum impact parameter for a given z occurs when $\alpha = \pi/2$: $b_{max} = R(1+z) = R_\infty$, that is the observed stellar radius from infinity. From Eq. 1.7, $\alpha = \pi/2$ corresponds to $\cos\psi_{max} \approx 1 - (1+z)^2$. For a typical $z \approx 0.2$, $\psi_{max} \approx 116°$, that means that more than half star is visible.

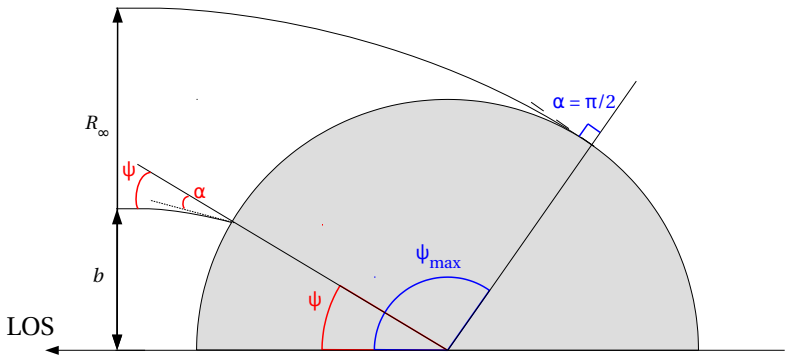

Figure 1.4: Schematic view of ray propagation. The angles α, ψ and ψ_{max} are also shown. b is the impact parameter for a given α (see Eq. 1.6), and $R_\infty = b_{max}$.

1.2.3 Rotation and magnetic field

There are two other important properties of neutron stars, that are the rotation and the magnetic field. The combined effect of these properties gives rise to the multiwavelength phenomena that characterize the neutron stars.

Neutron stars rapidly rotate with periods $P = 2\pi/\Omega$, that span from milliseconds to more than 10 seconds. The amount of kinetic rotational energy is

$$E = \frac{1}{2} I \Omega^2 \approx 10^{44} - 10^{52} \text{ erg}, \tag{1.8}$$

where $I \approx 10^{45}$ g cm^2 is the moment of inertia.

Neutron stars can be in a binary system, and then they spin up through accretion of the donor mass, or they can be isolated. In this case, they are observed to increase their periods: Richards & Comella [355] first measured the spin down of the Crab pulsar. The period first derivative, $\dot{P}$, spans the range $10^{-22} - 10^{-8}$ s s^{-1}, while the rate of loss of rotational kinetic energy is

$$\dot{E} = -I\Omega\dot{\Omega} = 4\pi^2 I \frac{\dot{P}}{P^3} \approx 10^{30} - 10^{35} \text{ erg s}^{-1}, \tag{1.9}$$

that is dubbed spin-down luminosity. If we assume that the physical mechanism responsible for the braking has an $\dot{E}$ that is a function of P and $\dot{P}$ only, then a differential equation for the period can be found by equating this $\dot{E}$ to Eq. 1.9:

$$\dot{P} = kP^{2-n}, \tag{1.10}$$

where n is called "braking index".

The simplest models relate the spin-down luminosity to the emission of electromagnetic radiation from a rotating magnetic field. In fact, it is believed that the strong magnetic fields of neutron stars originate from the supernova core-collapse with the conservation of magnetic flux: $B_{\rm NS} = \left(\frac{R_{\rm core}}{R_{\rm NS}}\right)^2 B_* \sim 10^{10} - 10^{12}$ G, where $R_{\rm core} \sim 10^5 - 10^6$ km, $R_{\rm NS} \sim 10$ km, and $B_* \sim 10^2$ G as typical values. Neutron stars are considered non-magnetized if their B is below

$$B_0 = \frac{m_e^2 c e^3}{\hbar^3} \approx 2.35 \times 10^9 \text{ G}, \tag{1.11}$$

and ultra-magnetized if their B is above the so-called "quantum critical field"

$$B_{\rm QED} = \frac{m_e^2 c^3}{e\hbar} \approx 4.41 \times 10^{13} \text{ G}. \tag{1.12}$$

B_0 and $B_{\rm QED}$ are obtained by equating the electron cyclotron energy

$$E_{\rm ce} = \frac{\hbar B}{m_e c} \approx 11.58\, B_{12} \text{ keV} \tag{1.13}$$

to the atomic binding energy and to the electron rest mass, respectively. Within these extreme values, a NS is more or less magnetized, which means that the effects of the magnetic field are important or negligible for the radiative transport, if Eq. 1.13 is greater or lower than the energy of the photons emitted by the NS itself.

When the dipolar magnetic torque is considered, $n = 3$ (see Section 1.3 for an analytical derivation), but other physical mechanisms have been investigated, as the outflow of relativistic particles (pulsar wind, $n = 1$ [269, 153]), or the emission of gravitational waves ($n = 5$ [6]). In order to measure n, we take the time derivative of Eq. 1.10 and we find that

$$n = 2 - P\ddot{P}\dot{P}^{-2}, \tag{1.14}$$

where $\ddot{P}$ is the second derivative of the period. It can be measured with enough precision only if the pulsar timing is particularly accurate and the observations are very long (see e.g. Hobbs et al. [178]), and if no short-term phenomena are present, such as glitches and timing noise. Espinoza et al. [90] elaborated a method to overcome this problem and to measure the braking index of the young glitching pulsars.

Table 1.1: Measured braking index values.

PSR Name	P	$\dot{P}$	$\ddot{P}$	n	Reference
	s	s s^{-1}	s s^{-2}		
B0531+21	0.033392412(1)	$4.20972(4) \times 10^{-13}$	$-1.815(2) \times 10^{-24}$	2.342(1)	[242]
B0540−69	0.050569703022(2)	$4.789091(4) \times 10^{-13}$	$-5.75(2) \times 10^{-25}$	2.13(1)	[92]
J1119−6127	0.40796298356(8)	$4.020220(3) \times 10^{-12}$	$-2.710(3) \times 10^{-23}$	2.684(2)	[433]
J1208−6238	0.44059072365(1)	$3.269514(2) \times 10^{-12}$	$-1.359(8) \times 10^{-23}$	2.598(1)	[68]
B1509−58	0.1512512583148(7)	$1.531467518(3) \times 10^{-12}$	$-1.287757437(2) \times 10^{-23}$	2.832(3)	[235]
J1734−3333	1.169340685(4)	$2.27941(8) \times 10^{-12}$	$5(2) \times 10^{-24}$	0.9(4)	[89]
J1833−1034	0.061883650010633(1)	$2.0201500(8) \times 10^{-13}$	$9.461(6) \times 10^{-26}$	1.857(1)	[363]
J1846−0258[a]	0.3248636173(1)	$7.08743(2) \times 10^{-12}$	$-9.918(1) \times 10^{-23}$	2.65(1)	[236]
J1846−0258[b]	0.32657128834(4)	$7.10745(4) \times 10^{-12}$	$1.875(4) \times 10^{-23}$	2.16(13)	[237]

Notes. [a] Spin parameters before the outburst of 2006 [100].
[b] Spin parameters after the outburst.

Although data on many pulsars are available in the literature, there are only eight pulsars generally accepted to yield reliable information on the pulsar breaking index (see Table 1.1, the recent compilation of Espinoza [91] and references therein). Examination of Table 1.1 shows that the measured braking index values are in the range $1 \lesssim n \lesssim 2.8$, which is consistently less than the predicted $n = 3$. There have been many attempts to extend/modify the basics of the magnetic-dipole braking model, or to include the energy loss through particle winds and gravitational waves (see, e.g., Hamil et al. [145, 146] and references therein), but there is no model currently available that would yield, consistently, the spread of the observed values.

1.3 Rotation-Powered Pulsars

The rotation-powered pulsars (RPPs) are a sub class of NSs that are detected because of their pulsed emission. Nowadays more than 2500 RPPs are known [249], and they have been detected from the radio band to the very-high energy γ-rays (see Section 1.4 for a description of the main observational features of each electromagnetic band).

The energy that sustains RPP emission is supplied by their fast rotation, via the braking operated by their intense magnetic field, that is assumed to be dipolar. In the following, I will present the classic model of Pacini [295, 296] and Gold [117, 118] of the magnetic-dipole

braking in the vacuum (Section 1.3.1) and its superseding model of Goldreich & Julian [119] (Section 1.3.2).

1.3.1 The magnetic-dipole braking model

Outside the star, the magnetic field assumes a dipole configuration (in polar coordinates):

$$B(r,\theta,\phi) = \frac{B_\mathrm{p}}{2}\left(\frac{R}{r}\right)^3 \begin{pmatrix} 2\cos\theta \\ \sin\theta \\ 0 \end{pmatrix}, \tag{1.15}$$

where B_p is the field at the magnetic pole and θ is the magnetic colatitude. The magnetic dipole moment μ, that has module $\mu = \frac{1}{2}B_\mathrm{p}R^3$, in general forms an angle ξ with the rotation axis Ω. As the star rotates, according to the Larmor formula, it dissipates energy at a rate

$$\dot{E} = \frac{2}{3c^3}|\ddot{\mu}|^2 = \frac{2}{3c^3}\mu^2\sin^2\xi\,\Omega^4 = \frac{32\pi^4}{3c^3}\left(\frac{1}{2}B_\mathrm{p}\sin\xi\right)^2 R^6 P^{-4}. \tag{1.16}$$

This formula is valid in vacuum conditions and there is an actual dissipation only if $\sin\xi \neq 0°$, i.e. the pulsar is not an aligned rotator. With these assumptions, one can infer the characteristic surface magnetic field (that is half B_p, while for simplicity $\sin^2\xi = 1$ is assumed) that is responsible for the energy loss by equating Eq. 1.9 with Eq. 1.16:

$$B_\mathrm{s} = \frac{1}{2}B_\mathrm{p}\sin\xi = \sqrt{\frac{3c^3 I}{8\pi^2 R^6}P\dot{P}} = 3.2\times10^{19}\,(P\dot{P})^{1/2}\ \mathrm{G}. \tag{1.17}$$

B_s generally ranges from 10^8 to 10^{15} G and a typical value is 10^{12} G, in agreement with the expected values discussed above.

If we assume that the magnetic field is constant in time, from Eq. 1.17 it also follows that $\dot{P} \propto P^{-1}$, that is Eq. 1.10 with braking index $n = 3$. If it is integrated over time [247], the age of the pulsar can be evaluated:

$$\tau = \frac{P}{(n-1)\dot{P}}\left[1 - \left(\frac{P_0}{P}\right)^{n-1}\right], \tag{1.18}$$

where P_0 is the initial period and $n \neq 1$; if $P_0 \ll P$ and $n = 3$ are assumed, then Eq. 1.18 becomes

$$\tau_c = \frac{P}{2\dot{P}}, \tag{1.19}$$

that is known as "characteristic age". Actually, τ_c is a good approximation of the real NS age (that can be evaluated through different methods, e.g. from historical records, SNR associations, the kinematics or the cooling properties of the source) if the spin period of the star at birth was much smaller than today. On the contrary, it will over-estimate the true age: as an example, the Crab pulsar has $\tau_c = 1259$ years, but it actually is 965 years old.

P and $\dot{P}$ play a fundamental role in characterizing the NS properties (see Eqs. 1.17 and 1.19) and the Galactic NS population is usually represented in the $P-\dot{P}$ diagram (shown in Figure 1.5), as the ordinary stars are represented in the Hertzsprung-Russell diagram.

RPPs, the most abundant population, fill the central region of the plot; a newborn pulsar appears in the top-left corner and, according to the magnetic-dipole braking model, it evolves

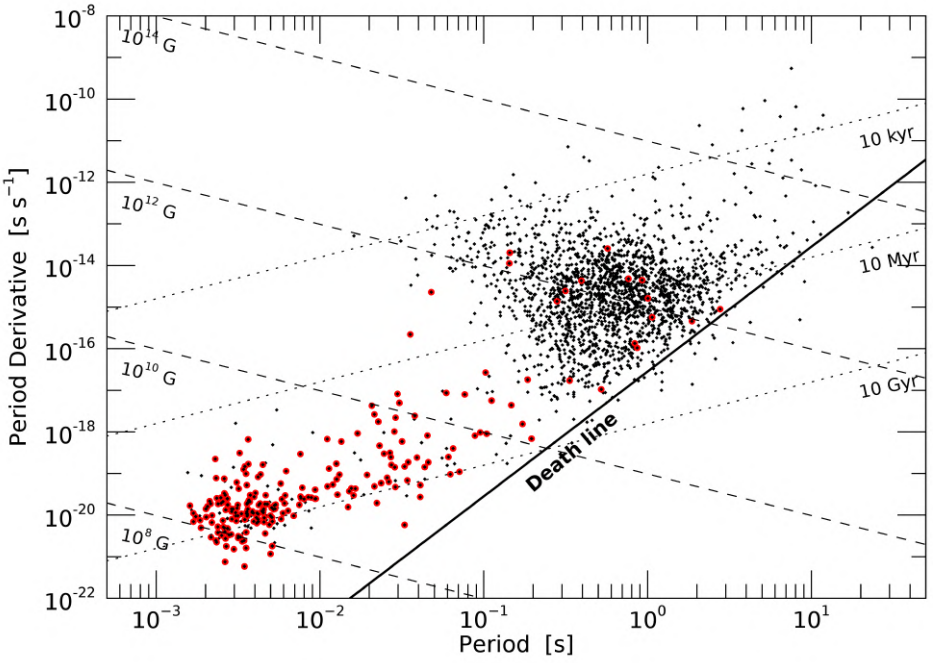

Figure 1.5: $P - \dot{P}$ diagram of rotation-powered pulsars. A significant fraction (10%) are in a binary system (red circles). Lines of equal characteristic age (dotted, $10^4 - 10^{10}$ yr) and equal dipole magnetic field (dashed, $10^8 - 10^{14}$ G) are indicated. The radio pulsar death line $B/P^2 = 1.7 \times 10^{11}$ G s^{-2} [37] is also shown. The data are taken from the ATNF Pulsar Catalogue [249].

along the B_s constant lines (dashed), crossing the τ_c constant lines (dotted). The bottom-right corner of the plot is empty because when pulsars cross the so-called "death line" [37], they are too old and too weak to emit a pulsating signal [24, 25].

Actually, there is a population of RPPs that have $\tau_c \gtrsim 1$ Gyr that are still detected: they are known as "millisecond" pulsars (MSPs) because of their short and stable period ($P \lesssim 10$ ms, $\dot{P} \lesssim 10^{-18}$ s s^{-1}). See e.g. Manchester [246] for a recent review. They are old pulsars that have been spun up through the accretion of matter from the binary companion at some time in the past, as part of a binary system. The majority of them still have a companion star, as it can be seen in Figure 1.5, where the pulsars in a binary system are represented by a red empty circle.

1.3.2 The magnetosphere

As it was first noted by Goldreich & Julian [119] in their classic paper, the above-described model fails, because a rotating neutron star cannot be surrounded by vacuum: the intense magnetic fields coupled with the fast rotation of the star will induce electric fields. At the stellar surface, they exceed the gravitational field by many orders of magnitude and thus they are capable of pulling charges out of the star.

Charges orient themselves along the magnetic field lines above the star surface, and together they form the so-called magnetosphere of the NS. The magnetosphere corotates with the star for distances from the spin axis up to the radius at which the corotation velocity equals

the speed of light:

$$R_{\rm LC} = \frac{c}{\Omega} \sim 5 \times 10^9 \; P \text{ cm}. \tag{1.20}$$

$R_{\rm LC}$ is called light-cylinder radius and it delimits the region of the magnetosphere where the charges are in a force-free regime:

$$\mathbf{E} + \frac{\mathbf{\Omega} \times \mathbf{r}}{c} \times \mathbf{B} = 0. \tag{1.21}$$

It is straightforward to show that $\mathbf{E} \cdot \mathbf{B} = 0$: this means that charges cannot be accelerated along the magnetic field lines. They have a charge density

$$\rho_{\rm GJ} = \frac{\nabla \cdot \mathbf{E}}{4\pi} = -\frac{\mathbf{\Omega} \cdot \mathbf{B}}{2\pi c(1 - |\mathbf{\Omega} \times \mathbf{r}/c|^2)}, \tag{1.22}$$

known as Goldreich-Julian or corotation charge density. Outside the light cylinder, there is the open field lines region. $\rho_{\rm GJ}$ can be positive or negative according to the sign of Eq. 1.22: $\mathbf{\Omega} \cdot \mathbf{B} = 0$ defines a null charge surface and it spatially separates the opposing charges (see Figure 1.6, left panel).

When the effect of the magnetosphere is taken into account in the force-free models, the energy losses is well approximated by [378]:

$$\dot{E}_{\rm ff} = -\frac{B_{\rm p}^2 R^6 \Omega^4}{4c^3}(1 + \sin^2 \xi). \tag{1.23}$$

The power in this case is a factor $1.5(1 + \sin^2 \xi)$ larger than for the vacuum orthogonal rotator (see Eq. 1.16), and it is non-zero even in the aligned case ($\xi = 0^\circ$). Therefore, the relations 1.17 and 1.19 of the previous section still hold.

In this framework there is an internal problem: if the magnetosphere is completely force-free, then no acceleration of charges, currents or radiation would exist. A real pulsar must operate between the two extremes of the vacuum and the force-free states, but a self-consistent, global solution has not yet been found [147]. Right after the work of Goldreich and Julian, many different models that predict the existence of vacuum regions (or gaps) have been proposed. They can be divided into two classes depending on where the gaps are (see Figure 1.6, right panel): the polar cap model, in the regions above the magnetic polar caps [386, 365, see also Section 3.3], and the outer gap model, in the regions extending from the null charge surface to the light cylinder [65, 66, 67]. The latter applies only to γ-ray emission and therefore decouples the γ-emitting region from the radio one, but it is not supported by the recent γ-ray observations [152].

In the polar cap model, the particles, accelerated by rotation-induced electric fields above the polar cap, move along the dipole open magnetic field lines and produce curvature radiation. In this environment, photons above 1 GeV are absorbed by the magnetic field and produce $e^+ - e^-$ pairs, which radiate synchrotron photons and produce a second generation of pairs. Such a cascade continues until the synchrotron photons fail to meet the energetic requirements to pair-produce and can escape to contribute to the high-energy pulsar emission; the remaining pairs may supply particles to a coherent process that is responsible for the radio emission. This is how the multiwavelength pulsating emission, that allowed us to discover more than 2500 pulsars so far [249], is produced.

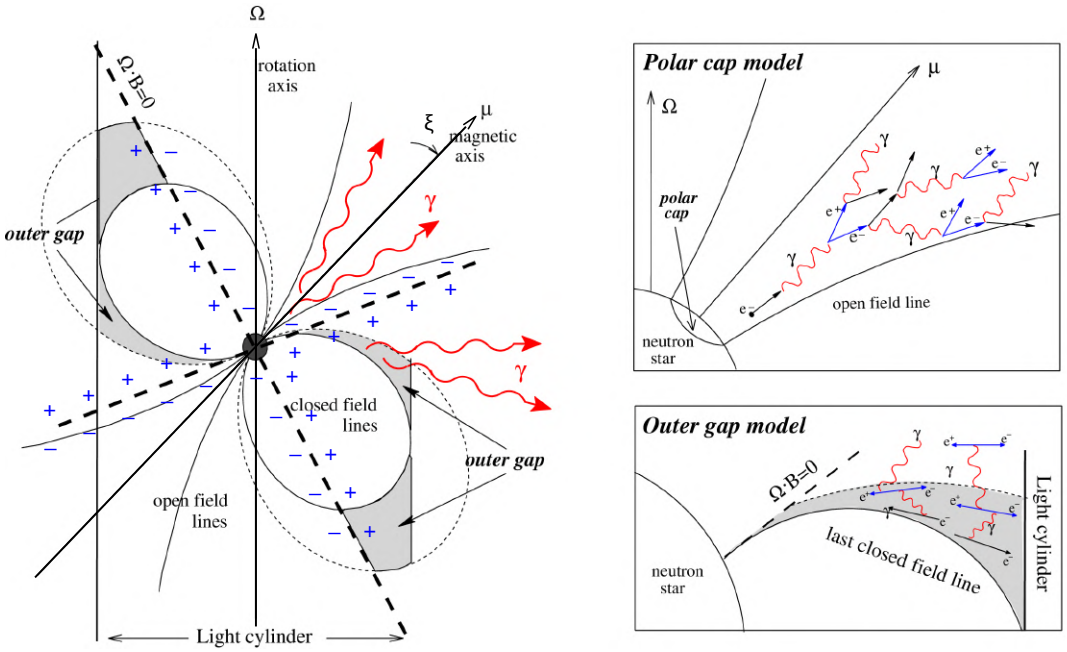

Figure 1.6: Left panel: Scheme of a pulsar magnetosphere, with the light cylinder and the null charge surface ($\mathbf{\Omega} \cdot \mathbf{B} = 0$), that induces a charge separation. The pulsar spin axis is misaligned with the magnetic axis of an angle ξ. Right panel: Illustration of the two main mechanisms of high-energy emission: the polar cap model, according to which the particles are accelerated above the magnetic polar caps, and the outer gap model, according to which the radiation is produced in the outer magnetosphere, between the null charge surface and the light cylinder, along the last closed line. Adapted from Lopez et al. [238].

1.4 Observational properties

Almost the totality of the known pulsars are radio pulsars (Section 1.4.1), but a few hundreds of them are now detected as high-energy emitters (Sections 1.4.2 and 1.4.3). More recently, new neutron stars and counterparts of known radio or X-ray pulsars have been detected also in the infrared, optical and ultraviolet bands (Section 1.4.4). Here, I briefly summarize the neutron star phenomenology in different energy bands.

1.4.1 Radio band

The most common manifestation of a NS is the detection of very regular pulses in the radio band (about 96.5% of the total known pulsars). The individual pulses of a source have different shapes, but the superimposition of some hundreds of them gives an integrated pulse profile, which is stable and characteristic for each pulsar. A review of the radio emission will be presented in Chapter 2, with a particular attention to the phenomenology of the individual pulses (Section 2.3).

Pulsar coherent radio emission originates within the flux tube of the open force lines of dipolar magnetic field, but the details of the emission mechanisms are poorly understood. From

an observational point of view, the efficiency of the radio emission is $10^{-7} - 10^{-5}$ with respect to the spin-down power [239]. The radio spectrum follows a power-law distribution $S_\nu \propto \nu^\alpha$, with spectral index in the range $-4 < \alpha < 0$ [252]; this spectral shape is indeed an imprint of the synchrotron emission. Another observational feature that can be ascribed to the magnetic field is the intense linear polarization [278].

The broadband emission of pulsars can be used to probe the physical conditions of the interstellar medium (ISM). Specifically, radio waves traveling in the ISM are dispersed by free electrons such that there is a delay Δt in the times of arrival of signals of different frequencies $\Delta\omega$ (see e.g. Chapter 10.4 of Shapiro & Teukolsky [371] for the mathematical derivation):

$$\frac{\Delta t}{\Delta\omega} = -\frac{4\pi e^2}{m_e c\omega^3}\mathrm{DM}, \tag{1.24}$$

where m_e and e are the mass and the charge of the electron, respectively, and the dispersion measure DM is defined as

$$\mathrm{DM} = \int_0^d n_e \, dl. \tag{1.25}$$

The DM is expressed in pc cm^{-3}, and it represents the integrated column density of free electrons along the line of sight. Models of the electron distribution in the Galaxy have been developed by Taylor & Cordes [399], Cordes & Lazio [72], Yao et al. [439]: by specifying the galactic coordinates and the DM, the distance of the pulsar is inferred from Eq. 1.25. A typical error on this distance is $\sim 20\%$, that depends on the uncertainties of the electron distribution model rather than the measuring error of DM, given that it depends on well-measured quantities as Δt and $\Delta\omega$.

1.4.2 X-rays

At present, about 100 X-ray pulsars are known (see Table B.1). A more in-depth discussion of the X-ray phenomenology will be presented in Chapter 3, but here I briefly summarize the characteristics of the X-ray spectral components.

A thermal component is emitted by the hot surface of the NS, that after the earlier stages has a surface temperature of about 10^6 K; assuming a blackbody emission, the spectrum peaks at ≈ 0.1 keV. If the surface temperature has a non-uniform distribution (see Section 3.2), the light curve of this component is modulated as a function of the stellar rotation phase.

A nonthermal component is instead strongly pulsed, because it is produced in the magnetosphere and emitted in beams due to the anisotropies caused by the magnetic field (see Section 3.3). The spectrum follows a power-law distribution with slope $\Gamma \approx 1 - 4$ [27]; the observed X-ray efficiency is about $10^{-4} - 10^{-3}$. In addition, several young and/or energetic pulsars are surrounded by nebulae that can emit X-rays through synchrotron emission (called pulsar wind nebulae, PWNe). This radiation is non-pulsed and nonthermal and its properties depend also on the local conditions, like the density of the ambient interstellar medium or the interaction with the remnants of the supernova that formed the neutron star. For a review on the PWNe see, e.g., Gaensler & Slane [96].

In middle-aged pulsars, a third spectral component can be present. It is thermal-like, well-fitted by a blackbody with $kT \approx 0.1 - 0.3$ keV and a radius that is a small fraction of the star radius, but its origin is linked to the nonthermal emission (see Section 3.4). In fact, in the photon-pair cascade, some particles are backward accelerated, collide with the star surface and

heat it [11, 149, 150]. Given that the reheating is localized in the polar cap regions, hot spots are observed and the light curve is pulsed.

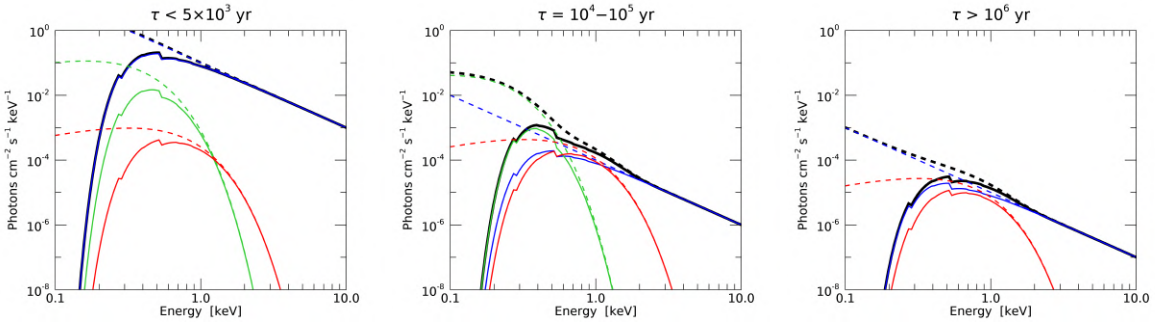

Figure 1.7: Scheme of the absorbed (black solid line) and unabsorbed (black dashed line) X-ray spectra of RPPs for different evolutionary stages: $\tau < 5 \times 10^3$ yr (left panel), $\tau = 10^4 - 10^5$ yr (central panel) and $\tau > 10^6$ yr (right panel). The three spectral components are nonthermal (blue line), thermal from the cooling surface (green line) and thermal from the polar caps (red line).

The relative importance of the spectral components mentioned above varies with the pulsar ages (see Figure 1.7): young and energetic pulsars ($\tau \lesssim 5 \times 10^3$ yr) are dominated by nonthermal emission phenomena; middle-aged pulsars ($10^4 \lesssim \tau \lesssim 10^5$ yr) show all the three spectral components; old pulsars ($\tau \gtrsim 10^6$ yr) are too cold to emit in the X-rays from the whole surface, and a mixture of nonthermal and polar cap thermal components is observed. This scenario holds for the ordinary RPPs (see Chapter 8), but things are much more complicated for other X-ray emitting isolated neutron stars, whose emission is not driven by the rotation (see Section 1.5).

The softest part of the X-ray spectrum is absorbed by the bounded electrons of the ISM because of the photoelectric effect. The amount of extinction, which is expressed in terms of the equivalent atomic hydrogen column density $N_{\rm H}$, is sensitive to gas and molecular clouds, which trace the warm and cold phases of the ISM [434]. He et al. [154] showed that there is a correlation between the DM defined in Eq. 1.25 and $N_{\rm H}$:

$$N_{\rm H} = 0.30^{+0.13}_{-0.09}\ {\rm DM}, \tag{1.26}$$

where $N_{\rm H}$ is in units of 10^{20} cm^{-2} and DM in pc cm^{-3}. Given that radio wave dispersion is due to free electrons, and X-ray absorption is due to bound electrons, this relation can be used to infer the (average) ISM ionization: from Eq. 1.26, a ionization of 10^{+4}_{-3}% is derived.

In some cases, the spectral continuum is absorbed by broad features (see Table 1.2). In fact, in the presence of a strong magnetic field, the electron transverse momentum is quantized with typical transverse dimension of the electron Landau orbit

$$\lambda_\perp = \left(\frac{\hbar c}{eB}\right)^{1/2}, \tag{1.27}$$

whereas the longitudinal (parallel to B) momentum can change continuously. The quantization of electron motion leads to the appearance of cyclotron emission and absorption lines at the so-called cyclotron energy $E_{\rm cyc}$, defined in Eq. 1.13 [443, 327]. Observationally speaking, the measure of $E^{\infty}_{\rm cyc}$ in the soft X-ray spectra can be used to obtain a direct measurement of the surface magnetic field:

$$B_{\rm ce} = \frac{E^{\infty}_{\rm cyc}}{1{\rm keV}} \frac{m_e c}{\hbar e} (1+z)^{-1} \approx \frac{E^{\infty}_{\rm cyc}}{1{\rm keV}}\, 7.2 \times 10^{10}\ {\rm G} \tag{1.28}$$

if the absorbed particles are electrons,

$$B_{\rm cp} = \frac{E^{\infty}_{\rm cyc}}{1{\rm keV}} \frac{m_p c}{\hbar e} (1+z)^{-1} \approx \frac{E^{\infty}_{\rm cyc}}{1{\rm keV}} \, 1.3 \times 10^{14} \, {\rm G} \tag{1.29}$$

if the absorbed particles are protons.

X-ray features could also be produced by bound-bound transitions of the H atom moving in a strong magnetic field [307]. The spectral profile of the bound-bound opacities becomes continuous in a wide frequency range, resembling a reversed bound-free profile, because of the magnetic broadening due to the thermal motion of atoms across the magnetic field (not to be confused with the Doppler shift) [302]. Thus, narrow spectral lines should not be expected in the thermal-like NS spectrum even if it is emitted from a region of nearly uniform magnetic field. To date, the calculation of the cross section of photons with bound states of atoms and ions has been realized for atoms of hydrogen [328, 329] and helium [283], and for exotic ions [412].

1.4.3 γ-rays

Being among the most energetic objects in the Universe, the neutron stars are perfect candidates to be γ-rays emitters (see Caraveo [58] for a review). The Crab and Vela pulsars were the first two γ-ray sources identified in the 1970's by SAS-2 [93] and COS-B [390], and in the 1990's the Compton Gamma-Ray Observatory brought the pulsar grand total to ten; one of them, Geminga, was undetected at radio wavelengths [40]. The current generation of γ-ray detectors (The Large Area Telescope (LAT) on the Fermi Gamma-Ray Space Telescope [17] and AGILE [396]), has vastly increased the population of known of γ-ray pulars, approaching to more than 200 objects[4]. Figure 1.8 shows the sky distribution (in Galactic coordinates) of the known γ-ray pulsars, that can be radio-quiet or radio-loud, ordinary RPPs or MSPs.

The increasing statistics of high-energy pulsars helps to constrain the emission models, providing information about the region of magnetospheric emission and the involved electromagnetic processes, like curvature radiation and inverse Compton. The γ-ray efficiency is about $10^{-2} - 10^{-1}$ and an heuristic relation between L_γ and $\dot{E}$ was found by Thompson [408]:

$$L_\gamma = \sqrt{10^{33} \frac{\dot{E}}{{\rm erg \, s^{-1}}}} \, {\rm erg \, s^{-1}}, \tag{1.30}$$

that is valid for $\dot{E} > 10^{34}$ erg s^{-1}. This relation has subsequently been explained by, e.g., Harding et al. [151].

γ-ray pulsars were thought to be steady emitters, until an unexpected flux variation in PSR J2021+4026 was discovered [8]. The flux decrease, which took place in less than one week, was associated with a 4% increase in the pulsar spin-down rate and a change in the light curve.

1.4.4 Infrared, optical and ultraviolet bands

Neutron stars are intrinsically faint in the ultraviolet, optical and infrared wavelengths. Soon after the discovery of pulsars, Cocke et al. [69], Nather et al. [287] discovered optical signals from the Crab pulsar, that nowadays is by far the most intense pulsar at optical wavelengths.

[4]See the Fermi-LAT fourth source catalogue [403] and http://confluence.slac.stanford.edu/display/GLAMCOG/Public+List+of+LAT-Detected+Gamma-Ray+Pulsars for an updated list of the detected γ-ray pulsars.

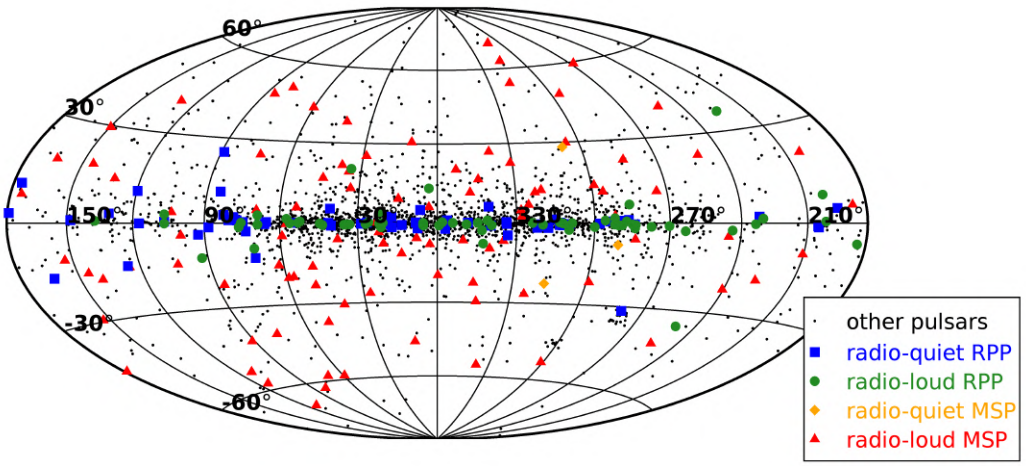

Figure 1.8: Pulsar sky map in Galactic coordinates; γ-ray pulsars are highlighted by colored symbols. Data are taken from the ATNF Pulsar Catalogue [249] and from the GLAST LAT Multiwavelength Coordinating Group web page [footnote 4].

However, technological advances recently led to the identification of counterparts of a few tens of pulsars (see Mignani [270] and references within).

Studying optical light curves, together with the X-ray and γ-ray ones, completes the mapping of the emission regions in the magnetosphere, while the measurement of polarization is crucial to test magnetosphere models. The spectroscopy can constrain the cooling model, because these bands include the bulk of thermal emission of cold stars with ages $\gtrsim 1$ Myr. Last but not least, the good angular resolution of optical observations allows one to measure proper motions and parallaxes, getting fair estimates of distances.

1.5 Classes of isolated neutron stars

X-ray observations have been crucial to discover other manifestations of isolated NSs, that differ from the ordinary RPPs. According to their phenomenology, they have been divided in different classes: there are the magnetars (Section 1.5.1), the X-ray-dim isolated neutron stars (XDINSs, Section 1.5.2), the central compact objects (CCOs, Section 1.5.3), and a transitional class of RPPs characterized by a high magnetic field (high-B, Section 1.5.4).

Each of these classes sits in a particular location on the $P - \dot{P}$ diagram, as shown in Figure 1.9 with a zoom-in of the slowly-rotating isolated pulsars.

1.5.1 Magnetars

Magnetars are a small group[5] of isolated, slowly rotating ($P \sim 2 - 12$ s) neutron stars. For recent reviews see Mereghetti et al. [265], Turolla et al. [416], Kaspi & Beloborodov [206].

Magnetars were historically classified in two distinct groups according to their manifestations: some are characterized by repeating X- and soft γ-ray bursting activity and therefore are called soft gamma repeaters (SGRs), others are less active and were first discovered by

[5] A catalog of magnetars can be found at http://www.physics.mcgill.ca/~pulsar/magnetar/main.html.

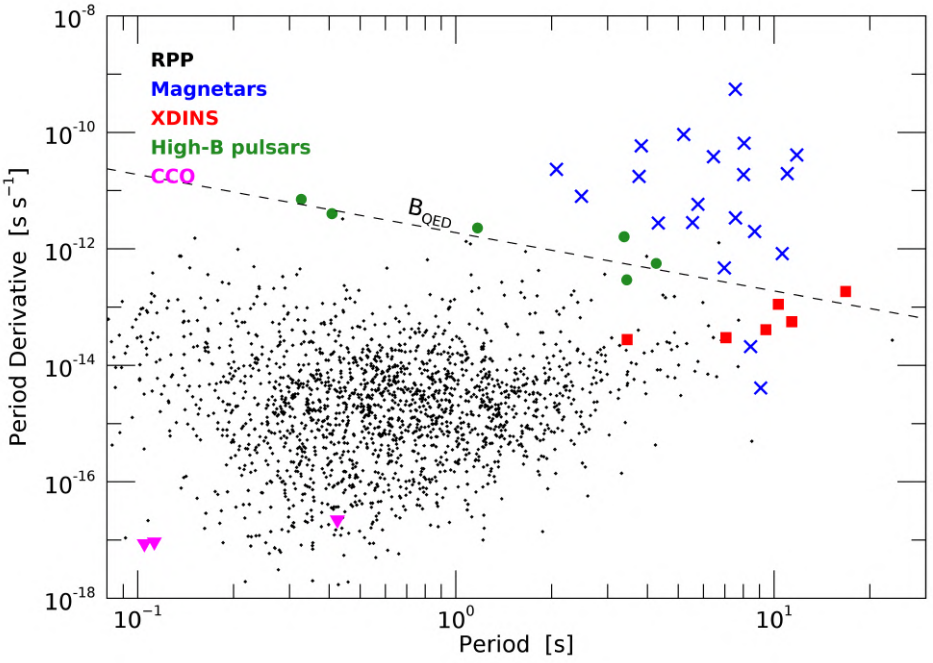

Figure 1.9: $P - \dot{P}$ diagram of isolated rotation-powered pulsars (black dots) and other classes of isolated neutron stars (colored symbols) discussed in the text. The line of constant $B = B_{\rm QED}$, defined in Eq. 1.12, is indicated by a dashed line. The data are taken from the ATNF Pulsar Catalogue [249].

observations of persistent X-ray pulsations (anomalous X-ray pulsars, AXPs). However, this distinction has been increasingly blurred as most sources now show properties of both classes (e.g., [99, 208, 436, 351, 189]) and both are regarded as magnetars.

From magnetars timing parameters, obtained by X-ray observations, very intense magnetic fields of about $10^{14} - 10^{15}$ G are derived assuming the dipole formula. This field strength is well above $B_{\rm QED}$ defined in Eq. 1.12. Some theories predict that under such a strong field, pair creation will become ineffective due to photon splitting, thus suppressing the radio emission [24, 25].

Magnetars are rather young objects ($\tau \sim 10^3 - 10^4$ yr), and some of them have a SNR association [354, e.g.]. It is generally believed that magnetar X-ray luminosity, that is greater than its $\dot{E}$, is powered by the decay of the ultra-high magnetic field [88, 406, 407, 404]. No stellar companions have been discovered in magnetars, ruling out accretion as a possible source of energy.

The main manifestations of magnetars occur in the X-ray energy range. All known confirmed magnetars show pulsations in the soft X-ray band (< 10 keV) and many of them have also been detected in hard X-rays, up to $\sim 100 - 200$ keV. In the GeV-TeV ranges, only upper limits are available [1], while in the radio band only few magnetars are detected, and they are characterized by large variability both in flux and pulse profile shape on timescale of days, by a very flat spectrum ($S_\nu \propto \nu^\alpha$, with $\alpha > -0.5$), and high polarization [56, 57].

The emission is characterized by short- and long-term variability. Magnetars exhibit bursts with duration of $0.1 - 1$ s (short) and $1 - 40$ s (intermediate), during which the luminosity increases of several order of magnitude, and giant flares, that are rare events with an energy

output of $\sim 10^{44} - 10^{47}$ erg [416]. Long term variations can occur as gradual and moderate changes in the flux, accompanied by variations in the spectrum, pulse profile, and spin-down rate. Finally, some sources show outbursts[6] [73], i.e. sudden enhancements of the X-ray flux up to a factor of 1000 with respect to the value in the quiescence phase, during a period of about 1 yr, frequently associated with burst emission. In some cases [76, e.g.], outburts were key in revealing previously undetected sources, with a quiescence emission too faint to be observed.

The persistent X-ray emission is characterized by soft thermal spectra ($kT \sim 0.3 - 0.9$ keV) plus a power-law component in the hard X-ray band with photon index $\Gamma = 2 - 4$. It is commonly interpreted as repeated resonant scattering of thermal photons from the star surface on to charged particles flowing in the twisted magnetosphere [405, 289, 290]. The continuum is often absorbed by proton cyclotron lines, due to the high magnetic fields [383, 350, 35]. Magnetars display X-ray pulse profiles with a variety of shapes (from simple sinusoids to multipeaked) and spanning a large range of pulsed fractions (from less than 10 % to nearly 100 %) [265].

1.5.2 X-ray-Dim Isolated Neutron Stars

Observations with the *ROSAT* satellite in the mid-1990s led to the discovery of a small group of nearby (a few hundred parsecs) isolated neutron stars characterized by thermal emission at soft X-rays, now known as XDINSs (X-ray-dim isolated neutron stars; see Haberl [137], Turolla [414] for reviews). The XDINSs have spin periods in the range $P \sim 3 - 17$ s and period derivatives of a few 10^{-14} s s^{-1}, which result in characteristic ages of $\tau_c \approx 1 - 4$ Myr and magnetic fields of the order of a few 10^{13} G.

The XDINSs have X-ray luminosities of $10^{31} - 10^{32}$ erg s^{-1}, higher than their spin-down power. Their X-ray spectra are very soft, with blackbody temperatures of $kT \sim 45 - 110$ eV, often showing the presence of broad absorption lines. If these lines are interpreted as proton cyclotron features or atomic transitions [196, e.g.], the magnetic fields estimated from their energies are of the same order as those derived from the spin-down rate assuming magnetic dipole braking. The X-ray emission of XDINSs, consisting only of thermal components, is believed to come directly from the star surface and, given the small distance of these sources, it is little affected by photoelectric absorption in the interstellar medium. Recently, the X-ray continuum of the seven known XDINSs have been fitted with two blackbody components, to account for a temperature distribution on the surface [440].

All the XDINSs have an optical/ultraviolet counterpart (five secure and two likely identifications [197]). The emission is thermal-like, but the flux is about a factor $5 - 50$ above the extrapolation at low energies of the best-fitting X-ray blackbody. The origin of this optical excess is still an open question [431, 430]. The discovery of XDINS counterparts made it possible to measure their parallax [428, 402] and their proper motions, revealing that their birthplace is probably the Gould Belt [321]. As a consequence, the XDINSs have about $0.3 - 1$ Myr and therefore they are younger than inferred from the timing parameters.

Another distinctive property of the XDINSs is that they are not detected in the radio band[7] [214]. The reason for the lack of radio emission is still uncertain. One possibility is that this is due to their old age and long spin period [24, 25]. However, a few radio pulsars with periods $\gtrsim$ 10 s have recently been discovered: PSR J0250+5854 with $P = 23.5$ s [393], and PSR J2251−3711 with $P = 12.1$ s [281]. Another explanation might be related to the geometrical configuration

[6] See also http://magnetars.ice.csic.es/#/welcome for a complete catalogue of outbursting magnetars.

[7] The possible detection of pulsed emission from two XDINSs at very low frequencies [244, 245] is so far unconfirmed.

of their magnetosphere that, especially if they are old magnetars, might be strongly nondipolar [416]. Finally, it cannot be excluded that (at least some of) the XDINSs are simply ordinary radio pulsars with radio beams unfavorably aligned with respect to the Earth (see Section 6.5).

1.5.3 Central Compact Objects

The central compact objects (CCOs) form a class of isolated NSs that are found in the center of young ($0.3 - 7$ kyr) SNRs, that emit only in the X-rays and have no counterparts at any wavelength [273]. See the recent reviews of Gotthelf et al. [130], De Luca [78]. At present, the class counts a dozen objects, three of which are pulsators [452, 127, 125]. The CCOs are detected in the soft X-ray range, and their spectra are exclusively thermal, with high temperatures ($0.2 - 0.5$ keV) and very small emitting radii (ranging from 0.1 to a few km). Two sources show absorption features at $0.7 - 0.8$ keV [41, 128].

The three pulsating CCOs have periods of $0.1 - 0.4$ s and spin derivatives of about 10^{-17} s s^{-1} [139, 130], from which weak dipole magnetic fields ($B_{\rm s} \approx 10^{10}$ G) and high characteristic ages ($\tau_c \approx 10^8$ yr) are derived. This is at variance with the SNR associations, and the reason could be that the approximation of Eq. 1.18 is no longer valid because these sources have $P \approx P_0$.

Also the picture of CCOs as weakly-magnetized NSs has issues: the high pulsed fraction (up to 64 % [139]) and the high contrast-ratio temperature surface distribution cannot be easily explained without invoking magnetic fields of $10^{14} - 10^{15}$ G [369].

1.5.4 High-B pulsars

Among the RPPs, there is a sub-sample of objects having high magnetic fields ($B \gtrsim B_{\rm QED}$), which shows distinctive properties of other classes of isolated neutron stars (see the review of Ng & Kaspi [288]).

PSR J1846−0258 is the youngest pulsar known ($\tau_c \approx 700$ yr), located at the center of the supernova remnant Kes 75 [126]. It was behaving like a common radio-quiet RPP [158] with a high magnetic field ($B_{\rm s} = 5 \times 10^{13}$ G), when in 2006 Gavriil et al. [100] reported five short X-ray bursts from the pulsar, along with temporary changes in the spectral and timing noise properties (see also Table 1.1). Coincidentally, Kumar & Safi-Harb [221] reported the increase in the pulsar X-ray flux of a factor 7 and the softening in its spectrum. These observations suggested the magnetar-like nature of PSR J1846−0258. A very similar outburst has been detected from a second high-B RPP [133], namely the radio pulsar PSR J1119−6127, that has $\tau_c = 1600$ yr and $B_{\rm s} = 4 \times 10^{13}$ G.

At present, PSR J1819−1458 is the only rotating radio transient (RRAT) detected in X-rays [258, 352, 274]. This class of radio pulsars does not exhibit regular radio pulses, but sporadic and brief radio bursts with time separations of minutes to a few hours [258, 259, 211]. PSR J1819−1458 is a 0.1 Myr pulsar with a magnetic field of 5×10^{13} G, that exhibits a thermal X-ray spectrum with $kT \approx 130$ eV and a broad absorption feature, possibly composed of two lines at 1.0 and 1.3 keV [274].

Finally, PSR J0726−2612 is an ordinary RPP that has spin period $P = 3.44$ s and $\dot{P} = 2.93 \times 10-13$ s s^{-1}, implying a characteristic age $\tau_c = 2 \times 10^5$ yr and $B_{\rm s} = 3 \times 10^{13}$ G. It was discovered in the Parkes High-Latitude Survey [54] with a single-peaked profile. It was observed in the X-ray band in the 2006 with the *Chandra* satellite, and Speagle et al. [376] reported a soft thermal spectrum with blackbody temperature $kT \approx 87$ eV, and pulsations with a sinusoidal,

double-peaked profile. PSR J0726−2612 timing parameters and X-ray spectrum strongly resemble those of the XDINSs, but the main difference is the radio emission, that characterizes PSR J0726−2612 but that is absent in all the XDINSs. The analysis of a deeper *XMM-Newton* observation, presented in Chapter 6, reinforces the similarities and discusses the differences.

1.5.5 Grand Unification of Neutron Stars

The attempt to explain the different manifestations of NSs in the context of a unified evolutionary picture is one of the current challenges in the study of neutron stars [205, 187]. The idea is to find a combination of initial distributions of parameters (e.g. P, B, v...) and evolutionary laws that allows us to unite all the known types of sources in one general framework. This must also include transitions between different types of activity and appearance of hybrid behaviors, as the RPPs with high magnetic field discussed above. A trivial argument that the different NS classes belong to the same family is that the sum of their inferred birth rates exceeds the Galactic core-collapse supernova rate [210, e.g.].

Nowadays it is believed that the link between different classes of NSs can be found in the magnetic field and its evolution [120, 101, 12]. In a few words, the magnetic field evolves in the solid crust decaying due to the Ohmic dissipation and the Hall drift [180, 181, 75]. On the other hand, the surface temperature lowers because of the NS cooling. Given that these two quantities are related to each other and evolve together [121], they have to be studied in a comprensive auto-consistent model, called "magneto-thermal evolution" [319, 5, 4, 320]: temperature affects crustal electrical resistivity, which in turn affects magnetic field evolution, while the decay of the field can produce heat that then affects the temperature evolution.

Viganò et al. [425, see also [423] for further details] developed a code to follow the magneto-thermal evolution of NSs, according to the initial value of the magnetic field B_0 (other additional parameters are the NS mass, microphysics input etc). During an initial epoch, $t \approx 10^3 - 10^5$ yr, the magnetic field is almost constant, and then it starts to decay and an asymptotic value of P is reached after about 10^5 yr or several 10^6 yr. The duration of the initial epoch and of the velocity of the decay depend on B_0: stronger initial magnetic fields decay more rapidly than weaker ones. Following the evolutionary tracks of B on the $P - \dot{P}$ diagram, a link emerges between different classes of NSs: firstly the magnetars, youngest and with the highest magnetic field, then the high-B pulsars, and finally the XDINSs. In this framework, then, the XDINSs might be the descendants of magnetars (it was firstly pointed out by Heyl & Kulkarni [169], Colpi et al. [70]), while the high-B pulsars are a transitional class that exhibit a magnetar-like behavior (as PSR J1846−0258 and PSR J1119−6127) or a XDINS-like behavior (as PSR J0726−2612).

The low-B CCOs could be understood in the above picture as being the lowest B_0 neutron stars, X-ray bright only because of their true young ages. However, the low magnetic field does not explain the large surface anisotropies observed in the X-ray. Shabaltas & Lai [369] proposed that CCOs could be quiescent magnetars, with an extremely weak dipole field, but with a strong crustal magnetic field, emerging in local "sunspot" structures [102, 103, 104]. Another picture, known as the "buried field" scenario [176, 424, and references therein], assumes that the prompt accretion of supernova fallback material could bury the magnetic field of the newborn NS beneath its surface; the field could then re-emerge by diffusion on a timescale $\lesssim 10^4 - 10^5$ yr and then the evolved CCOs are common RPPs. Among the old isolated NSs with low B and a thermal spectrum, there is the radio-quiet pulsar dubbed Calvera [366, 445, 142]. However, a lack of any constraint on its distance (hence on its luminosity) as well as on its true age does

not allow us to draw a firm conclusion [140].

Table 1.2: Cyclotron absorption line properties.

INS Name	Class	P	$\dot{P}$	$B_{\rm p}$	$E^{\infty}_{\rm cyc}$	σ	$B_{\rm cyc}$	Spectrum and
		s	s s^{-1}	G	eV	eV	G	Reference
XTE J1810−197	MAG	5.54	2.8×10^{-12}	2.5×10^{14}	1150	130	$(1.5) \times 10^{14}$	3BB [35]
SGR 1806−20[a]	MAG	7.56	5.5×10^{-10}	4.1×10^{15}	500 ± 20	240 ± 100	$(6.6 \pm 0.3) \times 10^{13}$	PL [185, 186]
1RXS J1708−400	MAG	11.01	2.0×10^{-11}	9.4×10^{14}	8100 ± 100	200 ± 100	$(1.06 \pm 0.01) \times 10^{15}$	BB+PL [350]
SGR 1900+14	MAG	5.20	9.2×10^{-11}	1.4×10^{15}	6400 ± 220	...	$(8.4 \pm 0.3) \times 10^{14}$	BB [383]
RX J0720.4−3125	XDINS	16.78	1.9×10^{-13}	1.1×10^{14}	254^{+25}_{-30}	97^{+13}_{-12}	$(3.3 \pm 0.4) \times 10^{13}$	2BB [440]
RX J0806.4−4123	XDINS	11.37	5.6×10^{-14}	5.1×10^{13}	241^{+11}_{-12}	125 ± 4	$(3.2 \pm 0.2) \times 10^{13}$	2BB [440]
RX J1308.6+2127	XDINS	10.31	1.1×10^{-13}	6.9×10^{13}	390 ± 6	$183.6^{+1.6}_{-1.5}$	$(5.12 \pm 0.08) \times 10^{13}$	2BB [440]
RX J1605.3+3249	XDINS	...	...	...	353^{+19}_{-48}	96^{+15}_{-7}	$(4.6^{+0.2}_{-0.6}) \times 10^{13}$	2BB [440]
RX J2143.0+0654	XDINS	9.43	4.1×10^{-14}	4.0×10^{13}	326^{+56}_{-79}	87^{+23}_{-24}	$(4.3^{+0.7}_{-1.0}) \times 10^{13}$	2BB [440]
RX J0822−4300	CCO	0.11	9.3×10^{-18}	6.6×10^{10}	790 ± 30	53^{+33}_{-22}	$(5.7 \pm 0.2) \times 10^{10}$	2BB [128]
1E 1207.4−5209[a]	CCO	0.42	2.2×10^{-17}	2.0×10^{11}	720 ± 20	130 ± 30	$(5.2 \pm 0.1) \times 10^{10}$	2BB [41]
PSR J0726−2612	HB	3.44	2.9×10^{-13}	6.4×10^{13}	390^{+20}_{-30}	80^{+30}_{-20}	$(5.1^{+0.3}_{-0.4}) \times 10^{13}$	2BB [358]
PSR J1819−1458[a]	HB	4.26	5.6×10^{-13}	9.9×10^{13}	1000 ± 10	4 ± 1	$(1.31 \pm 0.01) \times 10^{14}$	BB [274]
PSR B0656+14	RPP	0.38	5.5×10^{-14}	9.3×10^{12}	540^{+20}_{-30}	100 ± 30	$(7.1^{+0.3}_{-0.4}) \times 10^{13}$	2BB+PL [14]
PSR B1133+16[a]	RPP	1.19	3.7×10^{-15}	4.3×10^{12}	220 ± 6	15^{+12}_{-4}	$(2.89 \pm 0.08) \times 10^{13}$	PL [356]
PSR J1740+1000	RPP	0.15	2.1×10^{-14}	3.7×10^{12}	548 ± 12	35^{+22}_{-15}	$(7.2 \pm 0.2) \times 10^{13}$	2BB+PL [202]

Notes. $B_{\rm p}$ is the magnetic field at the pole evaluated from timing parameters (see Eq. 1.17), while $B_{\rm cyc}$ is the magnetic field obtained from Eq. 1.28 in the case of CCOs, Eq. 1.29 for the other classes.
[a] Multiple absorption lines, only the fundamental line is reported.

Despite the large variety of isolated NS, a common manifestation are the cyclotron absorption lines. As discussed in the previous sections, they are observed in the (thermal) X-ray spectra of the isolated NSs that have the right magnetic field in order to observe electron (CCOs, see Eq. 1.28) or proton (XDINSs and magnetars, see Eq. 1.29) absorption lines. On the contrary, for the ordinary RPPs (with $B \approx 10^{12}$ G) neither of this conditions is satisfied at the star surface and hence no analogous spectral features are expected in soft X-rays. Nevertheless, Kargaltsev et al. [203] reported the discovery of cyclotron features in the rotation-powered pulsar PSR J1740+1000, and, recently, other few objects follow (PSR B1133+16 [356], PSR B0656+14 [14]).

If the electrons are responsible for such features, they must be located high in the magnetosphere, at several stellar radii above the stellar surface in a weaker magnetic field ($B \propto (r/R)^{-3}$). Thus, the X-ray photons can be produced on the surface or in the magnetosphere. Alternatively, if the lines are attributed to protons close to the star surface, then the actual magnetic field is higher than the one inferred in a dipole approximation and a multipole model is needed. In this scenario, however, the presence of a thermal component is needed in order to justify an absorption right above the stellar surface. Table 1.2 lists the isolated NSs that shows confirmed absorption lines in their X-ray spectra.

Chapter 2

Physics and geometry of radio emission

Pulsars were discovered serendipitously with radio observations in 1967 [168]; since then, more than 2500 radio pulsars have been discovered [249]. Their fingerprint is a pulse profile, with a peak less than 20° wide, that is due to the fast rotation of the neutron star coupled with the beaming of the radio emission. The superimposition of some hundreds of single radio pulses gives an integrated pulse profile, which is stable and characteristic for each pulsar. The study of individual pulses, on the contrary, revealed that often pulsar emission can be very variable.

This chapter is based mainly on Lyne & Manchester [241] and Lorimer & Kramer [239]: after a brief introduction where the so-called "lighthouse model" is presented (Section 2.1), a more detailed description of the integrated and the individual pulses follows (Sections 2.2 and 2.3). Finally, three pulsars with a variable emission both in the radio and in the X-ray bands are presented (Section 2.4).

2.1 Introduction

Pulsar radio emission is generally understood in terms of beams of coherent plasma radiation from highly relativistic particles. According to the standard "lighthouse model", we observe a pulse as the beam crosses the Earth. However, there is no satisfactory theory that explains the radio emission mechanisms or even the magnetospheric conditions that determine whether a neutron star emits at radio wavelengths.

One can distinguish between antenna mechanisms (i.e. emission by bunches of particles), relativistic plasma emission and maser mechanisms [262]. Most of them make use of secondary pair plasma and place the origin of the pulsar radiation in the inner region of the magnetosphere. The plasma flows along the open field lines, emitting in a beam centered on the magnetic axis of the pulsar.

It is thus clear that the pulsar geometrical configuration, that is described in Section 2.1.1, strongly affects the observational characteristics of the radio emission (Section 2.1.2).

2.1.1 Geometry of radio emission

The observed properties of pulsars depend on the angles ξ and χ that the star magnetic axis and the line of sight (LOS), respectively, make with the spin axis. A third angle, η, is called "impact parameter" and it represents the closest approach of the LOS to the magnetic axis:

$$\cos\eta = \cos\xi\cos\chi + \sin\xi\sin\chi\cos\phi\,, \tag{2.1}$$

where ϕ is the rotational phase. When the LOS, the magnetic and rotation axes lie in the same plane, $\cos\phi = \pm 1$ and $\eta = |\chi \mp \xi|$. If $\chi < \xi$, this provides $\chi = \xi - \eta$ (inside traverse), while in the opposite case ($\chi > \xi$) it is $\chi = \xi + \eta$ (outside traverse). The two configurations are represented in Figure 2.1, together with the angles ξ, χ and η.

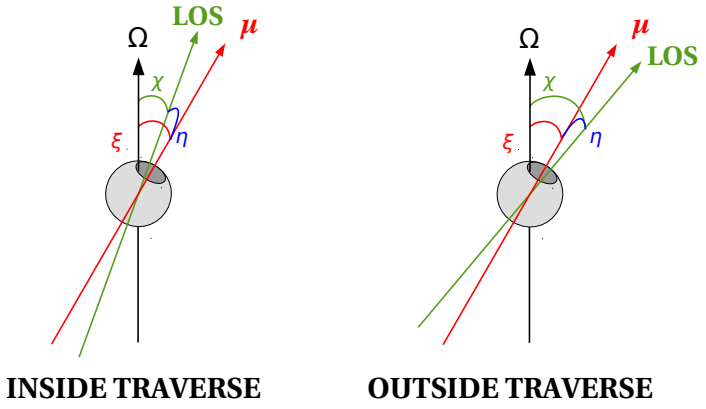

Figure 2.1: Schematic picture of the inside (left panel) and outside traverse configurations (right panel): ξ is the angle between the magnetic and the rotation axis, χ is the angle between the line of sight (LOS) and the rotation axis, and η is the impact parameter.

As shown in Figure 1.6, the existence of a light cylinder divides the dipole magnetic field lines into two groups: field lines that close within the light cylinder radius (closed field lines) and the ones that do not close (open field lines). The open field line region defines the polar cap on the NS surface, centered on the magnetic pole. Its boundary is defined by the last open field line which is tangential to the light cylinder. For a given dipole field line, the expression $\sin^2\theta/r$ is constant:

$$\frac{\sin^2\theta}{r} = \frac{1}{R_{\rm LC}} = \frac{\sin^2\theta_{\rm PC}}{R}, \tag{2.2}$$

where $R_{\rm LC} = Pc/2\pi$ is the light cylinder radius defined in Eq. 1.20. If the radius of the polar cap measured on the surface, $R_{\rm PC} = R\sin\theta_{\rm PC}$, is not too large, we can find

$$\begin{aligned} R_{\rm PC} &\simeq R\sqrt{\frac{R}{R_{\rm LC}}} = R\sqrt{\frac{2\pi R}{Pc}} \\ &\approx 145\, P^{-1/2}\ \text{m}, \end{aligned} \tag{2.3}$$

for $R = 10$ km.

2.1.2 Observational features

For most pulsars, the radio pulse is visible during a small fraction of the period, corresponding to between 5° and 20° of angular rotation. The width of the pulse W is observed to depend mainly on the frequency and the pulsar period with $W \propto \nu^{-a}$ (with $0.25 < a < 1$) and $W \propto P^{-0.5}$, respectively. These scale relations can be explained, to the first order, only with simple geometrical arguments.

The toy model of radio emission assumes that the emission beam is a cone, centered on the magnetic axis, with opening angle ρ. As the pulsar rotates, the beam sweeps across the observer LOS tracing a curved path (see Figure 2.2). The emission along this path is observed as the pulse profile, and the path length is the pulse width W. It can be related to ρ by applying simple spherical geometry [110, 277]:

$$\cos\rho = \cos\xi\cos(\xi+\eta) + \sin\xi\sin(\xi+\eta)\cos\left(\frac{W}{2}\right). \tag{2.4}$$

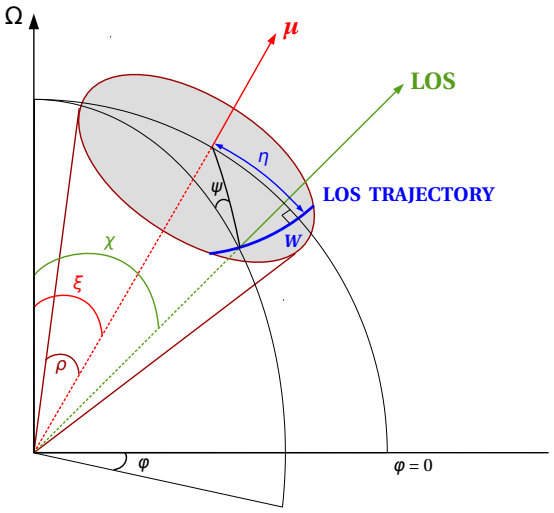

Figure 2.2: The geometry of the conal beam, that models the pulsar radio emission. The cone has an opening angle ρ and is centered on the magnetic axis, that is misaligned of ξ with respect to the rotation axis. A distant observer, inclined with χ, sees a pulsation when the beam sweeps past its line of sight (LOS) once per rotation. The zero of longitude ϕ is defined as the meridian through the magnetic axis, and the polarization position angle (PPA) ψ is measured with respect to the projected direction of the magnetic axis. Adapted from Lyne & Manchester [241].

If the emission cone is confined by the last open field line, we can relate the opening angle of the cone to the polar coordinates (r,θ) of the field lines [98]:

$$\tan\theta = -\frac{3}{2\rho} \pm \sqrt{2+\left(\frac{3}{2\tan\rho}\right)^2}. \tag{2.5}$$

For regions close to the magnetic axis (i.e. $\theta \lesssim 20°$ and $\rho \lesssim 30°$), this relation simplifies to $\theta \approx 2\rho/3$. By considering Eq. 2.2, ρ can be related to the emission site of coordinates $(r_{\rm em}, \theta_{\rm em})$:

$$\rho \approx \frac{3}{2}\theta_{\rm em} \approx \sqrt{\frac{9\pi r_{\rm em}}{2cP}} = 1°.24\left(\frac{r_{\rm em}}{10\ {\rm km}}\right)^{1/2} P^{-1/2}. \tag{2.6}$$

First, we corroborate the behavior $W \propto \rho \propto P^{-1/2}$, that has been observed by many authors (see e.g. Gil & Kijak [115], Rankin [345], Kramer [215]). Moreover, we demonstrate that the width of the pulse profile decreases with increasing observing frequency, if we assume that high radio frequencies are emitted from closer to the surface than low radio frequencies [213].

This phenomenon is known as radius-to-frequency mapping [71]. Thorsett [409] suggested an empirical relation for the observed pulse width as a function of the frequency, which seems to provide an adequate description of the observed behavior:

$$\rho(\nu) = \rho_\infty(1 + K\nu_{\mathrm{GHz}}^{-a}), \tag{2.7}$$

where $K = 0.066 \pm 0.010$, a is in the range $0.25 - 1$, and ρ_∞ is the opening angle of the emission cone at infinite radio frequency [277]. It should correspond to the opening angle measured on the surface, and thus approximately to the angular size of the polar cap $\rho \approx 3\theta_{\mathrm{PC}}/2$.

As the pulsar becomes older, P increases and as a consequence, both ρ and R_{PC} decrease. Moreover, there is a tendency for the magnetic axis to align with the rotation axis, on a timescale of the order of 5×10^6 yr. The idea that the magnetic axis aligns with the rotation axis was first studied analytically by Jones [192, see also Tauris & Manchester [395]], and observational evidence for alignment has been put forward by many authors [337, 241, 223]. The magnetosphere, responsible for the pulsar spin down, may also generate a torque to align the rotational axis and magnetic axis [314].

Among the best arguments for the cone model there is the behavior of the linear polarization, observed in the integrated profiles. Radio pulses are linearly polarized in the direction of the magnetic field at the moment of emission, that varies during the rotational phase. Radhakrishnan & Cooke [339] showed that the polarization position angle (PPA, dubbed ψ in Figure 2.2) varies according to

$$\tan\psi = \frac{\sin\xi\sin\phi}{\cos\xi\cos\chi\cos\phi - \sin\xi\sin\chi}. \tag{2.8}$$

In principle, the measure of the PPA would allow to determine ξ and χ, and to distinguish between the inside and the outside traverse configurations [286]. However, the range of pulse longitudes with a well defined PPA is usually limited by the small pulse duration, and these considerations apply only for a few pulsars (see e.g. the Vela pulsar [219]). On the contrary, the steepest gradient of Eq. 2.8 can easily be determined and it is related to ξ and η as follows:

$$\left|\frac{d\psi}{d\phi}\right|_{\mathrm{max}} = \frac{\sin\xi}{\sin\eta}, \tag{2.9}$$

which is measured when $\phi = 0^\circ$. This simple model has been extended by including corrections due to aberration, retardation, magnetic sweep-back and the effects of plasma currents [44, 170, e.g.]. Moreover, circular polarization is observed when the LOS is close to the magnetic pole, i.e. when the field lines have the lowest curvature [241].

2.2 Integrated pulse profiles

The morphological characteristics of the observed pulse profiles are much more variegate than discussed in Section 2.1. First, there is an enormous variation between individual pulses received from any individual pulsar, that disappears when hundreds of pulses are superimposed to make an integrated pulse profile.

A second complication is that the integrated profiles differ greatly between one pulsar and another. Most pulsars have a single-peaked pulse profile, but it is no rare to observe two pulses separated by 180° in longitude: the brightest peak is called "main pulse", while the second "interpulse". This configuration can easily been explained if we consider that both sides of the emission beam are seen within a single rotation, i.e. the pulsar is an orthogonal rotator

(the angle between the magnetic and the rotation axis $\xi \approx 90^\circ$) seen with a small impact angle ($\eta \approx 0^\circ$). Third, the main pulse is often made up by two or more peaks, separated by a few degrees in longitude; Figure 2.3, left panel, shows a sample of integrated profiles at 408 MHz, on a single scale of longitude.

Based on the available data, in the '90s radio astronomers developed an Empirical Theory of pulsar emission (ET: I-VII, [341, 342, 343, 344, 340, 345, 279]), which explains the large diversification of the observed pulse profiles with a unique coherent model. The emission beam presented in Section 2.1.2 is actually hollow, with a central core. The resultant pulse profile, given a certain geometry of the pulsar and of the cone, depends only on the observer orientation. Moreover, the emission within the hollow cone and the core is not a continuum, but comes from discrete spikes/bunches, as shown in Figure 2.3, right panel.

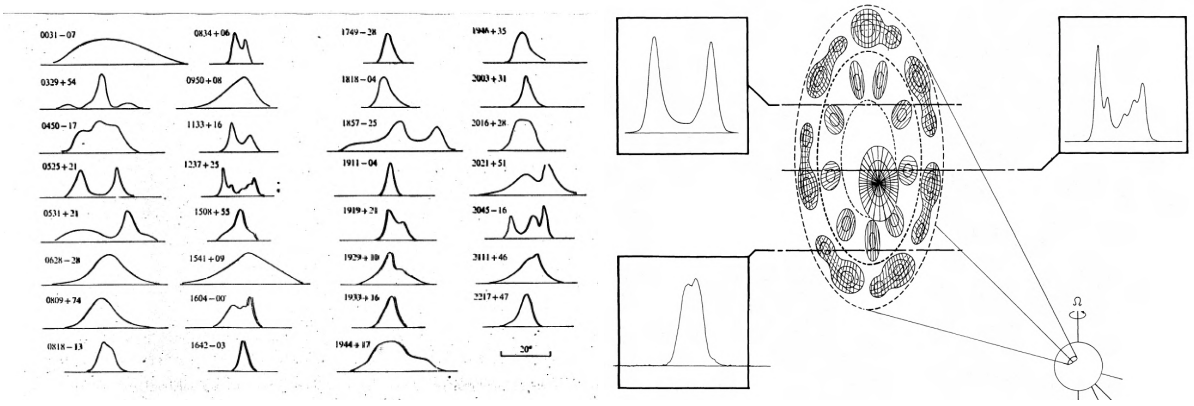

Figure 2.3: Left panel: Integrated profiles at 408 MHz of a few representative pulsars, on a single scale of rotational longitude of 20°. Credits to Lyne & Manchester [241]. Right panel: Schematic diagram of pulsar polar cap geometry representing the ET classification system. An out-of-axis core component and two conal components are shown, and the resulting pulse profile depends only on the LOS. The azimuthal, radial, and eccentric hatching is indicative of possible linear and circular polarization orientations in the various zones. Credits to Rankin [341].

The morphological characteristics of polarized average profiles led to the distinction of five species: single core and single cone (S_t and S_d, respectively), double (D), triple (T), and five-component or multiple (M). The distinction between species is not that strict, as they evolve from one to another as a function of the frequency. Moreover, they seem to evolve also as a function of the pulsar age: S_t pulsars are by far the youngest, T stars are of intermediate age, and the remaining species are relatively old.

While it is pretty easy to distinguish between D, T and M stars, S_t and S_d pulsars both show a single pulse. Nevertheless, they have a different spectrum (S_t pulsars have a steeper spectrum) and a different polarization (S_t pulses are mainly circularly polarized, S_d pulses are linearly polarized). Moreover, S_t and S_d pulsars are observed to occupy a different location on the $P - \dot{P}$ diagram; this can be explained considering that their radio emission is produced at different heights, and thus with a different acceleration potential (see Sections 2.2.1 and 2.2.2).

2.2.1 The core emission region

Pulsars with a core emission region are about 70% of the known pulsars, and they belong to S_t, T and M species. The core radiation is not necessarily axial, as shown in Figure 2.3, right panel, and gives rise to pulses of relatively small angular width ($W_{\text{core}} \lesssim 10^\circ$) and with an

antisymmetric circular polarization. These characteristics argue that core radiation is generated at much lower height than the conal emission and that the beam is observed with a small impact parameter η.

Core emission pulsars have been intensively studied by Rankin [344], who found a relation between the observed $W_{\rm core}$ (at 1 GHz), the angle ξ, and the period P:

$$W_{\rm core} = 2^\circ.45 \, \frac{1}{\sin\xi\sqrt{P}}. \tag{2.10}$$

Considering $\eta \approx 0^\circ$, from Eq. 2.4 we find $W \approx 2\rho/\sin\xi$, and thus Eq. 2.6 becomes

$$W_{\rm core} = 2\frac{\rho}{\sin\xi} \approx 2^\circ.48 \, \left(\frac{r_{\rm em}}{10 \text{ km}}\right)^{1/2} \frac{1}{\sin\xi\sqrt{P}}. \tag{2.11}$$

The analysis of six core emission pulsars with well measured $W_{\rm core}$ and $\xi \approx 90^\circ$ (known because of the interpulse presence) showed a strong correlation between $W_{\rm core}$ and P:

$$W_{\rm core} = 2^\circ.45 \, P^{-0.50}. \tag{2.12}$$

Both equations 2.10 and 2.11 have a $P^{-1/2}$ term, and thus it appears that the period dependence of the core width has a geometrical origin. Furthermore, in order to reconcile the two expressions, the emission height (from the center of the star) must be nearly 10 km. This in turn suggests that the core emission comes from very near the stellar surface.

2.2.2 The conal emission region

Pulsars with a conal emission region are S_d, D, T and M stars. The integrated pulses of the conal component is linearly polarized, and the plane of linear polarization is tied to the magnetic field lines, resulting in a characteristic S-shaped curve. PPA (see Eqs. 2.8 and 2.9) is measured with respect to the projected direction of the magnetic axis and rotates throughout the pulse by at most 180°.

The existence of M pulsars with five peaks, as PSR B1237+25 and PSR B1857−26, tells us that there are two conal emission zones, defined by $\rho_{\rm inner}$ and $\rho_{\rm outer}$. Rankin [345, 346] studied about twenty M pulsars in order to establish a scale relation between observable quantities of the conal pulsars, similar to that found for the core ones. The M pulsars are the perfect candidates because they have the two conal components, and the core component, which can be exploited to determine ξ via Eq. 2.10. η, on the contrary, can be measured through Eq. 2.9. ξ, η, $W_{\rm inner}$ and $W_{\rm outer}$ (for $\nu = 1$ GHz) are used to infer the opening angle both for the inner and the outer cones. Rankin [345] found that they scale with the pulsar period as follows:

$$\rho_{\rm inner} = 4^\circ.33 \, P^{-0.52}, \tag{2.13}$$

$$\rho_{\rm outer} = 5^\circ.75 \, P^{-0.50}. \tag{2.14}$$

Finally, the emission height of the conal component is (see Eq. 2.6)

$$r = \frac{10 \text{ km}}{(2^\circ.45/2)^2} \, \rho^2 P = 6.66 \, \rho^2 P \text{ km}, \tag{2.15}$$

that corresponds to $r_{\rm inner} \approx 125$ km and $r_{\rm outer} \approx 200$ km for the two components. They are indeed higher than the emission height of the core component. Nevertheless, these results are

difficult to reconcile with recent observations, where the emission heights of the core and conal components are emitted from similar heights in the same pulsar [280, 374].

Moreover, later studies (see e.g. Mitra & Deshpande [277]) showed the need of a nested cone structure with at least three distinct cones, although only one or more of the cones may be active in a given pulsar. In this case, the cone opening angle spans the range

$$2^\circ \lesssim \rho \lesssim 8^\circ, \tag{2.16}$$

for $P = 1$ s and $\nu = 1$ GHz.

2.3 Individual pulses

The well-organized pulse profiles obtained by integrating hundreds of individual pulses conceal a rich diversity of behavior among the individual pulses.

The components of an individual pulse are often identifiable as characteristic subpulses, with a typical width in longitude of 1° to 3°. These subpulses may occur apparently at random longitudes within the window defined by the integrated profile, or they may reveal a structure. This is the case of the "subpulse-drifting" phenomenon (Section 2.3.1 and Figure 2.4, left panel), in which the single subpulses drift in pulse longitude to form ordinate bands.

In other cases, the individual pulses can switch off for a certain amount of time (that can be hours or several days) and the pulsar will appear radio quiet, or they can change their mean properties so that the integrated pulse will appear deeply changed: it is the case of the "pulse-nulling" (Section 2.3.2 and Figure 2.4, central panel), and the "mode-changing" (Section 2.3.3 and Figure 2.4, right panel) phenomena, respectively.

All three effects have been extensively studied, and they have been discussed in the ET framework by Rankin [343]. Nowadays, a small number of radio pulsars revealed the presence of all of the three phenomena, suggesting that a reorganization of the entire magnetosphere occurs (see Basu et al. [26] and references therein).

2.3.1 Subpulse drifting

The "subpulse drifting" is a phenomenon in which the single subpulses drift in an organized fashion through the pulse window, to form drift bands [432] (see Figure 2.5, left panel).

Early studies [21, 365] proposed that the subpulse-drifting phenomenon is due to emission columns that circulate in a hollow cone around the pulsar magnetic axis. This toy model, known as "the carousel model" and displayed in Figure 2.5, right panel, predicts a relation between the carousel circulation period around the magnetic axis, P_4, and the periodicities of the drift bands (P_2 and P_3, see Figure 2.5, left panel):

$$P_4 \approx \frac{P_3 P}{P_2(1 + nP_3/P)} = \frac{P_3}{P_2} P, \tag{2.17}$$

where P is the usual rotation period of the pulsar and n accounts for eventual subpulses beating with P [220]; in the last equality, $n = 0$.

It is easy to demonstrate that, if N is the number of emission columns that cause the drifting subpulses, then $P_2 = 1/N$ and

$$\frac{P_4}{P} = NP_3. \tag{2.18}$$

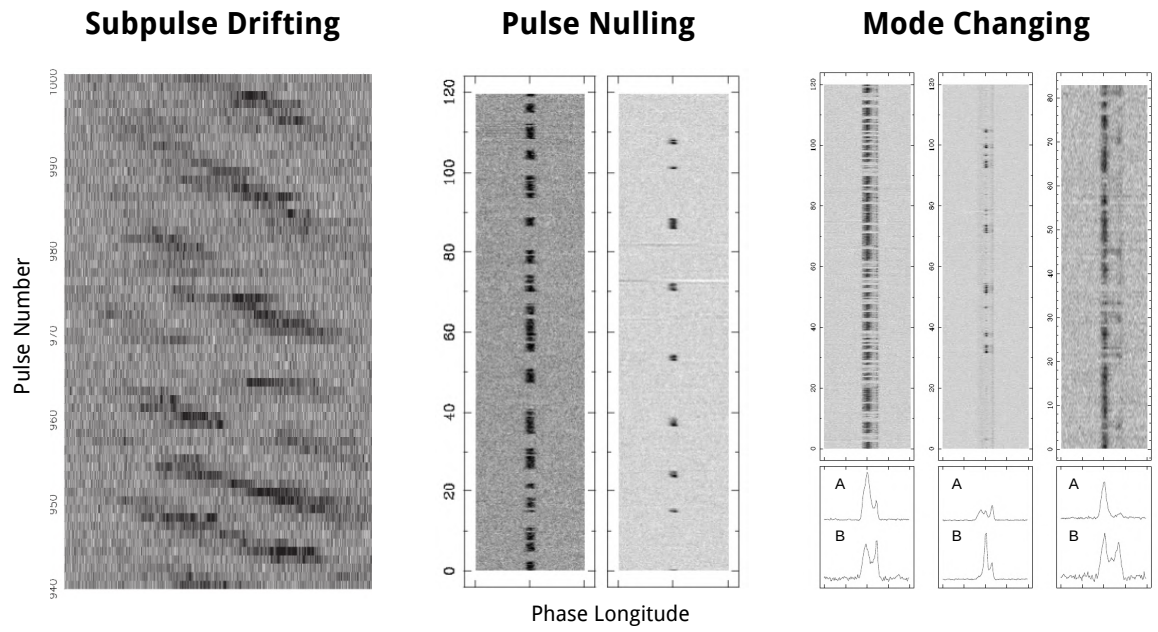

Figure 2.4: Pulse-stack (pulse number vs. phase longitude) of a hundred successive pulses of some example pulsars showing subpulse drifting (left panel), pulse nulling (central panel) and mode changing (right panel). For the latter, also mean pulse profiles for the two observed modes (A and B) are shown. Adapted from Weltevrede et al. [432], Wang et al. [429].

In the magnetosphere model of Ruderman & Sutherland [365], the drifting subpulses are interpreted in terms of spark-associated plasma columns rotating around the magnetic axis due to the $\mathbf{E} \times \mathbf{B}$ drift, where $\mathbf{B}$ is the background magnetic field and $\mathbf{E}$ is the electric field in the frame corotating with the star. To the observer, the movement appears as a drift of subpulses in the form of sub-rotation (see Section 3.4.2 for further details).

2.3.2 Pulse nulling

"Pulse nulling" is a phenomenon in which the pulse energy suddenly drops to zero or near zero and then just suddenly returns to its normal state. Nulling is relatively common in pulsars: based on data for 72 well-observed pulsars, Biggs [39] found evidence for nulling in 43. Nulls vary widely in duration (from just one or two pulses to many hours or even days), and in "null fraction", the fraction of time when the pulsar is in a null state, which can range from 0% (for the Vela pulsar) to more than 50%.

Kramer et al. [218] showed that in PSR B1931+24, which has long-duration quasi-periodic nulls with a cycle time of about 40 days, the spin-down rate is reduced by about one-third when the pulsar is in a null state, demonstrating that the magnetospheric currents responsible for the pulse emission also contribute to the pulsar braking [429].

2.3.3 Mode changing

There are a dozen of pulsars that alternate two or more quasi-stable average profiles, and thus are called "mode-changing" or "mode-switching" pulsars. It is not clear yet if mode changing is unusual in the pulsar population, or if it is only hard to identify because short-duration se-

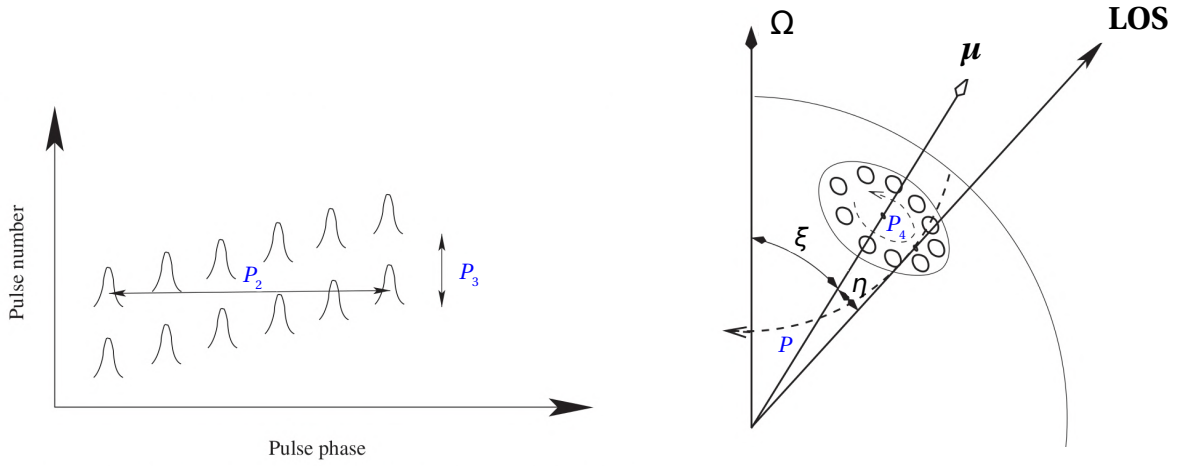

Figure 2.5: Left panel: Schematic picture of drifting subpulses in a stacked pulse diagram. P_2 and P_3 are measured in units of P. Right panel: The carousel of N emission columns corotates as a whole with the pulsar but drifts around the magnetic axis μ, here with a period P_4. The LOS crosses the carousel as indicated with the arrow back to front. ξ and η are the usual angles defined in this chapter. Adapted from Kuijpers [220].

quences are not classified as distinct modes. Mode-changing pulsars all exhibit rather complex average profiles, as the M pulsar B1237+25, the first to have been identified [20].

In addition to the pulse profile shape, also the flux normalization and small-scale features as drifting, quasi-periodic modulation, microstructure and polarization, are affected by mode changing, showing that it represents a fundamental change in the emission process. Both nulling and mode changing are broad-band and they may be different manifestations of the same basic phenomenon, that involves a reorganization of core and conal emission [429].

Among the mode-changing pulsars, three were observed with simultaneous radio and X-ray coverage. The results are presented in the following section.

2.4 Mode changing in the X-rays

Among the known pulsars that show the mode-changing phenomenon, three have been observed with simultaneous radio and X-ray coverage, and showed three different behaviors about radio/X-ray correlation. Here, I briefly present these pulsars and the obtained results: PSR B0943+10 (Section 2.4.1), PSR B1822−09 (Section 2.4.2) and PSR B0823+26 (Section 2.4.3).

2.4.1 PSR B0943+10

PSR B0943+10 is an old RPP of 5 Myr, that in the radio band alternates between two different states: when it is in the so-called B (*burst-like* or *bright*) mode, the radio emission displays a regular pattern of drifting subpulses, while it is chaotic, and on average fainter, in the Q (*quiescent*) mode [389]. The pulsar has a single pulse and a very steep spectrum, $S_\nu \propto \nu^{-2.9}$ [243], that makes observation above 1 GHz extremely complicated to be performed. The B-mode shows the subpulse-drifting phenomenon with a well-measured periodicity $P_{4,\mathrm{B}} = 37.4^{+0.4}_{-1.4}\,P$, and $P_3 = 2$, yielding $N \approx 20$ sparks [86]. More recentely, Rankin & Suleymanova [348] found

that also the Q-mode exhibits a strong low frequency modulation, with an associated circulation time $P_{4,Q} = 36.4 \pm 0.9\,P$. Moreover, they found that in the transition between the Q- and the B-mode, the circulation period relaxes from $P_{4,Q}$ to $P_{4,B}$ in a roughly exponential fashion with a characteristic time of 1.2 h.

Rankin [345, 346], Deshpande & Rankin [85] classified PSR B0943+10 as a S_d pulsar, and stated that our LOS grazes its beam so narrowly that we miss its emission at higher frequencies. Deshpande & Rankin [85] used a set of trial values of ξ and χ, and compared the resulting PPA (see Eq. 2.9) with the observed one. Both the inside and outside traverse models resulted in a PPA value close to the observed one, but the latter configuration gave inconsistent results on the number of sparks. As a results, the expected ranges for ξ and χ according to Deshpande & Rankin [85] are $10^\circ < \xi < 15^\circ$ and $5^\circ < \chi < 10^\circ$.

More recently, Bilous [42] reconsidered the assumptions of Deshpande & Rankin [85]: by taking a wider range for ρ (see Eq. 2.16), she found $5^\circ < \xi < 30^\circ$. Moreover, she considered both the inside and the outside traverse configurations because her modeling gave the same results on the number of sparks. Bilous [42] found that for each value of ξ, only two well-defined values of χ are possible and are in the ranges $3^\circ < \chi < 22^\circ$ (inside traverse) or $7^\circ < \chi < 38^\circ$ (outside traverse).

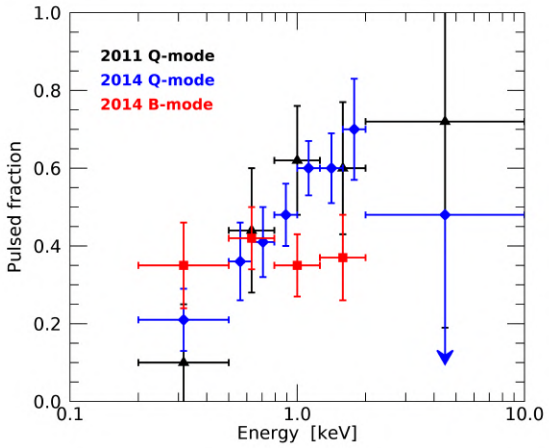

Figure 2.6: Pulsed fraction of PSR B0943+10 as a function of energy, as measured by Hermsen et al. [161] (Q-mode: black triangles) and by Mereghetti et al. [266] (Q-mode: blue diamonds, B-mode: red squares).

X-rays from PSR B0943+10 were discovered with the *XMM-Newton* satellite in 2003, but due to the short exposure it was not possible to precisely characterize its spectrum and search for pulsation [454]. Other *XMM-Newton* observations, obtained in 2011 with simultaneous radio coverage with LOFAR (140 MHz) and the GMRT (320 MHz), were crucial to show that the X-rays correlate with the radio modes: the X-ray flux is brighter and pulsed during the radio Q-mode, while when the pulsar is in the B-mode the X-rays are a factor ~ 2.5 fainter and apparently unpulsed [161].

The X-ray spectrum of the Q-mode is fitted well by the sum of a nonthermal power-law component and a thermal blackbody component. Using also the timing information, these authors simultaneously derived the spectra of the pulsed and unpulsed emission. During the Q-mode, the pulsed emission is thermal and fitted well by a blackbody, while the unpulsed emission is a power law. The pulsed fraction of the Q-mode varies as a function of the energy (see Figure 2.6). On the other hand, the results were less constraining for what concerns the

B-mode: either a blackbody or a power law could fit equally well the spectrum, while a three sigma upper limit of 0.56 on the pulsation was derived [264].

A further campaign of simultaneous X-ray and radio observations of PSR B0943+10 was carried out with an *XMM-Newton* Large Program and the LOFAR, LWA, and Arecibo radiotelescopes in 2014 November [266]. Thanks to the larger statistics provided by these data, it was possible to detect X-ray pulsations and to rule out a single power-law spectrum also in the B-mode. The spectral analysis of the pulsed and unpulsed emission confirmed the findings of Hermsen et al. [161]. The pulsed fraction of the Q- and the B-mode as a function of the energy is shown in Figure 2.6.

These results are at variance with the geometry inferred by the radio data: how can an almost aligned rotator produce an highly-pulsed X-ray emission? Storch et al. [382] showed that the large pulsation of the Q-mode can be explained invoking a magnetized atmosphere on top of the emitting area.

A detailed analysis of the sum of 2011 and 2014 data, and a possible answer to the puzzle, will be presented in Chapter 7.

2.4.2 PSR B1822−09

PSR B1822−09 is radio pulsar of 0.2 Myr and a period of 0.77 s. It is a mode-changing pulsar, and it alternates every few minutes two emission modes: the weaker Q-mode, that has an interpulse, and the brighter B-mode, that has a precursor 15° prior to the main pulse, but a barely detectable interpulse. The natural interpretation is that PSR B1822−09 is an orthogonal rotator. In both modes, the pulsar shows a strong modulation of the subpulses with periods $P_{3,Q} \approx 47$ and $P_{3,B} \approx 70$ for the two modes, but not showing organised drifting [230].

PSR B1822−09 was detected in a short X-ray observation by Prinz & Becker [336]. Hermsen et al. [162] carried out an X-ray/radio campaign on PSR B1822−09 with *XMM-Newton* and simultaneous radio observations with WSRT (1380 MHz), GMRT (325 MHz) and the Jodrell Bank Observatory Lovell telescope (1420 MHz).

In the radio observations, Hermsen et al. [162] discovered for the first time in a mode-changing pulsar a relationship between the duration of the Q- and the B-mode and their periodicity P_3. On the other hand, they found no significant difference in the X-ray emission between the two modes, nor in the spectrum shape (well modeled by two blackbodies), nor in pulse profile (a broad sinusoid strongly pulsed). Moreover, there is no evidence for a relationship between the X-ray count rate and the underlying modulation time scale P_3.

The authors interpreted the lack of X-ray variation as a consequence of the pulsar geometry (nearly orthogonal), and/or that the physics of the short moding is quite different.

2.4.3 PSR B0823+26

PSR B0823+26 is a 5 Myr old pulsar, with a period of 0.53 s. In the radio band, it shows a main pulse, an interpulse, and a post-cursor emission. It switches between two modes, the B-mode (70% of the total time) and the Q-mode (the remaining 30%), both lasting many hours, possibly even days. The B-mode shows a single-pulse modulations with a repetition period $P_3 = 5$ [21, 432], while the Q-mode is characterized by the nulling phenomenon: Young et al. [441] found the nulls can last minutes or even hours. Finally, the analysis of the PPA revealed $\xi = 81°$ and $\chi = 84°$.

PSR B0823+26 was also detected at X-rays with *XMM-Newton* [32]. Hermsen et al. [163] carried out an X-ray/radio campaign on PSR B0823+26 with 6×25 ks of *XMM-Newton* obser-

vations, and simultaneous radio observations with GMRT (325 MHz) and LOFAR (150 MHz). They found that, when the pulsar is in the Q-mode, it is not detected in the X-rays. On the contrary, it is well detected in the B-mode, even if a flux variation of $\pm 20\%$ around the average value was reported. The B-mode has a broad sinusoidal pulse, lagging the radio main pulse by 0.20 ± 0.01 in phase, and a pulsed fraction of about 0.75 in the range $0.2 - 2\,\mathrm{keV}$.

The B-mode spectrum is fitted well by the sum of a power law and one blackbody, or by two blackbodies (the latter is statistical preferred). The authors also fitted the spectrum with a more realistic model of a magnetized atmosphere and found that both the polar caps are visible within a rotation, and $\chi = 66^\circ$, in conflict with the accurately radio-derived value.

In conclusion, PSR B0943+10 and PSR B0823+26 show evidence of a correlation between the radio and X-ray flux variability (for PSR B0943+10 it is an anti-correlation), even if they have a different geometrical configuration according to the analysis of the PPA. PSR B1822−09 is an orthogonal rotator as PSR B0823+26, but its X-ray flux does not vary according to the radio switching modes. According to Hermsen et al. [162, 163], this is probably due to fact that in PSR B1822−09 the onset of both the B and Q modes occurs within a few pulses, and the Q-mode is only half dimmer than the B-mode. Another possibility is that in PSR B0823+26 we are not seeing "true" mode changing but the sudden appearance of strong bursts whose intensities follow a self-similar (fractal) distribution over a wide range of timescales [22]. The same phenomenon is used to explain the RRAT[1] behavior [258].

[1]The rotating radio transient pulsars, see Section 1.5.4.

Chapter 3

X-rays emission models

X-rays from pulsars are produced by thermal and nonthermal processes. The thermal component, that can be produced by the whole stellar surface or by small hot spots, is at the first order described by a blackbody. However, the presence of a magnetized crust and/or a magnetized atmosphere deeply modifies the spectral shape of this thermal component. The realistic emission models that currently are adopted to fit the NS spectra are described in Section 3.1. Thank to these, a reliable bolometric luminosity can be evaluated and, together with the NS age, compared to the theoretical cooling curves (Section 3.2).

The nonthermal component of the spectrum is instead produced by relativistic particles accelerated in the strong magnetic fields which corotate with the star (Section 3.3). A fraction of these particles is accelerated backward and returns on the stellar surface, heating it in localized regions of the magnetic polar caps (Section 3.4).

3.1 Realistic emission models

The vast majority of the NS thermal spectra is fitted with a blackbody model, mainly because this needs the lowest number of assumptions and the statistical quality does not allow to constrain more elaborate models. For example, the blackbody emission does not depend on the magnetic field and is isotropic. On the contrary, the emission from more realistic thermal models depends on the angles that the wave vector makes with the surface normal, namely θ_k and ϕ_k (see Figure 3.1). Moreover, if a magnetic field of strength B and inclination θ_B with respect to the normal is present, also the angle α is relevant for the radiative transport equations.

In the following, I discuss the effects on the emergent radiation of a magnetic envelope (Section 3.1.1), an atmosphere (magnetic or not, Section 3.1.2), and a condensed surface (Section 3.1.3). The latter has a deep impact on the surrounding magnetosphere (Section 3.3.1).

3.1.1 Boundary conditions and the envelope model

The bulk of thermal energy is stored in the NS interior, that is essentially isothermal, and arises from the envelope, that is only 100 m thick and has a density up to 10^{10} g cm^{-3}. Due to its relatively low density, its thermal relaxation timescale is much shorter than that of the crust and it can be considered stationary. Models assuming a non-magnetized ($B < B_0$, see Eq. 1.11) envelope made of iron and iron-like nuclei show that the surface temperature T_s is related to

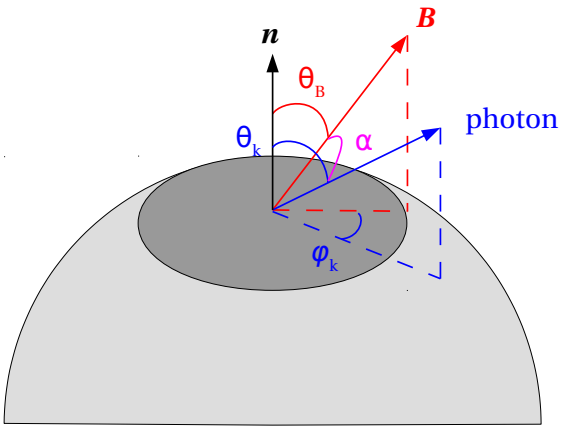

Figure 3.1: Scheme of the relevant angles for the surface emission equations: θ_B is the angle between the magnetic field B and the local normal to the surface n; θ_k and ϕ_k are the angles between n and the wave vector; α is the angle between B and the wave vector.

the interior temperature T_b as follows [136]:

$$T_{b,8} = 1.288 \left[\frac{T_{s,6}^4}{g_{14}} \right]^{0.455} , \tag{3.1}$$

where g_{14} is the surface gravity in units of 10^{14} cm s^{-2}, $T_{b,8}$ is the interior temperature in units of 10^8 K, and $T_{s,6}$ is the surface temperature in units of 10^6 K. The heat transport is due to photons in the upper layers and to electrons in the lower layers; here, the ions are in a liquid phase [135, 136, 165]. In the absence of magnetic field, the heat transport in the envelope is isotropic, and the resulting surface temperature is uniform over the star.

On the contrary, in the presence of a strong magnetic field, the electron transport in directions perpendicular to the field is strongly suppressed, while it is enhanced parallel to the field. Photon opacities are also affected, but the Rosseland mean, the relevant quantity for the heat transport, is only slightly anisotropic: the electrons are the real responsible for the nonuniform heat conduction, and as a result the temperature reaches a maximum at the magnetic poles and a minimum along the magnetic equator [164, e.g.].

Given that the envelope is thin compared to the stellar radius, the magnetic field is uniform across it and the heat conduction can be studied in a plane-parallel approximation. Thus the surface temperature depends only on the angle between the field and the radial direction θ_B (see Figure 3.1), and on the local field strength through the thermal conductivity tensor K_{ij} [297].

Greenstein & Hartke [134] decomposed K_{ij} into $K_\perp$ and $K_\parallel$, the conductivity components perpendicular and parallel to the magnetic field lines, respectively, and considered them constant within the envelope. Moreover, they argued that the radial temperature gradient dT/dr is much larger than the temperature gradient along the star surface dT/dx; with these assumption, the surface temperature varies as follow:

$$T_s^4(\theta_B) = T_p^4 \left(\cos^2\theta_B + \frac{K_\perp}{K_\parallel} \sin^2\theta_B \right) , \tag{3.2}$$

where $T_p = T_s(\theta_B = 0°)$ is the temperature at the magnetic poles. For a purely dipolar magnetic field (see Eq. 1.15), θ_B is related to the magnetic colatitude θ via

$$\tan\theta_B = \frac{1}{2}\tan\theta. \tag{3.3}$$

The temperature distribution of Eqs. 3.2 and 3.3 is shown in Figure 3.2, left panel. In the case of isotropic conduction ($K_\perp = K_\parallel$) the temperature is constant over the star, but as $K_\perp$ reduces with respect to $K_\parallel$, the equatorial regions become cooler, reaching a zero temperature in the approximation $K_\perp/K_\parallel = 0$. The latter is physically plausible for fields $\gg 10^{11}$ G [442], and Eq. 3.2 reduces to

$$T_s(\theta_B) = T_p|\cos\theta_B|^{1/2}. \tag{3.4}$$

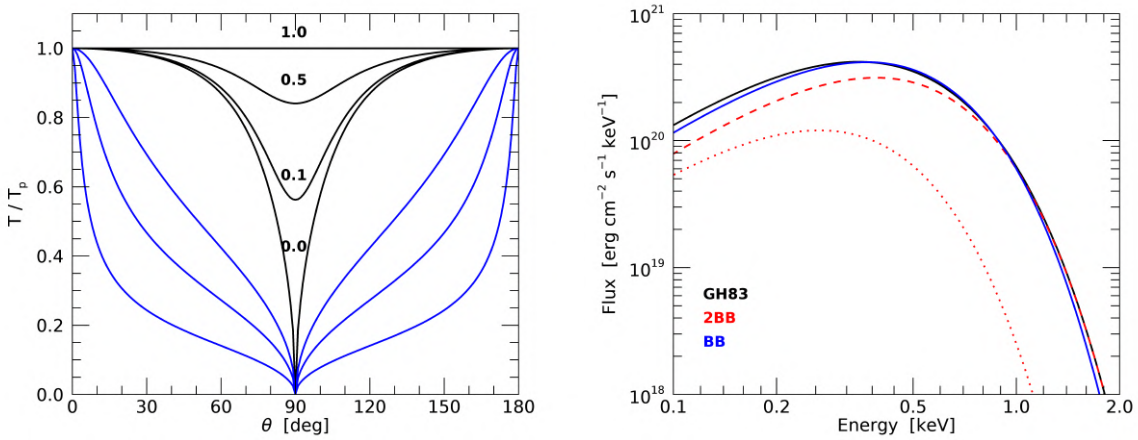

Figure 3.2: Left panel: Temperature distribution as a function of the magnetic colatitude θ according to Greenstein & Hartke [134] (black lines), for different values of the ratio $K_\perp/K_\parallel$, and according to Suleimanov et al. [388] (blue lines), for different anisotropy degrees. Right panel: Emergent spectrum from a NS envelope with $T_p = 1.75$ MK and distribution following Eq. 3.4 (black line), fitted by two blackbodies of $T_1 \approx 1$ MK and $T_2 \approx 1.6$ MK (red lines) or a single blackbody of $T \approx 1.5$ MK (blue line).

Locally, each patch of the stellar envelope at a magnetic colatitude θ emits with the temperature of Eq. 3.4. If we assume that this emission is isotropic, the resulting spectrum is a composite blackbody, shown in Figure 3.2, right panel, with a black solid line. If the data are not that-high-quality, the sum of two blackbodies is an adequate approximation for this temperature distribution; of the two blackbodies, the hotter fits the pole region (red dashed line), the colder fits the equatorial region (red dotted line). This is the case of several thermal objects, especially the CCOs [301, 128, 139] and the XDINSs [440]. On the contrary, a single blackbody (blue solid line) fits badly the spectrum, especially at the lower energies.

Other emission models have been proposed instead of a pure blackbody: magnetized atmospheres (Section 3.1.2) or magnetized condensed surface (Section 3.1.3). They do not appreciably change the relation of Eq. 3.1, but the ongoing radiation is affected by the magnetic field direction, as the emission properties deeply depend on the angle α between the wave vector and the magnetic field (see Figure 3.1). As a consequence, also the surface temperature distribution is modified (see e.g. Pérez-Azorín et al. [311], Suleimanov et al. [388], and Figure 3.2, left panel).

3.1.2 Atmospheric emission models

It is currently accepted that above the envelope there is a thin atmospheric layer, with scale height of about $1-10$ cm and a density of $0.1-10$ g cm^{-3} [447]. A pure hydrogen atmosphere is expected if the phenomena of fallback and/or accretion occur after NS formation; the total mass of hydrogen needed to form an optically thick atmosphere can be less than 10^{16} g. Alternatively, a helium atmosphere may be possible as a result of diffusive hydrogen burning on the NS surface [62, 63]. Finally, a heavy-element (as carbon) atmosphere may exist if no accretion takes place or if all the accreted matter is consumed by thermonuclear reactions [282].

Early works on atmospheric spectra [361] assumed emission from light-element, unmagnetized atmospheres; the computed spectra exhibit significant deviation from a Planckian shape and distinctive hardening with respect to a blackbody. This is linked to the ν^{-3} spectral dependence of the absorption coefficient for a fully ionized medium: hard photons are emitted from deeper and thus hotter layers in the atmosphere. Observationally, if we use a blackbody model to fit a spectrum emerging from an atmosphere, we overestimate the temperature by a factor 2-3 and, as a consequence, we underestimate the emitting radius [48, e.g.].

In a magnetized plasma, the electromagnetic radiation propagates in the form of extraordinary (X) and ordinary (O) normal modes, which have different opacities and polarization vectors as a function of the angle α [116, 268]; it can be shown that under typical conditions [226], the X-mode opacity κ is strongly suppressed with respect to the O-mode one according to the formula

$$\kappa_{\rm X} \sim \left(\frac{\nu}{\nu_{\rm B}}\right)^2 \kappa_{\rm O}, \tag{3.5}$$

where $\nu_{\rm B}$ is the electron cyclotron frequency. As a result, the X-mode photons escape from deeper, hotter layers of the NS atmosphere with respect to the O-mode photons, and the emergent radiation is linearly polarized to a high degree (as high as 100%).

It is well known that polarization of the vacuum due to virtual $e^+ - e^-$ pairs becomes significant when $B \gtrsim B_{\rm QED}$. Vacuum polarization modifies the dielectric property of the medium and the polarization of photon modes, altering the radiative scattering and absorption opacities [226, 225]. Of particular interest is the "vacuum resonance" phenomenon, which occurs when the effects of the vacuum and plasma on the linear polarization of the modes cancel each other, and both modes become circularly polarized. The vacuum resonance occurs at the energy

$$E_{\rm V} \simeq 1.02 (Y_e \rho_1)^{1/2} B_{14}^{-1} f \ \ {\rm keV}, \tag{3.6}$$

where Y_e is the electron fraction, ρ_1 is the density in units of 1 g cm^{-3}, B_{14} is the magnetic field strength in units of 10^{14} G, and $f = f(B)$ is a slowly-varying function of B and is of order unity (see Eq. 2.41 of Ho & Lai [177]).

When a photon propagates in an inhomogeneous medium, its polarization state evolves adiabatically if the density variation is sufficiently gentle. Thus, an X-mode or O-mode photon is converted into an O-mode or X-mode one, respectively, as it traverses the vacuum resonance [226]. Because the two photon modes have vastly different opacities, the mode conversion (partial or complete, see van Adelsberg & Lai [419]) induced by vacuum polarization can significantly affect radiative transfer in NS atmospheres, even for $B < B_{\rm QED}$ [225]: a lower density of X-mode photons (which carry the bulk of the thermal energy) depletes the high-energy tail of the spectrum and makes the spectrum closer to blackbody, although the spectrum is still harder than blackbody because of nongray opacities (see Figure 3.3). Also in this case, colder temperatures and larger radii with respect to a blackbody fit are found [449, 357]. A second effect of the vacuum resonance is the suppression of the ion cyclotron lines, but only for $B \gtrsim B_{\rm QED}$ [173].

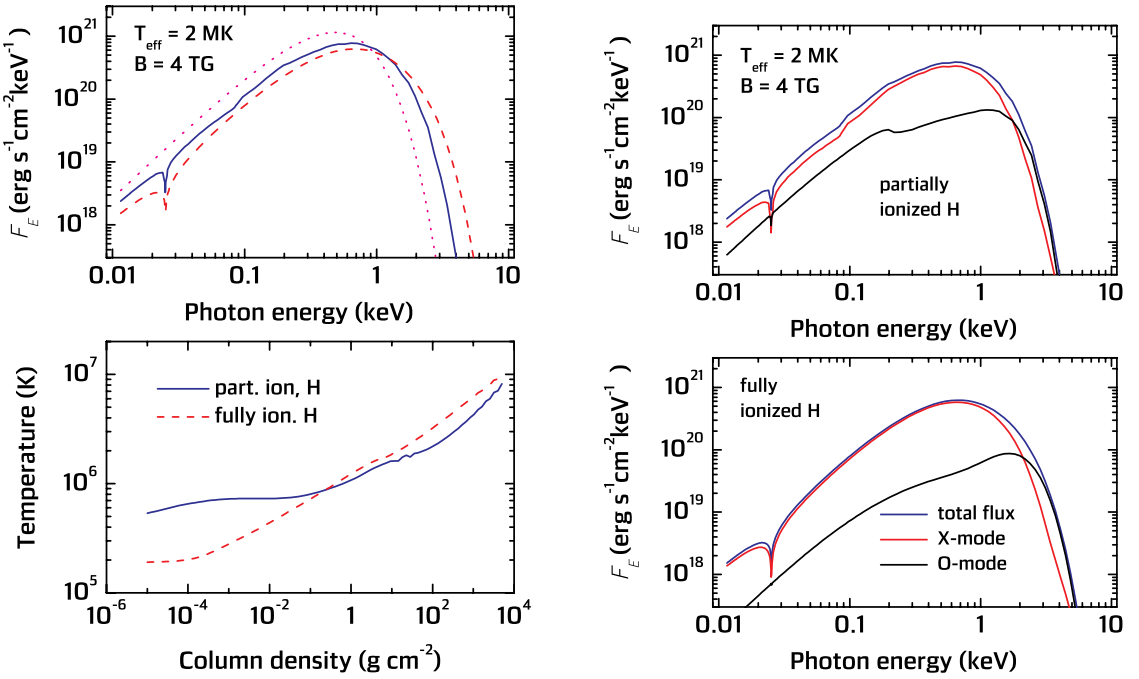

Figure 3.3: Left panel: Emergent spectra and temperature profiles of a partially ionized hydrogen atmosphere (blue solid line) and a fully ionized hydrogen atmosphere (red dashed line) with a surface temperature $T_{\rm eff} = 2$ MK and a magnetic field normal to the surface of intensity 4 TG. A blackbody of the same temperature is shown as a comparison (magenta dotted line). Right panel: Emergent spectra decomposed in the X-mode (red lines) and the O-mode (black lines), for a partially ionized atmosphere (upper panel) and for a fully ionized one (lower panel). Courtesy of V. Suleimanov.

Model atmospheres of highly magnetized neutron stars were computed by many authors, following the pioneering work of Shibanov et al. [372] (see, e.g., Potekhin et al. [334] for a review and references therein). As in the case of the magnetized envelope, models of magnetized atmosphere are computed in the plane-parallel approximation. The models differ on the choice of the magnetic field strength and distribution, on the atmospheric chemical composition, and on the ionization degree of the medium. In fact, because the strong magnetic field significantly increases the binding energies of atoms, molecules, and other bound states (see, e.g., Lai [224] for a review), these bound states may have abundances appreciable enough to contribute to the opacity in the atmosphere [227, 335] and partially ionized atmosphere models [177] superseded the fully ionized ones to interpret the NS thermal emission. Some of these models have been implemented in XSPEC in two families, namely NSA [304] and NSMAXG [174, 172].

The main improvement of the NSMAXG models is the option to vary $\theta_{\rm B}$. If we consider the magnetic field perpendicular to the surface, $\theta_{\rm B} = 0^\circ$ and α becomes equal to θ_k. It is the simplest case, because the opacities depend on α, and the geometry of radiation propagation depends on θ_k. This approximation applies well if the emitting regions are the magnetic polar caps, because they are small enough to have no appreciable variation of $\theta_{\rm B}$ [415, e.g.]. On the contrary, if $\theta_{\rm B}$ is arbitrary (as if we consider the emission of the whole stellar surface), the opacities depend also on ϕ_k and it is necessary to solve radiation transfer equations for a significantly larger number of directions. Usually, in this case the stellar surface is divided in a few patches, each of them

having constant θ_B [171, e.g.].

Figure 3.3, left panel, shows the emergent spectra and the temperature profiles of a partially ionized hydrogen atmosphere (blue solid line) and a fully ionized hydrogen atmosphere (red dashed line) with a surface temperature $T_{\rm eff} = 2$ MK and a magnetic field of intensity 4 TG and normal to the surface. The fully ionized model is harder than the partially ionized one, and they are both harder than a blackbody of the same temperature (magenta dotted line). The electron cyclotron absorption line can also be observed at $E_{\rm ce}(B = 4\ {\rm TG}) \approx 0.025$ keV. Figure 3.3, right panel, shows instead the emergent spectrum decomposed in the X-mode (red line) and the O-mode (black line), the latter being less intense because of Eq. 3.5. This effect is less pronounced for a partially ionized atmosphere (upper panel) than for the fully ionized one (lower panel).

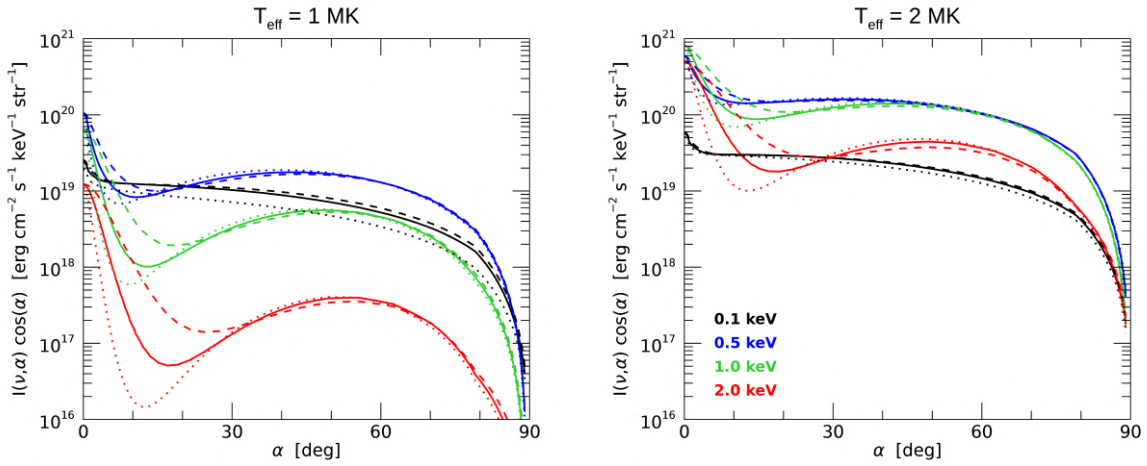

Figure 3.4: Angular dependence of the emergent intensity for a hot spot covered by a magnetized, partially ionized hydrogen atmosphere with $T_{\rm eff} = 1$ MK (left panel) and 2 MK (right panel) for three different magnetic fields: 2 TG (dashed lines), 4 TG (solid lines) and 8 TG (dotted lines). The curves of different colors refer to different photon energies as specified in the legend.

However, the most relevant aspect of the emission of a magnetized atmosphere (especially if the ionization is partial) is the anisotropy that the magnetic field imprints on the emergent radiation, even if the surface temperature is uniform [303, 450, 448, e.g.]. Figure 3.4 shows the angular dependence of the specific intensity at the magnetic pole for different photon energies in the case of $T_{\rm eff} = 1$ MK (left panel) and 2 MK (right panel), for three different magnetic fields. The pronounced peak along the magnetic field, called "pencil-beaming", is related to the reduction in the opacity of both polarization modes at small α [387]. However, the total flux in that peak is relatively small because it occupies a small solid angle. Most of the radiation escapes in the second broad maximum at intermediate angles, that gives rise to the so-called "fan-beamed" emission. This off-axis maximum is caused by the opacity reduction in the X-mode at large angles [303, 387]. Finally, we note a gradual softening of the specific intensity at higher angles approaching 90°, because relatively cold surface atmospheric layers contribute substantially at these angles. The emerging specific intensity becomes more anisotropic with increasing photon energies, as the relative importance of electron scattering to the total opacity increases, and with increasing B and decreasing T, as the fraction of bound states increases.

3.1.3 Condensed surface emission models

In 1971, Ruderman [364] suggested that in the presence of a strong magnetic field, the NS surface can undergo a phase transition to a condensed state. As said, high magnetic fields strongly affect the properties of atoms, molecules, and plasma, because the typical transverse dimension of the electron Landau orbit (see Eq. 1.27) becomes smaller than the Bohr radius when $B \geq B_0$ [268]. This may lead to the formation of linear molecular chains aligned with the magnetic field, that can form a condensate via covalent bonding. Later studies (see Medin & Lai [260], and references therein) have provided support for this conjecture, although the critical temperature $T_{\rm crit}$, below which this condensation occurs, remains very uncertain. Condensed surface density ρ_s is usually estimated as

$$\rho_s = 0.56 \times 10^6 \, \eta A Z^{-0.6} B_{12}^{1.2} \ {\rm g \ cm^{-3}}, \tag{3.7}$$

where $\eta \sim 1$ is an unknown numerical factor, which absorbs the theoretical uncertainties [224, 261]. The values of $T_{\rm crit}$ largely depend on the surface chemical composition. Lai & Salpeter [227, see also Lai [224]] firstly derived an estimation for $T_{\rm crit}$ in the case of hydrogen

$$T_{\rm crit} \approx 1.6 \times 10^4 \, B_{12}^{0.7} \ {\rm K}. \tag{3.8}$$

A comprehensive study carried out by Medin & Lai [261, 260] provided an estimation of $T_{\rm crit}$ for helium, carbon and iron:

$$T_{\rm crit} = 0.08 \, Q_s, \tag{3.9}$$

where Q_s is the cohesive energy of the three-dimensional condensate. Their numerical results can be roughly (within a factor of 1.5) described as

$$T_{\rm crit} = 5 \times 10^4 \, Z^{1/4} B_{12}^{3/4} \ {\rm K}, \tag{3.10}$$

that is valid for $1 \lesssim B_{12} \lesssim 1000$ [330].

Figure 3.5 shows the behavior of $T_{\rm crit}$ as a function of the magnetic field strength according to Eqs. 3.8 and 3.10 for hydrogen and iron composition, respectively. The location in the $B - T$ plane of some isolated NSs is also shown. If the surface composition is Fe, then strong-field NSs ($B \gtrsim 10^{13}$ G) with moderate surface temperatures ($T \lesssim 1$ MK) should have atmospheres/vapours that are effectively transparent to thermal radiation, so that the emission becomes that from a bare condensed surface. This may explain the nearly blackbody-like radiation spectrum observed from the XDINS RX J1856.5−3754 [417, 420, e.g.]. On the contrary, all the thermal-emitting RPPs have a surface temperature well above $T_{\rm crit}$ for their dipole magnetic field and no surface condensation is expected.

Models for the emission from the condensed surface of a bare NS have been developed by different authors (see e.g. Brinkmann [51], Turolla et al. [417], van Adelsberg et al. [420], Pérez-Azorín et al. [310]). Potekhin et al. [332] developed a simple analytical expression for the emissivity from a condensed iron surface with two extreme approximations for the response of ions to electromagnetic waves: one neglects the Coulomb interactions between ions ("free-ions" case), while the other treats ions as frozen at their equilibrium positions in the Coulomb lattice ("fixed-ions" case). The true radiation properties of a condensed magnetized surface should be in-between these limits (see the discussion in Turolla et al. [417]).

The condensed surface emits radiation with monochromatic intensity $I_\nu = J_\nu B_\nu$, where B_ν is the Planck spectral radiance and J_ν is the dimensionless emissivity, that is a function of the ion/electron cyclotron energies, the electron plasma energy (see Potekhin et al. [332, Section 2]),

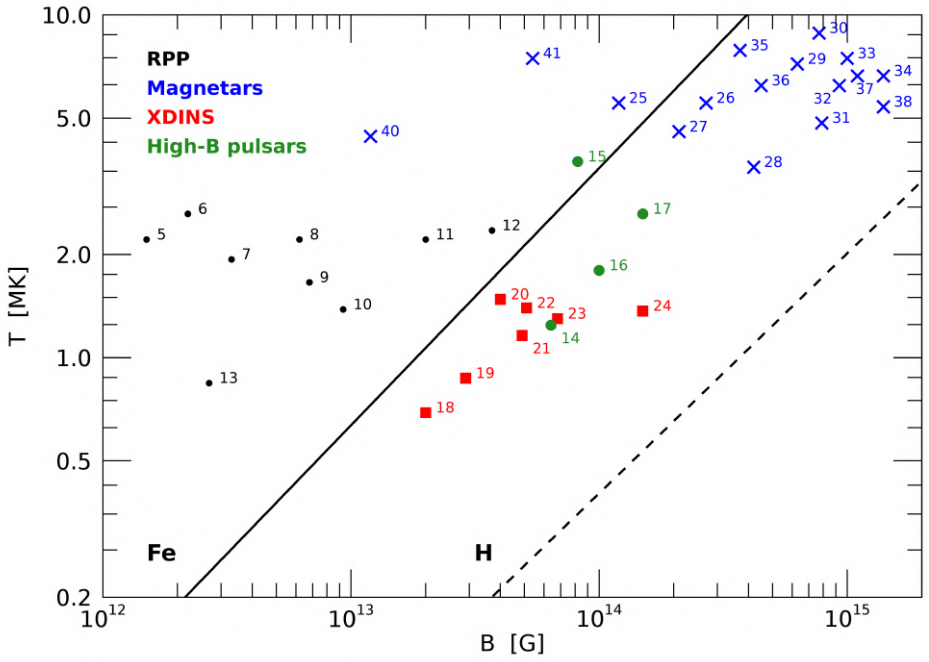

Figure 3.5: Surface temperature as a function of the magnetic field strength below which the magnetic condensation is allowed for iron (solid line) and hydrogen (dashed line), according to Eqs. 3.8 and 3.10 for $Z = 26$. The colored symbols represent the measured values of surface temperature and the dipole magnetic field. The same color coding as in Figure 1.9 is used, and the neutron stars are numbered according to Potekhin & Chabrier [331].

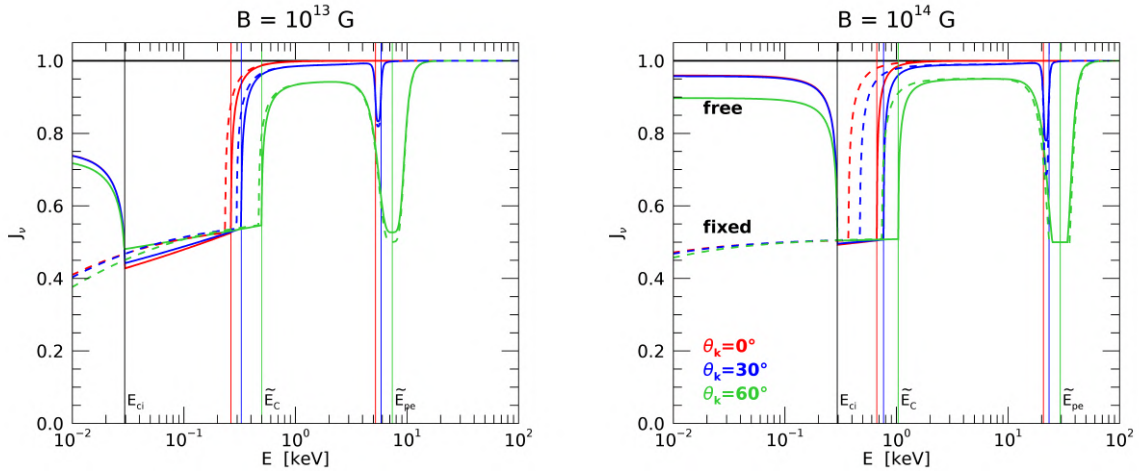

Figure 3.6: Emissivity as a function of photon energy for a condensed iron surface (free ions, solid lines; fixed ions, dashed lines) for a magnetic field $B = 10^{13}$ G (left panel) and $B = 10^{14}$ G (right panel) normal to the surface ($\theta_B = 0°$) and $\rho_s = 1.1 \times 10^6$ g cm^{-3}, see Eq. 3.7. $J_\nu = 1$, represented with a black solid line, is the emissivity of a blackbody. The red lines correspond to an incident angle $\theta_k = 0°$, the blue ones to $\theta_k = 30°$, and the green ones to $\theta_k = 60°$. The vertical lines indicate the values of E_{ci}, $\tilde{E}_C$, and $\tilde{E}_{pe}$ (see Eqs. 3.11 and 3.12).

and the usual angles θ_B, θ_k and ϕ_k (see Figure 3.1). As mentioned in the previous section, for nearly point-like magnetic polar caps, $\theta_B = 0^\circ$ and the emissivity has azimuthal symmetry.

Figure 3.6 shows the behavior of the total emissivity in both the free- and fixed-ions approximations, for an iron condensed surface, with $B = 10^{13}$ G (left panel), $B = 10^{14}$ G (right panel), $\theta_B = 0^\circ$, and three different incident angles ($\theta_k = 0^\circ$, 30°, and 60°). The main deviation from the blackbody model, which is represented in the figure by a black solid line, is for low energies, below E_{ci} ($\approx 0.029\, B_{13}$ keV in the case of iron). Here, is also where the free- and the fixed-ions models differ the most. Above this energy, they both behave as a blackbody except near the energies

$$\tilde{E}_{pe} = E_{pe}\sqrt{3 - 2\cos\theta_k}, \tag{3.11}$$

where $E_{pe} \approx 0.028\sqrt{\rho_{s,1} Z/A}$ keV is the electron plasma energy, and

$$\tilde{E}_C = E_{ci} + \frac{\tilde{E}_{pe}^2}{E_{ce}}. \tag{3.12}$$

As a result, the emergent spectrum is a blackbody above E_{ci} with features at $\tilde{E}_{pe}$ and $\tilde{E}_C$. The emission from a solid condensate is isotropic except near these energies, where it is beamed along the magnetic field direction.

The weak dependence of J_ν on the temperature has been neglected (as the temperature increases, the transitions of J_ν between characteristic energy ranges become smoother). The bulk of the calculations employed in the fitting was done at $T_{eff} = 1$ MK, but a change up to a factor 3 affects the results by an amount similar to the typical error in the fits, as it is discussed in Potekhin et al. [332].

3.2 Thermal emission from cooling neutron stars

After the very early stages of evolution that last about 100 years (see Section 1.2.1), a neutron star has a surface temperature of $\approx 10^6 - 10^7$ K and it gradually cools down through the emission of neutrinos (up to 10^5 yr) and photons. The theoretical cooling curves strongly depend on the mass, the envelope composition and the crustal magnetic field, and on the microphysics adopted to describe the NS interior. Therefore, a comparison between the cooling curves and the measured temperatures, obtained from X-ray observations, would allow us to distinguish between the many theoretical models. However, measuring the surface temperature of a NS is anything but trivial.

First, when the neutron star is young (age lower than 10^4 years), the thermal emission is covered by the more energetic nonthermal emission from the magnetosphere and/or the PWN (see e.g. the Crab pulsar), and no thermal spectrum can be observed. We are allowed to see the star surface only for young isolated NSs, as the CCOs and the magnetars, but in this case the surface temperature map is nonuniform (see Section 3.1.1): there is no unique temperature that can be measured through a blackbody fit. Moreover, badly constrained photoelectric absorption from the interstellar medium and/or absorption features constitute a source of error in temperature measurements.

Last but not least, it is well established that simple blackbody emission is insufficient to describe the complex interaction between the thermal photons and the condensed magnetized surface and/or the thin magnetized atmosphere that cover the star. However, these models (described in Sections 3.1.2 and 3.1.3) introduce many parameters, as the chemical composition, the star mass and radius, the system geometry, that in most cases are unknown. The overall

effect of fitting the thermal spectrum with an atmosphere model is to obtain larger radii and smaller temperatures, with respect to a blackbody model, but similar bolometric luminosities.

For all of these reasons, the luminosity constitutes a better choice to compare data and theoretical models. Since it is an integrated quantity, it averages effects of anisotropy and the choice of the spectral model. The main uncertainty on the luminosity is often due to the poor knowledge of the source distance, that in the worst cases, can be larger than 50%.

Finally, also the NS age has its source of uncertainty. If both the spin period and the period derivative are known, the characteristic age of Eq. 1.19 can be used as an approximation to the real age, but only if the initial period was much shorter than the current value. Unfortunately, this is not the most common situation, and usually, for middle-aged and old objects, τ_c is found to be larger than the real age, when the latter has been obtained by other methods: a SNR association (see Allen & Horvath [9] for a review) or historical records (as for the CCO in Cas A [16]) for young NSs, or the proper motion with an association to a birthplace, for a few other nearby sources (e.g., some XDINSs [402] and magnetars [400]).

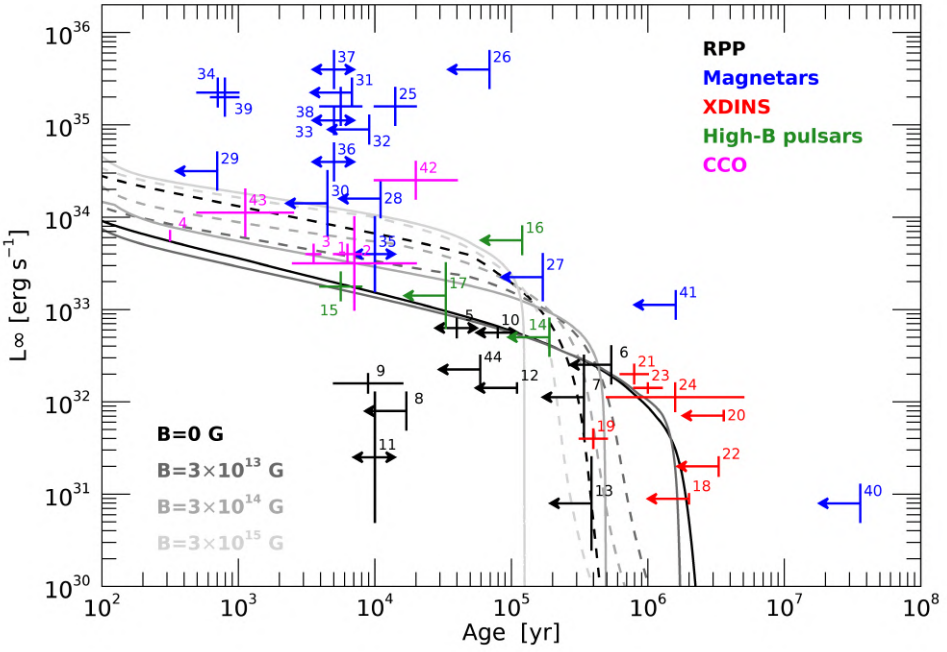

Figure 3.7: Age-luminosity diagram. The same color coding as in Figure 1.9 is used. The lines are the theoretical cooling curves of a neutron star with mass $M = 1.2\ M_\odot$ and dipole magnetic field $B_p = 0$, 3×10^{13}, 3×10^{14}, 3×10^{15} G, with the heat blanketing outer envelope composed either of iron (solid lines) or of accreted light elements (dashed lines). The horizontal error bars show the uncertainties of kinematic ages, when available; otherwise the bars are replaced by arrows or upper limits in case only the characteristic age is known. The data are taken from, and numbered according to, Viganò et al. [425], Potekhin et al. [333], Potekhin & Chabrier [331]; the cooling curves are a courtesy of A.Y. Potekhin.

Figure 3.7 shows the bolometric luminosity L_∞ measured at infinity as a function of the NS age. The theoretical cooling curves, with heavy (solid lines) and light (dashed lines) chemical elements in the outer heat-blanketing envelope, are calculated for a neutron star of mass $M = 1.2\ M_\odot$ and a dipole magnetic field $B_p = 0$, 3×10^{13}, 3×10^{14}, 3×10^{15} G. The NS envelopes are more transparent to the heat flux if they are composed of light chemical elements, because

of the lower collision rate and the smaller radiative opacities in the photosphere. The effects of superstrong magnetic fields ($B \gtrsim 10^{14}$ G) are the quantum enhancement of longitudinal electron conductivity and the formation of a condensed surface. However, the stored thermal energy is spent more rapidly as a consequence of rapid energy loss, and the luminous lifetime of the superstrong-field NS becomes shorter.

The code of Potekhin & Chabrier [331] was used, with the equation of state named "Brussels-Skyrme" (BSk24, [308]), and the singlet pairing-type superfluidity of neutrons and protons was considered, according to Margueron et al. [251] and Baldo & Schulze [23], respectively, both in the parametrized form of Ho et al. [175]. The triplet pairing-type superfluidity of neutrons is included according to the model "Av18 SRC+P" of Ding et al. [87], which accounts for the strong suppression of this type of superfluidity by the effects of many-particle correlations.

Error bars and arrows show observational estimates of the ages and thermal luminosities of 44 neutron stars with confirmed thermal emission. They are numbered according to Potekhin & Chabrier [331], which followed the catalog of Viganò et al. [425][1], and I have updated the luminosity of PSR J0726−2612 according to the results of Chapter 6. Horizontal error bars are estimated ranges of kinematic ages, that are replaced by short horizontal arrows in the cases where no confidence interval is found in the literature. If no kinematic age is available, the characteristic ages are adopted and they are represented as upper limits.

From Figure 3.7, we can observe that the thermal luminosity is clustered depending on the NS classes. As an example, high-B pulsars are more luminous than the RPPs of corresponding age, and the XDINSs are the only NSs of about 1 Myr that can emit thermal X-rays from cooling. The luminosity of high-B pulsars and XDINSs is well explained by the cooling curves of $B \lesssim 3 \times 10^{13}$ G, and the objects with an apparently too high luminosity are those with the less constraining age measure: if the decay of the magnetic field is strong, the characteristic age could overestimates the real age of more than one order of magnitude.

The RPP luminosity can be explained with the nonmagnetic cooling curves, only by varying the NS mass; remarkably, the higher the mass, the more powerful the cooling is (see Figure 1.1). The dimmest sources (e.g., objects number 8, PSR B1706−44; 9, Vela; 11, PSR B2334+61) require an iron envelope and the activation of fast cooling processes, possible only if the mass is $> 1.5\ M_\odot$ [257, e.g.]. CCOs have very low $\dot{P}$ implying a weak external magnetic field, that apparently contrasts with the observed surface anisotropies and high luminosities. Light-element envelope models can reconcile their young age and large luminosity, and they are favored in the hidden magnetic field scenario, in which the CCO has actually a strong subsurface magnetic field, which has been screened by the initial fallback of the supernova debris on to the NS (see Section 1.5.3).

Finally, the magnetars are the most luminous, with $L_\infty \approx 10^{34} - 10^{36}$ erg s^{-1}, and apparently none of the considered cooling curves can explain their luminosities. This indicates that additional heating mechanisms, that were intentionally neglected in the computation of these cooling curves, are probably important for the thermal evolution of magnetars, in agreement with previously published conclusions (e.g., Viganò et al. [425], Kaminker et al. [195], Beloborodov & Li [34]).

[1] A regularly updated online catalog can be found at http://www.neutronstarcooling.info, with abundant links to references for each source.

3.3 Nonthermal emission

3.3.1 Magnetosphere acceleration potential drop

A rotating, magnetized neutron star is surrounded by a magnetosphere filled with plasma (see Section 1.3.2). The plasma is assumed to be an excellent conductor, such that the charged particles, with charge density $\rho_{\rm GJ} \propto -\Omega \cdot B$ defined in Eq. 1.22, move to screen out any electric field parallel to the local magnetic field. However, above the polar cap region, the magnetic field lines are open (see Section 2.1.1) and particles can outflow. To maintain the required magnetosphere charge density, these particles have to be replenished by the stellar surface. Remarkably, if $\Omega \cdot B < 0$ the needed particles are ions, vice versa they are electrons (Figure 1.6 represents the case $\Omega \cdot B > 0$ and the particles above the polar caps are negative charged).

Ions and electrons can be extracted from the surface if the thermal energy is above the the ion binding energy $\mathcal{E}_{\rm B}$ and the electron work function Φ, respectively. For NSs in general, Φ is much less than the thermal energy, so electrons can easily escape from the condensed surface. On the other hand, $\mathcal{E}_{\rm B}$ can be higher if an intense magnetic field is present: Medin & Lai [260] showed that if

$$T < T_{\rm i} = 0.04\, Q_s, \tag{3.13}$$

ions are trapped on the surface, and a vacuum gap develops just above the polar cap region. In this vacuum gap zone the parallel electric field $E_{\parallel}$ is no longer screened and particles are accelerated across the gap, until a pair cascade is produced. The "vacuum gap" (VG) model was first developed in 1975 by Ruderman & Sutherland [365, see also Usov & Melrose [418]], and then revisited by Gil et al. [111], which considered that the pure vacuum potential drop can be partially screened by thermal ions; for this reason, the model is dubbed "partially screen gap" (PSG, see Section 3.4.2 for further details). Since $T_{\rm i}$ is half the value of $T_{\rm crit}$ (see Eq. 3.9), the conditions for the vacuum gap to occur are the same for the surface condensation, and they are verified for high-B pulsars, XDINSs and magnetars [456] (see Figure 3.5), or for RPPs with a non-dipolar magnetic field [114].

In ordinary RPPs, electrons and ions are easily extracted from the surface, but a vacuum gap above the polar caps can still be created due to field line curvatures [11] and the relativistic frame dragging effect [285]. These conditions are verified high above the polar caps, at some stellar radii. This model, called "space charge limited flow" (SCLF, see Section 3.4.1 for further details), has been developed by Arons & Scharlemann [11], Harding & Muslimov [148].

Both the VG/PSG and the SCLF models predict that particle accelerators will be self-limited because of the development of pair cascades. In fact, particles are accelerated by the parallel component of

$$\nabla \cdot \mathbf{E} = 4\pi(\rho - \rho_{\rm GJ}) \tag{3.14}$$

until they reach Lorentz factors high enough to radiate γ-ray photons. They, in turn, can pair produce if they are coupled with a strong magnetic field and if they have an energy above

$$\epsilon_{\gamma}^{\rm PP} = \frac{2 m_e c^2}{\sin \alpha}, \tag{3.15}$$

where α is the angle between the photon propagation and the local magnetic field. The emitted photons have very small angles with respect to the magnetic field ($\alpha_0 \sim 1/\gamma$, where γ is the Lorentz factor), so the one-photon pair production rate for these photons is initially zero. However, after they travel a distance z, the intersection angle will grow as z/R_c, where R_c is the local radius of curvature of the polar magnetic field line. For a pure dipole field, R_c is of

the order of $\sqrt{Rc/\Omega} \approx 10^8 P^{1/2}$ cm, but a more complex field topology at the polar cap could reduce the curvature radius to $\approx 10^6$ cm [105], small enough to satisfy the threshold condition of Eq. 3.15.

The radiated photons produce more pairs, that radiate other photons, in an avalanche process. The pair cascade can be initiated either by curvature radiation (CR) [77] or by resonant[2] or non-resonant inverse-Compton scattering (ICS) of stellar thermal X-rays by primary electrons [385]. Since for a given Lorentz factor the peak CR photon energy

$$\epsilon_\gamma^{\rm CR} = \frac{3h\gamma^3}{2R_c m_e c} \tag{3.16}$$

is much lower than the ICS peak energy[3]

$$\epsilon_\gamma^{\rm ICS} \sim \gamma, \tag{3.17}$$

the production of CR photons requires a much higher Lorentz factor. As a consequence, only young and energetic pulsars can activate pair production from CR photons [149], while the older pulsars can produce pairs only from ICS photons [150].

The observed γ-ray emission is interpreted as the primary CR and ICS radiation, while the X-ray nonthermal emission is due to the higher generation pairs, that emit through synchrotron radiation (SR) and ICS of softer frequencies. This scenario predicts a relation between the high-energy luminosity and the rotational power loss of the pulsar $\dot{E}$; in particular

$$L_\gamma \propto \dot{E}^{1/2} \tag{3.18}$$

and

$$L_X \propto 10^{-3}\dot{E}, \tag{3.19}$$

according to Zhang & Harding [455].

3.3.2 The $L_X - \dot{E}$ relation

From an observational point of view, the X-ray nonthermal emission dominates the higher energy part of the spectrum, above ~ 2 keV, and it is fitted well by a power law with photon index $\Gamma \approx 1 - 4$ [27]. The light curve of this component is strongly pulsed, because it is emitted in beams due to the anisotropies caused by the magnetic field. The pulse profile overall is sinusoidal, but it can show one or two narrow peaks. Because in most cases the amount of beaming is unknown, L_X is calculated assuming an isotropic radiation pattern. In addition, several young and/or energetic pulsars are surrounded by a PWN, whose emission is nonthermal and unpulsed, and often cannot be resolved because of the instrumental PSF.

For all of these reasons, it is not trivial to derive the actual L_X produced by the magnetosphere: bad-oriented beaming with respect to the Earth could decrease the observed luminosity, on the contrary unresolved PWNe could enhance it. Moreover, great uncertainties on the pulsar distance can alter the luminosity of more than one order of magnitude. Nevertheless, many authors devoted their efforts to study the efficiency of the X-ray emission with respect to the spin-down luminosity.

A correlation between these quantities was first noticed in 1988 by Seward & Wang [368], and later investigated by Becker & Truemper [29] using a sample of 27 pulsars detected with

[2]The electron makes a transition from the ground Landau level to the first excited level, see e.g. Herold [166].
[3]In the extreme Klein-Nishina limit.

ROSAT in the soft X-rays, $0.1 - 2.4\,\mathrm{keV}$. They found $L_X \propto 10^{-3}\dot{E}$, but as said, this energy band is affected by contamination from the thermal component. For this reason, Possenti et al. [326] analyzed 41 objects, 31 rotation-powered and 10 millisecond pulsars, observed by *ASCA*, *RXTE*, *Beppo*SAX, *Chandra* and *XMM-Newton* in the energy range $2 - 10\,\mathrm{keV}$, and found $L_X = 10^{-15.34}\ \dot{E}^{1.34}$. Finally, Becker [27] found for 63 objects (43 RPPs and 20 MSPs) $L_X = 10^{-15.72}\ \dot{E}^{1.336}$. This fit has been confirmed by the discovery of 9 additional RPPs and many constraining upper limits [336].

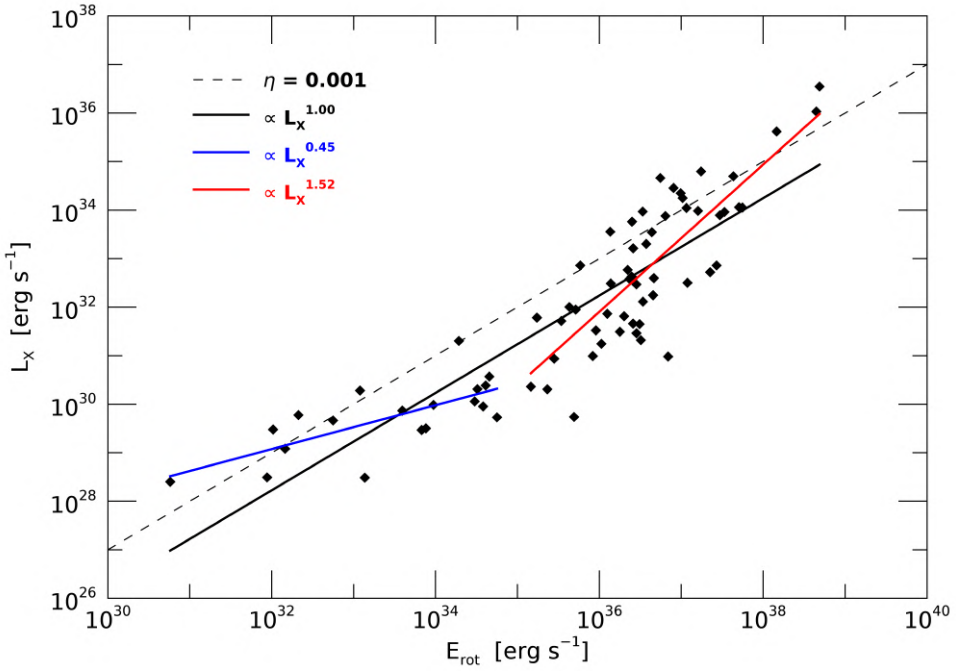

Figure 3.8: The $L_X - \dot{E}$ relation in the $2 - 10\,\mathrm{keV}$ energy band for the 72 RPPs that show nonthermal X-ray emission. The best fit gives $L_X = 10^{-3.88}\ \dot{E}^{1.00}$ (black solid line), that is approximatively one order of magnitude below the relation of Eq. 3.19 (black dashed line). The fits for $\dot{E}$ lower and greater than $10^{35}\ \mathrm{erg\ s^{-1}}$ give $L_X = 10^{14.6}\ \dot{E}^{0.45}$ (blue line) and $L_X = 10^{-22.7}\ \dot{E}^{1.52}$ (red line), respectively.

Figure 3.8 shows the $L_X - \dot{E}$ relation for the 72 known RPPs that emit nonthermal X-ray radiation. The spectral parameters, through which I evaluated the luminosities in the $2 - 10\,\mathrm{keV}$ energy band, are listed in Table B.2. I found $L_X = 10^{-3.88}\ \dot{E}^{1.00}$, implying an efficiency $(1 - 2) \times 10^{-4}$, one order of magnitude below the expected relation of Eq. 3.19 and represented in the figure by a dashed line. This should be considered as a maximum efficiency rather than a fixed correlation, obtained by pulsars which are seen with an optimal viewing geometry. The global lower luminosity, as well as the large scatter, is due to random viewing geometry and the inability to apply a beaming correction.

On the other hand, some objects show $L_X > 10^{-3}\dot{E}$: possible explanations are badly constrained distances and the contamination of the PWNe, expecially for the younger pulsars. Instead, intrinsically less energetic pulsars ($\dot{E} < 10^{33}\ \mathrm{erg\ s^{-1}}$) are too old to create a PWN, and the majority of them have parallax-based distances; therefore, the higher efficiency seems to be real. Unfortunately, the absence of low-efficiency old pulsars might be only a selection effect, due to observational detection limits.

Nevertheless, I tried to divide the sample into two sub-samples, according to the pulsar spin-down power (I arbitrarialy choose $\dot{E}_{\rm break} = 10^{35}$ erg s^{-1}). I obtained a significant change in the slope of the $\dot{E} \propto L_X^{\alpha}$ relation, as already found by Szary [391] for the same energy break. It resembles the behavior noticed by Harding et al. [151] for the γ-ray luminosity, due to the transition from CR to ICS regime as the pulsar becomes older and less energetic, even if the authors found a steepening of the slope for $\dot{E} < \dot{E}_{\rm break}$.

3.4 Polar caps heating

In the pair-production phenomenon discussed above, half of the particles are accelerated backward, and return on the stellar surface. There are two main consequences: these particles partially screen the voltage drop, and they heath the NS surface, in the region of the polar cap.

The thermal emission of hot polar caps is seen in pulsars of $\tau \gtrsim 10^5$ yr, when both the non-thermal and the cooling components have weakened enough. Pulsars that show this thermal component in their X-ray spectra are listed in Table 8.4 and will be discussed in Section 8.4, while in the following I present the theoretical expectations from the two concurrent models on the reheating of the polar caps: the SCLF (Section 3.4.1) and the PSG (Section 3.4.2) models.

3.4.1 Space Charge Limited Flow model

In SCLF model of Arons & Scharlemann [11], Harding & Muslimov [148, 149, 150], Harding et al. [151], vacuum gaps are created high above the polar caps, at some stellar radii, because both ions and electrons can be freely stripped off the neutron star surface. Therefore, both $\Omega \cdot B < 0$ and $\Omega \cdot B > 0$ pulsars can accelerate particles and initiate the pair production.

Let's consider the electrons as the primary particles ($\Omega \cdot B > 0$): they accelerate upward from the stellar surface and produce pairs at different altitudes above the pair formation front (PFF). The positrons decelerate and turn around in a distance short compared to the PFF altitude, and each reversing positron creates a small excess of negative charge. As more positrons are produced and decelerated, the space charge becomes more negative until the entire charge deficit $\delta\rho = (\rho - \rho_{\rm GJ})$ that produced the $E_{\parallel}$ is accounted for. Since the charge deficit is small compared to the primary charge ($\delta\rho \ll \rho_{\rm GJ}$), the screening length scale is a very small fraction of the PFF altitude. The flux of returning positrons, as a fraction of the primary flux, is approximately

$$f_+ \approx \frac{\rho_+}{\rho_{\rm GJ}} = \left.\frac{\rho_{\rm GJ} - \rho}{2\rho_{\rm GJ}}\right|_{z_0} \approx \frac{3}{2}\frac{x}{1-x} z_0, \tag{3.20}$$

where z_0 is the PFF height above the stellar surface and x is the stellar compactness parameter. The corresponding polar cap heating luminosity is

$$L_+ \approx f_+ \phi(z_0) \dot{n}_{\rm prim}, \tag{3.21}$$

where $\dot{n}_{\rm prim}$ is the primary particle flux and $\phi(z_0)$ is the potential drop at z_0.

As said in Section 3.3, the CR photon production requires a much higher energy of the primary particles, and therefore it occurs at higher altitude and L_+ is expected to be much higher in the CR rather than in the ICS scenario (see Figure 3.9). Moreover, the screening region above ICS PFFs takes place over a larger scale length, and even when ICS screening is locally complete, an unscreened charge deficit can develop at higher altitudes. If a CR PFF forms at higher altitude, then a complete screening occurs, otherwise the screening is only partial. Harding &

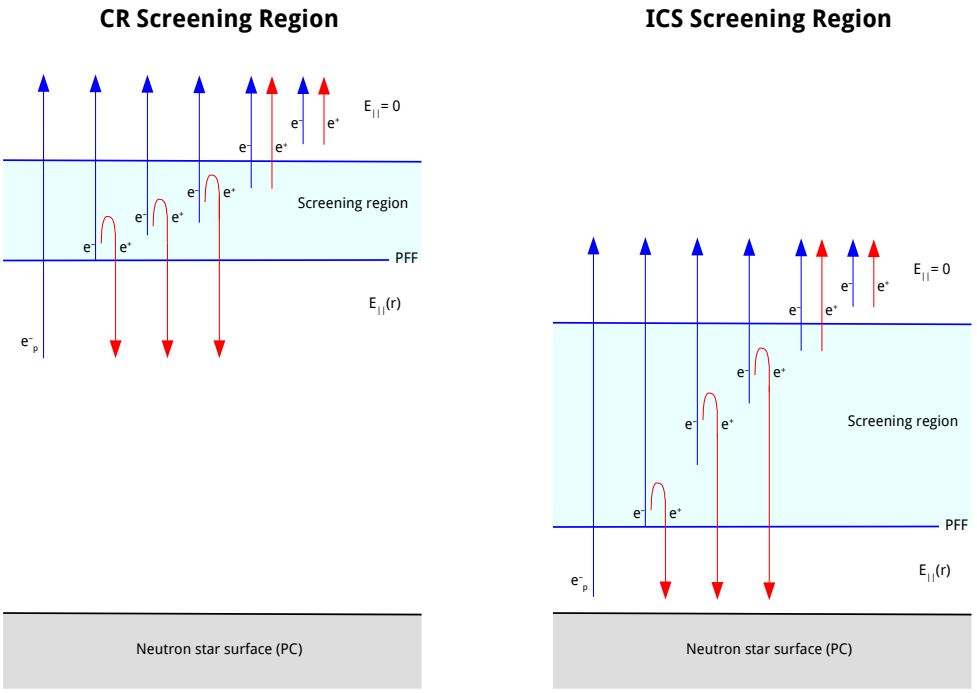

Figure 3.9: Illustration of electric field screening in SCLF model ($\Omega \cdot B > 0$ case), both in the CR (left panel) and the ICS (right panel) scenarios. $e_{\rm p}^{-}$ represents the primary electron flux accelerating upward from the neutron star surface. e^{+} and e^{-} represent electron-positron pairs created by the primary electron above the pair formation front. Adapted from Harding [147].

Muslimov [149, 150] derived analytic expressions for L_{+}, that provide a good estimate of the bolometric luminosity of the polar caps in the case of complete screening, and upper limits in the case of incomplete screening, both for the CR and the ICS scenario:

$$L_{+}^{\rm CR} \simeq 10^{31}\ {\rm erg\ s^{-1}} \begin{cases} 0.4\ P^{-6/7}\tau_6^{-1/7} & \text{if } P \lesssim 0.1 B_{12}^{4/9} \\ 1.0\ P^{-1/2} & \text{if } P \gtrsim 0.1 B_{12}^{4/9} \end{cases} \tag{3.22}$$

$$L_{+}^{\rm ICS} \simeq 10^{28}\ {\rm erg\ s^{-1}} \begin{cases} 0.3\ P^{-3/2} & \text{if } P \lesssim 0.4 B_{12}^{4/7} \\ 0.2\ P^{-3/2} & \text{if } P \gtrsim 0.4 B_{12}^{4/7} \end{cases} \tag{3.23}$$

3.4.2 Partially Screened Gap model

In the PSG model of Gil & Mitra [109], Gil et al. [111, 112, 113], the ions are trapped on the stellar surface ($\Omega \cdot B < 0$), when the surface temperature is below the critical value $T_{\rm i}$ defined in Eq. 3.13. As a consequence, a vacuum gap is formed above the polar cap region. Electrons are accelerated backward and bombard the polar cap surface, causing a thermal ejection of ions, which causes a partial screening of the acceleration potential drop.

Because of the exponential sensitivity of the accelerating potential drop to the surface temperature [260], the mechanism is thermostatically regulated. In fact, the thermionic emission enhances the surface temperature that overcomes $T_{\rm i}$, and as a consequence the potential drop decreases so that no positrons or electrons, that caused the thermionic emission in the

first place, are accelerated. As a result of these two oppositely directed tendencies, a quasi-equilibrium state should be established, in which heating due to electron bombardment is balanced by cooling due to thermal radiation.

Another consequence of the PSG model, first noticed by Ruderman & Sutherland [365], is that the phenomenon of drifting subpulses observed in many radio pulsars (see Section 2.3.1) is naturally explained in terms of the $\mathbf{E} \times \mathbf{B}$ circulation of plasma filaments produced by vacuum discharges. The speed of the drift motion around the magnetic axis is

$$v_{\rm d} = \frac{cE_{\perp}}{B_{\rm s}}, \tag{3.24}$$

where $E_{\perp}$ is the perpendicular component of the electric field caused by charge depletion (see Eq. 3.14); $E_{\parallel}$, on the contrary, is responsible for the acceleration of charged particles in the gap and it can be written that $E_{\perp} = \alpha E_{\parallel}$, where α is a numerical coefficient close to unity [114].

In this framework, the period of the drift motion P_4, i.e. the period of the carousel circulation (see Eqs. 2.17 and 2.18), can be written as

$$P_4 = \frac{2\pi d}{v_{\rm d}}, \tag{3.25}$$

where d is the is circulation distance of sparks from the local magnetic pole, that depends on the polar cap radius and the emission height.

Gil et al. [112, 113, see also the Appendix of Gil et al. [114]] derived a simple formula only considering a quasi-equilibrium condition between the electron bombardment heating and the cooling of the polar cap, and that the two phenomena are caused by different components of the same electric field:

$$\frac{L_{\rm bol}}{\dot{E}} = 0.63 \left(\frac{\alpha^{-2}}{I_{45}}\right) \left(\frac{P_4}{P}\right)^{-2}, \tag{3.26}$$

where $I_{45} = 1^{+0.25}_{-0.22}$ is the NS moment of inertia in units of 10^{45} g cm^2, and $\alpha \approx 1$ is the ratio between the perpendicular and the parallel components of the electric field.

If $L_{\rm bol}$ is written in terms of $A_{\rm bol}\sigma T_{\rm s}^4$ and $\dot{E}$ in terms of P and $\dot{P}$ (see Eq. 1.9), the quasi-equilibrium surface temperature $T_{\rm s}$ should be

$$T_{\rm s} = 5\ {\rm MK}\ b^{1/4} \dot{P}_{-15}^{1/4}\ P^{-1/2} \left(\frac{P_4}{P}\right)^{-1/2}, \tag{3.27}$$

where

$$b = \frac{B_{\rm s}}{B_{\rm d}} = \frac{A_{\rm PC}}{A_{\rm bol}} \tag{3.28}$$

is the ratio between the actual magnetic field at the surface over the canonical dipolar component at the polar cap; because of magnetic flux conservation, b is also equal to the ratio between the areas that include the field open lines: $A_{\rm PC} = \pi R_{\rm PC}^2$ in the dipolar case (see Eq. 2.3), $A_{\rm bol}$ is measured directly from X-ray observations.

Chapter 4

Modeling the X-ray emission from magnetic polar caps

In this chapter, I describe how I generated synthetic spectra and pulse profiles using thermal emission models, that consider polar caps covered by a magnetized hydrogen atmosphere or with a condensed iron surface. I relied on an existing software that was developed by R. Turolla, S. Zane, and R. Taverna [442, 398, 123]. The ray-tracer code, that is briefly described in Section 4.1, evaluates the emerging intensity of the radiation from the surface elements which are in view at different rotation phases from a stationary observer at infinity.

The intensity of the radiation depends on the assumed physical parameters, as the surface temperature and the magnetic field, and on the emission mechanisms. The ray-tracer code takes into account the emission from a magnetized envelope, following Greenstein & Hartke [134], and from a condensed surface, following the analytic derivation of Potekhin et al. [332]. Instead, the emergent radiation from a magnetized atmosphere was computed with an independent software in two steps: first, evaluating the photon opacities; second, solving the radiative transport equations. These were done by A. Y. Potekhin and by V. Suleimanov, respectively.

I adapted the ray-tracer code to the specific case of emission from small magnetic polar caps, and I convolved the obtained flux with the instrumental response matrix, in order to perform spectral and timing analysis of the observed data. My contribution is described in Section 4.2.

4.1 The ray-tracer code

The computation of the phase-dependent spectrum emitted by a NS, as seen by a distant observer, is done in three steps: i) defining the stellar parameters; ii) evaluating the local spectrum emitted by each patch of the surface; iii) collecting all the contributions of surface elements that are in view at different rotation phases, accounting for general relativistic effects (discussed in Section 1.2.2).

First, the relevant stellar parameters in the case of thermal emission are: the mass M and the radius R, that determine the surface gravity; the surface temperature T and magnetic field B and their physical distribution; the angles ξ and χ that the rotation axis makes with the magnetic axis and with the line of sight (LOS), respectively. In Section 3.1.1, I discussed that the electron transport in a magnetized envelope induces a nonuniform temperature distribution on the surface; if the magnetic field is dipolar, Greenstein & Hartke [134] demonstrated that the surface temperature $T_{\rm s}(\theta_{\rm B}) = T_{\rm p}|\cos\theta_{\rm B}|^{1/2}$, where $T_{\rm p}$ is the temperature at the magnetic poles,

and θ_B is the magnetic colatitude. The general relativistic effects also include the magnetic field vector:

$$B^{GR}(r,\theta,\phi) = \begin{pmatrix} B_r^{GR} \\ B_\theta^{GR} \\ B_\phi^{GR} \end{pmatrix} = \begin{pmatrix} f_{dip} B_r \\ g_{dip} B_\theta \\ B_\phi \end{pmatrix}, \tag{4.1}$$

where (see Page & Sarmiento [298])

$$\begin{cases} f_{dip} &= -\dfrac{3}{x^3}\left[\ln(1-x) + \dfrac{1}{2}x(x+2)\right] \\ g_{dip} &= \sqrt{1-x}\left(-2f_{dip} + \dfrac{3}{1-x}\right) \end{cases} \tag{4.2}$$

with $x = R_S/R$, and B_r, B_θ and B_ϕ are written in terms of the magnetic field at the pole, B_p (see Eq. 1.15). The last relevant characteristic is the pulsar orientation and viewing geometry, parameterized by the angles ξ and χ (see also Section 2.1.1). The angles of the radiative transport equations, namely α, θ_k, ϕ_k (defined in Section 3.1) can be written as functions of ξ and χ (see Chapter 3 of Taverna [397]).

In order to proceed, the star surface is divided into a given number of patches using a mesh (θ,ϕ). Each surface element contributes with an intensity $I_\nu(\theta,\phi)$ that depends on the surface physical conditions but also on the assumed emission model. If we consider a blackbody, then I_ν is a function only of the temperature, according to the Planck spectral radiance B_ν. However, as already pointed out in Section 3.1.3, in the presence of a strong magnetic field the NS surface can undergo a phase transition to a condensed state. In this case, $I_\nu = J_\nu B_\nu$, where J_ν is the dimensionless emissivity, function of θ_B, θ_k and ϕ_k. The ray-tracer code followed the analytic expression developed by Potekhin et al. [332] in the two extreme approximations of free and fixed iron ions.

Finally, if a magnetized atmosphere model is considered (see Section 3.1.2), the atmospheric structure and radiative transfer can then be computed locally by approximating each atmospheric patch with a plane parallel slab, infinitely extended in the transverse direction and emitting a total flux σT^4. In this Thesis, I used the emergent radiation evaluated by Suleimanov et al. [387, 388] from partially ionized hydrogen atmospheres, with polarization-dependent opacities according to Potekhin & Chabrier [328], Potekhin et al. [333]. The partial mode conversion due to vacuum polarization, as described by van Adelsberg & Lai [419], was taken into account. The radiation transfer equation was solved for about 200 photon energies from 0.01 to 40 keV at 40 angles to the atmosphere normal, uniformly distributed on a logarithmic scale from 1° to 89°.9 with the addition of a further point at 0°.1.

Once the emission model is specified, the spectrum at infinity is computed collecting the contributions from each patch, accounting for general relativistic effects; if (Θ,Φ) are the colatitude and azimuth in the observer fixed frame, then the emitted flux at energy $h\nu$ and at phase γ is

$$F(\nu,\gamma) = \int_0^{2\pi} d\Phi \int_0^1 I_\nu(\theta,\phi;\gamma)\, du^2, \tag{4.3}$$

where $u = \sin\bar{\Theta}$. The two angles Θ and $\bar{\Theta}$ are related through the elliptic integral of Eq. 1.5. Finally, the flux observed at infinity distance d is

$$F^\infty(\nu,\gamma) = \frac{R_\infty^2}{d^2} F(\nu(1+z),\gamma)(1+z)^{-3}, \tag{4.4}$$

where z is the gravitational redshift defined in Eq. 1.1.

For each emission model, the emerging radiation flux is stored in a eight-dimensional array $F^{\infty}(\nu, \gamma, B_{\rm p}, T_{\rm p}, \theta_{\rm B}, \alpha, \xi, \chi)$, which associates at each set of the parameters the (discrete) values of the energy- and phase-dependent intensity.

4.2 Emission from magnetic polar caps

In the case of a magnetized atmosphere model, the radiative transfer equations have to be solved for each α, θ_k and ϕ_k that vary as a function of $B_{\rm p}$ and $\theta_{\rm B}$, in order to derive the surface temperature of each patch in view at a certain rotation phase. This is, of course, very time-consuming. It may be not necessary to perform such a calculation if we are interested in the emission of the magnetic polar caps, because they are centered at $\theta_{\rm B} = 0^{\circ}$ and, if they are sufficiently small, $\theta_{\rm B}$ does not vary appreciably. Thus, α becomes equal to θ_k, implying also azimuthal symmetry (no dependence on ϕ_k, see Figure 3.1). Turolla & Nobili [415] computed that the polar caps can be considered pointlike if the semiaperture of the cap is $\lesssim 5^{\circ}$. For stellar radii of 10 km, this implies a polar cap radius $\lesssim 850$ m, that is larger than the polar cap radius evaluated in a dipolar approximation $R_{\rm PC} \approx 145\ P^{-1/2}$ m for $P \gtrsim 0.1$ s (see Eq. 2.3).

4.2.1 Numerical implementation

The ray-tracer code has been developed to evaluate the radiation emerging from the whole stellar surface. I adapted the code to the specific case of the emission from magnetic polar caps assuming that the stars does not emit X-ray radiation in the remaining part of the surface, i.e. $I_{\nu}(\gamma) = 0$ for $|\cos\theta_{\rm B}| > \cos\theta_{\rm cap}$.

Secondly, I increased the resolution of the mesh (u, Φ) in order to resolve the small polar cap. I considered an opening angle of the cap $\theta_{\rm cap} = 2^{\circ}$, that is small enough to be safely considered pointlike. To resolve it, the bin size $(du, d\Phi)$ has to be:

$$\begin{cases} \dfrac{du}{\sqrt{1-u^2}} & < 2^{\circ} = 0.035 \text{ rad} \\ \\ u\, d\Phi & < 2^{\circ} = 0.035 \text{ rad}. \end{cases} \tag{4.5}$$

At the pole, $u = 1$ and no matter how thin the grid is, the cap would never be resolved. I fixed $u = 0.9994$, corresponding to $\bar{\Theta} = 88^{\circ}$, and I obtained $du = 0.0012$ and $d\Phi = 0.035$; given that $u \in [0, 1]$ and $\Phi \in [0, 2\pi]$, these values lead to a minimum number of bins $N_u \approx 850$ and $N_{\Phi} \approx 200$. In the following, I conservatively chose $N_u = N_{\Phi} = 1000$.

For $|\cos\theta_{\rm B}| \leq \cos\theta_{\rm cap}$, $I_{\nu}(\gamma)$ was computed as described in Section 4.1, and fixed to zero elsewhere. This was done for a blackbody emission, a condensed iron surface in the free- and in the fixes-ions cases, and for a magnetized hydrogen atmosphere for reasonable values of $B_{\rm p}$ and $T_{\rm p}$, and for each ξ and χ uniformly distributed in the range $[0, \pi/2]$. This resulted in a six-dimensional array

$$F^{\infty} = F^{\infty}(\nu, \gamma, B_{\rm p}, T_{\rm p}, \xi, \chi) \tag{4.6}$$

for each emission model.

The final step of this analysis consisted of convolving the array F^{∞} of Eq. 4.6 with the instrumental response matrix, in order to perform spectral and timing analysis of the observed data. In fact, a further integration of the obtained array over γ provides the phase-averaged

spectrum if γ is integrated in $[0, 2\pi]$, or it provides phase-resolved spectra if γ is integrated in $[\gamma, \gamma + \Delta\gamma]$. All the obtained phase-resolved spectra were then written in the FITS table format for use in the XSPEC software package. Likewise, the convolution of F^∞ can be integrated over ν to obtain the pulse profiles in a certain energy range.

4.2.2 Pulse profiles of magnetized atmosphere models

The morphology of the pulse profiles expected for two antipodal point-like hot spots has been studied by Beloborodov [33]. Let's introduce μ as the scalar product of the surface normal and the vector pointing toward the observer: this variable accounts for the visible part of the emitting region for each phase of the stellar rotation (this is the impact parameter defined in Eq. 2.1):

$$\mu(\gamma) = \cos\xi\cos\chi + \sin\xi\sin\chi\cos\gamma. \tag{4.7}$$

When the star rotates, μ varies periodically between $\mu_{\min} = \cos(\xi + \chi)$ and $\mu_{\max} = \cos(\xi - \chi)$. The emitting region is seen whenever $\mu(\phi) > -\kappa$, where

$$\kappa = \frac{R_S}{R - R_S} = \frac{x}{1 - x} \tag{4.8}$$

depends only on the star compactness. If there are two antipodal emitting spots, the primary has $\mu_P = \mu$, while the secondary has $\mu_S = -\mu$.

Owing to the gravitational light bending, more than half of the stellar surface is visible at once and, for some rotational phases, both spots can contribute to the observed flux [309, e.g.]. Beloborodov [33] focused on the emission from an isothermal blackbody and, depending on the values of ξ and χ, four classes of X-ray pulse profiles can be obtained: in class I, both angles are small and only one polar cap is always visible, producing a single sinusoidal pulse with a small pulsed fraction. As ξ and χ grow, the second cap emerges and the pulse profile shows a plateau when the visible contributions of the two antipodal hot spots add in such a way to give a constant sum. In this case either one (class II) or two (class III) peaks are present in the pulse profile. Finally, in class IV the emission from both caps is always visible and no (or very small) pulsations are expected. The boundaries between the four classes in the $\xi - \chi$ parameters space depend solely on κ; for the usual assumed redshift, $\arccos\kappa \approx 60^\circ$.

Let's define the pulsed fraction (PF) as

$$\mathrm{PF} = \frac{F^\infty_{\max} - F^\infty_{\min}}{F^\infty_{\max} + F^\infty_{\min}}; \tag{4.9}$$

in the approximation of Beloborodov [33], $F^\infty \propto \mu(1 - x) + x$, and

$$\mathrm{PF} = \begin{cases} \dfrac{\mu_{\max} - \mu_{\min}}{\mu_{\max} + \mu_{\min} + 2\kappa} & \text{class I,} \\ \dfrac{\mu_{\max} - \kappa}{\mu_{\max} + 3\kappa} & \text{class II, III,} \\ 0 & \text{class IV.} \end{cases} \tag{4.10}$$

The PF of the four classes on the $\xi - \chi$ plane is shown in Figure 4.1, left panel. The boundaries between the classes, shown with red lines, have been evaluated for $M = 1.5\ M_\odot$ and $R = 12$

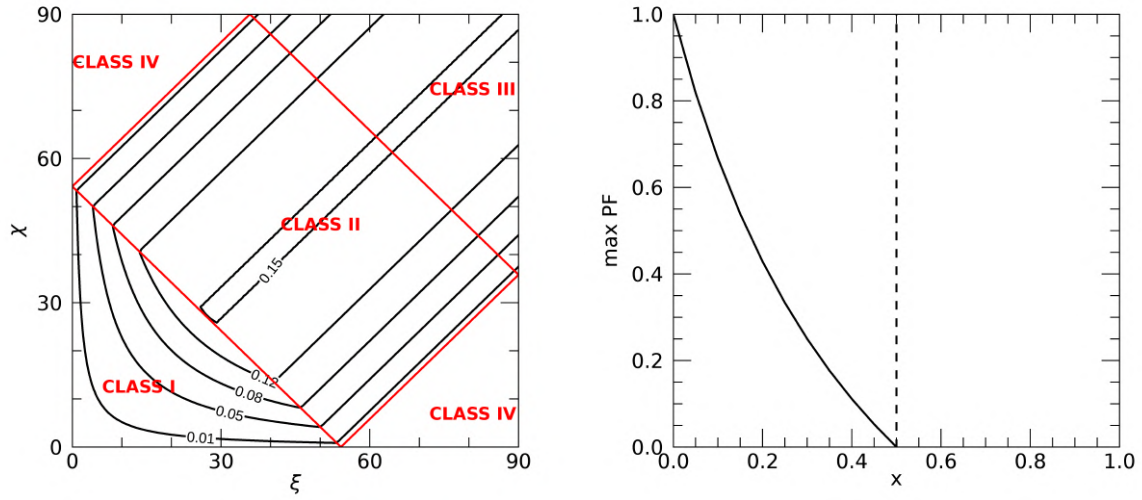

Figure 4.1: Left panel: PF of two antipodal hot spots that emit blackbody radiation according to the model of Beloborodov [33], see Eq. 4.10. The boundaries between the four classes in the $\xi - \chi$ parameters space are also shown with red lines, see Eq. 4.8. Both PF and κ have been computed for $R_S/R = 0.37$. Right panel: Maximum PF according to the model of Beloborodov [33] as a function of $x = R_S/R$, see Eq. 4.11. The model fails for $0.5 < x < 1$, where the elliptic integral has to be solved numerically.

km ($x = 0.37$). Despite the class, the PF reaches its maximum when $\mu_{\min} < \kappa$ and $\mu_{\max} = 1$, and it depends only on the stellar compactness:

$$\mathrm{PF}_{\max} = \frac{R - 2R_S}{R + 2R_S} = \frac{1 - 2x}{1 + 2x}. \tag{4.11}$$

Thus, the more the star is compact, the lower the PF is. Figure 4.1, right panel, shows the maximum PF as a function of x: in the non-relativistic case, the maximum PF possible is 1, but then it rapidly decreases until it reaches 0 for $R = 2R_S$; as already pointed out in Section 1.2.2, this configuration leads to $\psi_{\max} = \pi$, that means that the whole star surface is visible at once (see Eq. 1.7 and Figure 1.4). For $R_S < R < 2R_S$, the analytic approach of Beloborodov [33] is not longer valid and the elliptic integral of Eq. 1.5 has to be solved numerically.

The argument of Beloborodov [33] used to derive the PF of Eq. 4.10 assumed isotropic emission; on the contrary, magnetized atmosphere models have an anisotropic beaming pattern with two peaks (the pencil-beaming and the fan-beaming, see Section 3.1.2). As a result, the pulse profiles have an be extremely variegated morphology, with multiple peaks, unequal minima and possibly not sinusoidal. In fact, when both the primary and the secondary spots are visible, they can contribute with three maxima each (one of the pencil beam, two of the fan beam), and they combine each other according to the relative intensities that strongly depend on the temperature and the magnetic field (see Figure 3.4). Thus, there is no one-to-one relationship between the pulsar geometry and the number of the peaks or the PF, as in the case of the blackbody emission.

However, the wider range of possible pulse profiles can be used to explain phenomena that solely with a blackbody have no explanations, as for the two cases presented in Chapters 6 and 7 regarding PSR J0726−2612 and PSR B0943+10, respectively. In Figures 4.2 and 4.3, I show two possible examples of pulse profiles obtained in the integrated $0.5 - 2$ keV energy band from a magnetized hydrogen atmosphere with $T_p = 1$ MK and $B_p = 4 \times 10^{12}$ G, and $T_p = 0.5$ MK and

$B_{\rm p} = 4 \times 10^{13}$ G, respectively. The different panels in the figures refer to different combinations of viewing angles ξ and χ. The PF, numerically evaluated through Eq. 4.9, is also shown in red. Remarkably, for many geometrical configurations the peak of the pulse profile is not at zero phase, that corresponds to the location of the radio main pulse.

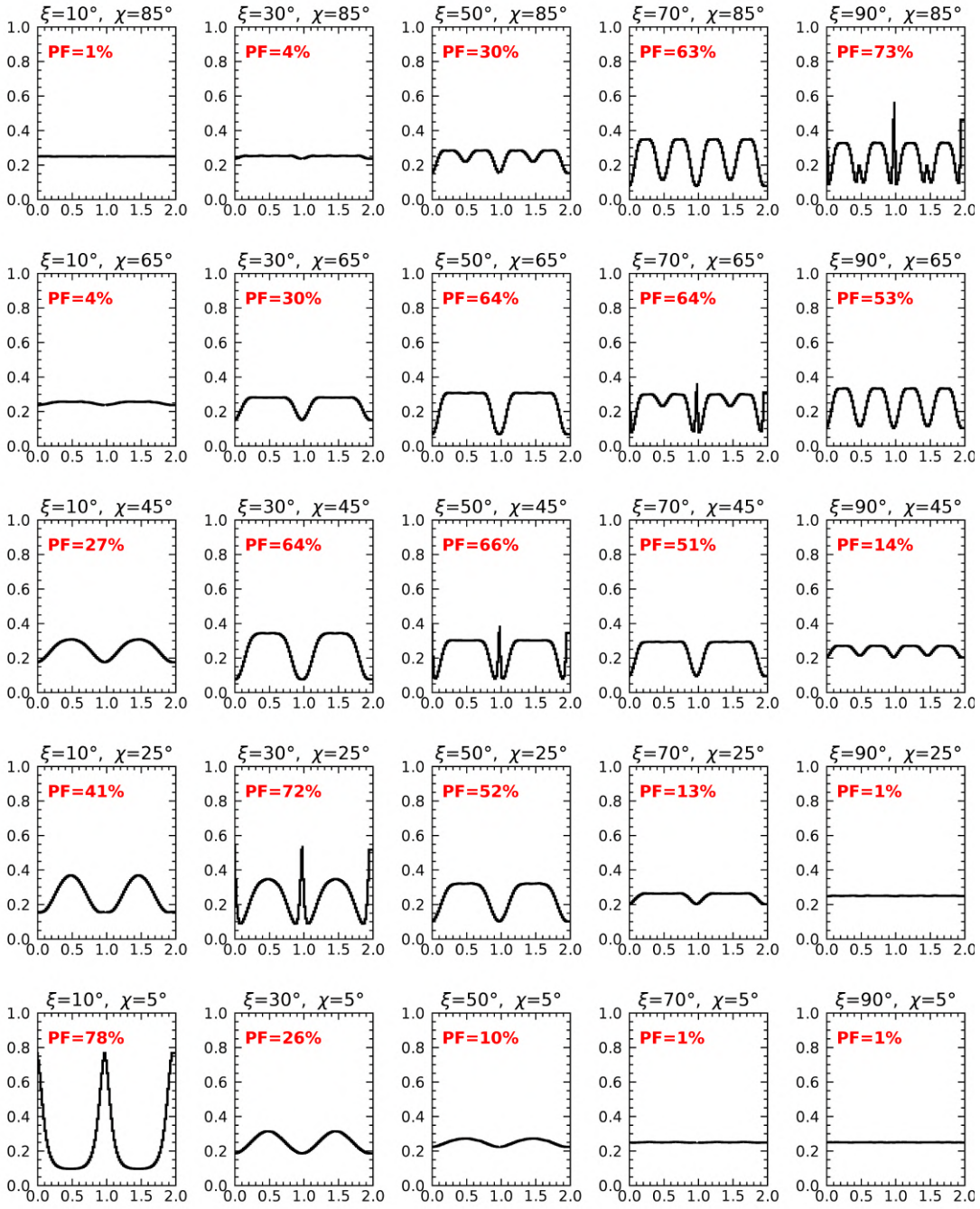

Figure 4.2: Integrated pulse profiles ($0.5 - 2$ keV) in normalized units obtained from a magnetized hydrogen atmosphere with $T_{\rm p} = 1$ MK, $B_{\rm p} = 4 \times 10^{12}$ G, $M = 1.5\, M_{\odot}$ and $R = 12$ km. The different panels refer to different combinations of viewing angles ξ and χ. The PF defined in Eq. 4.9 is also shown in red.

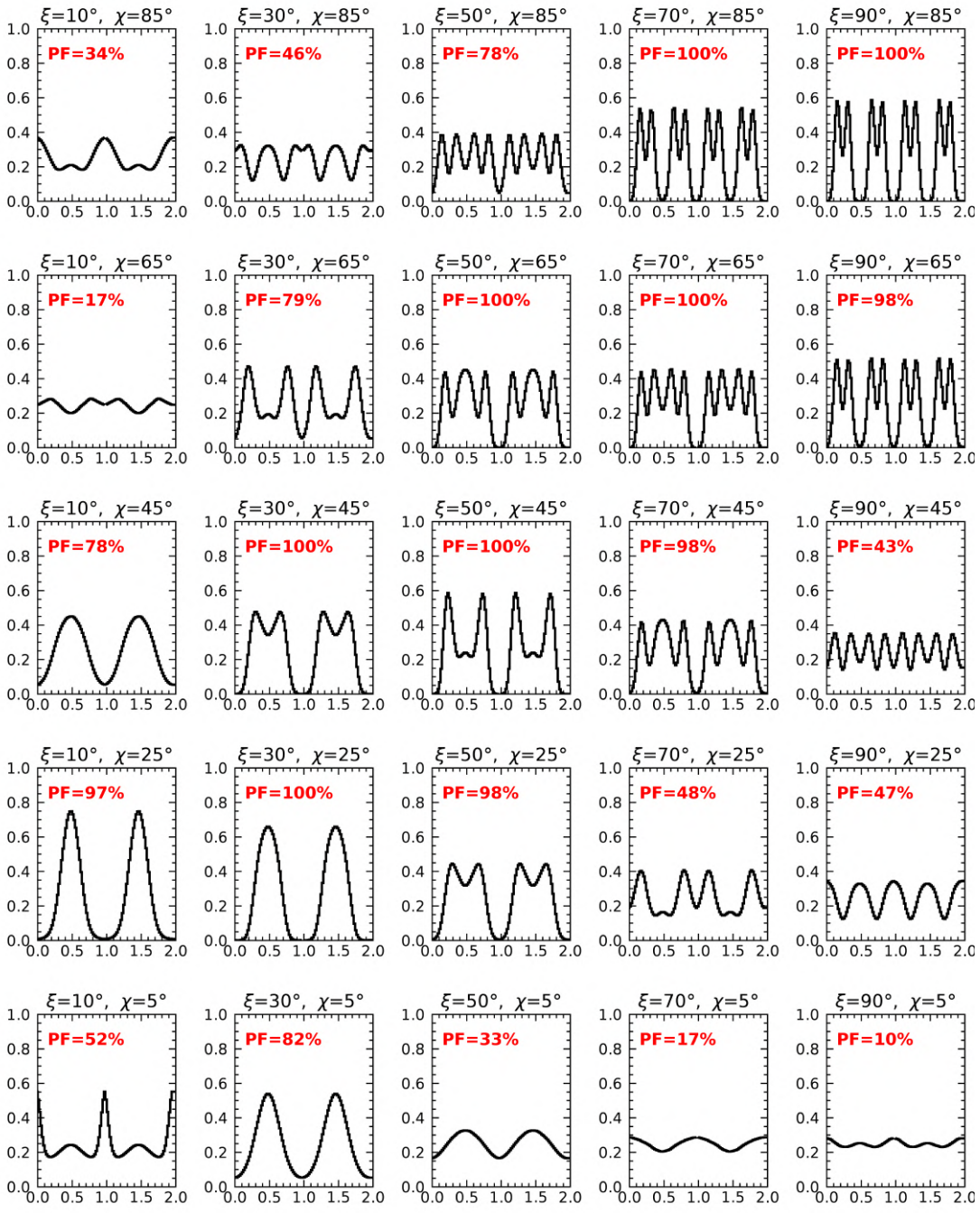

Figure 4.3: Same as Figure 4.2, but for $T_{\rm p} = 0.5$ MK and $B_{\rm p} = 4 \times 10^{13}$ G.

Chapter 5

The maximum likelihood method

The work of this Thesis was based mainly on data obtained with the *XMM-Newton* satellite of the European Space Agency, briefly presented in Section 5.1. To extract the best possible information from the data of rather faint X-ray sources, I implemented an analysis software that relies on the maximum likelihood (ML) method. Here, I briefly describe this statistical method (Section 5.2), how I implemented the software that can extract spectra and light curves (Section 5.3) and the tests that I performed to validate it (Section 5.4).

5.1 *XMM-Newton* and the EPIC instrument

The X-ray Multi Mirror Mission Newton (*XMM-Newton*, [190]) is a satellite launched in December 1999, whose original lifetime was designed to be 10 years, but thanks to the excellent performances of the instruments it is still fully operational. Immediately after launch, it had a highly elliptical, 40° orbit with a period of ~ 48 hr, an apogee of $\sim 114\,000$ km, a perigee of ~ 7000 km.

XMM-Newton carries on board three Wolter-type 1 X-ray telescopes, sensitive to the light in the energy range $0.15 - 15$ keV. Each of the X-ray telescopes has at its focus a European Photon Imaging Camera (EPIC), that uses charge-coupled devices (CCDs). The EPIC cameras offer the possibility to perform extremely sensitive imaging observations over the telescope field of view (FOV) of $30'$ with moderate spectral ($E/\Delta E \approx 20 - 50$) and angular (FWHM $= 6''$) resolution. Behind two of the three telescopes, about half of the X-ray light is utilized by the Reflection Grating Spectrometers (RGS, [84]). Each RGS consists of an array of reflection gratings which diffracts the X-rays to an array of dedicated CCD detectors. The RGS instruments achieve a resolving power $E/\Delta E \approx 150 - 800$ over a range from 0.33 to 2.5 keV. The effective area peaks around 0.83 keV at about 150 cm^2 for the two spectrometers. Finally, a 30 cm diameter Ritchey Chretien Optical/UV Monitor Telescope (OM, [253]) is mounted on the mirror support platform of *XMM-Newton* alongside the X-ray mirror modules. It provides coverage between 170 nm and 650 nm and has a FOV of $17'$. It allows multiwavelength observations of the same target both in the X-rays and optical-UV bands.

In the course of my Thesis I did not make use of data obtained by RGS and OM because the sources I analyzed had a flux below the sensitive threshold of the two instruments. Therefore, in the following I will concentrate only on EPIC.

5.1.1 EPIC technical details

The *XMM-Newton* spacecraft is carrying a set of three X-ray CCD cameras, named EPIC. Two of the cameras are EPIC-MOS [413], adopting metal oxide semi-conductors (MOS) CCDs. They are installed behind the X-ray telescopes that are equipped with the gratings of the RGS, that divert about 44% of the original incoming flux reaches the MOS cameras. The third X-ray telescope has an unobstructed beam; the EPIC instrument at the focus of this telescope uses pn CCDs and is referred to as the pn camera [384].

There are seven EEV type 22 front-illuminated CCDs in the focal plane of each MOS camera, made up of a matrix of 600×600 pixels. Each pixel is a square of 40×40 μm^2 and covers 1.1×1.1 asec^2 on the FOV. The EPIC-pn detector is a back-illuminated CCD camera, composed of twelve CCDs. Each CCD is a 400×400 pixel matrix of 6×6 cm^2, and the pixel size is 150×150 μm^2 (4.1×4.1 asec^2). Since the depth of the pn chip is of 300 μm, the pn camera is more responsive to high energy X-ray photons, with respect to the MOS, that have a chip with thickness of only 40 μm.

All EPIC CCDs operate in photon counting mode, registering for each photon its position, arrival time and energy with a frame readout frequency that depends on the science mode of data acquisition. The faster the readout time, the less pixels are read. For the MOS cameras, the readout modes are:

- "Full Frame": all pixels are read out and the whole FOV is covered, thus the number of images taken per second is rather limited. In this mode the observer receives a full 600×600 pixels image every 2.6 s;
- "Partial Window": in this mode only part of the CCD of the MOS is read out. The possible modes are the Large Window Mode (a 300×300 pixels image every 0.9 s) or the Small Window Mode (a 100×100 pixels image every 0.3 s);
- "Timing Mode": a one dimensional 100×600 pixels image is produced at high speed (1.75 ms). As the two MOS cameras are oriented at an angle of 90° from each other, the resulting imaging directions are perpendicular to each other.

For the pn camera the readout modes are:

- "Full Frame": a 376×384 pixels image every 73.5 ms;
- "Extended Full Frame": a 376×384 pixels image every 199.1 ms;
- "Partial Window": it includes the Large Window Mode and the Small Window Mode. In the Large Window Mode half of the area of the 12 CCDs is read out and a 198×384 pixels image is produced every 47.7 ms. In the Small Window Mode only a part of CCD number 4 is used, and a 63×64 pixels image is produced at a speed of 5.7 ms;
- "Timing Mode": a one-dimensional 64×200 pixels image is produced every 0.03 ms;
- "Burst Mode": this mode allows very high time resolution (7 μs).

As the EPIC detectors are not only sensitive to X-ray photons but also to IR, visible and UV light, the cameras include aluminised optical blocking filters to reduce the contamination of the X-ray signal by those photons. There are four filters in each EPIC camera. Two are thin filters made of 1600 Å of polyimide film with 400 Å of aluminium evaporated on to one side; one is the medium filter made of the same material but with 800 Å of aluminium deposited

on it; and one is the thick filter. This is made of 3300 Å thick Polypropylene with 1100 Å of aluminium and 450 Å of tin evaporated on the film. The filters are self-supporting and 76 mm in diameter. The remaining two positions on the filter wheel are occupied by the closed (1.05 mm of aluminium) and open positions, respectively. The former is used to protect the CCDs from soft protons in orbit, while the open position could in principle be used for observations where the light flux is very low, and no filter is needed.

The used filter modifies the effective area of the EPIC cameras; another factor to be taken into account is their the quantum efficiency. It is the quantum efficiency of the MOS chips that limits the energy passband at its high energy end, while the pn camera can detect photons with high efficiency up to 15 keV. The on-axis effective area of the three EPIC cameras, thin filter, as a function of the energy are represented in Figure 5.1, left panel. The effective area of the two MOS cameras combined together is also shown.

5.1.2 EPIC Point Spread Function

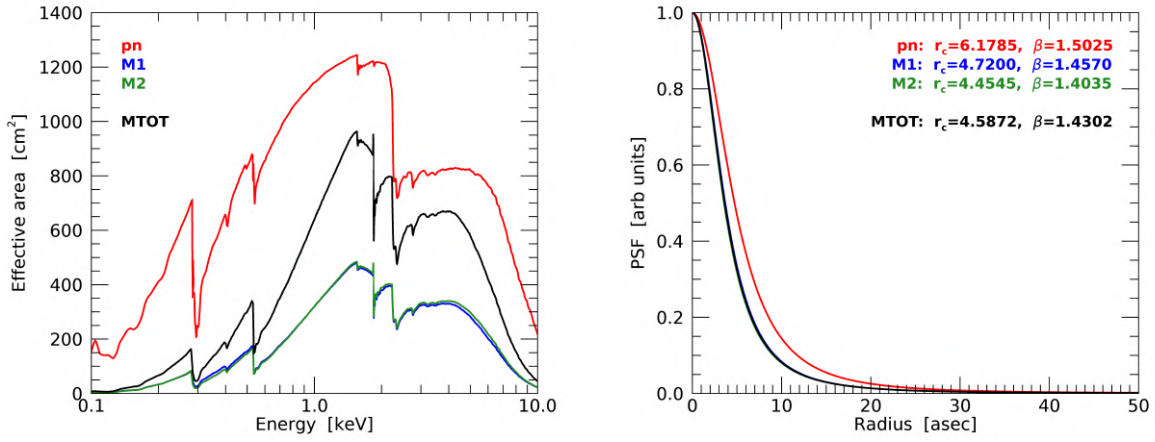

Figure 5.1: Left panel: Effective area, on-axis and thin filtered, of the three EPIC cameras: pn (red line), MOS1 (blue line) and MOS2 (green line); in addition, the effective area of the summed MOS1/MOS2 cameras (black line). Right panel: Point spread function of the three EPIC cameras with the parameters r_c and β derived from the in flight calibration [106] for $E = 1.5$ keV and $\Theta = 0'$.

The point spread function (PSF) describes the response of an imaging system to a point source: if the source is located in (x_0, y_0), $\mathrm{PSF}(x, y)$ represents the fraction of the source counts detectable at the position (x, y). The EPIC PSF profile can be analytically represented by a King function, which is function of the core radius r_c and the slope β:

$$\mathrm{PSF}(x,y) = \frac{\beta - 1}{\pi r_c^2}\left(1 + \frac{(x-x_0)^2 + (y-y_0)^2}{r_c^2}\right)^{-\beta}. \tag{5.1}$$

One of the main advantages of this function is that it is analytically integrable in $r\,dr$ and therefore the integral profile (or Encircled Energy Fraction, EEF), and correspondingly the total flux of a source, are also analytically characterized:

$$\mathrm{EEF}(r) = \int_0^r \mathrm{PSF}(r')2\pi r'\,dr' = 1 - \left(1 + \frac{r^2}{r_c^2}\right)^{1-\beta}. \tag{5.2}$$

Thanks to the choice of the normalization, $\mathrm{EEF}(\infty) = 1$. r_c and β are functions of the photon energy E, in units of keV, and of the off-axis angle Θ, in units of amin. They have been inferred for the three EPIC cameras through a systematic in flight calibration of the instrumental response by Ghizzardi [106], and they can be written as

$$r_c(E,\Theta) = a + b \times E + c \times \Theta + d \times E \times \Theta, \tag{5.3}$$

and

$$\beta(E,\Theta) = x + y \times E + z \times \Theta + w \times E \times \Theta. \tag{5.4}$$

The parameters of the fits are reported in Table 5.1, and the resulting r_c and β for different values of energies and off-axis angles are shown in Figures 5.2 and 5.3 for the pn and the MOS cameras, respectively. Finally, the on-axis PSFs of the three cameras are shown in Figure 5.1, right panel.

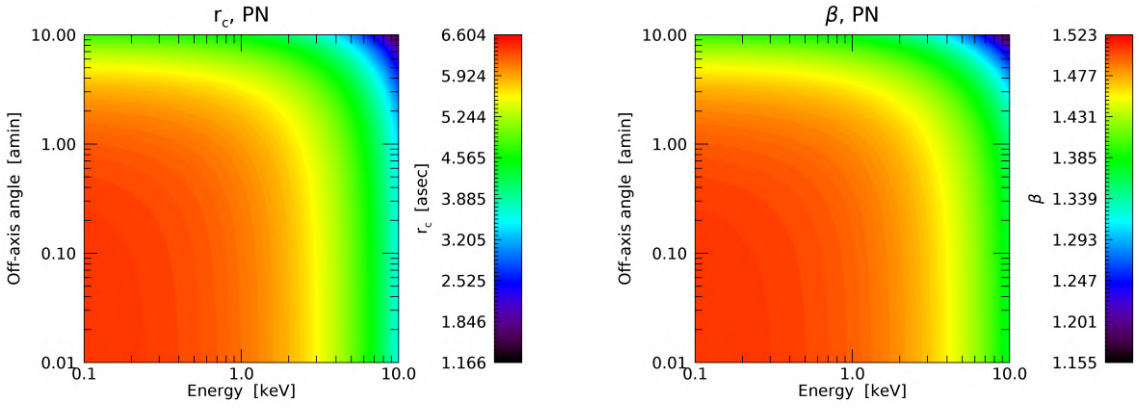

Figure 5.2: Values of r_c (left panel) and β (right panel) evaluated from the in flight calibration of the PSF for the pn camera [106] for different values of energies and off-axis angles.

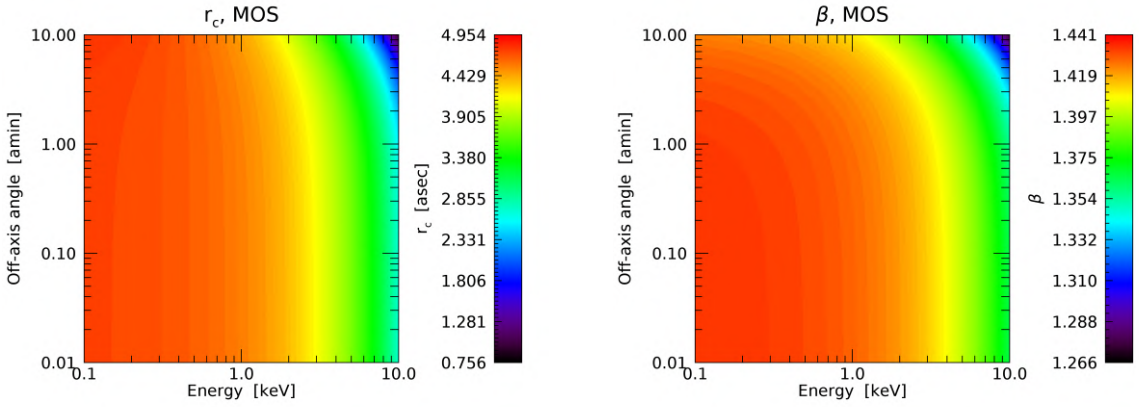

Figure 5.3: Same of Figure 5.2, but for the MOS cameras.

Table 5.1: PSF parameters of the EPIC cameras

		pn		
r_c	$a = 6.636 \pm 0.020$	$b = -0.305 \pm 0.032$	$c = -0.175 \pm 0.010$	$d = -0.0067 \pm 0.0185$
β	$x = 1.525 \pm 0.001$	$y = -0.015 \pm 0.001$	$z = -0.012 \pm 0.001$	$w = -0.0010 \pm 0.0004$
		MOS1		
r_c	$a = 5.074 \pm 0.001$	$b = -0.236 \pm 0.001$	$c = +0.002 \pm 0.001$	$d = -0.0180 \pm 0.0006$
β	$x = 1.472 \pm 0.003$	$y = -0.010 \pm 0.001$	$z = -0.001 \pm 0.002$	$w = -0.0016 \pm 0.0013$
		MOS2		
r_c	$a = 4.759 \pm 0.018$	$b = -0.203 \pm 0.010$	$c = +0.014 \pm 0.017$	$d = -0.0229 \pm 0.0133$
β	$x = 1.411 \pm 0.001$	$y = -0.005 \pm 0.001$	$z = -0.001 \pm 0.002$	$w = -0.0002 \pm 0.0011$

Notes. r_c and β best fits according to Eqs. 5.3 and 5.4 for pn, MOS1 and MOS2 cameras [106]. r_c is expressed in asec, β is dimensionless.

5.2 The maximum likelihood software

Traditionally, source detection and spectral analysis are performed are performed by estimating the number of net source counts from the comparison of two measures: the number of counts in a "source" region, that contains both a source and background contribution, and the number of counts in a "background" region, that is used to estimate the number of counts to be subtracted from the "source" region. The source counts are collected from a circular region of radius tipically in the range $R_s \approx 15 - 40''$ and centred in the source position; the counts are spread around the source poition because of the PSF, and the fraction of source counts recovered within R_s are $\mathrm{EEF}(R_s) \approx 60 - 85\%$. The choice of R_s is a trade-off between maximizing the EEF and minimizing the number of the contaminating counts of the background. Their contribution is estimated by choosing a second extraction area, typically larger and distant from the source position ($R_b \approx 60''$). The net source counts, then, are the difference between the counts extracted within R_s and the background counts expected within R_s, but measured elsewhere. Finally, the total source counts are recovered by dividing the background-subtracted counts by $\mathrm{EEF}(R_s)$, in order to correct for the fraction of counts lost because of the PSF:

$$N_{\mathrm{net}} = \frac{N_s - N_b(R_s/R_b)^2}{\mathrm{EEF}(R_s)}. \tag{5.5}$$

The statistical uncertainty on N_{net} is

$$\sigma_{\mathrm{net}} = \frac{\sqrt{N_s + N_b(R_s/R_b)^4}}{\mathrm{EEF}(R_s)}, \tag{5.6}$$

that is larger than the only Poissonian error $\sqrt{N_{\mathrm{net}}}$.

When a source is dim, the estimation of the source net counts strongly depends on the arbitrary choices of the extraction area, and σ_{net} could be significantly larger than $\sqrt{N_{\mathrm{net}}}$, as

Figure 5.4 shows. For these cases, the solution is to adopt and alternative approach, that relies on the maximum likelihood (ML) estimation method: it exploits all the events of the FOV to estimate the source counts and therefore it does not suffer of bias and it maximizes the statistics. In the first part of my PhD project, I developed a software that uses the ML to extract count rates and spectra of dim X-ray sources.

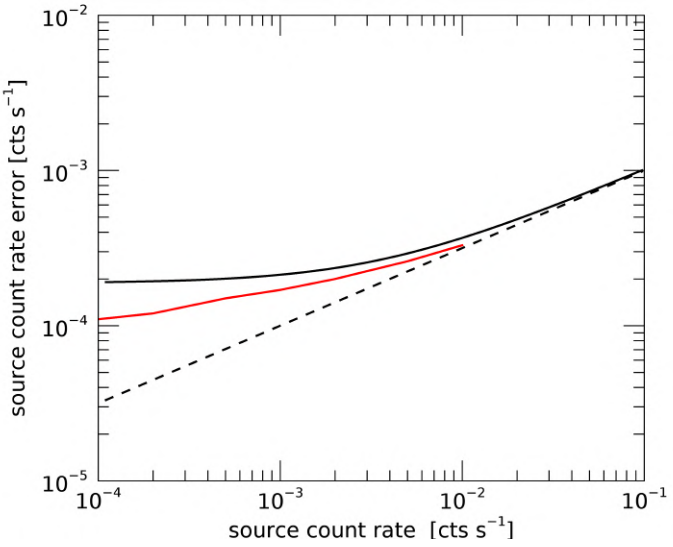

Figure 5.4: Source count rate typical error as a function of the source count rate, inferred from Eq. 5.6 with $N_b/\pi R_b^2 = 0.1$ cts asec^{-2} and $R_s = 30''$ (black solid line). The red line shows the error inferred with the ML analysis, while the black dashed line shows the Poissonian error $\sqrt{N_{net}}$.

.

5.2.1 The method

The ML is a method of Bayesian analysis. Briefly, it consists of estimating the most probable parameters that reproduce the observed data, assuming a model. In the case of source detection, the source events are assumed to be spatially distributed according to the instrumental PSF, while the background events are not. This method has the advantage to exploit all the events that are located in the region of interest, and not only those within R_s from the source position, and to measure the background locally, and not in some distant region.

The method relies on the Poissonian nature of the counting process. The selected events are sorted according to their spatial coordinates (x, y) to produce a skymap of counts into a 2D grid, and then the Poissonian probability to measure in the pixel (i, j) N_{ij} counts, when the expected value is μ_{ij}. The likelihood function L is the product of all of these probabilities (or, better, is the sum of their logarithms):

$$\begin{aligned} L &= \ln \prod_{ij} \left(\frac{e^{-\mu_{ij}} \mu_{ij}^{N_{ij}}}{N_{ij}!} \right) \\ &= \sum_{ij} \left(-\mu_{ij} + N_{ij} \ln \mu_{ij} - \ln N_{ij}! \right). \end{aligned} \tag{5.7}$$

In the case of a point source that is scattered in the detector because of the PSF, the expectation value is

$$\mu_{ij} = b \times f_{ij} + s \times \mathrm{PSF}_{ij}, \tag{5.8}$$

where b are the background counts per unit area (cts asec^{-2}), s are the source counts, and PSF_{ij} is the PSF defined with Eq. 5.1 in the pixel (i, j) of the detector, that provides four more parameters: x_0, y_0, r_c, and β. In principle, also the background could be distributed according to a certain function f_{ij} dependent from the position on the detector; if there are not evidences for variable background, then $f_{ij} = 1$.

5.2.2 Significance and standard errors

Let's define θ as an n-dimensional vector that contains the parameters, and $\hat{\theta}$ as the vector of the parameters that maximizes the likelihood function. In our case, $\theta = (b, s, x_0, y_0, r_c, \beta)$ and $\hat{\theta}$ is the best estimator of these parameters.

The quantity that accounts for the reliability of $\hat{\theta}$ is called maximum likelihood ratio (MLR), and it is defined as the difference between the likelihood function evaluated for $\hat{\theta}_1 = (b, s, x_0, y_0, r_c, \beta)$ and the one evaluated for $\hat{\theta}_0 = (f, 0, 0, 0, 0, 0)$, i.e. a flat spatial distribution of the counts. In few words, the MLR compares the likelihood of having a point source with respect to having only background.

The significance of the detection, σ, is the square root of the MLR:

$$\sigma = \sqrt{\mathrm{MLR}} = \sqrt{L(\hat{\theta}_1) - L(\hat{\theta}_0)}. \tag{5.9}$$

The second derivative matrix of L, evaluated at $\hat{\theta}$, contains information on the uncertainties of the derived parameters. The variance of $\hat{\theta}$ is calculated by:

$$\mathrm{var}(\hat{\theta}) = [-H(\hat{\theta})]^{-1}, \tag{5.10}$$

where the Hessian $H(\theta)$ is the matrix of second derivatives of the likelihood with respect to the parameters evaluated at the maximum value $\hat{\theta}$:

$$H(\hat{\theta}) = \left.\frac{\partial^2 L(\theta)}{\partial\theta\partial\theta'}\right|_{\theta=\hat{\theta}}. \tag{5.11}$$

The standard errors of the parameters are just the square roots of the diagonal terms in the variance-covariance matrix $\mathrm{var}(\theta)$.

5.3 The maximum likelihood analysis

I implemented in my code the IDL routine AMOEBA[1], which performs multi-dimensional maximization of a function using the downhill simplex method. It accepts as inputs θ_0, that specifies the initial starting point of each parameter, and a vector containing the length scale of the variation for each parameter. It returns $\hat{\theta}$ and $L(\hat{\theta})$. In my code, I allow the user to choose which parameter is free or fixed in the calculus.

[1] http://www.harrisgeospatial.com/docs/AMOEBA.html.

5.3.1 Source detection

The first part of the ML analysis consists in the source detection. The spatial grid is created rebinning the events into spatial pixels of 1×1 asec^2. The analysis is carried out on a small area of the detector, that is a trade off between including all the source counts and not having too many background counts or other sources. This of course depends on the field and on the source intensity, but I found acceptable results for an area of $\approx 10^4$ asec^2.

The source and background counts are evaluated by maximizing L with respect to b, s, x_0, and y_0, while r_c and β are fixed to the values obtained for an averaged energy value. As starting values, b and s are estimated with the traditional photon counting technique.

This method can be generalized for n point sources in the field. This is particularly useful when the sources are almost overlapped (i.e., their distance is a few times the angular resolution of EPIC). In this case, the expectation value is

$$\mu_{ij} = b \times f_{ij} + s_1 \times \mathrm{PSF}_{i_1 j_1} + s_2 \times \mathrm{PSF}_{i_2 j_2} + \cdots + s_n \times \mathrm{PSF}_{i_n j_n} \tag{5.12}$$

and each source has its s, x_0 and y_0.

5.3.2 Timing and spectral analysis

With the same procedure discussed above, it is straightforward to derive a light curve or a pulse profile: the data set is divided into temporal bins and the ML source detection is performed for each bin. s is a free parameter while b, x_0 and y_0 are fixed to a common value for all the temporal bins, because we do not expect them to vary.

The spectrum is build up with the ML analysis with a position fixed to that found in the source detection analysis, and the PSF parameters suitable for each energy bin. As for the light curve, the source detection is performed for each energy bin, and then the resulting counts are transformed into FITS table format for use in the XSPEC software package. The spectral analysis is carried out with no background file and with the ancillary response of extended sources, because the ML method itself accounts for background subtraction and PSF corrections.

The energy bins are chosen in such a way to have a significant detection, that means at least 20 counts per bin and a significance (see Eq. 5.9) greater than 5 for relatively bright sources (i.e. a count rate $\approx 10^{-2}$ cts s^{-1}), or than 2.5 for dimmer sources. I also ask for a well-determined background, i.e. I required a ratio between the background value and its error greater than the above defined significance thresholds. In the highest energy bin, if these criteria are not satisfied, I adopted the upper energy boundary yielding the largest source significance, or the best upper limit. Figure 5.5 represents a comparison between a spectrum obtained with the traditional method (left panel) and with the ML method (right panel).

5.3.3 Phase-resolved analysis

The above method can be generalized to take into account the pulse phase information of the events for periodic sources. If the events are binned in spatial and phase coordinates, a tridimensional space is defined and the bins are labeled with indices (i, j, k). Therefore, in this 3D-ML approach, the expectation value of the bin (i, j, k) is

$$\mu_{ijk} = b \times f_{ij} + s_{\mathrm{u}} \times \mathrm{PSF}_{ij} + s_{\mathrm{p}} \times \mathrm{PSF}_{ij} \times \Phi_k. \tag{5.13}$$

Now s_{u} and s_{p} represent the source counts for the unpulsed and pulsed components, respectively, while Φ_k is the normalized pulse profile at phase bin k. The pulse profile can be either a

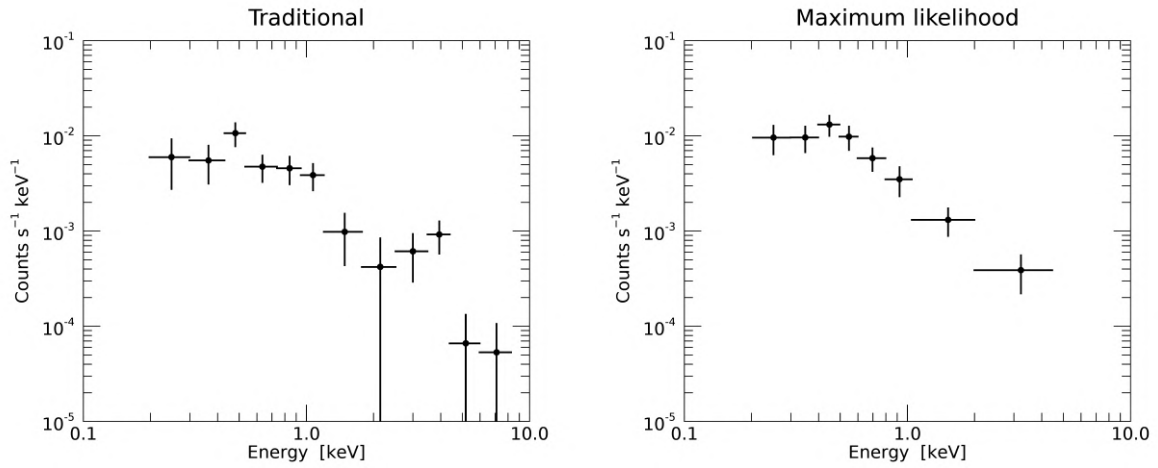

Figure 5.5: Comparison between a spectrum obtained with the traditional method and corrected for the PSF (left panel) and with the ML method (right panel).

sinusoid

$$\Phi_k = 1 + \sin(2\pi(x_k - x_0)), \tag{5.14}$$

or a Gaussian function

$$\Phi_k = \frac{1}{\sqrt{2\pi\sigma_0^2}} \, \mathrm{e}^{-\frac{(x_k - x_0)^2}{2\sigma_0^2}}, \tag{5.15}$$

where x_k is the normalized phase, x_0 is the absolute phase and σ_0 is the characteristic Gaussian width. The significance of the pulsation detection is now obtained as a comparison between the likelihood of having a pulsating source with respect the likelihood of having a source with constant emission:

$$\sigma_{3\mathrm{D}} = \sqrt{L(\hat{\theta}_{\Phi=\Phi_k}) - L(\hat{\theta}_{\Phi=\mathrm{const}})}. \tag{5.16}$$

If the 3D-ML analysis is applied in different energy bins, spectra for the unpulsed and the pulsed components are derived. In this context, the pulsed fraction is defined as the ratio between the pulsed and the total counts, as a function of the energy:

$$\mathrm{PF}(E) = \frac{s_\mathrm{p}(E)}{s_\mathrm{u}(E) + s_\mathrm{p}(E)}. \tag{5.17}$$

5.4 Simulations and tests

5.4.1 Numerical implementation

I generated a synthetic dataset through Monte Carlo simulations. Each dataset is made up by N events, and each event is characterized by a position (x, y), an energy PI and an arrival time t. I first defined the extraction region, a box of area 100×100 asec^2. Of the total N events, N_b are background events with positions uniformly distributed within the region, and N_s are source events with positions distributed according to the instrumental PSF (see Eq. 5.1); both N_b and N_s are Poissonian distributed. I fixed (x_0, y_0) at the center of the region of interest for simplicity, while r_c and β are chosen according to Eqs. 5.3 and 5.4 for the pn and the MOS cameras.

The energy PI of the N events can be fixed to a certain value, uniformly distributed within a certain energy range, or distributed according to a realistic spectral model. The time t is likewise generated with a uniform distribution within $t_{\max} - t_{\min} =$ expo, or in order to reproduce a periodic signal. Each simulation is made up of 1000 runs.

In the following, I assumed $b = 10^{-1}$ cts asec^{-2}, that is a reasonable value given that the typical EPIC background in $0.2 - 10$ keV is $\sim 10^{-6} - 10^{-5}$ cts s^{-1} asec^{-2}, and I handled observations of $\sim 10^4 - 10^5$ s. Nevertheless, the results were tested also for different values. For what concerns the PSF, I used the pn PSF with $E = 1.5$ keV and $\Theta = 0'$, unless differently specified.

5.4.2 Source and background counts

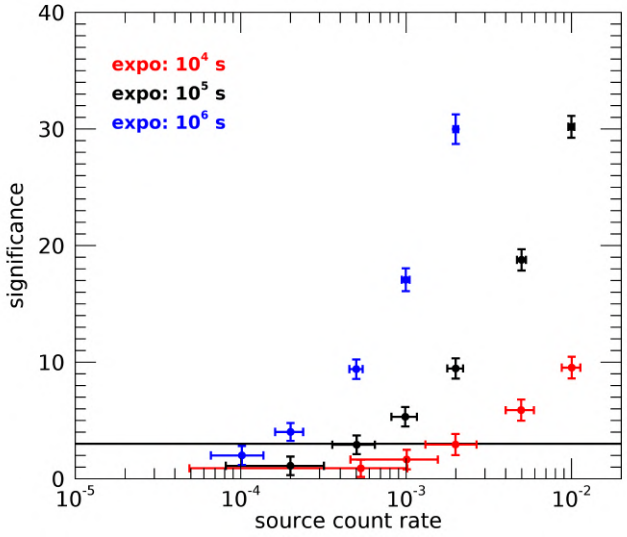

Figure 5.6: Significance of the detection, as defined in Eq. 5.9, as a function of the simulated source count rate, for three different exposure times (10^4, 10^5 and 10^6 s). The threshold $\sigma = 3$ is also shown with a black line.

I simulated sources of count rate from 10^{-4} to 10^{-2} cts s^{-1}, and a typical EPIC background of 10^{-6} cts s^{-1} asec^{-2}. I applied the ML analysis on the simulated data letting free the parameters b and s, while the others was kept fixed. Figure 5.6 shows the significance σ (see Eq. 5.9) of the detections as a function of the source count rate, for three different exposure times (10^4, 10^5, and 10^6 s). I fixed the significance threshold at $\sigma = 3$, and the ML analysis could detect sources with a count rate of 2×10^{-3} cts s^{-1} even for a short exposure time of 10^4 s. If the exposure time is increased, the ML can detect sources of $\geq 5 \times 10^{-4}$ cts s^{-1} and of $\geq (1-2) \times 10^{-4}$ cts s^{-1} for exposures of 10^5 and 10^6 s, respectively.

Figure 5.7 shows instead the distribution of the b and s parameters (left and right panel, respectively) for a good detection, i.e. a source with a count rate of 10^{-2} cts s^{-1} in 10^5 s of exposure. The distribution of b has mean 0.1001 cts asec^{-2} and standard deviation 0.0038 cts asec^{-2}. The latter is in perfect agreement with the mean error $\sigma_b = 0.00379(7)$ cts asec^{-2}, derived with the ML analysis as explained in Section 5.2.2. Likewise, the distribution of s has mean 1000 cts and standard deviation 41 cts, while $\sigma_s = 40.9(7)$ cts. I found similar results for all of the significant detections of Figure 5.6. The errors are in general smaller of those found with a traditional analysis, see Figure 5.4.

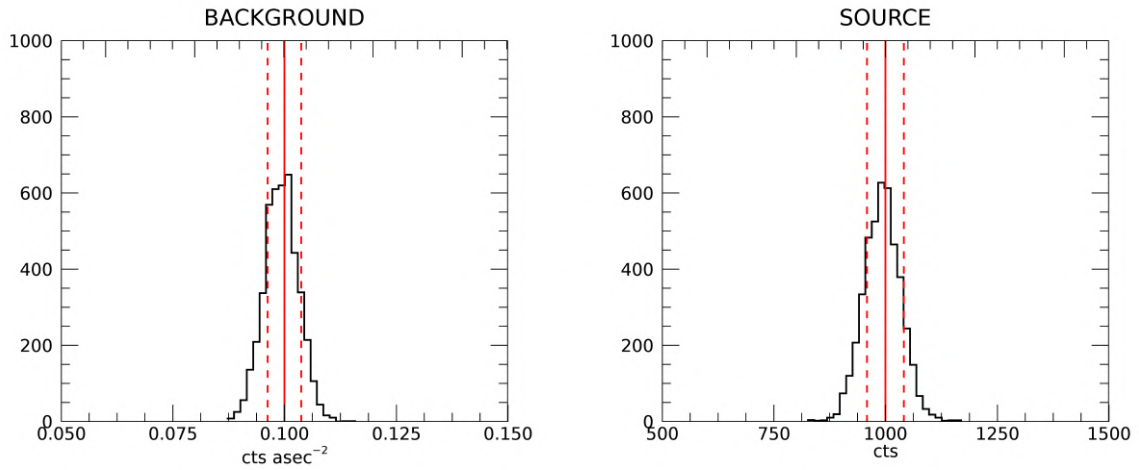

Figure 5.7: Distribution of the b and s parameters of 5000 runs with exposure 10^5 s.

5.4.3 Source position

I performed the same simulations described in the previous section, with sources of count rate in the range $5 \times 10^{-4} - 10^{-2}$ cts s^{-1}, but in addition to b and s, also x_0 and y_0 are free parameters; the results are summarized in Figure 5.8. With 10^4 s of exposure, the ML recovers the correct position of the source with an error below 1″ only if the source has a count rate of $\geq 10^{-2}$ cts s^{-1}. On the contrary, with 10^5 s of exposure, the position is well determined if the source count rate is $\geq 2 \times 10^{-3}$ cts s^{-1}; for deeper exposures, even dim sources of some 10^{-4} cts s^{-1} are well localized.

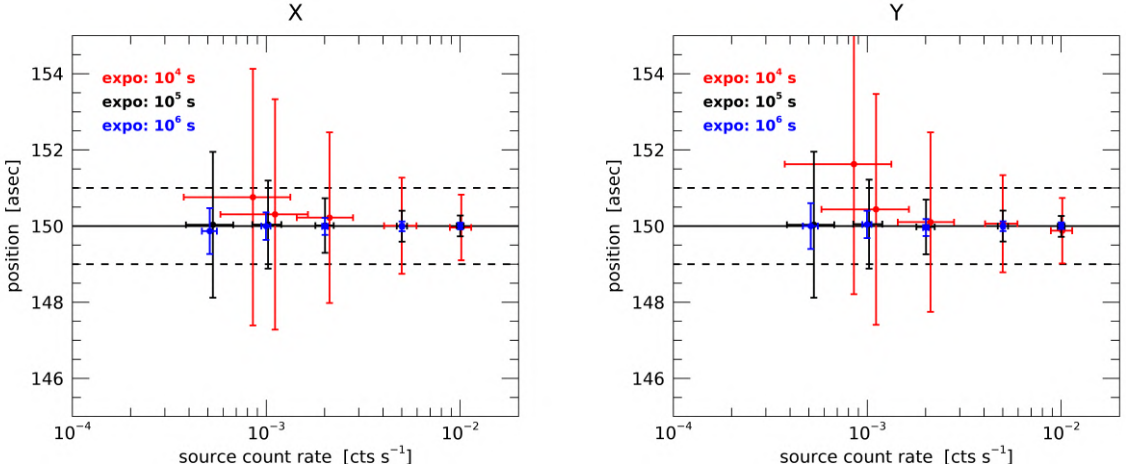

Figure 5.8: Estimation of the source position (x, y) and corresponding errors, for sources of count rate in the range $5 \times 10^{-4} - 10^{-2}$ cts s^{-1} and for exposure times in the range $10^4 - 10^6$ s.

The ML technique is particularly effective when there are two or more sources whose distance is a few times the angular resolution of EPIC. I considered two sources of equal intensity, separated by $10 - 30''$, and I used 10^5 s of exposure time. First, I applied the ML as if only one source was present and I measured the corresponding likelihood $L(\hat{\theta}_{\rm one})$; then I applied the ML on the same dataset using the formula of Eq. 5.12 for two sources, and I measured the

corresponding $L(\hat{\theta}_{\rm two})$. In Figure 5.9, I show the significance of the two-source detection, that is $\sqrt{L(\hat{\theta}_{\rm two}) - L(\hat{\theta}_{\rm one})}$, as a function of the separation of the sources. The performances of the ML analysis depend on the sources count rate: bright sources (count rate $\geq 2 \times 10^{-3}$ cts s^{-1}) can be resolved by the ML even if they are separated by 10″, while dimmer sources (count rate 5×10^{-4} cts s^{-1}) can be resolved only if their angular separation is $\gtrsim$20″.

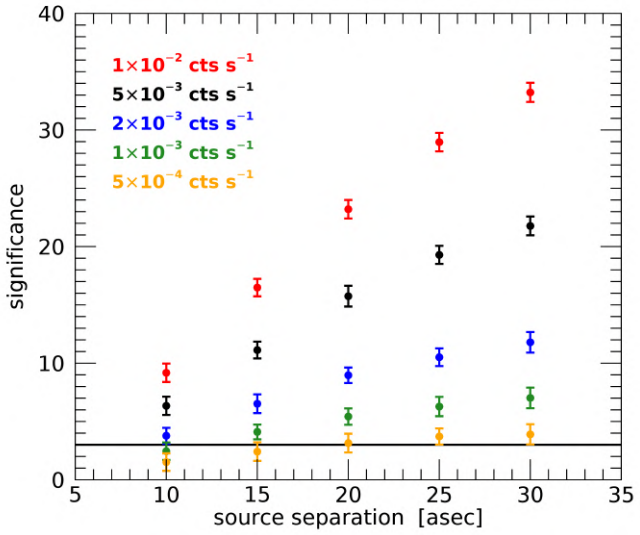

Figure 5.9: Significance of the detection of two sources as a function of their angular separation. The sources, that have equal intensity, are simulated with a count rate in the range $5 \times 10^{-4} - 10^{-2}$ cts s^{-1} with 10^5 s of exposure time. The threshold $\sigma = 3$ is also shown with a black line.

5.4.4 PSF parameters

Finally, I tested the response of the ML software in the recovery of the PSF parameters r_c and β for different count rates and exposure times: the results are shown in Figure 5.10. The parameters are estimated with an error lower than 10% only for sources with a count rate $\geq 2 \times 10^{-2}$ cts s^{-1} if the exposure time is of 10^5 s. This is the required sensitivity in order to discern from different r_c and β in the $0.2 - 2$ keV energy range of on-axis sources (see Figures 5.2 and 5.3).

As a consequence, given that the PSF parameters of the MOS1 and MOS2 cameras are consistent within 2% for any energy and off-axis angle, the data from the two MOS cameras can be analyzed together, in a summed file event, because the committed errors are well within the statistical uncertainties. On the contrary, the summed data of all of the EPIC cameras can be analyzed as an unique file event only if the total count rate is of some 10^{-3} cts s^{-1}, because r_c and β of the pn and MOS cameras differ of about $10 - 20$%.

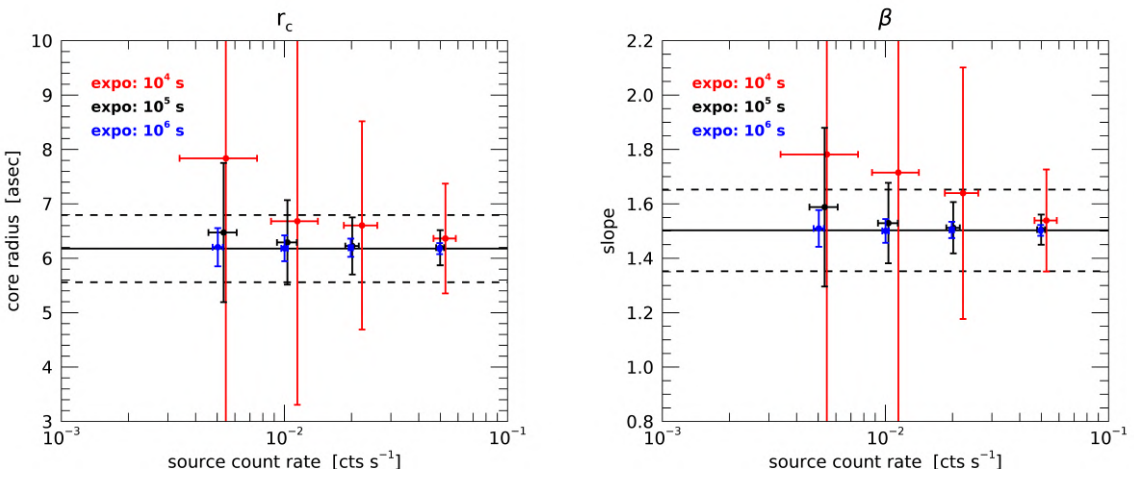

Figure 5.10: Estimation of the PSF parameters r_c and β and corresponding errors, for sources of count rate in the range $5 \times 10^{-3} - 10^{-1}$ cts s^{-1} and for exposure times in the range $10^4 - 10^6$ s.

Chapter 6

PSR J0726−2612

PSR J0726−2612 is a 200 kyr old radio pulsar that shows strong similarities with the NS class of the XDINSs (see Sections 1.5.2 and 1.5.4). Here, I report the results of *XMM-Newton* observations of PSR J0726−2612, as presented in Rigoselli et al. [358], and discuss similarities and differences between this pulsar and the XDINSs.

6.1 Introduction

PSR J0726−2612 has spin period $P = 3.44$ s and $\dot{P} = 2.93 \times 10^{-13}$ s s^{-1}, implying a characteristic age $\tau_c = 2 \times 10^5$ yr and a dipolar magnetic field at the poles $B_{\rm d} = 6 \times 10^{13}$ G.

The distance of PSR J0726−2612 is unknown. Its dispersion measure DM $= 69.4 \pm 0.4$ pc cm^{-3} [54] implies a distance $d = 2.9$ kpc, assuming the Galactic electrons distribution of Yao et al. [439]. However, there are a few facts suggesting that this is probably an overestimate. For example, such a large value for d would give a distance of 230 pc from the Galactic plane, implying that if PSR J0726−2612 was born close to the plane and its true age were similar to τ_c, its velocity would be of the order of a thousand kilometers per second. This value is not impossible, but it would be at the far end of the pulsar velocity distribution [179].

More importantly, for such a large d, one would expect an X-ray absorption corresponding to a sizeable fraction of the total Galactic H I column density, which in this direction is $\sim 5 \times 10^{21}$ cm^{-2} [194], while the observed value is a factor ten smaller. Finally, the line of sight toward PSR J0726−2612 crosses the Gould belt, which is not included in the electron distribution model of Yao et al. [439]. This could explain the large distance inferred from the DM. This local structure ($d \sim 200 - 400$ pc) comprises several OB associations that have been proposed as the birthplace of the XDINSs [321, 322]. Speagle et al. [376] suggested that PSR J0726−2612 could also be associated with the Gould belt and hence be closer than ~ 1 kpc.

In the following, I scale all the distance-dependent quantities to $d_{\rm kpc} = 1$ kpc and adopt representative values of mass and radius of 1.2 $M_\odot$ and 12 km, respectively.

6.2 Observations and data reduction

PSR J0726−2612 was observed with the EPIC instrument with a single pointing lasting 108 ks on 2013 April 8. The pn and the MOS cameras were operated in full frame mode with the thin optical filter. While the pn time resolution (73.4 ms) is adequate to reveal the pulsations of the source, this is impossible for the MOS given its resolution time of 2.6 s (see Section 5.1.1).

The data reduction was performed using the EPPROC and EMPROC pipelines of version 15 of the Science Analysis System (SAS)[1] I selected single- and multiple-pixel events (PATTERN ≤ 4 and PATTERN ≤ 12) for both the pn and MOS. I then removed time intervals of high background using the SAS program ESPFILT with standard parameters. The source was detected by EPIC at coordinates R.A. = $07^h\ 26^m\ 08^s.1$, Dec. = $-26^\circ\ 12'\ 38''$, fully consistent with the radio position of R.A. = $07^h\ 26^m\ 08^s.12$, Dec. = $-26^\circ\ 12'\ 38''1$. The source events were selected from a circle of radius $40''$ centered at the radio position, while the background was extracted from a nearby circular region of radius $60''$, and the counts were handled with a traditional analysis method due to the relatively high count rate of the source[2] (see Section 5.4); the resulting net exposure times and source events are listed in the first part of Table 6.1.

Table 6.1: Exposure times and source counts for PSR J0726−2612 in the three EPIC cameras.

Data	EPIC camera	Exposure time ks	Source counts $0.15-1.5$ keV
Phase-averaged	pn	37.8	$18\,938 \pm 140$
	MOS1	64.0	$4\,499 \pm 69$
	MOS2	70.4	$5\,212 \pm 74$
Min 1	pn	9.4	$3\,823 \pm 63$
Max 1	pn	9.4	$5\,576 \pm 76$
Min 2	pn	9.4	$4\,088 \pm 65$
Max 2	pn	9.4	$5\,447 \pm 75$

6.3 Results

6.3.1 Timing analysis

PSR J0726−2612 is barely detected above 1.5 keV, therefore I limited the timing analysis to the energy band $0.15-1.5$ keV. An epoch folding search of the EPIC-pn data gave a best period of $P = 3.442396(1)$ s, which is consistent within 0.7σ with the value expected at the *XMM-Newton* observation epoch (56,390 MJD) using the ATNF ephemeris reported in [249]. The background-subtracted pulse profile in the energy band $0.15-1.5$ keV is shown in Figure 6.1, left panel. The position of the radio pulse is indicated, with its 1σ uncertainty, as a vertical red line.

The EPIC-pn pulse profile shows two peaks with the same intensity (net count rate of $\mathrm{max}_1 = 0.62 \pm 0.02$ cts s^{-1} and $\mathrm{max}_2 = 0.64 \pm 0.02$ cts s^{-1}), separated by about 0.5 cycles. The two minima of the pulse profile are instead significantly different: $\mathrm{min}_1 = 0.34 \pm 0.01$ cts s^{-1} and $\mathrm{min}_2 = 0.39 \pm 0.01$ cts s^{-1}. The pulse profile is symmetric in phase with respect to any of the two minima, but a fit with a constant plus a sine function at half of the spin period is not acceptable ($\chi^2_\nu = 2.7$ for 17 dof). The pulsed fraction[3] is $30 \pm 2\%$.

Figure 6.1, right panel, shows that the soft ($0.15-0.4$ keV) and hard ($0.4-1.5$ keV) energy ranges have slightly different pulsed fractions: $26 \pm 3\%$ and $37 \pm 3\%$, respectively. Moreover,

[1] http://www.cosmos.esa.int/web/xmm-newton/sas.
[2] Remarkably, at the corresponding count rates pile-up effects are not relevant.
[3] Defined as (max(CR)-min(CR))/(max(CR)+min(CR)), where CR is the background-subtracted count rate.

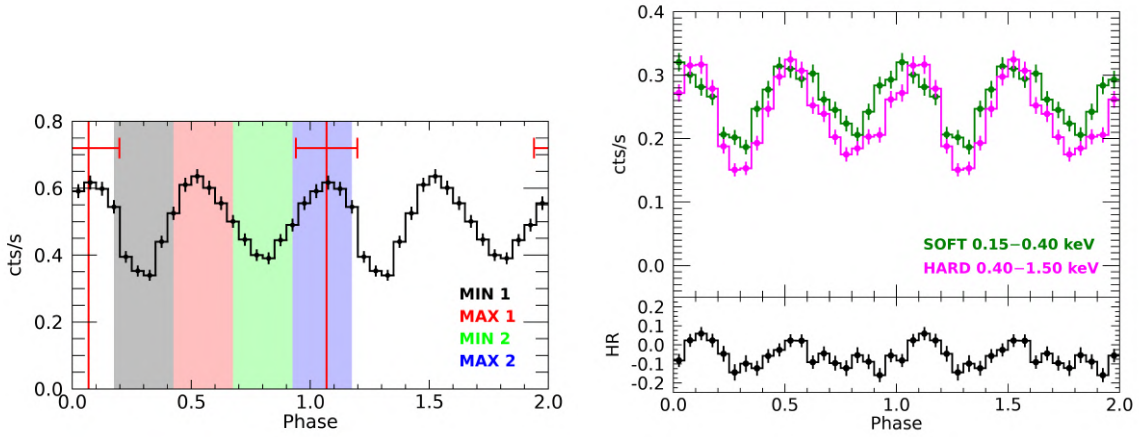

Figure 6.1: Pulse profile of PSR J0726−2612 obtained by folding the EPIC-pn data in 20 phase bins at the period derived from the radio ephemeris [249]. Left panel: Pulse profile in the energy range $0.15 - 1.5$ keV; the vertical red line represents the location of the radio pulse (derived from Speagle et al. [376]), with its uncertainty (1σ). The colored bands indicate the intervals used for the phase-resolved spectroscopy. Right panel: Pulse profile in the energy ranges $0.15 - 0.40$ keV (soft) and $0.40 - 1.50$ keV (hard) together with the corresponding hardness ratio.

the positions of the first minimum and of the second maximum are shifted of about 1 bin between the two energy ranges, but the symmetry around the minima is preserved in both bands. Fits with a constant plus sine function give $\chi^2_\nu = 1.6$ and $\chi^2_\nu = 3.5$ for the soft and hard profiles, respectively. The hardness ratio[4], shown in the lower panel of the same figure clearly indicates the presence of phase-dependent spectral variations: the source is softer during the minima and harder during the maxima.

6.3.2 Spectral analysis

The spectral analysis was performed using XSPEC (version 12.8.2). The spectra were rebinned using the GRPPHA tool with a minimum of 50 counts per bin. The spectra of the three cameras were fitted simultaneously, including a renormalization factor to account for possible cross-calibration uncertainties. Errors on the spectral parameters are at 1σ confidence level.

I used the photoelectric absorption model TBABS, with cross sections and abundances from Wilms et al. [434]. Both a single power law and a blackbody did not provide acceptable fits, giving $\chi^2_\nu \approx 6$ and $\chi^2_\nu = 1.37$ for 213 dof (null-hypothesis probability, nhp, of 3×10^{-4}), respectively. I then attempted a fit with magnetized hydrogen atmosphere models (NSA and NSMAXG in XSPEC, [304, 174, 172]). However, neither of the two sets of available models (the first with a single surface B and $T_{\rm eff}$, the second with B and $T_{\rm eff}$ varying across the surface according to the magnetic dipole model) gave an acceptable fit ($\chi^2_\nu > 2.2$ for 213 dof). In conclusion, I could not find a good fit with single-component models.

Furthermore, modeling the spectra with a blackbody plus power law or with the sum of two blackbodies was unsatisfactory. With the former I obtained a negative photon index for the power law, while with the latter, the second thermal component had a negligible flux, and

[4]Defined as (hard(CR)-soft(CR))/(hard(CR)+soft(CR)), where the soft energy range is $0.15 - 0.4$ keV, the hard one is $0.4 - 1.5$ keV.

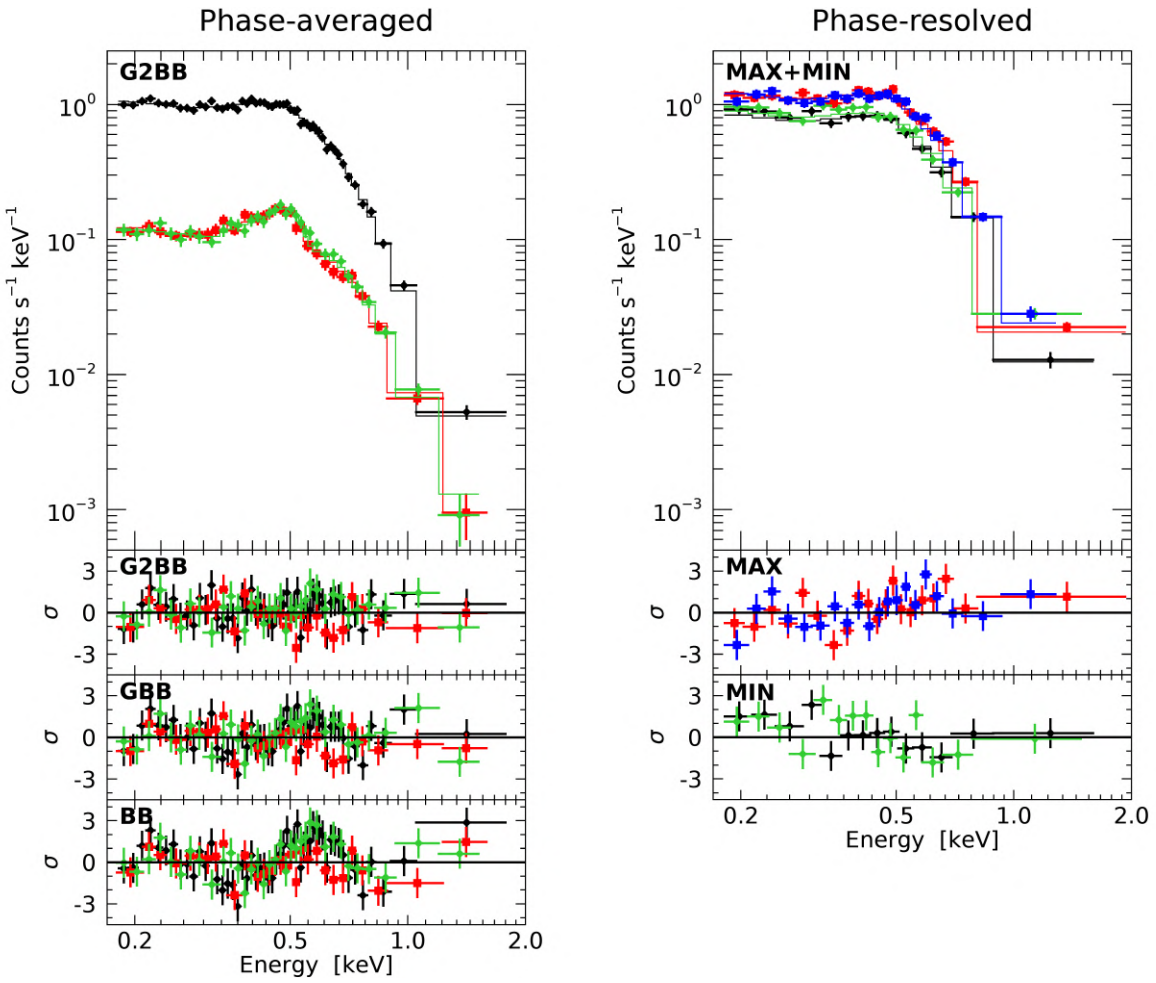

Figure 6.2: Left panel: EPIC-pn (black), -MOS1 (red) and -MOS2 (green) phase-averaged spectra of PSR J0726−2612. The top panel shows the best fit using a Gaussian absorption feature at $E = 0.39$ keV and two blackbodies (G2BB). The lower panels show the residuals of the best fit (G2BB), of a Gaussian absorption feature at $E = 1.09$ keV and one blackbody (GBB), and of a single blackbody (BB) in units of σ. Data have been rebinned for display purposes only. Right panel: EPIC-pn phase-resolved spectra fitted with the G2BB model used for the phase-averaged spectra (the color code is the same as in Figure 6.1, left panel). The overall normalization is the only free parameter. The residuals of the spectra at maxima and minima, in units of σ, are shown in the lower panels. Data have been rebinned for display purposes only.

did not improve the quality of the fit with respect to that of a single blackbody ($\chi^2_\nu = 1.32$ for 211 dof, nhp $= 10^{-3}$).

A real improvement in the fit was obtained by adding to the blackbody a broad absorption line modeled with a Gaussian (GBB) centered at $E = 1.09 \pm 0.09$ keV and width $\sigma = 0.28 \pm 0.08$ keV ($\chi^2_\nu = 1.12$ for 210 dof). Following the recent results of Yoneyama et al. [440], I explored the possibility of adopting a two-blackbody component model plus a Gaussian line in absorption (G2BB). With this model I found a good fit with the line placed at $E = 0.39^{+0.02}_{-0.03}$ keV and with a broadening of $\sigma = 0.08^{+0.03}_{-0.02}$ keV ($\chi^2_\nu = 1.00$ for 208 dof). The addition of the line yields an improvement of the χ^2 of $F = \chi^2_{\rm 2BB}/\chi^2_{\rm G2BB} = 1.32$. To assess the statistical significance of the line, I estimated through Monte Carlo simulations the probability of obtaining by chance

an equal (or better) fit improvement: I estimate a probability of $\sim 10^{-5}$ of having $F \geq 1.32$, corresponding to a $\sim 4.4\sigma$ significance of the line. The cold blackbody ($kT_1 \approx 0.074$ keV) has an emitting radius $R_1 = 10.4^{+10.8}_{-2.8}\, d_{\rm kpc}$ km, compatible with emission from the whole neutron star, while the hot blackbody has $kT_2 \approx 0.14$ keV and $R_2 = 0.5^{+0.9}_{-0.3}\, d_{\rm kpc}$ km.

A good fit was also found with the magnetized atmosphere models with a dipole distribution of the surface magnetic field ($B = 10^{13}$ G at the poles) plus a Gaussian line in absorption. With the NSA model, I found an effective temperature $T_{\rm eff} = 0.40 \pm 0.08$ MK (corresponding to an observed temperature $kT = 0.029 \pm 0.001$ keV), $d = 121^{+13}_{-12}$ pc, and $E = 0.37^{+0.02}_{-0.03}$ keV, $\sigma = 0.09^{+0.02}_{-0.01}$ keV for the Gaussian line ($\chi^2_\nu = 1.03$ for 210 dof). With the NSMAXG model, for an impact parameter (that is the angle between the line of sight and the dipole axis) $\eta = 90^\circ$, the model parameters are $T_{\rm eff} = 0.39 \pm 0.02$ MK ($kT = 0.028 \pm 0.001$ keV), $d = 63^{+26}_{-17}$ pc and $E = 0.28 \pm 0.09$ keV, $\sigma = 0.14^{+0.06}_{-0.04}$ keV for the Gaussian line ($\chi^2_\nu = 1.02$ for 210 dof). Using instead the same model with $\eta = 0^\circ$, the fit was not acceptable ($\chi^2_\nu = 2.38$ for 210 dof).

The spectral results are summarized in the first part of Table 6.2, while in Figure 6.2, left panel, the best blackbody fits are shown.

Table 6.2: Results for the phase-averaged and phase-resolved spectra of PSR J0726−2612.

Model	$N_{\rm H}$ [a]	kT_1	$R_1^{\rm b}$	kT_2	$R_2^{\rm b}$	E	σ	strength[c]	$F_{0.1-2}^{\rm unabs}$	χ^2_ν/dof	nhp
	10^{20} cm^{-2}	keV	km	keV	km	keV	keV	keV	erg s^{-1} cm^{-2}		
Phase-averaged spectra:											
BB	4.1 ± 0.2	0.0896(6)	4.90 ± 0.15	…	…	…	…	…	$1.60^{+0.06}_{-0.05}$	1.37/213	3×10^{-4}
2BB	4.3 ± 0.2	0.0888(7)	5.1 ± 0.2	> 0.33	< 0.018	…	…	…	$1.65^{+0.07}_{-0.06}$	1.32/211	1×10^{-3}
GBB	2.8 ± 0.3	0.11 ± 0.01	$2.9^{+0.5}_{-0.4}$	…	…	1.09 ± 0.09	0.28 ± 0.08	$1.0^{+1.1}_{-0.6}$	$1.37^{+0.35}_{-0.09}$	1.12/210	0.11
G2BB	$5.3^{+1.2}_{-0.8}$	$0.074^{+0.006}_{-0.011}$	$10.4^{+10.8}_{-2.8}$	$0.14^{+0.04}_{-0.02}$	$0.5^{+0.9}_{-0.3}$	$0.39^{+0.02}_{-0.03}$	$0.08^{+0.03}_{-0.02}$	$0.12^{+0.13}_{-0.05}$	$3.30^{+3.85}_{-0.85}$	1.00/208	0.47
GAT [e]	$6.9^{+0.8}_{-1.1}$	0.029(1)	14.3[d]	…	…	$0.37^{+0.02}_{-0.03}$	$0.09^{+0.02}_{-0.01}$	$0.17^{+0.07}_{-0.04}$	9.0 ± 1.1	1.03/210	0.36
GAT [f]	$5.9^{+3.4}_{-4.2}$	0.028(1)	14.3[d]	…	…	0.28 ± 0.09	$0.14^{+0.06}_{-0.04}$	$0.62^{+1.26}_{-0.33}$	$19.3^{+9.7}_{-7.0}$	1.02/210	0.40
G2BB phase-resolved:											
Maxima 1	5.3[d]	0.074[d]	10.4[d]	0.110(7)	$1.55^{+0.40}_{-0.30}$	0.39 ± 0.01	0.07 ± 0.01	$0.11^{+0.02}_{-0.01}$	3.6 ± 0.2	1.00/80	0.47
Maxima 2	5.3[d]	0.074[d]	10.4[d]	0.111(9)	$1.40^{+0.45}_{-0.35}$	0.39 ± 0.01	0.06 ± 0.01	0.10 ± 0.01	3.6 ± 0.2	0.95/78	0.61
Minima 1	5.3[d]	0.074[d]	10.4[d]	$0.17^{+0.07}_{-0.04}$	$0.20^{+0.31}_{-0.13}$	$0.40^{+0.01}_{-0.02}$	$0.14^{+0.04}_{-0.02}$	$0.23^{+0.05}_{-0.03}$	$2.90^{+0.45}_{-0.25}$	1.14/49	0.23
Minima 2	5.3[d]	0.074[d]	10.4[d]	$0.29^{+0.72}_{-0.09}$	$0.06^{+0.05}_{-0.03}$	$0.39^{+0.02}_{-0.03}$	$0.13^{+0.03}_{-0.02}$	$0.20^{+0.04}_{-0.02}$	$3.1^{+0.3}_{-0.2}$	1.28/52	0.08

Notes. Joint fits of EPIC-pn+MOS1+MOS2 phase-averaged spectra and EPIC-pn phase-resolved spectra of PSR J0726−2612. The fluxes, corrected for the absorption, are expressed in units of 10^{-12} erg s^{-1} cm^{-2}. Temperatures and radii are observed quantities at infinity. Errors at 1σ.
[a] Derived with the photoelectric absorption model TBABS [434].
[b] Radius for an assumed distance of 1 kpc.
[c] Parameter of GABS model such as the optical depth at line center is $\tau = {\rm strength}/\sqrt{2\pi}\sigma$.
[d] Fixed value.
[e] NSA model [304] with $M = 1.2\ M_\odot$, $R = 12$ km, $B = 10^{13}$ G and a uniform temperature distribution. This model yields a best fit distance $d = 121^{+13}_{-12}$ pc.
[f] NSMAXG model [174, 172] with $M = 1.2\ M_\odot$, $R = 12$ km, a dipole distribution of the magnetic field ($B = 10^{13}$ G at the poles) and consistent temperature distribution, seen with $\eta = 90^\circ$. This model yields a best-fit distance of $d = 63^{+26}_{-17}$ pc.

The pulse profiles and hardness ratio shown in Figure 6.1, right panel, indicate that a spectral variation occurs as a function of the rotation phase. Therefore, I extracted the EPIC-pn spectra of the phase intervals corresponding to the two minima and the two maxima of the pulse profile, as shown in Figure 6.1, left panel (the number of source events in each spectrum is listed in the second part of Table 6.1). In order to illustrate the spectral variations, I fitted the spectra with the G2BB model, fixing all of the parameters at the best fit values of the phase-averaged spectrum, except for an overall normalization. The residuals shown in the two lower panels of Figure 6.2, right panel, indicate that the spectra of the two maxima are similar and significantly harder than those of the minima. Their normalization factors with respect to the phase-averaged spectrum are consistent ($N_{\rm max1} = 1.16 \pm 0.02$ and $N_{\rm max2} = 1.14 \pm 0.02$), while those of the two minima are different ($N_{\rm min1} = 0.85 \pm 0.01$ and $N_{\rm min2} = 0.80 \pm 0.01$).

I then fitted the four spectra separately, keeping only the interstellar absorption and the parameters of the cold blackbody fixed, because they are not expected to vary during a stellar rotation. The results are given in the second part of Table 6.2. The absorption line is at the same energy in the four spectra, but it has different widths and normalizations. The hot blackbody temperature is lower ($kT \approx 0.11$ keV) and its emission radius is larger ($R \approx 1.5\ d_{\rm kpc}$ km) at the two maximum phases than at the first minimum ($kT \approx 0.17$ keV and $R \approx 0.20\ d_{\rm kpc}$ km), while these parameters are poorly constrained at the second minimum. I also tried other fits allowing more parameters to vary, but the results were inconclusive due to the strong parameter degeneracy.

6.4 Discussion

The *XMM-Newton* results for PSR J0726−2612 are consistent with those previously obtained with *Chandra* [376], but thanks to a significant detection with good statistics over a broader energy range, they provide more information on the spectrum and pulse profile of this pulsar.

6.4.1 The X-ray spectrum

I found that the spectrum of PSR J0726−2612 is more complex than the single blackbody that was adequate to fit the *Chandra* data. The single blackbody fit requires the addition of a broad absorption line at $E \approx 1.09$ keV. A better fit was obtained with two blackbody components, but also in this case a line at $E \approx 0.39$ keV is required. The colder blackbody component has an emitting area consistent with a large fraction of the star surface ($R_1 = 10.4^{+10.8}_{-2.8}\ d_{\rm kpc}$ km), while the hotter one can be attributed to a small hot spot ($R_2 = 0.5^{+0.9}_{-0.3}\ d_{\rm kpc}$ km), likely located at the magnetic pole.

My results confirm that the interstellar absorption is about a factor of ten smaller than the value ($N_{\rm H} = 2.1 \times 10^{21}$ cm^{-2}) inferred from the dispersion measure and the usual assumption of a 10% ionization of the interstellar medium (see Section 1.4.2). This might be due to the line of sight crossing the Gould belt.

An equally good fit was obtained with a magnetized hydrogen atmosphere covering the whole surface of the star, but also in this case the presence of an absorption line at $E \approx 0.37$ keV (NSA model) or $E \approx 0.28$ keV (NSMAXG model) is required. I note that the constant (polar) value of the magnetic field in the NSA (NSMAXG) model is fixed in the fits at $B = 10^{13}$ G, and that the NSA model assumes a uniform distribution of the temperature. The NSMAXG model is more realistic, but it assumes that the dipole axis is orthogonal to the line of sight, which is

not necessarily true for the case of PSR J0726−2612. Moreover, the inferred distance of ≈63 pc seems unrealistically small.

The absorption lines I found in the spectrum can be interpreted as proton cyclotron features at $E_{\rm cyc} = 0.063\, B_{13} \times (1+z)$ keV, where z is the gravitational redshift and B_{13} the magnetic field in units of 10^{13} G. In the case of G2BB model, for $E_{\rm cyc} = 0.39$ keV and $z \approx 0.2$, I get $B \approx 5 \times 10^{13}$ G, in good agreement with the dipole magnetic field evaluated at the poles ($B_{\rm p} \approx 6 \times 10^{13}$ G). However, I caution that other explanations cannot be ruled out, including the possibility that the lines are simply an artifact resulting from an oversimplified modeling of the continuum emission. In fact, Viganò et al. [426] showed that nonhomogeneus temperature distributions on a neutron star surface can in some cases lead to the appearance of broad features when the spectra are fitted with simple blackbody models.

6.4.2 The X-ray pulse profile

Contrary to the previous *Chandra* results, I also found that the double-peaked pulse profile of PSR J0726−2612 is not well described by a sinusoid, owing to the significant difference in the flux of the two minima. Remarkably, the pulse profile is symmetric for phase reflection around any of the two minima. Within the limits due to their lower statistics, these properties seem to hold also for the profiles in the soft and hard X-ray bands. The pulse profiles are moderately energy dependent, with evidence for a harder emission in correspondence of the two peaks.

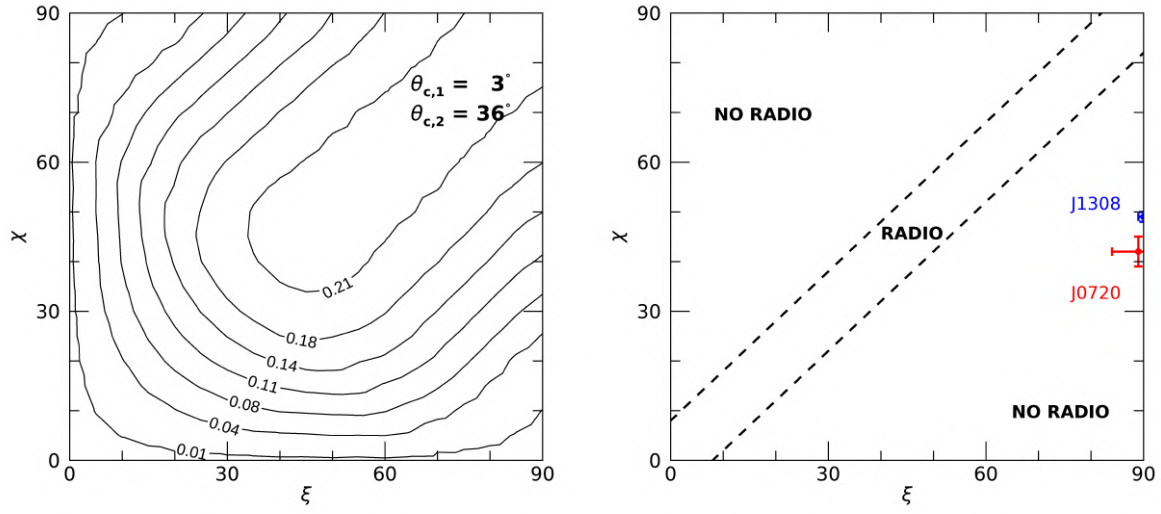

Figure 6.3: Left panel: Pulsed fraction for the G2BB model, where the blackbody emission comes from two, antipodal "cap+ring" spots centered on the magnetic poles. The aperture of the hot cap ($kT = 0.14$ keV) is $\theta_{c,1} = 3°$, while the colder ($kT = 0.074$ keV) ring extends from $\theta_{c,1}$ to $\theta_{c,2} = 36°$. The considered energy range is $0.15 - 1.5$ keV, and a compactness of $M/R = 0.1\ M_\odot$/km has been assumed. Right panel: Visibility of a radio beam with aperture of $\sim 8°$ as a function of the ξ and χ angles. The estimated positions of RX J0720.4−3125 [144] (red dot) and RX J1308.6+2127 [143] (blue dot) are shown.

Although a detailed modeling of PSR J0726−2612 pulse profile is beyond the scope of the present work, I explored whether or not a simple model based on blackbody emission components with parameters consistent with the spectral results could reproduce it. I assumed

that the hotter blackbody comes from two antipodal magnetic polar caps with opening angle $\theta_{c,1} = 3°$, while the colder one from two annuli extending between $\theta_{c,1}$ and $\theta_{c,2} = 36°$. The temperatures of the emitting regions were set to the values derived from the spectral analysis (model G2BB, $kT_1 = 0.074$ keV, $kT_2 = 0.14$ keV) and the angular apertures were chosen in such a way as to reproduce the emitting radii derived from the fit for a NS radius of 12 km. I also added interstellar absorption and a Gaussian absorption line, with parameters fixed to those of the phase averaged spectrum. Synthetic pulse profiles (energy range $0.15 - 1.5$ keV) were computed using the method described in Chapter 4, accounting for general-relativistic effects and the EPIC instrumental response. The results depend on the angles χ and ξ that the rotation axis makes with the line of sight and the magnetic axis, respectively. As shown in Figure 6.3, left panel, this simple model is unable to yield the observed pulsed fraction even for the most favorable geometry (PF $\approx 21\%$ for $\xi \approx \chi \gtrsim 35°$). This is also true if only two antipodal point-like polar caps are considered, which is the configuration yielding the maximum pulsed fraction using isotropic emission (see Eq. 4.11). Another problem is that, owing to the intrinsic symmetry of the model, the resulting pulse profiles cannot exhibit different minima, as observed in PSR J0726−2612.

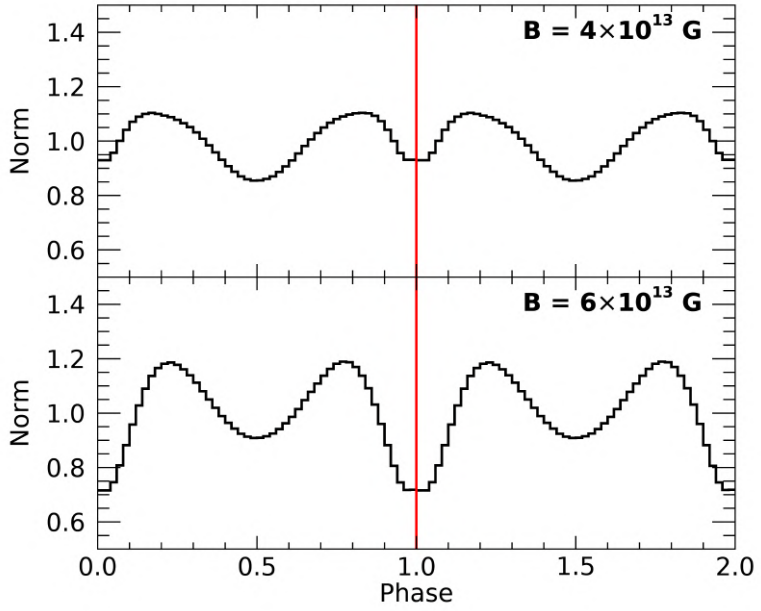

Figure 6.4: Pulse profiles in the $0.15 - 1.5$ keV range in the case of emission from a hydrogen atmosphere model at two point-like polar caps with $T_{\rm eff} = 0.5$ MK and $B = 4 \times 10^{13}$ G (upper panel), and $B = 6 \times 10^{13}$ G (lower panel). I assumed $\xi = 30°$, $\chi = 35°$ and a compactness $M/R = 0.1\ M_\odot$/km. The vertical red line shows the phase expected for the radio peak.

Indeed, this model is oversimplified and unlikely to apply to the real case. Whatever the mechanism responsible for the surface emission, the presence of a strong magnetic field results in some degree of anisotropy in the emitted radiation. In the case of a magnetized atmosphere, more complicated energy-dependent beaming patterns are produced (see Section 4.2.2). The angular pattern of the emerging intensity depends also on the local surface temperature and magnetic field, meaning that the morphology of the pulse profiles can be extremely variegated. Using a partially ionized hydrogen atmosphere model [387] with improved opacities from

Potekhin et al. [333], I computed the expected pulse profiles, as described in Chapter 4. The best match with the data was obtained assuming emission from two antipodal hot spots with an effective temperature of 0.5 MK, and $\xi = 30^\circ$, $\chi = 35^\circ$. In Figure 6.4, I show two examples with representative values of the magnetic field, $B = 4 \times 10^{13}$ G and $B = 6 \times 10^{13}$ G. Although these pulse profiles qualitatively resemble that observed in PSR J0726−2612, I note that they have been computed considering only the X-ray emission from the polar caps. The addition of a contribution from an extended part of the star surface would reduce the pulsed fractions of the pulse profiles shown in Figure 6.4.

6.5 Connections with the XDINSs

Table 6.3: Comparison between PSR J0726−2612 and the XDINSs.

Num	Source	P	$\dot{P}$	B_p	E_cyc	B_cyc	$L_X/\dot{E}$	Pulse	PF	Timing
	RX	s	10^{-14} s s^{-1}	10^{13} G	eV	10^{13} G			%	Reference
1	J0420.0−5022	3.45	2.76	2.0	…	…	0.31 − 0.38	single	13	[138]
2	J0720.4−3125	16.78	18.6	11.3	254^{+25}_{-30}	$3.4^{+0.3}_{-0.4}$	99 − 157	double	11	[144]
3	J0806.4−4123	11.37	5.6	5.1	241^{+11}_{-12}	$3.2^{+0.2}_{-0.2}$	10.6 − 16.7	single	6	[138]
4	J1308.6+2127	10.31	11.2	6.9	390^{+6}_{-6}	$5.16^{+0.08}_{-0.08}$	31.5 − 39.6	double	18	[143]
5	J1605.3+3249	…	…	…	353^{+19}_{-48}	$4.7^{+0.3}_{-0.6}$	…	…	<1.4	[317]
6	J1856.5−3754	7.06	2.98	2.9	…	…	9.6 − 15.2	single	1.2	[410]
7	J2143.0+0654	9.43	4.1	4.0	326^{+56}_{-79}	$4.3^{+0.7}_{-1.0}$	33.2 − 41.8	single	4	[444, 272]
	PSR J0726−2612	3.44	29.3	6.4	390^{+10}_{-20}	$5.2^{+0.1}_{-0.3}$	1.1 − 3.0	double	30	[358]

Notes. B_p and B_cyc are the magnetic field at the poles evaluated from the timing parameter and from the cyclotron energy, respectively. E_cyc values are taken from Yoneyama et al. [440], while L_X values from Viganò et al. [425].

The spectral results, and in particular the presence of a broad absorption line, strengthen the similarity between PSR J0726−2612 and the XDINSs, for which similar spectral features have been reported (see Figure 6.5 and Table 6.3).

While most of the XDINSs have single-peaked pulse profiles, two of them (RX J0720.4−3125 [144] and RX J1308.6+2127 [143]) show double-peaked profiles similar to PSR J0726−2612, although with smaller pulsed fractions (18% and 11%, respectively). Assuming a distance of 1 kpc, the luminosity of PSR J0726−2612 is $L_\infty = (4.0^{+4.4}_{-1.0}) \times 10^{32}$ erg s^{-1}. This is greater than its spin-down luminosity, as for the XDINSs (see Table 6.3), but is in reasonable agreement with the expected thermal luminosity of a $\sim$200 kyr-old pulsar (see Figure 3.7).

The remarkable difference between PSR J0726−2612 and these two XDINSs is the presence of radio emission in the former. Here I discuss the possibility that this is due to an unfavorable orientation of their radio beam. Based on the radio beaming fraction of long-period pulsars, Kondratiev et al. [214] estimated that a much larger number of XDINSs (~ 40) would need to be observed to detect one with the radio beam crossing our line of sight.

I marked in Figure 6.3, right panel, the values of the angles ξ and χ estimated for RX J1308.6+2127 and RX J0720.4−3125 by Hambaryan et al. [143] and Hambaryan et al. [144]. They imply that these two pulsars are nearly orthogonal rotators ($\xi \approx 90^\circ$) seen with a large

impact parameter $\eta = |\chi - \zeta| \approx 45°$. With the usual assumption that the radio beam coincides with, or is close to, the magnetic dipole axis, such a large impact parameter can naturally account for the fact that their radio emission is not visible from the Earth. As an example, the dashed lines in Figure 6.3, right panel, indicate the region where $\zeta \approx \chi$ for which a radio beam with an aperture of $\sim 8°$ would be visible. Contrary to the two XDINSs, PSR J0726−2612 should lie inside this region. The atmosphere model used to compute the pulse profiles of Figure 6.4 predicts that the radio pulse appearing when the magnetic axis is in the plane defined by the line of sight and rotation axis is in phase with one of the two minima of the X-ray profile. Considering the current relative error in the radio and X-ray phase alignment (see Figure 6.1, left panel), this possibility cannot be excluded.

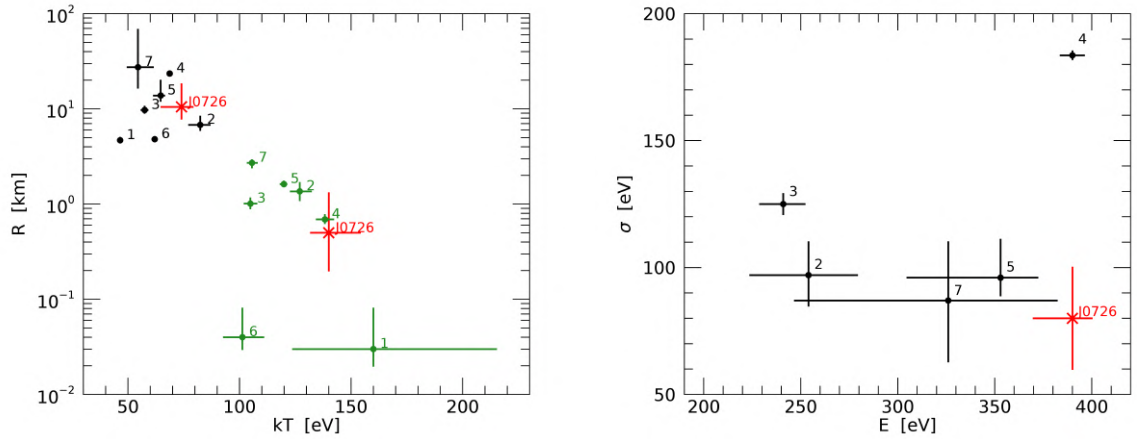

Figure 6.5: Comparison of the spectral parameters of the XDINSs (from Yoneyama et al. [440]) and PSR J0726−2612 obtained with two blackbodies and a Gaussian absorption line model (G2BB). Left panel: Blackbody radii (black: cold component; green: hot component) of the XDINSs and of PSR J0726−2612 (red cross). Right panel: Line width vs. line centroid energy (black dots are of XDINSs and the red cross of PSR J0726−2612). The XDINSs are numbered according to Table 6.3.

Chapter 7

PSR B0943+10

PSR B0943+10 is a mode-switching radio pulsar characterized by two emission modes with different radio and X-ray properties. Remarkably, the X-ray flux is higher in the Q-mode, when it is lower in the radio band, with respect the radio brighter B-mode. In other words, the X-ray and radio intensities are anti-correlated.

Previous studies [161, 264, 266] (see also Section 2.4.1), based on simple combinations of blackbody and power-law models, showed that its X-ray flux can be decomposed in a pulsed thermal plus an unpulsed nonthermal components. Despite PSR B0943+10 is a nearly aligned rotator, it shows an intense pulsed emission in the X-ray band.

In this chapter, I present the analysis of *XMM-Newton* observations of PSR B0943+10, modeling its spectrum with realistic thermal emission models in order to account for the high pulsed emission. Part of this work has been published in Rigoselli et al. [357].

7.1 Introduction

The timing parameters of PSR B0943+10 (spin period $P = 1.1$ s and $\dot{P} = 3.5 \times 10^{-15}$ s s^{-1}) give a characteristic age $\tau_c = 5$ Myr, a dipolar magnetic field at the poles $B_\mathrm{d} = 4 \times 10^{12}$ G, and a rate of rotational energy losses $\dot{E} = 10^{32}$ erg s^{-1}. Its dispersion measure is DM $= 15.31845(90)$ pc cm^{-3} [43], which, using the recent model for the Galactic electron density distribution by Yao et al. [439], corresponds to a distance of 0.89 kpc[1].

As discussed in Section 2.4.1, the radio properties of PSR B0943+10 have been considered indications that the pulsar is a nearly aligned rotator, i.e. the angle between magnetic and spin axis is rather small ($10^\circ < \xi < 15^\circ$). Moreover, it is seen pole-on, that means that also the angle between our line of sight and the spin axis is small ($5^\circ < \chi < 10^\circ$).

Recently, Bilous [42] reconsidered the problem of the geometry of PSR B0943+10: assuming a wider range for the emission cone $\rho_{1\,\mathrm{GHz}}$ (see Eq. 2.16), she found $5^\circ < \xi < 30^\circ$. Moreover, at variance with the previous works [85], Bilous [42] considered both the inside and the outside traverse configurations; for each value of ξ only two well-defined values of χ are possible and are in the ranges $3^\circ < \chi < 22^\circ$ (inside traverse) or $7^\circ < \chi < 38^\circ$ (outside traverse).

In the following, I consider four representative pairs of ξ and χ for the inside traverse case and the corresponding ones for the outside traverse, as indicated in Table 7.1.

[1] Several previous works adopted a distance of 0.63 kpc, based on Cordes & Lazio [72].

Table 7.1: Possible geometries of PSR B0943+10 considered in this work.

ξ	5°	10°	20°	30°
$\eta \approx \rho_{1\,\mathrm{GHz}}$	2°	4°	6°	8°
$\chi = \xi - \eta$ (inside traverse)	3°	6°	14°	22°
$\chi = \xi + \eta$ (outside traverse)	7°	14°	26°	38°

Notes. ξ is the angle between the magnetic and spin axis; χ is the angle between the line of sight and the spin axis; η is the impact angle (see Eq. 2.1).

7.2 Observations and data reduction

XMM-Newton observed PSR B0943+10 in 2003, 2011, and 2014. In all the analyses reported here, I used the sum of the 2011 and 2014 observations, after checking that the individual data sets give consistent results. From the exposure times and number of source counts reported in Table 7.2 one can see the increase in the statistics, compared to previous works based on the individual data sets (more details on the 2011 and 2014 observations can be found in Hermsen et al. [161] and Mereghetti et al. [266], respectively).

Although there are no simultaneous radio data for the 2003 observations, the average X-ray flux measured in 2003 December suggests that the pulsar was in the B-mode for most of the time [263]. In principle, I could have added these data to those analyzed here, but also in view of their short exposure, I decided to restrict my analysis to the 2011 and 2014 data sets for which the mode identification based on radio observations is certain.

During all observations, the EPIC-pn camera was operated in full frame mode, which provides a time resolution of 73 ms, while the two MOS cameras were used in small window mode (0.3 s of time resolution, see Section 5.1.1). For the three cameras the thin optical filter was used. I used single- and multiple-pixel events for both the pn and MOS. The events detected in the two MOS cameras were combined into a single data set and analyzed with averaged exposure maps and response files.

I reprocessed the EPIC-pn data to reduce the detector noise at the lowest energies using the task EPREJECT of version 15 of the Science Analysis System (SAS)[2] To remove the periods of high background I used the same cuts adopted in Mereghetti et al. [266], i.e. I excluded all the time intervals with a pn count rate in the range $10 - 12$ keV higher than 1.2 cts s^{-1}. The resulting net exposure times are given in Table 7.2. To separate the data of the B- and Q-modes, I used the times derived from radio data in the previous works by Hermsen et al. [161] and Mereghetti et al. [266].

To extract the source counts and spectra, I used the maximum likelihood (ML) technique, as described in Chapter 5. I applied the ML analysis to a circular region centered at R.A. = $09^h\ 46^m\ 07^s.8$, Dec. = $+09^\circ\ 52'\ 00''.8$, with a radius of $30''$, from which I excluded a circle of radius $30''$ centered at R.A. = $09^h\ 46^m\ 10^s.7$, Dec. = $+09^\circ\ 52'\ 26''.4$ to avoid a nearby source. For the spectral analysis, I obtained 23 energy bins for the pn ($0.2 - 7$ keV) and 8 for the MOS ($0.2 - 4.3$ keV) for the Q-mode, and 13 energy bins for the pn ($0.2 - 6.7$ keV) and 7 for the MOS ($0.2 - 5.5$ keV) for the B-mode. In the spectral fits, I used the interstellar absorption model PHABS of XSPEC, version 12.8.2. All of the errors are at the 1σ level. For the timing analysis, the pulse phases of PSR B0943+10 counts were computed using the ephemeris given in Mereghetti et al. [266], which are valid from 54861.014 to 57011.249 MJD (2009 January to 2014 December).

[2] http://www.cosmos.esa.int/web/xmm-newton/sas.

Table 7.2: Exposure times and number of detected counts for PSR B0943+10 in the Q- and B-modes.

Year	Radio mode	Epic camera	Exposure time ks	Counts[a] $0.2-10$ keV
2011	Q	pn	48.5	590 ± 40
2011	Q	MOS	53.4	293 ± 26
2011	B	pn	40.9	191 ± 26
2011	B	MOS	45.2	99 ± 17
2014	Q	pn	123.6	1450 ± 66
2014	Q	MOS	133.8	680 ± 40
2014	B	pn	174.2	944 ± 61
2014	B	MOS	189.9	410 ± 35
2011+2014	Q	pn	172.5	2054 ± 77
2011+2014	Q	MOS	187.2	973 ± 48
2011+2014	B	pn	215.6	1134 ± 66
2011+2014	B	MOS	235.1	512 ± 39

Notes. [a] Total (background-subtracted) source counts derived with the maximum likelihood method.

7.3 Results

7.3.1 Blackbody thermal emission

As a first step, I considered fits to the total (i.e. pulsed plus unpulsed) emission of PSR B0943+10 using only power-law and blackbody spectral components. I obtained best-fit parameters (Table 7.3) fully consistent with those found in previous analyses [161, 266] and in general with slightly smaller uncertainties, thanks to the better statistics provided by joining the 2011 and 2014 data.

In the Q-mode, single-component models are clearly rejected (see Figure 7.1, left panel), while good fits are obtained with a blackbody plus power law or with the sum of two blackbody components. In the B-mode, a single power law is clearly rejected ($\chi^2_\nu = 2.28/18$ degrees of freedom, dof, corresponding to a null hypothesis probability nhp = 0.004). A blackbody model with temperature $kT = 0.22 \pm 0.01$ keV is marginally acceptable ($\chi^2_\nu = 1.66/18$ dof, nhp = 0.04), but the shape of the residuals shown in the right panels of Figure 7.1 indicates that a second spectral component is needed. In fact, similarly to the Q-mode, a good fit can be obtained by using either a power law plus a blackbody or the sum of two blackbodies (see Table 7.3).

I also examined the spectra of the pulsed and unpulsed emission in the two radio modes, using an ML analysis that also takes into account the timing information of each photon (see details in Section 5.3.3). The results, again in agreement with those obtained with the 2014 data alone, are summarized in Table 7.4.

Although modeling the thermal emission with blackbody components gives formally acceptable results from the point of view of the spectral fits, there are obvious problems to reproduce the observed energy dependence of the folded pulse profiles. In fact, the blackbody emission from an element of the NS surface is isotropic and the light curves produced by a rotating hot spot do not depend on energy. Therefore, the PF depends only on the geometrical parameters and on the compactness ratio M/R of the star.

Energy-dependent pulse profiles can be obtained if an unpulsed power-law component is added to the blackbody, as shown in Figure 7.6, left panel, for emitting polar caps of different temperatures. The figure refers to the geometric configuration of Table 7.1 yielding the highest modulation, i.e. $\xi = 30^\circ$ and $\chi = 38^\circ$. In all cases, I adopted a polar cap size consistent with the spectral results of the Q-mode and included the corresponding best-fit unpulsed power

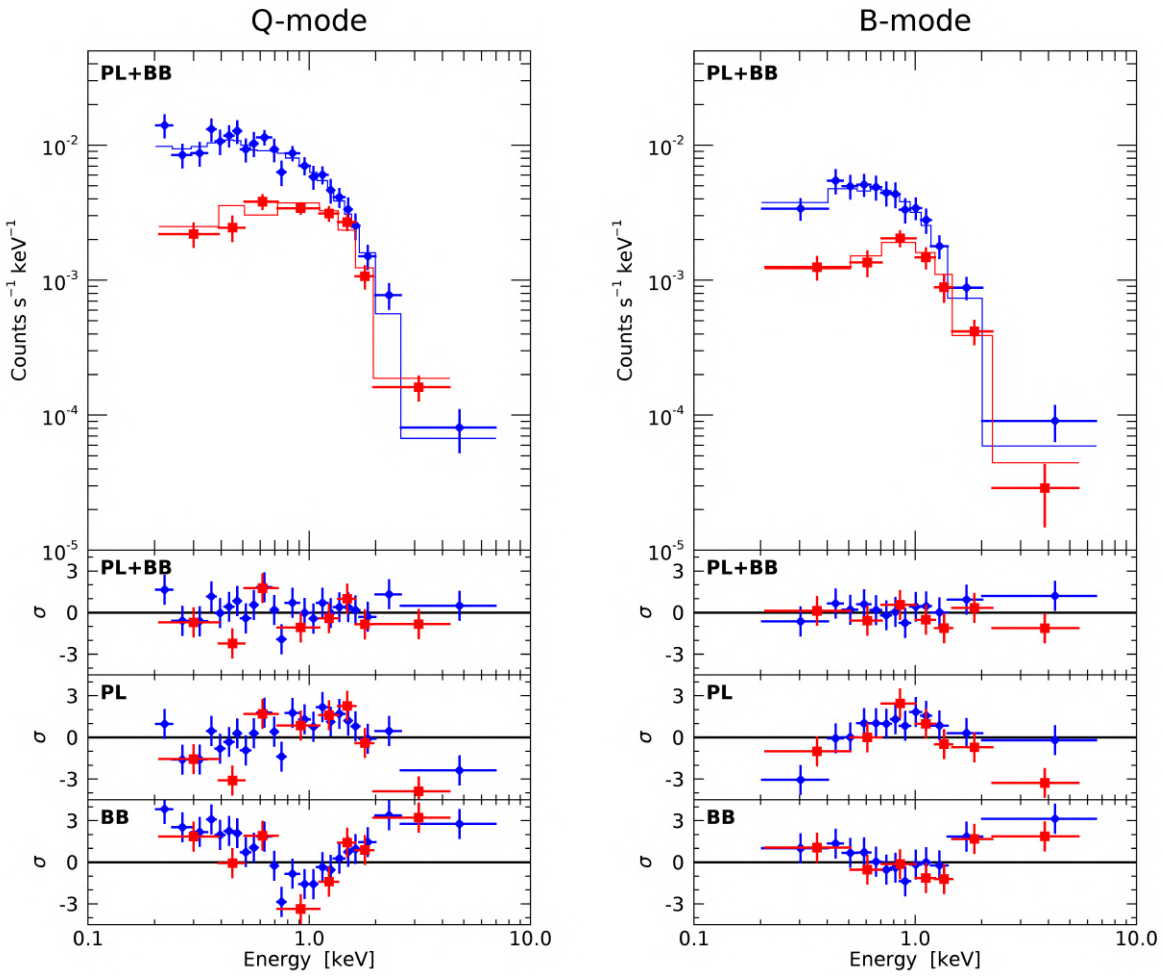

Figure 7.1: EPIC-pn (blue diamonds) and EPIC-MOS (red squares) X-ray phase-averaged spectra of PSR B0943+10 in the Q-mode (left) and in the B-mode (right). The top panels show the best fit using absorbed power law plus blackbody models; the lower panels show the residuals of the best fit (PL+BB) of an absorbed power-law model (PL) and of an absorbed blackbody model (BB) in units of σ.

law. The dashed line gives for comparison the PF that would be obtained in the absence of the unpulsed power-law component.

For completeness, even if not of direct interest for the case of PSR B0943+10, Figure 7.6, left panel, shows also the PF expected in the case of thermal emission from the whole NS surface with an inhomogeneous temperature T_s given by the relation of Greenstein & Hartke [134], discussed in Section 3.1.1. As expected, such a large emitting area produces an even smaller PF.

7.3.2 Magnetized hydrogen atmosphere

I assume that the atmosphere that covers PSR B0943+10 consists of partially ionized hydrogen (Section 3.1.2). I followed the approach described in Chapter 4: 84 model atmospheres were computed for 7 surface effective temperatures (0.5, 0.8, 1, 1.2, 1.5, 2, and 3 MK) and 12 values of the magnetic field (1, 1.5, 2, 2.4, 2.7, 3, 3.5, 4, 5, 6, 7, and 8 $\times 10^{12}$ G). The surface gravity $\log g = 14.241$ was fixed to the adopted NS parameters, $M = 1.5\ M_\odot$ and $R = 12$ km. The magnetic field was assumed to be normal to the surface. As argued in Section 4.2, this is a good

Table 7.3: Best-fit parameters for the phase-averaged spectra of the Q- and B-modes.

	Q-mode PL + BB	Q-mode BB + BB	B-mode PL + BB	B-mode BB + BB
Γ	$2.6^{+0.2}_{-0.1}$	...	$2.2^{+0.2}_{-0.3}$	...
K^{a}	$2.9^{+0.4}_{-0.5}$	...	1.0 ± 0.3	...
$F_{\rm PL}^{0.5-2}$	$6.6^{+0.9}_{-1.1}$	...	$2.3^{+0.6}_{-0.8}$	...
$F_{\rm PL}^{0.2-10}$	18 ± 2	...	6 ± 1	...
kT_1 (keV)	0.30 ± 0.02	$0.35^{+0.03}_{-0.02}$	0.21 ± 0.02	0.48 ± 0.08
$R_{\rm BB_1}^{b}$ (m)	27^{+5}_{-4}	25 ± 4	41^{+10}_{-9}	6^{+3}_{-2}
$F_{\rm BB_1}^{0.5-2}$	6.0 ± 1.1	$9.2^{+0.9}_{-1.2}$	$3.4^{+0.7}_{-0.8}$	$1.7^{+0.6}_{-0.7}$
$F_{\rm BB_1}^{0.2-10}$	7.6 ± 1.4	12 ± 1	4 ± 1	$3.2^{+0.6}_{-0.7}$
kT_2 (keV)	...	0.12 ± 0.01	...	0.17 ± 0.01
$R_{\rm BB_2}^{b}$ (m)	...	200^{+55}_{-40}	...	72^{+11}_{-9}
$F_{\rm BB_2}^{0.5-2}$	...	$3.75^{+1.05}_{-1.25}$	...	$4.1^{+0.5}_{-0.7}$
$F_{\rm BB_2}^{0.2-10}$	...	9.2 ± 1.0	...	$6.2^{+0.5}_{-0.7}$
$F_{\rm TOT}^{0.5-2}$	12.6 ± 0.4	13.0 ± 0.4	5.7 ± 0.3	5.85 ± 0.25
$F_{\rm TOT}^{0.2-10}$	25.9 ± 1.1	21.3 ± 0.8	10.8 ± 0.8	9.4 ± 0.5
χ^2_ν/dof	1.08/27	1.25/27	0.51/16	0.43/16
nhp	0.36	0.18	0.94	0.98

Notes. Joint fits of pn + MOS spectra with $N_{\rm H}$ fixed to 4.3×10^{20} cm^{-2}. PL = power law, BB = blackbody. The fluxes, corrected for the absorption, are in units of 10^{-15} erg s^{-1} cm^{-2}. Errors at 1σ.
[a] Normalization of the power law in units of 10^{-6} photons cm^{-2} s^{-1} keV^{-1} at $E = 1$ keV.
[b] Blackbody radius for an assumed distance of 0.89 kpc.

approximation for small hot spots located around the magnetic poles.

For each set of parameters explored in the model, I computed the phase-averaged spectrum and implemented it in XSPEC. I found that, for any of the considered geometries (see Table 7.1), it was possible to find an acceptable fit to the phase-averaged spectra of both the Q- and B-modes using only the atmosphere model, without the need of an additional power-law component.

The best-fit parameters depend on the ξ and χ values. For all of the considered angles, the fits to the Q-mode spectra gave a small absorption, consistent with 0 (1σ upper limit of $N_{\rm H} < 6 \times 10^{19}$ cm^{-2}). The best-fit spectral parameters were in the ranges $B = 2 - 6 \times 10^{12}$ G, $kT = 0.10 - 0.15$ keV, and $R_{\rm cap} = 150 - 300$ m. In the B-mode, the absorption was poorly constrained; therefore, I fixed it to 6×10^{19} cm^{-2} and obtained best-fit values of kT similar to those of the Q-mode, but with $R_{\rm cap}$ in the range $100 - 200$ m and unconstrained values of B. For the Q-mode the best fit was found for $\xi = 5^\circ$ and $\chi = 3^\circ$, while all the considered geometries gave equally good fits ($\chi^2_\nu \approx 1$) to the B-mode spectra.

In order to distinguish between the different possibilities allowed by the atmosphere fits to the phase-averaged spectra, I examined the pulse profiles, which have a stronger dependence on the geometrical configuration. For each pair of ξ and χ values I computed the expected pulse profile in the energy range $0.5 - 2$ keV, where the pulsation is detected with the highest significance, taking into account the instrumental response of EPIC. For each geometrical con-

Table 7.4: Best-fit parameters for the spectra of the pulsed and unpulsed emission in the Q- and B-modes.

	Q-mode Unpulsed PL	Q-mode Pulsed BB	B-mode Unpulsed PL	B-mode Pulsed BB
Γ	2.50 ± 0.15	...	2.3 ± 0.2	...
K^{a}	3.10 ± 0.25	...	1.7 ± 0.2	...
kT (keV)	...	0.27 ± 0.02	...	$0.23^{+0.05}_{-0.03}$
R^{b}_{BB} (m)	...	32^{+6}_{-5}	...	25^{+10}_{-8}
$F^{0.5-2}$	7.1 ± 0.5	5.7 ± 0.5	3.8 ± 0.4	1.9 ± 0.3
$F^{0.2-10}$	19 ± 1	7.1 ± 0.6	10 ± 1	2.4 ± 0.4
χ^2_ν/dof	0.797/6	0.691/6	0.266/5	0.200/5
nhp	0.57	0.66	0.93	0.96

Notes. Joint fits of pn + MOS spectra with $N_{\rm H}$ fixed to 4.3×10^{20} g cm^{-3}. PL = power law, BB = blackbody. The fluxes, corrected for the absorption, are in units of 10^{-15} erg s^{-1} cm^{-2}. Errors at 1σ.
[a] Normalization of the power law in units of 10^{-6} photons cm^{-2} s^{-1} keV^{-1} at $E = 1$ keV.
[b] Blackbody radius for an assumed distance of 0.89 kpc.

figuration and mode I used the corresponding best fit values of kT, $R_{\rm cap}$ and B derived in the spectral analysis. The resulting pulse profiles were quantitatively compared to the observed ones using a Kolmogorov-Smirnov (KS) test. In this way, I found that the acceptable configurations (probability $> 10\%$ that the observed data come from the model) are $\xi = 5^\circ$, $\chi = 3^\circ$ and $\xi = 5^\circ$, $\chi = 7^\circ$ for the Q-mode. The B-mode analysis adds no information because all the configurations were acceptable (KS-test probability $> 13\%$).

More information can be obtained by performing phase-resolved spectroscopy. For this, I extracted with the ML technique the Q- and B-mode spectra of PSR B0943+10 in two phase intervals of duration 0.5 cycles centered at phase 0 (pulse maximum) and at phase 0.5 (pulse minimum). To fit these spectra, I used models specifically computed by integrating the predicted emission over the corresponding phase intervals as described above.

The joint fit of the four Q-mode spectra (two pn and two MOS) showed that the geometrical configurations with small angles are preferred (nhp = 0.06 for $\xi = 5^\circ$ and $\chi = 3^\circ$, nhp $< 3 \times 10^{-3}$ for all of the other cases), although the fit is worse than that of the phase-averaged spectra.

Better fits could be obtained by adding to the model a power-law component, which was assumed to be unpulsed by linking its parameters to common values in the two phase bins. I initially let the interstellar absorption as a free parameter, but as it was poorly constrained, I finally fixed it to the value of 4.3×10^{20} cm^{-2} used in previous analysis. In the Q-mode, for all of the considered geometrical configurations, good fits were obtained with a photon index $\Gamma \approx 2 - 2.5$. However, for $\xi \geq 20^\circ$ the best-fit models required values of magnetic field smaller than 10^{12} G, inconsistent with the value expected from the timing parameters of PSR B0943+10. All of the expected pulse profiles, together with the spectral parameters from which they are computed and the KS-test probability, are shown in Figure 7.2.

The configuration favored by both the KS test for the pulse profiles and the χ^2 test for the spectra is $\xi = 5^\circ$ and $\chi = 3^\circ$, which yields $\Gamma = 2.5 \pm 0.2$, $kT = 0.089^{+0.014}_{-0.005}$ keV, $R_{\rm cap} = 260^{+60}_{-70}$

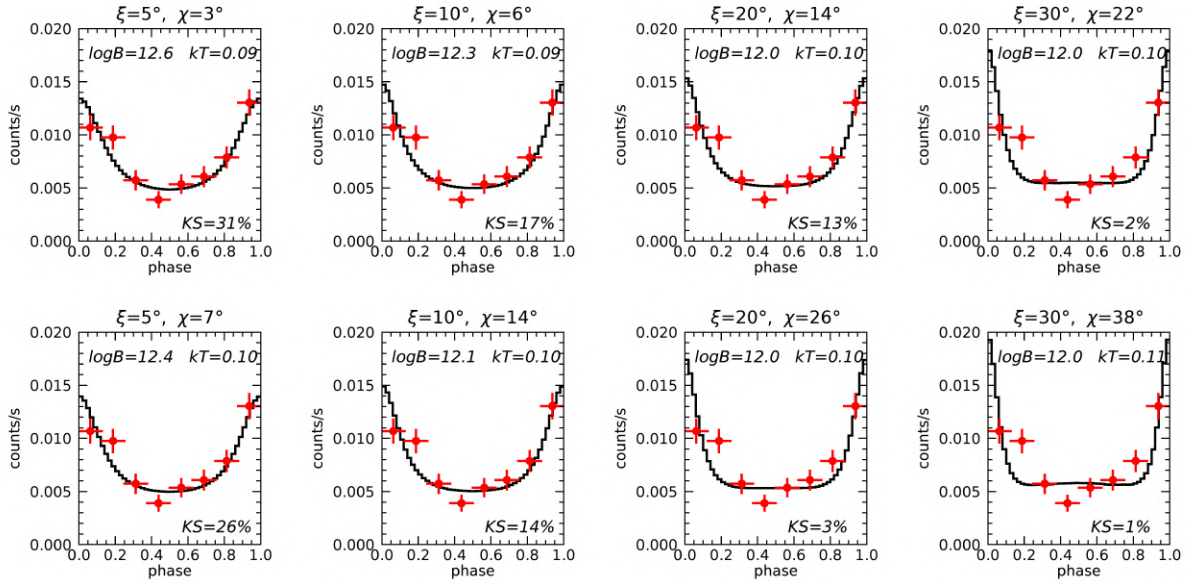

Figure 7.2: Expected pulse profiles in the $0.5 - 2$ keV range (solid lines), in the case of a hydrogen atmosphere model, for different pairs of ξ and χ and the corresponding best-fit spectral parameters for the Q-mode spectra. The KS-test probability is also shown. Upper panels: inside traverse; lower panels: outside traverse. The red dots with error bars show the observed Q-mode data.

m, and $B = (4.0^{+0.9}_{-0.7}) \times 10^{12}$ G (see Table 7.5 for all of the details). Figure 7.3 shows the best-fit phase-averaged (left panel) and phase-resolved (right panel) spectra. As a comparison, in the lower panels the residuals of the atmosphere model alone are shown: while in the phase-averaged case the addition of the power law is not required, the fit of the phase-resolved spectra (especially the spectra of the pulse maximum) is significantly improved.

For what concerns the B-mode, the atmosphere model alone can fit well the phase-resolved spectra, but only in the configurations with large ξ and χ (nhp > 0.47). With the addition of a power law (with fixed $\Gamma = 2.3$, due to the lower statistics in the B-mode) all of the geometrical configurations give acceptable spectral fits (nhp > 0.30) and pulse profiles (KS-test probability > 0.20). The latter are shown in Figure 7.4. The inferred magnetic field, although with large uncertainties, is lower than that found for the Q-mode. For the best-fitting geometry of the Q-mode ($\xi = 5°$, $\chi = 3°$), I get $kT = 0.082^{+0.003}_{-0.009}$ keV, $R_{\rm cap} = 170^{+35}_{-25}$ m, and $B = (2^{+2}_{-1}) \times 10^{12}$ G (see Table 7.5 for all of the details).

7.3.3 Condensed magnetized surface

I computed the spectra and pulse profiles produced by a hot polar cap with a condensed iron surface, using the baseline values for the geometry of PSR B0943+10, and different values of kT and B in the appropriate range to have a condensed surface (see Section 3.1.3). As previously done with the hydrogen atmosphere, for each set of parameters I produced a model of the phase-averaged spectrum and implemented it in XSPEC. I verified that for all of the pairs of ξ and χ in Table 7.1 it was possible to find an acceptable spectral fit, but only the most-misaligned geometries give rise to a light curve pulsed enough. Therefore, in the following, I consider only the most favorable case, $\xi = 30°$ and $\chi = 38°$.

The phase-averaged spectrum of the Q-mode could be fitted only with the addition of a

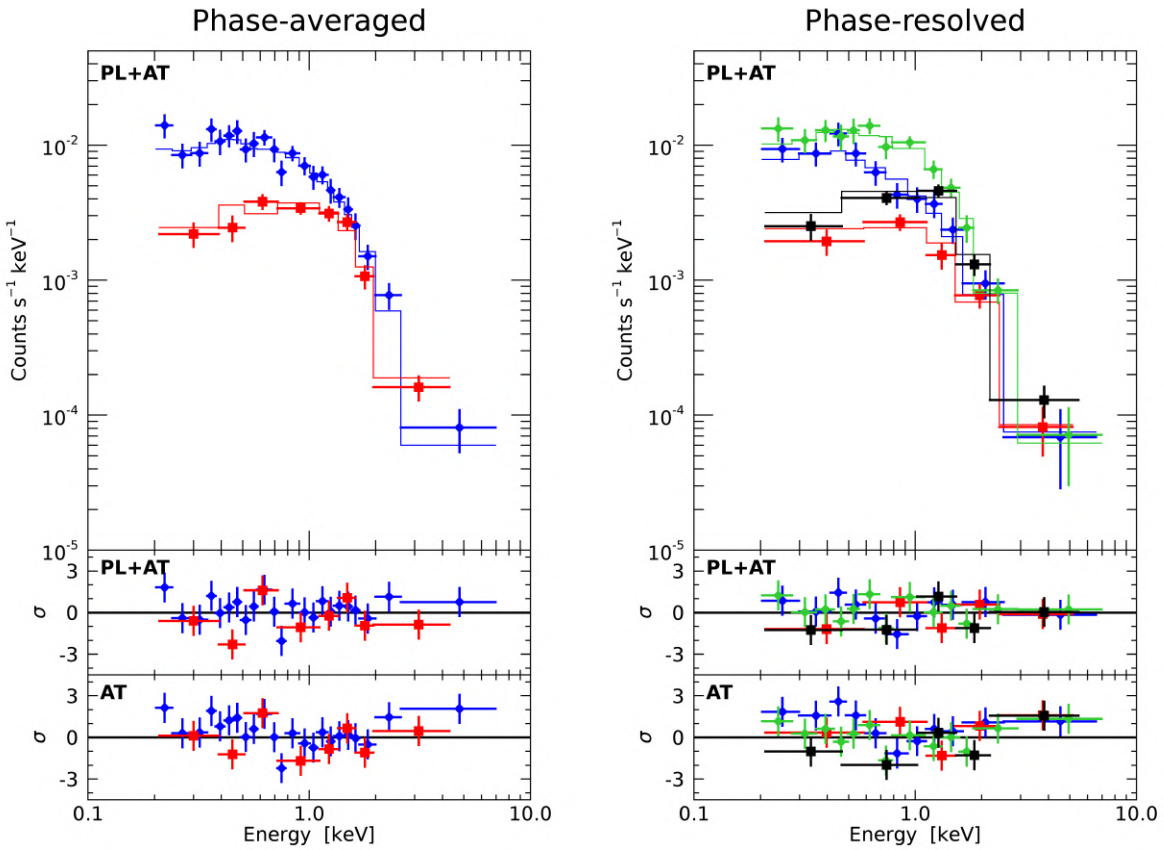

Figure 7.3: EPIC-pn (diamonds) and EPIC-MOS (squares) X-ray spectra of PSR B0943+10 in the Q-mode. Left panel: phase-averaged spectra (blue: pn, red: MOS). Right panel: phase-resolved spectra, where the spectra at the minimum phase are in blue (pn) and red (MOS), while those at maximum phase are in green (pn) and black (MOS). The top panels show the best fit of the case $\xi = 5°$ and $\chi = 3°$ using an absorbed power law plus hydrogen atmosphere model (PL+AT); the corresponding residuals in units of σ are shown in the middle panels. The lower panels show the residuals of the best-fitting atmosphere model (AT). While the fits of the phase-averaged spectra with the two models are equally good, the addition of the power-law component significantly improves the fit of the phase-resolved spectra.

nonthermal component, but it is impossible to reproduce the observed PF because in any case the power-law component adds more unpulsed counts. Similar results were found in the analysis of the B-mode data.

In conclusion, the condensed surface emission model requires the presence of an additional power-law component in the spectrum and, in order to reproduce the observed PF, this nonthermal component also has to be pulsed. Not surprisingly, this is similar to the case of blackbody thermal emission examined in Section 7.3.1. To quantify the required modulation of the nonthermal component, I performed phase-resolved spectroscopy using the two phase intervals defined above. I fitted with the condensed surface model plus a power law with normalization free to vary between the pulse maximum ($K_{\rm max}$) and minimum ($K_{\rm min}$). The best-fit parameters are summarized in Table 7.5, where the PF of the power law is also reported.

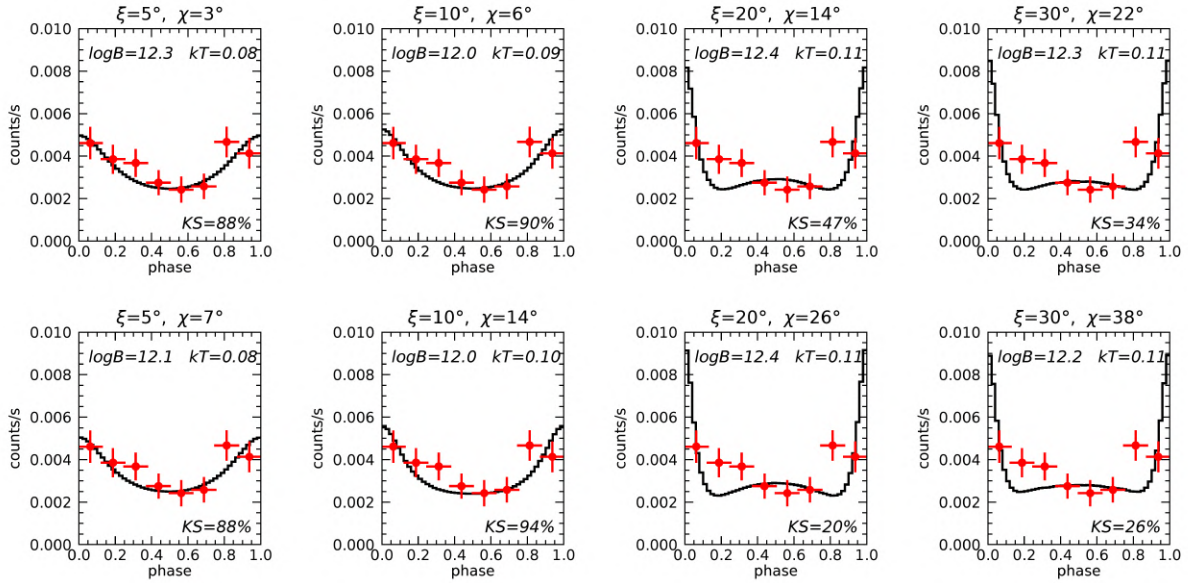

Figure 7.4: Same as Figure 7.2, but for the B-mode.

7.4 Discussion

Most previous analyses of the X-ray emission from the radio and X-ray mode-switching pulsar PSR B0943+10 [454, 161, 264, 266], with the notable exception of that in Storch et al. [382], were based on simple combinations of blackbody and power-law components to model the mix of thermal and nonthermal emission detected in such an old pulsar. The purpose of my work was to explore in a more quantitative way realistic models for the thermal emission of PSR B0943+10, exploiting all the available X-ray data and taking into account the most recent (and less constraining) geometrical configurations derived from the radio observations of this pulsar. In fact, compared to brighter X-ray pulsars that can provide spectra with a better statistics, PSR B0943+10 has the advantage of a rather well-known geometry. This is of great importance because it reduces the number of parameters (or at least their allowed ranges) on which the spectral and timing properties depend. In this work, I adopted a value of the neutron star mass to radius ratio $M/R = 1.5\ M_\odot/12\ \mathrm{km} = 0.125\ M_\odot/\mathrm{km}$. With lower values of the compactness it is possible to obtain higher PFs (for example, a compactness of 0.1 $M_\odot/\mathrm{km}$ was used by Storch et al. [382]).

I could adequately fit the 2011 plus 2014 X-ray spectra of PSR B0943+10 during both radio modes with the sum of a power law and a blackbody, confirming the results already reported with the individual data sets of the two observing campaigns [161, 266]. In addition, the higher statistics provided by the combined data disfavors the fit of the B-mode spectrum with a single blackbody, supporting the presence of thermal and nonthermal components in both modes, as proposed by these authors on the basis of their spectral-timing analysis of the pulsed and unpulsed emission.

It is natural to associate the pulsed thermal component with the polar caps, but as the geometric configuration of PSR B0943+10 implies that the emitting polar region is visible at all rotational phases, it is impossible to reproduce the large and energy-dependent (in the Q-mode) PF unless the thermal emission is magnetically beamed [382]. A further problem of fitting with simple blackbody models is that, for the geometry of PSR B0943+10, even the emission from a

Table 7.5: Results for the phase-resolved spectra of Q- and B-modes.

	Q-mode H atmosphere	Q-mode Free Ions	Q-mode Fixed Ions	B-mode H atmosphere	B-mode Free Ions	B-mode Fixed Ions
ξ [a] (°)	5	30	30	5	30	30
χ [a] (°)	3	38	38	3	38	38
Γ	2.5 ± 0.2	2.4 ± 0.2	$2.5^{+0.2}_{-0.1}$	2.3[a]	2.3[a]	2.3[a]
K^{b}_{min}	$2.3^{+0.3}_{-0.4}$	1.8 ± 0.5	$2.2^{+0.4}_{-0.2}$	1.0 ± 0.3	0.8 ± 0.3	1.0 ± 0.2
K^{b}_{max}	2.3[a]	$3.7^{+0.3}_{-0.6}$	$4.0^{+0.5}_{-0.2}$	1.0[a]	1.5 ± 0.3	1.5 ± 0.3
PF^{c}_{PL}	0.0	0.55 ± 0.11	0.46 ± 0.08	0.0	0.43 ± 0.16	0.30 ± 0.12
kT (keV)	$0.089^{+0.014}_{-0.005}$	0.23 ± 0.02	0.24 ± 0.02	$0.082^{+0.003}_{-0.009}$	$0.22^{+0.04}_{-0.01}$	0.20 ± 0.02
R^{d}_{cap} (m)	260^{+70}_{-60}	60 ± 17	55^{+5}_{-15}	170^{+45}_{-25}	38^{+7}_{-9}	60^{+20}_{-10}
B (G)	$(4.0^{+0.9}_{-0.7}) \times 10^{12}$	$(1.8 \pm 0.3) \times 10^{14}$	$> 6 \times 10^{15}$	$(2^{+2}_{-1}) \times 10^{12}$	$[1, 6] \times 10^{14}$	$> 8 \times 10^{15}$
$F^{0.5-2}_{min}$	8.9 ± 0.5	9.3 ± 0.5	9.2 ± 0.5	$4.4^{+0.4}_{-0.3}$	4.6 ± 0.3	4.5 ± 0.3
$F^{0.5-2}_{max}$	16.7 ± 0.6	17 ± 1	19 ± 1	6.9 ± 0.4	$6.9^{+0.4}_{-0.6}$	6.8 ± 0.4
χ^2_ν/dof	0.82/29	1.20/28	1.06/28	1.15/26	1.08/25	1.13/25
nhp	0.73	0.22	0.38	0.27	0.36	0.30
KS[e]	0.31	0.46	0.49	0.88	0.93	0.87

Notes. Joint fits of pn + MOS phase-resolved spectra with magnetized hydrogen atmosphere and condensed magnetized surface models. N_H is fixed to 4.3×10^{20} cm^{-2}. The fluxes, corrected for the absorption, are in units of 10^{-15} erg s^{-1} cm^{-2}. Errors and upper limits are at 1σ.
[a] Fixed value.
[b] Normalization of the power law in units of 10^{-6} photons cm^{-2} s^{-1} keV^{-1} at $E = 1$ keV.
[c] Pulsed fraction of the power-law component assuming a sinusoidal modulation.
[d] Radius of the cap for an assumed distance of 0.89 kpc.
[e] KS probability for the observed pulse profile.

hot polar cap itself supplies a significant amount of unpulsed flux, about 5 times brighter than the pulsed one. This is at variance with the results of previous analyses (confirmed here; see Table 7.4) showing that a single power law is adequate to fit the unpulsed emission [161, 266].

These problems cannot be solved adopting a model of thermal emission from polar caps with a condensed iron surface, as it could be expected in the presence of strong multipolar magnetic field components that could give a field higher up to orders of magnitude than the dipole. However, values as large as $\sim 10^{16}$ G, as obtained in the fixed ions case, seem rather unrealistic. Although the condensed iron surface model can fit well the phase-averaged spectra of both the Q- and B-modes, I faced the same problems found with the blackbody, even in the most-misaligned configuration consistent with the radio data ($\xi = 30°, \chi = 38°$). The observed pulse profiles can be reproduced only if I add in the fits a nonthermal power-law emission significantly pulsed (see Table 7.5).

For the case of a magnetized, partially ionized hydrogen atmosphere, acceptable fits to the phase-averaged spectra of the Q- and B-modes could be found for all of the geometrical configurations derived from the radio data. If only the phase-averaged spectra are considered, the fits with a hydrogen atmosphere are acceptable without the need of an additional power-law component, contrary to the case of blackbody and condensed surface models. In this case,

the absence of the power-law contribution at low energies leads to small values of interstellar absorption. The best-fit temperatures, in the range $kT = 0.10 - 0.15$ keV, are lower than those obtained with the blackbody model, as it is always the case when hydrogen model atmospheres are applied [449, e.g.]. Correspondingly, the emitting radii are larger and compatible with the expected size of the magnetic polar cap for a dipolar field, $R_{\rm PC}^{\infty} = (2\pi R^3/Pc)^{1/2}\,(1+z) \approx 215$ m (see Section 8.4 for further details). Compared to the results of Storch et al. [382] for the Q-mode, I find slightly lower best-fit temperatures and larger emitting radii (even accounting for the different distance used by these authors). Details of the models, as well as different assumptions for the star compactness, viewing geometry, and magnetic field, could possibly explain this discrepancy.

However, to fit the phase-resolved spectra an unpulsed power-law component is required in addition to the emission from the polar caps modeled with the magnetized hydrogen atmosphere. I found acceptable fits for all the considered geometrical configurations, even if the more misaligned ones are disfavored. In fact, for large ξ, I expect to see also the fan-beamed emission, that gives rise to a second peak in the pulse profile, at phase 0.5. The higher the magnetic field, the more intense the peak is. However, in the pulse profile of PSR B0943+10 this second peak is absent and this explains why the magnetic field derived with the fit is the lowest allowed in the grid. I do not expect that the match between the observed and the simulated pulse profile would improve for lower values of B that, moreover, would be inconsistent with the dipole field derived from the timing parameters of PSR B0943+10.

On the other hand, more aligned configurations predict a pulse profile with only one broad peak at phase 0, similar to the observed one. In fact, the best-fitting configuration for the Q-mode has $\xi = 5^\circ$ and $\chi = 3^\circ$, and the spectral parameters of the thermal component are $kT \approx 0.09$ keV, $R_{\rm cap} \approx 260$ m, and $B \approx 4 \times 10^{12}$ G. Remarkably, the magnetic field is fully compatible with the value at the poles derived in the dipole approximation.

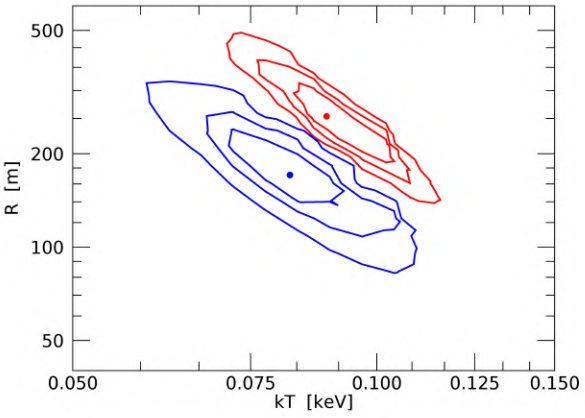

Figure 7.5: Confidence regions (1σ, 2σ and 3σ confidence levels) of the polar cap temperature and radius when PSR B0943+10 is in the Q-mode (red lines) and in the B-mode (blue lines). The spectral parameters are derived using a magnetized hydrogen atmosphere model.

The B-mode has a similar, but less pulsed, light curve. Owing to the lower counting statistics (see Table 7.2), all of the explored geometrical configurations give acceptable spectra and pulse profiles, but, using the same argument I put forward for the Q-mode, I tend to exclude the more misaligned configurations. For the most favored geometrical configuration of the Q-

mode, the best-fit B-mode parameters are $kT \approx 0.08$ keV, $R_{\rm cap} \approx 170$ m, and $B \approx 2 \times 10^{12}$ G. The confidence regions of $R_{\rm cap}$ and kT for the two radio modes are shown in Figure 7.5. It is clear that with the current data it is impossible to ascertain whether the flux difference between the two modes is due to a change in the temperature or in the size of the emitting area.

The hydrogen atmosphere model can also provide a better match with the observed PF of PSR B0943+10 than the blackbody and condensed surface models; see Figure 7.6, right panel. A similar result was recently reported for PSR B0823+26, another mode-switching pulsar with a mainly thermal spectrum and a large PF [163]. Remarkably, the best-fitting hydrogen atmosphere model for PSR B0823+26 was obtained for a geometrical configuration ($\xi = 81^\circ$ and $\chi = 66^\circ$) different from that derived from the radio data ($\xi = 81^\circ$ and $\chi = 84^\circ$).

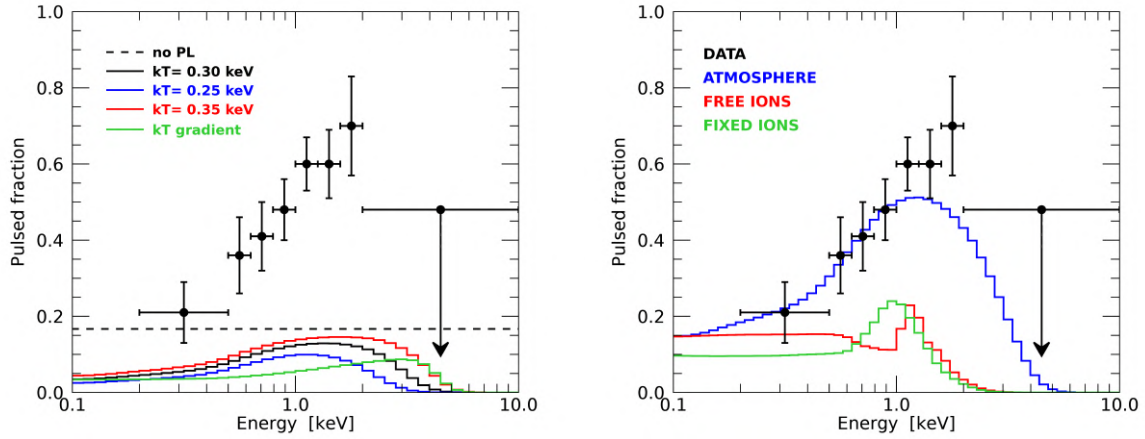

Figure 7.6: Left panel: Pulsed fraction as a function of energy computed for the case of blackbody thermal emission and the geometrical configuration of Table 7.1 producing the highest modulation ($\xi = 30^\circ$, $\chi = 38^\circ$). The dashed line is the PF expected if only the blackbody emission from the polar cap is present, while the solid lines show the PF given by a polar cap at temperatures $kT = 0.30$ keV (black), $kT = 0.25$ keV (blue), and $kT = 0.35$ keV (red) when also a nonthermal unpulsed emission is present (power law with $\Gamma = 2.6$). The pulsed fraction produced by the nonuniform temperature distribution of Eq. 3.4 is shown by the green line. The black dots indicate the observed pulsed fraction of the Q-mode. Right panel: Pulsed fraction as a function of energy computed for the case of a hydrogen atmosphere with $\xi = 5^\circ$ and $\chi = 3^\circ$ (blue line) and of a condensed iron surface with $\xi = 30^\circ$ and $\chi = 38^\circ$ in the free (red) and fixed (green) ions approximations. Different from the atmosphere model, in the condensed surface case the plotted lines refer only to the thermal contribution from the polar caps. The addition of an unpulsed power-law component would reduce the pulsed fraction. The black dots with error bars indicate the observed pulsed fraction of the Q-mode.

Chapter 8

X-ray emission from old pulsars

Here, I report the analysis of seven old and X-ray dim RPPs for which the ML analysis was applied. The seven RPPs have characteristic ages in the range $0.3 - 8$ Myr; see Table B.1 for further information about their timing properties. They are typical old RPPs that, in some cases, show radio variability phenomena, as subpulse drifting and nulling (see Section 2.3). In the X-rays, they are too old to emit thermal radiation from the whole cooling surface, but they could have a hot thermal component due to polar cap reheating (see Section 3.4).

Four of them had archival *XMM-Newton* data and already published analysis (PSR B0628−28, PSR B0919+06, PSR B0114+58 and PSR B1133+16). For them, the presence of the thermal component was uncertain or poorly constrained; the other three were observed for the first time with *XMM-Newton* in 2018 (PSR J1154−6250, PSR B0450−18 and PSR B1818−04). The analysis presented here was also reported in Rigoselli & Mereghetti [356], Igoshev et al. [188].

8.1 The sample

8.1.1 PSR B0628−28

The $\sim$3 Myr old PSR B0628−28 is the closest pulsar in this sample. Its distance of $0.32^{+0.05}_{-0.04}$ kpc is accurately known thanks to a radio VLBI parallax measurement [82, 422]. In the radio band, PSR B0628−28 sporadically shows drifting subpulses with $P_3 = 7 \pm 1$ [432].

A faint soft X-ray source positionally consistent with PSR B0628−28 was first seen in *ROSAT* data [30], but only thanks to the more accurate localization obtained with *Chandra*, and with the detection of X-ray pulsations with *XMM-Newton*, its association with the pulsar was confirmed [401, 31]. These authors pointed out that PSR B0628−28, with an X-ray efficiency of ~ 0.16, seemed to be "overluminous" compared to other pulsars. However, this resulted from their use of the distance of 1.45 kpc derived from the pulsar dispersion measure, which is now superseded by the more precise parallactic value that gives a smaller distance.

Previous analyses of the X-ray spectrum of PSR B0628−28 indicated that a single blackbody is statistically rejected, while a good fit is obtained with a power law, although slightly different values of the photon index were reported. Using *XMM-Newton* data, Becker et al. [31] found a photon index $\Gamma = 2.63^{+0.22}_{-0.15}$, while Tepedelenlıoğlu & Ögelman [401], simultaneously fitting the *XMM-Newton* and *Chandra* spectra, obtained $\Gamma = 3.20^{+0.26}_{-0.23}$.

Although the single power law provided a good fit, these authors considered also a power law plus blackbody model. In this case the best fits resulted in slightly harder power laws

and in the following parameters for the blackbody: $kT = 0.25^{+0.05}_{-0.04}$ keV and $R = 15^{+7}_{-6}$ m [31], $kT = 0.28^{+0.11}_{-0.05}$ keV and $R = 13^{+14}_{-10}$ m [401] (I rescaled the radii for the new distance of 0.32 kpc).

8.1.2 PSR B0919+06

The pulsed radio emission of PSR B0919+06 was first recorded in the second Molonglo pulsar survey [248]. By measuring the parallax of this pulsar, Verbiest et al. [422] derived a distance of $1.1^{+0.2}_{-0.1}$ kpc. This pulsar exhibits an "emission shift" of the brighter subpulses [347]. This behaviour is not a subpulse drift nor a conventional mode change, but it occurs on a fairly regular basis of approximately 700 rotation periods [427]. Some authors speculate that the shifting is the result of changes in absorption and/or altitude of emission region [347]. Other explanations that have been proposed include the presence of a companion star [427], or a fairly rapid change in tilt of the pulsar carousel [437].

XMM-Newton first revealed the faint X-ray counterpart of PSR B0919+06 [336]. Its spectrum was fitted well by a power law with photon index $\Gamma = 2.3^{+0.8}_{-0.4}$, while a single blackbody fit was rejected.

8.1.3 PSR B0114+58

PSR B0114+58 is the most distant pulsar in this sample ($d = 1.77 \pm 0.53$ kpc, [439]), but also the one with the largest spin-down power. It was discovered in the Princeton-NRAO pulsar survey [381], and an X-ray counterpart was first reported by Prinz & Becker [336] with *XMM-Newton*. They obtained a poorly constrained spectrum, which could be fitted equally well by a power law with $\Gamma = 3.3 \pm 0.5$ or by a blackbody with temperature $kT = 0.18 \pm 0.03$ keV and emitting radius $R = 322 \pm 161$ m (for $d = 1.77$ kpc).

8.1.4 PSR J1154−6250

PSR J1154−6250 is the oldest pulsar of this sample, with a characteristic age of about 8 Myr. The dispersion measure corresponds to a distance of 1.36 kpc. It was discovered in the Parkers multibeam pulsar survey [216], and it was observed in the X-rays for the first time with *XMM-Newton* in February 2018.

8.1.5 PSR B0450−18 and PSR B1818−04

PSR B0450−18 and PSR B1818−04 are two pulsars of about 1.5 Myr that were observed in September 2018 with *XMM-Newton*. Their distances, obtained with parallax measurements and corrected for the Lutz-Kelker bias, are $0.4^{+0.2}_{-0.1}$ kpc for PSR B0450−18 and $0.3^{+0.6}_{-0.2}$ kpc for PSR B1818−04 [64, 422]. These distances are reliable and supersede those derived from their dispersion measure, which have to assume a model of the electron distribution in the Galaxy and would place them at ~ 3 kpc [439]. The close distance of PSR B0450−18 has also been demonstrated by the analysis of its pulse broadening due to interstellar scattering, which gives a distance in agreement with the parallactic value but not with the DM one [338]. PSR B0450−18 is mostly known because it displays a long-term periodicity in its spin-down rate [240, 191].

8.1.6 PSR B1133+16

PSR B1133+16 is a $\sim$5 Myr old, nearby radio pulsar at a parallactic distance of 0.35 ± 0.02 kpc [422]. It has one of the largest proper motions among the known pulsars, $\mu_\alpha = (-73.95 \pm 0.38)$ mas yr^{-1} and $\mu_\delta = (368.05 \pm 0.27)$ mas yr^{-1}, which corresponds to a transverse velocity $V_\perp \simeq$ 630 km s^{-1} [52].

In the radio band, PSR B1133+16 shows a double-peaked pulse profile and drifting subpulses, with a circulation period of approximately 30 rotation periods [160]. It is known to spend $\simeq$ 15% of the time in a null state, in which it does not emit radio pulses [39]. The nulls are not randomly distributed but show exactly the same periodicity of the subpulses [160]. Moreover, PSR B1133+16 was found to produce broad-band giant pulses about 1% of the time [217].

PSR B1133+16 has both optical [458, 457] and X-ray [199] counterparts. According to these works, its X-ray spectrum can be described by either a power law or a blackbody (or a combination of them), but the statistics is too poor to distinguish between these models. Recently, Szary et al. [392] found that a power law with $\Gamma \approx 2.5$ describes the spectrum reasonably well, but the addition of a blackbody with $T = 0.25^{+0.05}_{-0.03}$ keV and a radius of 14^{+7}_{-5} m (for $d = 350$ pc) is also consistent with the data.

8.2 Observations and data reduction

The journal of *XMM-Newton* observations for each source is presented in Table 8.1. Note that while the pn time resolution was adequate to reveal the pulsations in all the targets, this is not true for the MOS data, except in the case of PSR B1133+16 (see Section 5.1.1). The data reduction and analysis were done using version 15 of the Science Analysis System (SAS)[1] and XSPEC (ver. 12.8.2) for the spectral fits.

I reprocessed the pn data using the SAS task EPREJECT to reduce the detector noise at the lowest energies. I then removed the time intervals of high background by rejecting all the periods with a pn count rate higher than 1.0 cts s^{-1} in the range $10 - 12$ keV. In the case of PSR J1154−6250, PSR B0450−18 and PSR B1818−04 I applied the ML analysis on both cleaned and uncleaned data, obtaining consistent results, with smaller errors on the uncleaned data because of the larger statistics. The resulting net exposure times for each pulsar are indicated in Table 8.1.

I used pn and MOS spectra, obtained as described in Section 5.3.2: the energy bins are chosen in such a way to have a significant detection, that means at least 20 counts per bin and a significance greater than 5 for relatively bright sources (PSR B0628−28, PSR B0919+06 and PSR B1133+16), or than 2.5 for dimmer sources (PSR B0114+58 and PSR J1154−6250). In order to obtain a well-determined background, I also required a ratio between the background value and its error greater than the above defined significance thresholds. In the highest energy bin, if these criteria were not satisfied, I adopted the upper energy boundary yielding the largest source significance, or the best upper limit.

In the case of PSR B0450−18 and PSR B1818−04, I could not extract a spectrum due to their faintness. For these sources, I converted the count rate into a flux with the use of the HEASOFT tools WEBPIMMS. I assumed a power-law spectrum with photon index $\Gamma = 2.5$, as the majority of the RPPs of the same age [324].

[1] http://www.cosmos.esa.int/web/xmm-newton/sas.

Table 8.1: Journal of *XMM-Newton* observations of the examined RPPs.

Pulsar Name	Obs. ID	Start time UT	End time UT	Effective Exposure (ks) Operative Modes[a] Filter		
				pn	MOS1	MOS2
PSR B0114+58	0112200201	2002 Jul 09 19:53:07	2002 Jul 09 22:23:28	5.40	5.95	5.97
				FW	FW	FW
				med	med	med
PSR B0450−18	0821890201	2018 Sep 15 17:27:18	2018 Sep 16 03:58:58	29.95	35.90	35.9
				FW	FW	FW
				thin	thin	thin
PSR B0628−28	0206630101	2004 Feb 28 02:19:26	2004 Feb 28 15:51:17	42.15	44.67	44.69
				PLW	FW	FW
				thin	med	med
PSR B0919+06	0502920101	2007 Nov 09 22:16:34	2007 Nov 10 09:45:10	24.07	25.61	25.63
				PLW	FW	FW
				thin	thin	thin
PSR B1133+16	0741140201	2014 May 25 12:18:42	2014 May 25 19:20:22	17.69	19.22	19.22
	0741140301	2014 May 31 11:34:51	2014 May 31 17:58:11	17.91	19.42	19.42
	0741140401	2014 Jun 14 07:47:26	2014 Jun 14 18:20:46	30.95	33.68	33.69
	0741140501	2014 Jun 22 07:22:13	2014 Jun 22 17:02:13	28.53	30.92	30.92
	0741140601	2014 Jun 28 10:58:52	2014 Jun 28 17:55:32	19.74	21.41	21.41
				FW	SW	SW
				thin	thin	thin
PSR J1154−6250	0804240201	2018 Feb 08 01:11:59	2018 Feb 08 18:10:02	49.95	58.90	58.90
				FW	FW	FW
				thin	thin	thin
PSR B1818−04	0821890101	2018 Sep 24 18:16:26	2018 Sep 25 03:26:26	25.75	31.16	31.16
				FW	FW	FW
				thin	thin	thin

Notes. [a] PLW = Prime Large Window (43 ms); FW = Full Window (pn 73 ms, MOS 2.6 s); SW = Small Window (0.3 s).

8.3 Results

As discussed in each section, the spectral analysis of the seven sources gave a poorly constrained absorption column density $N_{\rm H}$. Therefore, I compared and/or fixed it to the value inferred from the dispersion measure DM of radio pulses (see Eq. 1.25) of each pulsar. In fact, as discussed in Section 1.4.2, He et al. [154] found the correlation $N_{\rm H} \sim 0.3$ DM (with $N_{\rm H}$ in units of 10^{20} cm^{-2}), that moreover implies a 10% ionization of the interstellar medium. Figure 8.1 shows the best-fit parameters of the spectral analysis of PSR B0628−28, PSR B0919+06, PSR B0114+58 and PSR J1154−6250, and their DM-based value of $N_{\rm H}$.

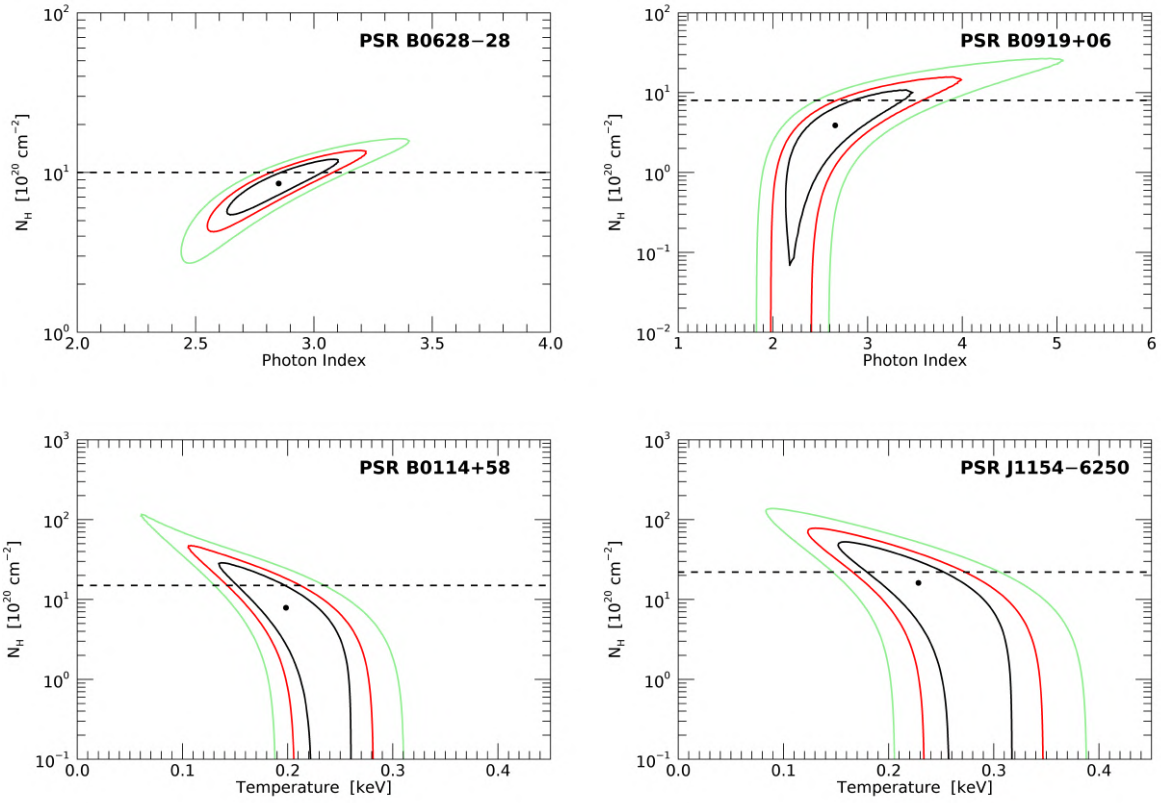

Figure 8.1: Confidence regions (1, 2, and 3 σ) of the best fit parameters for the spectra of (a) PSR B0628−28, (b) PSR B0919+06, (c) PSR B0114+58, and (d) PSR J1154−6250. The best fit values are indicated by a black dot and the DM-based value of $N_{\rm H}$ by a dashed line.

8.3.1 PSR B0628−28

I applied the ML analysis to a circular region of radius 60″ centered at R.A. = $06^{\rm h}\ 30^{\rm m}\ 51^{\rm s}.01$, Dec. = $-28^\circ\ 35'\ 06''.8$. In the energy range $0.3 - 10$ keV, this yielded 1021 ± 40 source counts in the pn and 527 ± 28 in the MOS, corresponding to a total count rate of $(4.0 \pm 0.1) \times 10^{-2}$ cts s^{-1}.

The spectral analysis was carried out in 20 energy bins for the pn and in 13 for the MOS. The two spectra were fitted simultaneously. Among single-component models, an absorbed power law gave the best fit with $\Gamma = 2.8 \pm 0.1$ and $N_{\rm H} = (7.7 \pm 2.1) \times 10^{20}$ cm^{-2} ($\chi^2_\nu = 0.71$ for 30 dof). The error regions of the parameters are shown in Figure 8.1 (a). A fit with a single blackbody

was not acceptable ($\chi^2_\nu = 4.14$ for 30 dof).

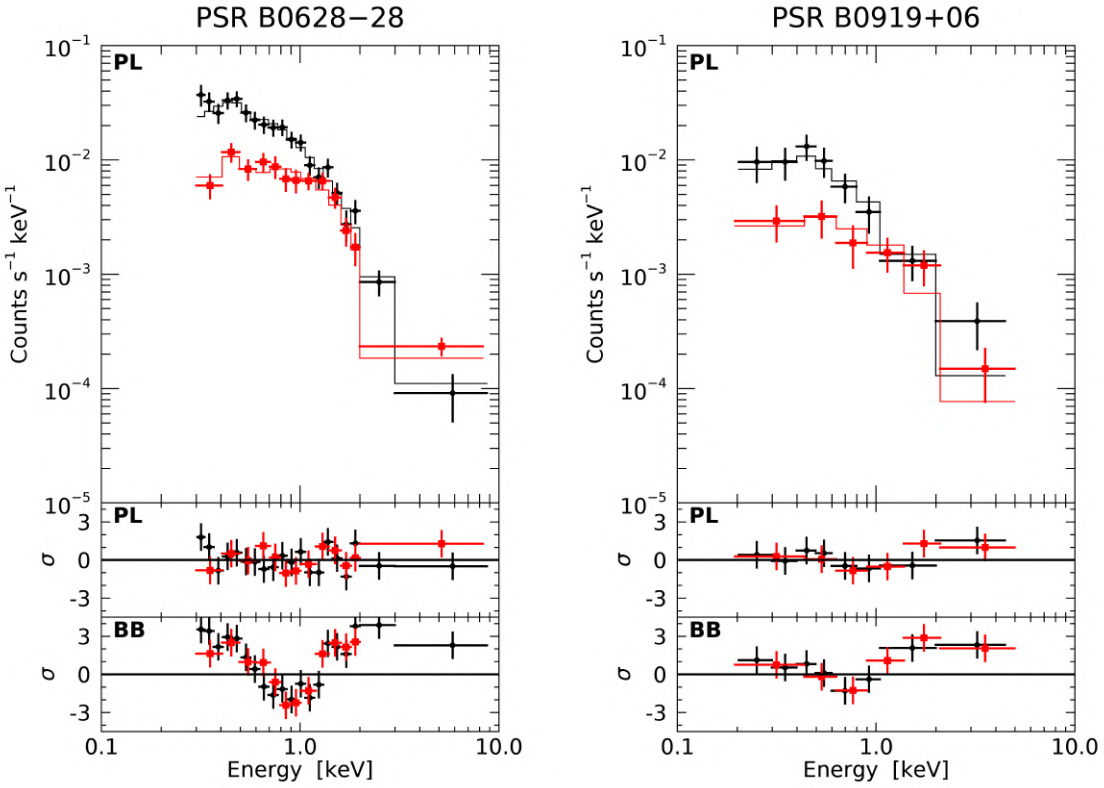

Figure 8.2: EPIC-pn (black diamonds) and -MOS (red squares) X-ray spectra of PSR B0628−28 (left panel) and of PSR B0919+06 (right panel). For each pulsar, the best-fit power law is shown in the top panel, and the corresponding residuals in the middle panel. The bottom panel shows the residuals obtained by fitting the spectra with an absorbed blackbody.

The best fit $N_{\rm H}$ is within 1σ of the value derived from the DM of 10^{21} cm^{-2}. Fixing $N_{\rm H}$ to this value, I get tighter constraints on the photon index, $\Gamma = 2.95 \pm 0.06$. The corresponding unabsorbed flux in the $0.2 - 10$ keV energy range is $F_{0.2-10} = (1.09 \pm 0.05) \times 10^{-13}$ erg s^{-1} cm^{-2}. The best-fit power-law spectrum, together with its residuals and those of the blackbody fit are shown in Figure 8.2, left panel, while the spectral parameters are listed in Table 8.2.

Using a power-law plus blackbody model I found that several combinations of blackbody temperature and normalization, which give only a limited flux contribution, are consistent with the data. The best-fit photon index is $\Gamma = 2.92 \pm 0.07$, while the blackbody parameters are poorly constrained: therefore, I derived an upper limit on its intensity as follows. I fitted the spectrum with a power-law plus backbody model ($N_{\rm H}$ fixed to 10^{21} cm^{-2}) and computed the 3σ confidence ranges of the blackbody normalization and temperature, leaving the power-law parameters free to vary. The results are shown in Figure 8.3, left panel; the upper panel refers to the emitting radius and the lower panel to the bolometric luminosity. The latter has been computed as $L_{\rm bol} = \pi R^2 \sigma T^4$ because the emission from a hot spot is being considered.

To investigate the spectral properties of the pulsed and unpulsed emission, I performed a 3D-ML analysis (see Section 5.3.2) on the pn data in seven energy bins in the range $0.3 - 10$ keV. The phases of the detected counts were computed using the period at the epoch of the *XMM-Newton* observation, $P = 1.2444225976(2)$ s, obtained from the ephemeris reported in the online

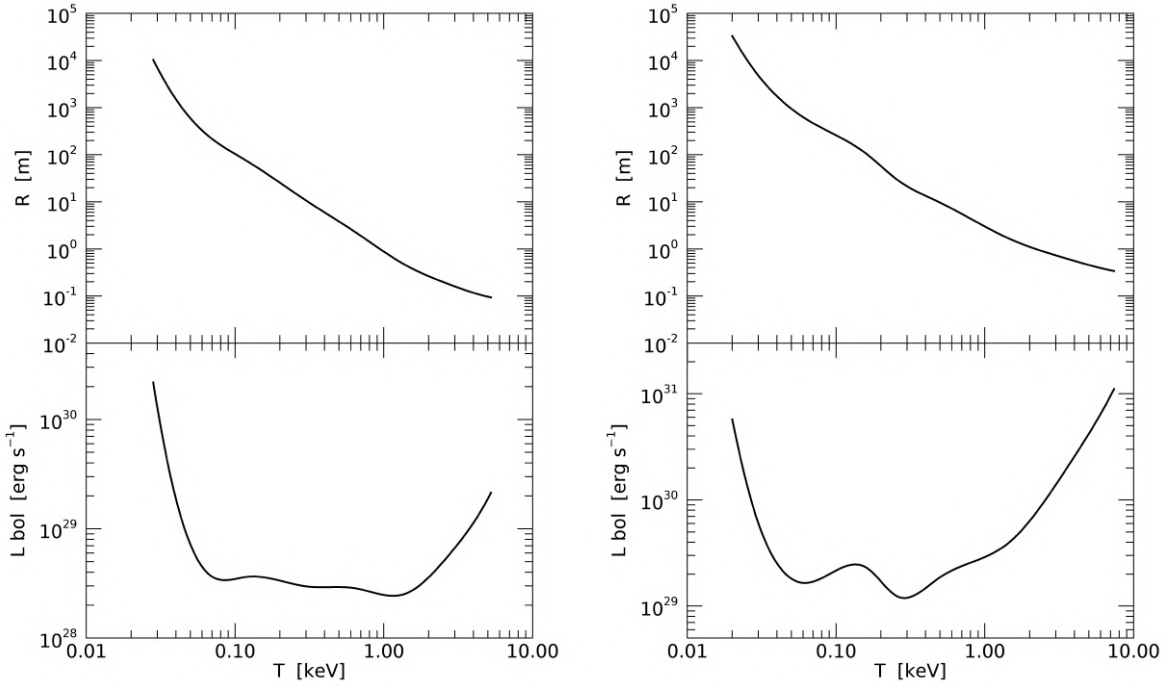

Figure 8.3: Upper limits (3σ confidence level) on the blackbody component in PSR B0628−28 (laft panel) and in PSR B0919+06 (right panel) spectra as a function of blackbody temperature. For each pulsar, the top panel gives the limits on the emitting radius, while the lower panel gives the corresponding limits on the bolometric luminosity computed as $L_{\rm bol} = \pi R^2 \sigma T^4$.

ATNF Pulsar Catalogue [249]. The pulsed fraction is higher in the $0.40 - 0.65$ keV range, with an average value of 0.46 ± 0.05, and decreases at lower and higher energies (Figure 8.4, left panel). The energy dependence of the pulsed fraction is also reflected in the different shape of the pulsed and unpulsed spectra (Figure 8.4, right panel). The unpulsed spectrum is fitted well by a power law with the same slope as that of the total spectrum, while that of the pulsed emission requires a significantly steeper power law or a blackbody with $kT = 0.10^{+0.02}_{-0.01}$ keV and $R = 150^{+80}_{-50}$ m (see Table 8.2).

8.3.2 PSR B0919+06

The ML analysis of PSR B0919+06 was carried out in a circular region with radius of $45''$ centered at R.A. = $09^{\rm h}\ 22^{\rm m}\ 14^{\rm s}.20$, Dec. = $+06^\circ\ 38'\ 33''.7$. In the energy range $0.2 - 10$ keV I obtained 223 ± 25 (pn) and 91 ± 15 (MOS) source counts, corresponding to a total count rate of $(1.3 \pm 0.1) \times 10^{-2}$ cts s^{-1}.

I simultaneously fitted the pn (eight energy bins) and the MOS (seven energy bins) spectra. The single-component model that best fits the data is an absorbed power law (see Fig. 8.1 (b)). The single blackbody model is statistically unacceptable ($\chi^2_\nu = 2.16$ for 11 dof). Fixing the absorption to the DM-based value 8×10^{20} cm^{-2}, I obtained $\Gamma = 3.1 \pm 0.2$ and an unabsorbed flux $F_{0.2-10} = (3.1 \pm 0.4) \times 10^{-14}$ erg s^{-1} cm^{-2}. Figure 8.2, right panel, shows the comparison between the power-law and the blackbody best fits, while Table 8.2 summarizes all the obtained results.

Although a good fit is also obtained with a power law plus blackbody, the blackbody pa-

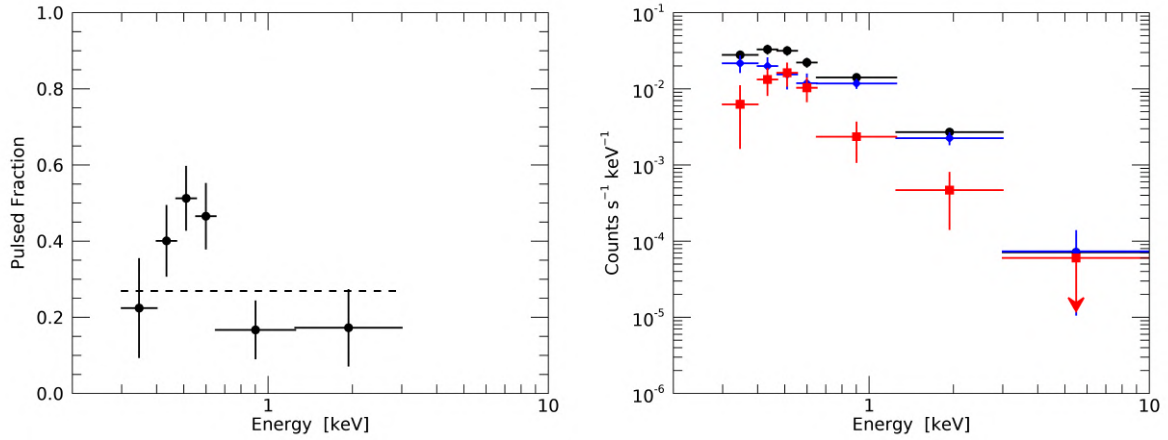

Figure 8.4: Left panel: Pulsed fraction of PSR B0628−28 as a function of energy obtained with the 3D-ML analysis. Right panel: EPIC-pn total (black circles), unpulsed (blue diamonds), and pulsed (red squares) spectra of PSR B0628−28.

rameters are not well constrained. Therefore, as done for PSR B0628−28, I derived the upper limits on its intensity as a function of kT, which is shown in Figure 8.3, right panel.

8.3.3 PSR B0114+58

I applied the ML analysis in a circular region centered at R.A. = $01^{\rm h}\ 17^{\rm m}\ 38^{\rm s}.24$, Dec. = $+59^\circ\ 15'\ 07''.8$ with a radius of $60''$, from which I excluded a circle centered in R.A. = $01^{\rm h}\ 17^{\rm m}\ 34^{\rm s}.87$, Dec. = $+59^\circ\ 15'\ 15''.4$ with a radius of $20''$ to avoid a nearby source. This resulted in 92 ± 13 pn counts and 42 ± 9 MOS counts in the range $0.2 - 4$ keV, corresponding to a total count rate of $(2.3 \pm 0.3) \times 10^{-2}$ cts s^{-1}. PSR B0114+58 is extremely soft and above 4 keV the source detection was below the significance threshold.

I simultaneously fit the pn (six energy bins) and the MOS spectra (four energy bins) with a single absorbed component model, and it was impossible to discriminate between a power law ($\chi^2_\nu = 0.34$ for 7 dof) and a blackbody ($\chi^2_\nu = 0.45$ for 7 dof). However, the photon index of the power law is unusually steep and the column absorption higher compared to the DM value of 1.5×10^{21} cm^{-2}; on the contrary, the blackbody fit gave consistent results (see Table 8.2 for the spectral parameters and Figure 8.1 (c)).

I fixed the $N_{\rm H}$ to the DM-based value and I found that the blackbody is preferred: $\chi^2_\nu = 0.50$ for 8 dof, compared to $\chi^2_\nu = 0.86$ for the power law (see Figure 8.5, left panel, especially the modulation of the pn-spectrum residuals). The best fit temperature is $kT = 0.17 \pm 0.02$ keV, the radius of the emitting area is $R = 405^{+110}_{-90}$ m, and the $0.2 - 10$ keV unabsorbed flux is $F_{0.2-10} = (4.8 \pm 0.7) \times 10^{-14}$ erg s^{-1} cm^{-2}. The corresponding bolometric luminosity is $L_{\rm bol} = \pi R^2 \sigma T^4 = (4.4 \pm 2.9) \times 10^{30}$ erg s^{-1}. The small emitting area indicates that the thermal radiation comes from a hot spot on the stellar surface, most likely from the polar cap; in fact, the expected polar cap radius for PSR B0114+58 is $R^\infty_{\rm PC} \approx 700$ m (see Section 8.4).

8.3.4 PSR J1154−6250

I applied the ML in a circular region positioned to avoid the gaps between the CCD chips (radius of $60''$, center at R.A. = $11^{\rm h}\ 54^{\rm m}\ 23^{\rm s}.2$, Dec. = $-62^\circ\ 49'\ 47''$). For the spectral extraction

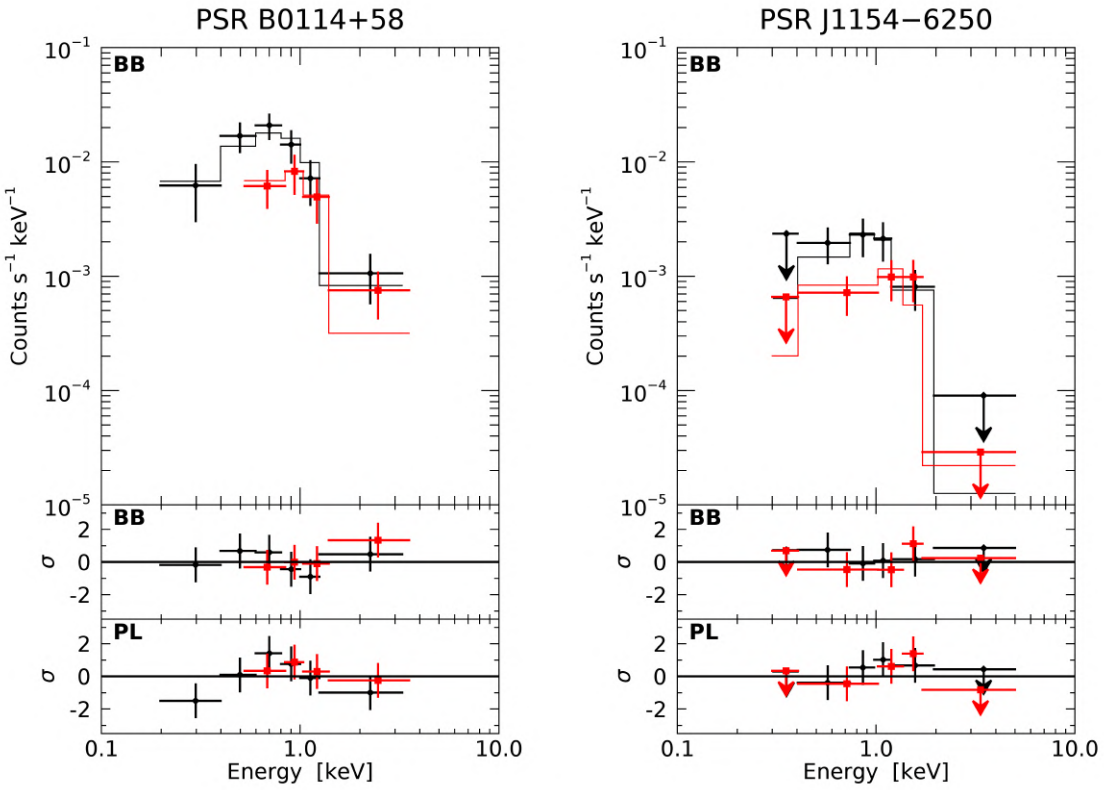

Figure 8.5: EPIC-pn (black diamonds) and -MOS (red squares) X-ray spectra of PSR B0114+58 (left panel) and of PSR J1154−6250 (right panel). For each pulsar, the best-fit blackbody is shown in the top panel, and the corresponding residuals in the middle panel. The bottom panel shows the residuals obtained by fitting the spectra with an absorbed power law.

I fixed the source position at the coordinates found by the ML in the pn+MOS image in the $0.4-2$ keV range (R.A. $= 11^{\rm h}\ 54^{\rm m}\ 20^{\rm s}.4$, Dec. $= -62^{\circ}\ 50'\ 04''.4$).

In the energy range $0.4-2$ keV the source was detected with 113 ± 21 counts (pn) and 66 ± 15 counts (MOS), which correspond to a total count rate of $(3.4 \pm 0.5) \times 10^{-3}$ cts s^{-1}. In this energy range, I obtained four energy bins for the pn and three for the MOS. Below 0.4 keV and above 2 keV, the source detection was below the significance threshold; therefore I derived upper limits on the source counts in these energy bins.

As I found for PSR B0114+58, the soft spectrum of PSR J1154−6250 is well fitted by a steep power law with high interstellar absorption, or by a hot blackbody with a small radius (see Table 8.2 for the spectral parameters and Figure 8.1 (d)).

I fixed the absorption column to the DM-based value of 2.2×10^{21} cm^{-2}. With a power-law model I find a rather high photon index value $\Gamma = 3.4 \pm 0.3$, but still compatible with the range of $\Gamma = 2-4$ noticed by Posselt et al. [324]. The unabsorbed flux is $F_{0.2-10} = (2.5^{+0.8}_{-0.6}) \times 10^{-14}$ erg s^{-1} cm^{-2}. For the blackbody model I obtained a temperature $kT = 0.21 \pm 0.02$ keV and a radius of the emitting region $R = 82 \pm 21$ m, which give an absorbed flux $F_{0.2-10} = (7.8 \pm 1.3) \times 10^{-15}$ erg s^{-1} cm^{-2} and a bolometric luminosity $L_{\rm bol} = \pi R^2 \sigma T^4 = (4.2 \pm 2.7) \times 10^{29}$ erg s^{-1}. Both the power law and the blackbody fit well the spectrum of PSR J1154−6250, as it can be seen in Figure 8.5, right panel, but the blackbody spectrum is statistically preferred ($\chi^2_\nu = 0.34/9$ versus $\chi^2_\nu = 1.00/9$).

Table 8.2: Spectral parameters of PSR B0628−28, PSR B0919+06, PSR B0114+58 and PSR J1154−6250.

Model	$N_{\rm H}$ 10^{20} cm^{-2}	Γ	PL Norm [a]	kT keV	$R_{\rm BB}^{\rm b}$ m	$F_{0.2-10}^{\rm unabs}$ erg s^{-1} cm^{-2}	χ^2_ν/d.o.f.	nhp
PSR B0628−28								
PL	7.7 ± 2.1	2.8 ± 0.1	13 ± 1	...	...	9.1 ± 1.3	0.71/30	0.88
BB	...	...	...	...	...	...	4.14/30	2×10^{-13}
PL	10[c]	2.95 ± 0.06	14.3 ± 0.5	...	...	10.9 ± 0.5	0.72/31	0.87
BB	10[c]	...	...	...	...	...	6.00/31	5×10^{-24}
PL unpulsed[d]	10[c]	2.7 ± 0.2	11 ± 1	...	...	7.3 ± 0.7	0.64/5	0.67
PL pulsed[d]	10[c]	$3.8^{+0.6}_{-0.5}$	3 ± 1	...	...	5^{+2}_{-1}	0.93/5	0.46
BB pulsed[d]	10[c]	...	...	$0.10^{+0.02}_{-0.01}$	150^{+80}_{-50}	$2.4^{+0.6}_{-0.5}$	0.75/5	0.59
PSR B0919+06								
PL	$2.7^{+3.5}_{-2.4}$	2.5 ± 0.3	3.2 ± 0.4	...	...	$1.9^{+0.7}_{-0.3}$	0.55/11	0.87
BB	...	...	...	...	...	...	2.16/11	0.01
PL	8[c]	3.1 ± 0.2	3.7 ± 0.5	...	...	3.1 ± 0.4	0.67/12	0.79
BB	8[c]	...	...	...	...	...	2.47/12	3×10^{-3}
PSR B0114+58								
PL	45 ± 17	5.3 ± 1.2	33^{+40}_{-15}	...	...	$[10^{-12.4}, 10^{-10.1}]$	0.34/7	0.94
BB	$6.3^{+9.7}_{-5.9}$	...	...	0.21 ± 0.04	220^{+220}_{-80}	$3.0^{+2.2}_{-0.8}$	0.45/7	0.87
PL	15[c]	3.2 ± 0.2	12 ± 1	...	...	10 ± 2	0.86/8	0.55
BB	15[c]	...	...	0.17 ± 0.02	405^{+110}_{-90}	4.8 ± 0.7	0.50/8	0.86
PSR J1154−6250								
PL	80^{+44}_{-29}	6.4 ± 1.6	15^{+38}_{-9}	...	...	$[10^{-12.5}, 10^{-9.1}]$	0.45/8	0.89
BB	17 ± 14	...	...	0.23 ± 0.05	67^{+101}_{-45}	$0.62^{+0.89}_{-0.26}$	0.37/8	0.94
PL	22[c]	3.4 ± 0.3	2.3 ± 0.3	...	...	$2.5^{+0.8}_{-0.6}$	1.00/9	0.43
BB	22[c]	...	...	0.21 ± 0.02	82 ± 21	0.78 ± 0.13	0.34/9	0.96

Notes. Joint fits of pn + MOS spectra of the listed RPPs. Errors at 1σ. The fluxes, corrected for the absorption, are expressed in units of 10^{-14} erg s^{-1} cm^{-2}.
[a] Normalization of the power law in units of 10^{-6} photons cm^{-2} s^{-1} keV^{-1} at $E = 1$ keV.
[b] Blackbody radii evaluated for the proper distances.
[c] Fixed value.
[d] pn spectrum only.

8.3.5 PSR B0450−18 and PSR B1818−04

In the analysis of PSR B0450−18, I applied the ML analysis to a circular region of radius 45″ centered at the pulsar radio position, R.A. = $04^{\rm h}\ 52^{\rm m}\ 34^{\rm s}.106$, Dec. = $-17^\circ\ 59'\ 23''.37$. The source was best detected in the energy range $0.3 - 2$ keV, in the position R.A. = $04^{\rm h}\ 52^{\rm m}\ 34^{\rm s}.0$, Dec. = $-17^\circ\ 59'\ 23''.4$, that is only 0.4σ distant from the radio position. I collected 55 ± 15 net counts in the sum of pn and MOS cameras at 3.1σ of significance ($0.3 - 2$ keV energy range), that corre-

spond to a count rate of $(1.7 \pm 0.5) \times 10^{-3}$ cts s^{-1}. The small amount of source counts makes impossible the extraction of a spectrum, thus I used the HEASOFT tools WEBPIMMS in order to estimate the source flux as described in Section 8.2 (an absorbed power law with $\Gamma = 2.5$ and $N_{\rm H} = 10^{21}$ cm^{-2}): I derived a flux corrected for the absorption $F_{0.2-10} \approx (7.8 \pm 2.3) \times 10^{-15}$ erg s^{-1} cm^{-2}, that for a distance of $0.4^{+0.2}_{-0.1}$ pc leads to a luminosity $L_{0.2-10} \approx 1.5^{+1.7}_{-0.6} \times 10^{29}$ erg s^{-1} and $L_{2-10} = 3.0^{+3.4}_{-1.2} \times 10^{28}$ erg s^{-1}. For a $\dot{E} = 1.4 \times 10^{33}$ erg s^{-1}, this value corresponds to $\eta_{2-10} = L_{2-10}/\dot{E} \approx 2 \times 10^{-5}$ that makes PSR B0450−18, along with PSR J2043+2740 [32], the old RPPs with the lowest nonthermal efficiency (see Figure 3.8).

For what concerns PSR B1818−04, I applied the ML analysis to a circular region of radius 40″ centered at the pulsar radio position, R.A. = 18$^{\rm h}$ 20$^{\rm m}$ 52$^{\rm s}$.610, Dec. = −4° 27′ 38″.12. At this position, in the energy range $0.3 - 2$ keV, I barely detected (1.5σ) a point source with 32 ± 17 counts (sum of pn and MOS cameras, $0.3 - 2$ keV energy range). I do not consider this as a significant detection and therefore I evaluated a 3σ upper limit of 3×10^{-3} cts s^{-1} that, with the same assumption of PSR B0450−18, leads to an unabsorbed flux $F_{0.2-10} < 1.4 \times 10^{-14}$ erg s^{-1} cm^{-2} and a luminosity $L_{0.2-10} < 6 \times 10^{29}$ erg s^{-1}, $L_{2-10} < 1.2 \times 10^{29}$ erg s^{-1}. The corresponding nonthermal efficiency is $\eta_{2-10} < 10^{-4}$.

8.3.6 PSR B1133+16

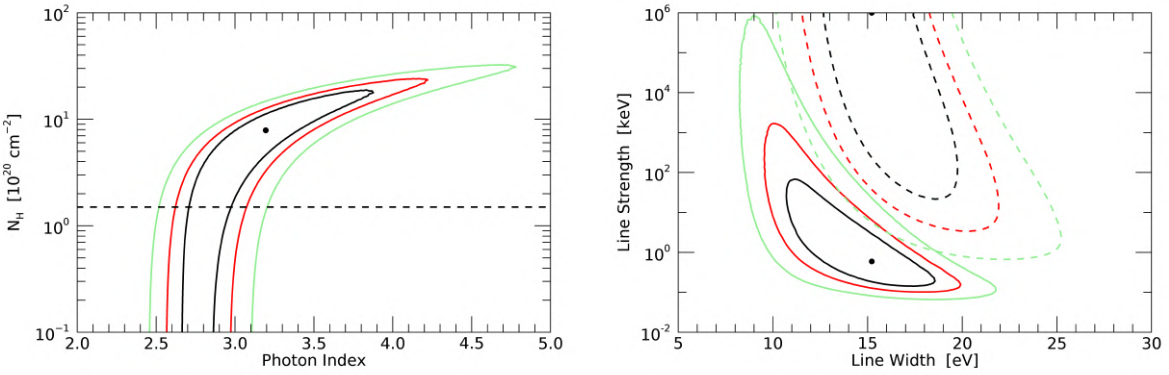

Figure 8.6: Left panel: Confidence regions (1, 2, and 3 σ) of the best-fit photon index vs. interstellar absorption of PSR B1133+16 spectrum. The best fit value is indicated by a plus and the DM-based value of $N_{\rm H}$ by a dashed line. Right panel: Confidence regions of the best-fit line strength vs. width of the two absorption lines in the spectrum of PSR B1133+16 (dashed lines: $E_1 \sim 0.22$ keV, solid lines: $E_2 \sim 0.44$ keV). The best fit values are indicated by a black dot.

PSR B1133+16 was observed with five separate pointings over a time of about one month. I verified that the analysis of the single observations gave fully consistent results. Therefore, I report only those obtained by combining the five pointings to extract a single pn and a single MOS spectrum. I applied the ML analysis in a circular region of radius 35″ and centered at R.A. = 11$^{\rm h}$ 36$^{\rm m}$ 02$^{\rm s}$.527, Dec. = 15° 50′ 59″.90. I detected the source with a count rate of $(1.06 \pm 0.05) \times 10^{-2}$ cts s^{-1} in the energy range $0.2 - 10$ keV. For the spectral analysis the 887 ± 46 pn and 363 ± 29 MOS counts were divided into 19 and 11 energy bins, respectively.

The pn and the MOS spectra were fitted simultaneously. I could not obtain acceptable fits with a single power law or blackbody, or any combination of the two because in all cases significant residuals were present below 0.5 keV. It is very unlikely that this was due to an

instrumental or calibration problem because the spectra of two nearby soft and very bright sources do not show similar features. The χ^2_ν and the nhp for each of these test are listed in the first part of Table 8.3.

Excluding the energy channels below 0.5 keV, I was able to obtain a good fit with an absorbed power law with photon index $\Gamma = 3.2 \pm 0.4$ and $N_{\rm H} = (7.9 \pm 6.3) \times 10^{20}$ cm^{-2} (Figure 8.6, left panel). With $N_{\rm H}$ fixed to the DM-based value of 1.5×10^{20} cm^{-2} I obtained a photon index of 2.8 ± 0.1 ($\chi^2_\nu = 0.82$, for 18 dof). A blackbody fit was rejected ($\chi^2_\nu \approx 2$ both for free and fixed $N_{\rm H}$).

A power-law fit of the pn spectrum over the whole energy range suggests the presence of two absorption lines at ~ 0.2 keV and ~ 0.44 keV. Therefore I fitted it with a model consisting of a power law with $N_{\rm H}$ fixed to 1.5×10^{20} cm^{-2} and two Gaussian absorption lines. The lines were constrained to be centered at $E_2 = 2 \times E_1$ and to have the same width $\sigma_1 = \sigma_2$. This model gave a good fit with $E_1 = 0.222 \pm 0.006$ keV and $\sigma_1 = 0.015^{+0.012}_{-0.004}$ keV ($\chi^2_\nu = 0.78$ for 13 dof). The best fit photon index is 2.9 ± 0.2, in good agreement with that found in the hardest part of the spectrum. The strength of the lines are poorly constrained, but they are 3σ above the 0 level (see Figure 8.6, right panel). The best fit spectrum, together with its residuals and those of the single power-law fit are shown in Figure 8.7.

If the lowest energy line is an electron cyclotron feature, the implied magnetic field ($B_e = 1.9 \times 10^{10}(1+z)$ G) is two orders of magnitude smaller than the surface field derived from the timing parameters of the pulsar ($B_{\rm s} = 2.1 \times 10^{12}$ G, under the usual dipole approximation). The electrons responsible for the feature should be high in the magnetosphere, and it is unclear how they could be confined in a small region with the appropriate magnetic field value. Alternatively, if the line is attributed to protons that could be in the atmosphere close to the NS surface, the required magnetic field is $B_{\rm p} = 3.5 \times 10^{13}(1+z)$ G, implying the presence of multipolar field components, as required for example in the PSG model (see Section 8.4.2).

A good fit was also obtained with a power law plus blackbody with an absorption line at ~ 0.45 keV ($\chi^2_\nu = 0.83$ for 11 dof). However, the $N_{\rm H} = (22 \pm 10) \times 10^{20}$ cm^{-2} is much higher than expected, the power law is quite steep ($\Gamma = 3.5^{+0.4}_{-0.7}$), and the blackbody has $kT = 0.045 \pm 0.010$ keV and a poorly constrained radius ($1 < R < 70$ km). This is compatible with emission from the cooling of the whole surface, but a bolometric luminosity of $\sim 7 \times 10^{31}$ erg s^{-1} of the cooling component is too high for such an old pulsar (see Figure 3.7), unless some reheating mechanism is operating.

To assess the statistical significance of the lines, I estimated the probability of obtaining by chance a fit improvement like the observed one through Monte Carlo simulations. I simulated pn spectra of PSR B1133+16 with the same exposure time as in the real observations using a model without lines, i.e. the best fit power-law model with $\Gamma = 2.36$ (Table 8.3). I fitted each simulated spectrum with a single power law and with a power law plus two harmonically spaced lines and computed the ratio of the corresponding χ^2 values $F = \chi^2_{\rm PL} \,/\, \chi^2_{\rm PL+lines}$. I found a probability of 8×10^{-4} of having a fit improvement better than that observed in the real data (i.e. $F > 2.47$), corresponding to a $\sim 3.1\sigma$ significance of the lines.

For the 3D-ML spectral-timing analysis, the phases were computed using the period at the epoch of the *XMM-Newton* observation, $P = 1.187916418694(5)$ s given by Szary et al. [392]. I found an average pulsed fraction of 0.29 ± 0.05, and no significant energy variation over the range $0.2 - 3$ keV in the pn (see Figure 8.8, left panel). A hint of pulsation was also found in the MOS, with a pulsed fraction of 0.25 ± 0.07 in the range $0.2 - 3$ keV, but it was not possible to extract the 3D spectra. The pn spectra of the total, pulsed, and unpulsed flux are plotted in Figure 8.8 (right panel). The unpulsed spectrum cannot be fitted by a single power

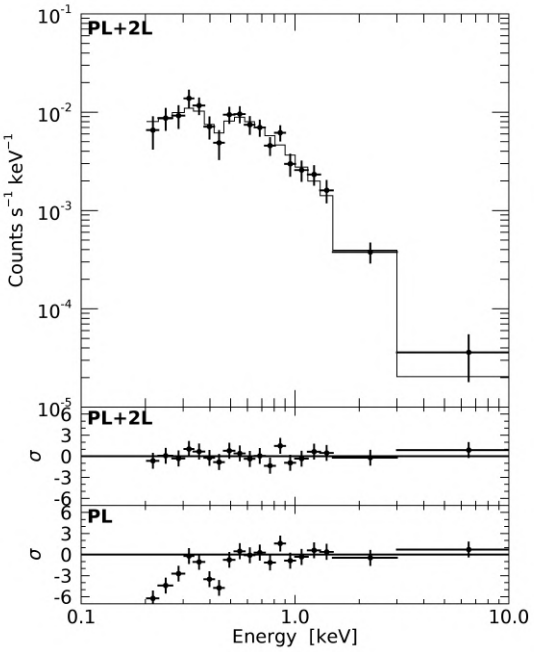

Figure 8.7: EPIC-pn spectrum of PSR B1133+16. The top panel shows the best fit with an absorbed power law plus two absorption lines at $E_1 \sim 0.22$ and $E_2 \sim 0.44$ keV. The corresponding residuals are shown in the middle panel. The bottom panel shows the residuals obtained by the best fit with a single power law in the range $0.5 - 10$ keV.

law ($\chi^2_\nu = 2.12$ for 5 dof), while it is fitted well by the same absorption features of the total model. On the contrary, the spectrum of the pulsed emission does not require the addition of the absorption lines, and a power law with $\Gamma = 2.4^{+0.5}_{-0.4}$ satisfactorily fits the spectrum. All the results of the spectral fits are summarized in the last part of Table 8.3.

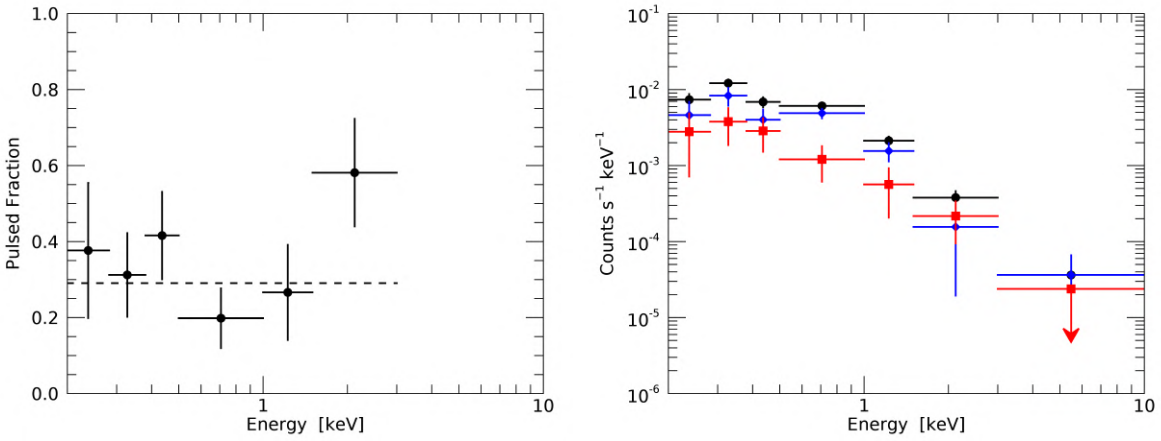

Figure 8.8: Left panel: Pulsed fraction of PSR B1133+16 as a function of energy obtained with the 3D-ML analysis. Right panel: EPIC-pn total (black circles), unpulsed (blue diamonds), and pulsed (red squares) spectra of PSR B1133+16.

Table 8.3: Spectral parameters of PSR B1133+16.

Model	$N_{\rm H}$	Γ	PL Norm	kT	$R^{\rm b}_{\rm BB}$	E_1	σ_1	$F^{\rm unabs}_{0.2-10}$	χ^2_ν/dof	nhp
	10^{20} cm^{-2}		[a]	eV	km	eV	eV	erg s^{-1} cm^{-2}		
PL	8.0 ± 2.2	2.9 ± 0.2	$3.4^{+0.4}_{-0.3}$	...	...	...	...	$2.6^{+0.8}_{-0.5}$	1.79/27	7×10^{-3}
PL	1.5[c]	...	...	...	...	...	...	...	2.32/28	9×10^{-5}
BB	...	...	...	...	...	...	...	...	2.32/27	1×10^{-4}
BB	1.5[c]	...	...	...	...	...	...	...	2.45/28	3×10^{-5}
PL+BB	< 3.3	2.0 ± 0.5	$1.1^{+0.7}_{-0.4}$	0.19 ± 0.02	22 ± 6	...	...	$1.2^{+0.2}_{-0.1}$	1.53/25	0.04
PL+BB	1.5[c]	2.2 ± 0.3	1.3 ± 0.3	0.19 ± 0.02	22 ± 6	...	...	1.28 ± 0.08	1.47/26	0.06
PL[d]	7.9 ± 6.3	3.2 ± 0.4	$3.6^{+1.0}_{-0.7}$	...	...	...	...	$3.3^{+2.8}_{-1.2}$	0.81/17	0.69
PL[d]	1.5[c]	2.8 ± 0.1	2.9 ± 0.1	...	...	...	...	2.0 ± 0.2	0.82/18	0.68
BB[d]	...	...	...	...	...	...	...	...	2.04/17	7×10^{-3}
BB[d]	1.5[c]	...	...	...	...	...	...	...	2.01/18	9×10^{-3}
PL[e]	1.5[c]	2.36 ± 0.08	2.60 ± 0.15	...	...	...	...	...	1.925/17	0.01
PL+2L[e]	< 2.5	2.8 ± 0.2	2.7 ± 0.2	...	...	221 ± 6	17^{+51}_{-4}	$1.13^{+0.19}_{-0.09}$	0.80/12	0.65
PL+2L[e]	1.5[c]	2.9 ± 0.2	2.9 ± 0.2	...	...	222 ± 6	15^{+11}_{-4}	$1.22^{+0.12}_{-0.09}$	0.78/13	0.68
PL+2L	1.5[c]	2.9 ± 0.1	2.9 ± 0.1	...	...	225 ± 6	17^{+20}_{-2}	1.17 ± 0.07	1.10/24	0.34
PL+BB+1L[e]	22 ± 10	$3.5^{+0.4}_{-0.7}$	4.8 ± 1.4	45^{+15}_{-9}	[1, 70]	450^{+5}_{-8}	$9.9^{+25.5}_{-0.8}$	73 ± 21	0.81/11	0.63
PL+2L unpul.[e]	1.5[c]	2.9 ± 0.2	2.1 ± 0.3	...	...	222[c]	15[c]	0.9 ± 0.1	0.58/5	0.72
PL+2L pulsed[e]	1.5[c]	$3.0^{+0.8}_{-0.6}$	0.8 ± 0.3	...	...	222[c]	15[c]	0.3 ± 0.1	0.44/5	0.82
PL pulsed[e]	1.5[c]	$2.4^{+0.5}_{-0.4}$	0.8 ± 0.2	...	...	...	...	0.5 ± 0.1	0.22/5	0.95

Notes. Joint fits of pn + MOS spectra of the PSR B1133+16. Errors at 1σ. The fluxes, corrected for the absorption, are expressed in units of 10^{-14} erg s^{-1} cm^{-2}.
[a] Normalization of the power law in units of 10^{-6} photons cm^{-2} s^{-1} keV^{-1} at $E = 1$ keV.
[b] Radius for an assumed distance of 0.35 kpc.
[c] Fixed value.
[d] Spectrum fitted for $E > 0.5$ keV.
[e] pn spectrum only.

8.4 Thermal X-rays from hot polar caps

If we exclude the recycled millisecond pulsars, the current census of pulsars with characteristic age $\tau \gtrsim 0.1$ Myr and with evidence of thermal emission from a small region of their surface consists of about 20 objects. For some of them (e.g. the Three Musketeers, see De Luca et al. [79]) this is well established, but for fainter old pulsars the spectra are less well constrained. A few objects require a power law plus blackbody (e.g. PSR B0943+10 and PSR B1929+10, [276]), but in many other cases it is not clear yet if the addition of a thermal component is statistically required in the spectral fits (e.g. PSR B0919+06 and PSR B1451−68 [325]). However, the possible presence of a thermal component can be investigated in some cases also through a phase-resolved spectral analysis (e.g. PSR B0628−28 and PSR J0108−1431 [15]).

In Table 8.4, I listed the properties of these thermal-emitting non-recycled rotation-powered pulsars. In addition to the objects where the presence of such emission is well established (first part of the table), I included pulsars for which there is only some evidence for it. In these cases I reported the upper limit on the bolometric luminosity (second part of the table).

The values of temperature and radius for each blackbody, evaluated at infinity, are taken

Table 8.4: Rotation-powered pulsars with polar cap thermal emission.

Num	Name PSR	P s	τ_c Myr	B_p 10^{12} G	R_{PC}^{∞} [a] m	d [b] kpc	P_4/P [c]	kT_{BB} eV	R_{BB} m	L_{BB} erg s^{-1}	Spectrum and Reference
1	J0108−1431	0.81	166	0.5	252	$0.21^{+0.09}_{-0.05}$ P	...	115 ± 12	100^{+40}_{-25}	$(5.7^{+5.1}_{-3.7}) \times 10^{28}$	PL+BB [15]
2	B0114+58	0.10	0.28	1.6	711	1.77 D	...	170 ± 20	405^{+110}_{-90}	$(4.4 \pm 2.9) \times 10^{30}$	BB [356]
3	B0355+54	0.16	0.56	1.7	573	$1.0^{+0.2}_{-0.1}$ P	...	160 ± 30	250 ± 50	$(1.3 \pm 1.1) \times 10^{30}$	PL+BB [212]
4	B0628−28	1.24	2.77	6.0	203	$0.32^{+0.05}_{-0.04}$ P	168 ± 7	100^{+20}_{-10}	150^{+80}_{-50}	$(7.3^{+9.7}_{-5.7}) \times 10^{28}$	PL+BB [356]
5	J0633+1746	0.24	0.34	3.3	465	$0.25^{+0.23}_{-0.08}$ P	...	164 ± 26	63 ± 16	$(9.3 \pm 7.5) \times 10^{28}$	PL+2BB [79]
6	B0656+14	0.38	0.11	9.3	365	0.28 ± 0.03 P	20 ± 1	108 ± 3	1680 ± 140	$(1.2 \pm 0.2) \times 10^{31}$	PL+2BB [79]
7	B0823+26	0.53	4.92	1.9	311	$0.32^{+0.08}_{-0.05}$ P	...	370 ± 30	8 ± 1	$(3.9 \pm 1.6) \times 10^{28}$	2BB [163]
		...	...	...	...	...	...	120 ± 10	70 ± 13	$(3.3 \pm 1.6) \times 10^{28}$	2BB [163]
8	B0834+06	1.27	2.97	6.0	200	0.19 D	30.2 ± 0.2	170^{+65}_{-55}	7^{+12}_{-3}	$(1.3^{+5.0}_{-1.2}) \times 10^{27}$	BB [114]
9Q	B0943+10 (Q)	1.10	4.98	4.0	216	0.89 D	36.4 ± 0.9	300 ± 20	27^{+5}_{-4}	$(1.9^{+0.9}_{-0.8}) \times 10^{29}$	PL+BB [357]
9B	B0943+10 (B)	...	...	...	...	...	$37.4^{+0.4}_{-1.4}$	210 ± 20	41^{+10}_{-9}	$(1.1 \pm 0.6) \times 10^{29}$	PL+BB [357]
10	B0950+08	0.25	17.5	0.5	450	0.261 ± 0.005 P	...	150 ± 20	50 ± 32	$(4.1^{+5.7}_{-3.7}) \times 10^{28}$	PL+BB [449]
11	B1055−52	0.20	0.54	2.2	510	0.35 A	22^{+11}_{-5}	154 ± 5	215 ± 30	$(8.4 \pm 2.6) \times 10^{29}$	PL+2BB [79]
12	J1154−6250	0.28	7.99	0.8	426	1.36 D	...	210 ± 20	82 ± 21	$(4.2 \pm 2.7) \times 10^{29}$	BB [188]
13	B1719−37	0.24	0.34	3.2	466	2.48 D	...	233^{+60}_{-50}	420^{+690}_{-220}	$(1.7^{+5.8}_{-1.5}) \times 10^{31}$	BB [293]
14	J1740+1000	0.15	0.11	3.7	577	1.23 D	...	148^{+16}_{-15}	560^{+240}_{-150}	$(4.9^{+4.7}_{-3.3}) \times 10^{30}$	PL+2BB [202]
15	B1822−09	0.77	0.23	12.9	258	$0.3^{+0.7}_{-0.2}$ P	...	187^{+26}_{-23}	29^{+14}_{-8}	$(3.3^{+3.7}_{-2.5}) \times 10^{28}$	2BB [162]
		...	...	...	...	...	...	83 ± 4	610^{+120}_{-110}	$(5.7 \pm 2.3) \times 10^{29}$	2BB [162]
16	B1929+10	0.23	3.10	1.0	476	$0.31^{+0.09}_{-0.06}$ P	50^{+15}_{-5}	300^{+20}_{-30}	28^{+5}_{-4}	$(2.1 \pm 1.0) \times 10^{29}$	PL+BB [276]
17	B0826−34	1.85	29.4	2.7	166	0.35 D	14 ± 1	...	...	$< 1.5 \times 10^{29}$	HR [114]
18	B0919+06	0.43	0.50	4.9	345	$1.1^{+0.2}_{-0.1}$ P	...	...	...	$< 2.9 \times 10^{29}$	PL [356]
19	B1133+16	1.19	5.04	4.3	208	0.35 ± 0.02 P	33 ± 3	...	...	$< 1.1 \times 10^{28}$	PL [356]
20	B1451−68	0.26	42.5	0.3	441	0.43 D	...	...	...	$< 2.1 \times 10^{29}$	PL [325]

Notes. [a] Observed polar cap radius $R_{PC}^{\infty} = (2\pi R^3/Pc)^{1/2}(1+z)$ with $M = 1.2\,M_{\odot}$ and $R = 12$ km.
[b] Distance measure methods: P, parallax; D, dispersion measure; A, association; see the corresponding reference.
[c] The data are taken from Weltevrede et al. [432], Gil et al. [114], Szary [391].

from the most recent works present in literature (references in the last column of Table 8.4), and, when needed, I rescaled the radii using updated distance values. The bolometric luminosities of these thermal components are evaluated as $L_{bol} = \pi R^2 \sigma T^4$ and I included the distance uncertainties in their errors.

For two objects (PSR B1822−09 [162] and PSR B0823+26 [163]) two thermal components are needed to fit the emission from the polar cap because of a nonuniform temperature distribution within the cap. In Table 8.4 I reported both blackbodies, but in the following plots, the bolometric luminosity is the sum of the two luminosities, while the radius refers to the bigger and cooler component, the temperature to the hot component.

All the temperatures are in the narrow range $0.1 - 0.3$ keV and do not depend significantly on the characteristic age. On the contrary, the emission radii span nearly two orders of magnitudes. The emitting region is expected to be related to the polar cap size, so I compared R_{BB} with the radius of the polar cap defined by the last closed lines in a dipolar field geometry (see Eq. 2.3). To be consistent, I considered the polar cap radius observed at infinity,

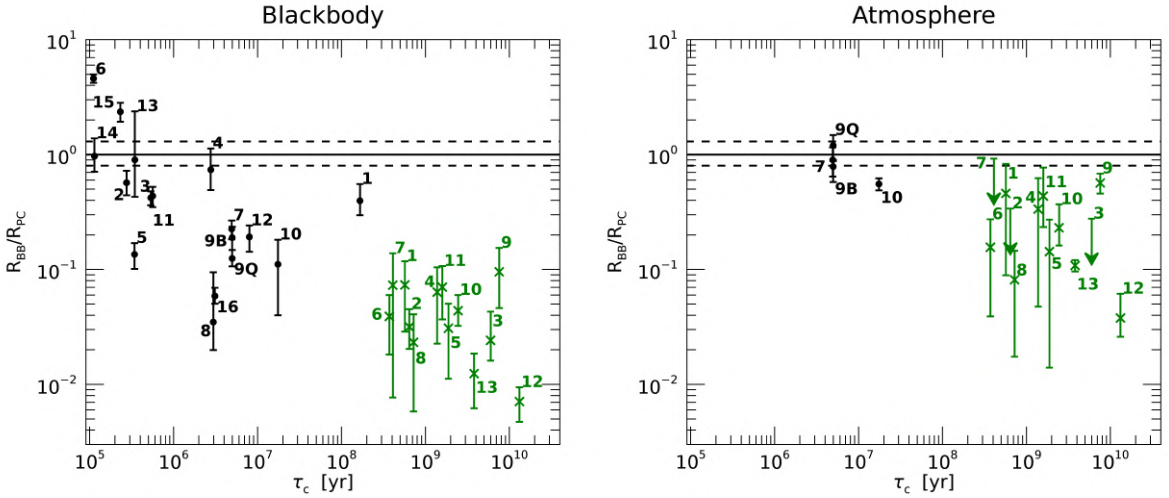

Figure 8.9: Ratio of the radius of emitting area inferred from the blackbody fit (left panel) or from atmosphere fit (right panel) to the polar cap radius as a function of the pulsar characteristic age. Black dots refer to ordinary RPPs, green crosses to MSPs. The pulsars are numbered according to Tables 8.4 and 8.5.

$R^{\infty}_{\rm PC} = (2\pi R^3/Pc)^{1/2}\,(1+z) \approx 230\ P^{1/2}$ m. Because of the uncertainties on the neutron star mass and radius ($M \approx 1.2-1.6\ M_{\odot}$ and $R \approx 10-14$ km), this values can vary in a range of $70-120\%$.

As shown in Figure 8.9, left panel, in most pulsars with $0.1 < \tau_c < 100$ Myr the two radii are consistent, considering the uncertainties (both on $R_{\rm BB}$ and $R_{\rm PC}$). However, even considering the large scatter of the sample, a trend of decreasing $R_{\rm BB}/R_{\rm PC}$ as the characteristic age increases is observed. This could be related to the different mechanisms of pair production that involve young (CR photons) and old (ICS photons) pulsars (see later).

Some pulsars, as PSR B0656+14, have a blackbody radius that is nearly ten times larger than $R_{\rm PC}$, as already noticed by De Luca et al. [79], suggesting the need for a different explanation of the hot thermal component in this pulsar. One possibility is that anisotropic thermal conduction in the crust likely causes temperature gradients on the surface (see Section 3.1.1), and the oversimplified modeling with just two blackbodies at different temperatures gives unrealistic parameters.

Other pulsars, on the contrary, have a $R_{\rm BB}$ significantly smaller than $R_{\rm PC}$, but this can be explained by geometrical effects. In fact, the radii inferred from the spectral fits correspond to the projected area of the emitting region averaged over the star rotational phase. Only for nearly aligned rotators seen pole-on $\pi R^2_{\rm BB}$ does correspond to the real emitting area. This should occur, e.g., for PSR B0943+10; however, it has $R_{\rm BB} < R_{\rm PC}$. The mismatch between the polar cap and the emitting radius can be explained considering that the blackbody model is inadequate to fit the thermal emission, and use more realistic atmosphere models. These models have been successfully applied to a large number of neutron stars, as XDINSs [143, 123, 144] and CCOs [301, 139, 46], that have spectra sensitive enough to costrain the many parameters of the atmosphere models. Nevertheless, for a few old pulsars a fit with magnetized hydrogen atmosphere has been performed, with a magnetic field that resulted equal to the dipole-approximation value, and the geometry is known from radio data: PSR B0943+10 (see Chapter 7), PSR B0823+26 (see Section 2.4.3) and PSR B0950+08 (with $\xi = \chi = 45^{\circ}$ assumed, see Zavlin & Pavlov [449]). As already discussed in Section 3.1.2, atmosphere models give a fitting radius larger than the blackbody model, which does not suffer of projection effects because

the geometry is an integral part of the model. As Figure 8.9, right panel, shows, the emitting radii of these three pulsars derived with atmosphere models are in a perfect agreement with the expected $R_{\rm PC}$.

The same conclusions apply to a larger sample of objects, i.e. the MSPs. They are old recycled pulsars, with $\tau_c \approx 1 - 10$ Gyr and a negligible dipolar magnetic field ($B_{\rm p} \approx 10^8 - 10^9$ G). Thermal X-ray emission has been detected in several MSPs (see Table 8.5), that has been fitted with blackbody and non-magnetized atmosphere models. The emitting radii obtained with these two models are shown with green crosses in Figure 8.9, left and right panel respectively.

Table 8.5: Millisecond pulsars with polar cap thermal emission.

Num	Name	P	τ_c	$B_{\rm p}$	$R^{\infty}_{\rm PC}$ [a]	d [b]	$kT_{\rm BB}$	$R_{\rm BB}$	$kT_{\rm AT}$	$R_{\rm AT}$	Spectrum [c] and
	PSR	s	Gyr	10^9 G	km	kpc	eV	km	eV	km	Reference
1	B0021−72E	3.54	0.57	1.19	3.81	4.5 A	151 ± 8	0.28 ± 0.17	76^{+10}_{-9}	1.75 ± 1.41	NSA [48]
2	B0021−72F	2.62	0.64	0.83	4.43	4.5 A	190^{+39}_{-30}	$0.14^{+0.06}_{-0.05}$	100 ± 30	< 1.50	NSATMOS [38]
3	J0024−7204ab	3.70	5.98	0.39	3.72	4.5 A	211^{+52}_{-39}	$0.09^{+0.07}_{-0.03}$	112^{+39}_{-30}	< 1.03	NSATMOS [38]
4	J0024−7204O	2.64	1.38	0.57	4.41	4.5 A	152 ± 13	0.28 ± 0.18	84^{+15}_{-13}	1.48 ± 1.27	PL+NSA [48]
5	J0024−7204Q	4.03	1.88	0.75	3.57	4.5 A	193 ± 17	0.11 ± 0.07	112^{+22}_{-18}	0.51 ± 0.46	NSA [48]
6	J0024−7204R	3.48	0.37	1.45	3.84	4.5 A	216 ± 14	0.15 ± 0.08	133^{+16}_{-15}	0.60 ± 0.45	NSA [48]
7	J0024−7204T	7.59	0.41	3.02	2.60	4.5 A	134 ± 14	0.19 ± 0.17	69^{+16}_{-13}	< 2.4	NSA [48]
8	J0024−7204U	4.34	0.72	1.30	3.44	4.5 A	238 ± 19	0.08 ± 0.06	157^{+23}_{-21}	0.28 ± 0.22	NSA [48]
9	J0030+0451	4.87	7.58	0.45	3.25	$0.28^{+0.10}_{-0.06}$ P	216 ± 9	0.08 ± 0.02	130^{+7}_{-6}	0.28 ± 0.18	PL+2NSATMOS [47]
		...	...	...	...	...	102 ± 7	$0.31^{+0.19}_{-0.16}$	60^{+7}_{-6}	$1.84^{+0.38}_{-0.35}$	PL+2NSA [47]
10	J0337+1715	2.73	2.45	0.44	4.34	1.30 ± 0.08 O	181 ± 17	$0.19^{+0.07}_{-0.05}$	86 ± 17	$1.0^{+0.6}_{-0.3}$	NSA [377]
11	J0437−4715	5.76	1.59	1.16	2.99	0.156 ± 0.001 P	272 ± 9	$0.05^{+0.02}_{-0.01}$	221^{+5}_{-7}	$0.17^{+0.03}_{-0.04}$	PL+2NSA+BB [45]
		...	...	...	...	...	130^{+7}_{-5}	$0.21^{+0.11}_{-0.10}$	86^{+3}_{-10}	$1.3^{+1.0}_{-0.6}$	PL+2NSA+BB [45]
12	J0636+5129	2.87	13.2	0.20	4.23	$0.21^{+0.03}_{-0.02}$ P	181 ± 17	0.03 ± 0.01	78 ± 9	$0.16^{+0.10}_{-0.05}$	NSA [377]
13	J2124−3358	4.93	3.80	0.64	3.23	$0.30^{+0.07}_{-0.05}$ P	207 ± 17	0.04 ± 0.02	112 ± 9	0.35 ± 0.04	PL+NSA [446]

Notes. [a] Observed polar cap radius $R^{\infty}_{\rm PC} = (2\pi R^3/Pc)^{1/2}\,(1+z)$ with $M = 1.2\ M_{\odot}$ and $R = 12$ km.
[b] Distance measure methods: A, association; P, parallax; O, other; see the corresponding reference.
[c] Spectral model in the case of an atmosphere model: NSA [451]; NSATMOS [156]. The authors used different values of NS mass and radius, see the corresponding reference.

Finally, let's consider the results of the non-recycled old pulsars in the theoretical framework discussed in Section 3.4, in particular analyzing the bolometric luminosity that is less affected by the choice of the spectral model (see also Section 3.2).

8.4.1 Polar cap heating in the SCLF model

Thermal emission from small hot spots has been explored in detail by Harding & Muslimov [148, 149, 150] in the context of polar cap models. According to their SCLF model, presented in Section 3.4.1, vacuum gaps are created high above the polar caps, at some stellar radii, because both ions and electrons can be freely stripped off the neutron star surface. The pair cascade can be initiated either by curvature radiation (CR) or by inverse-Compton scattering (ICS) of stellar thermal X-rays by primary electrons. The production of CR photons requires a much higher energy of the primary particles, and therefore it occurs at higher altitude and the pair heating luminosity is expected to be much higher in the CR rather than in the ICS scenario.

These processes can occur only above the corresponding "death lines" in the $\dot{P} - P$ diagram; pulsars in the region below the CR-pair death line, but above that of ICS, can produce pairs only from ICS photons [151].

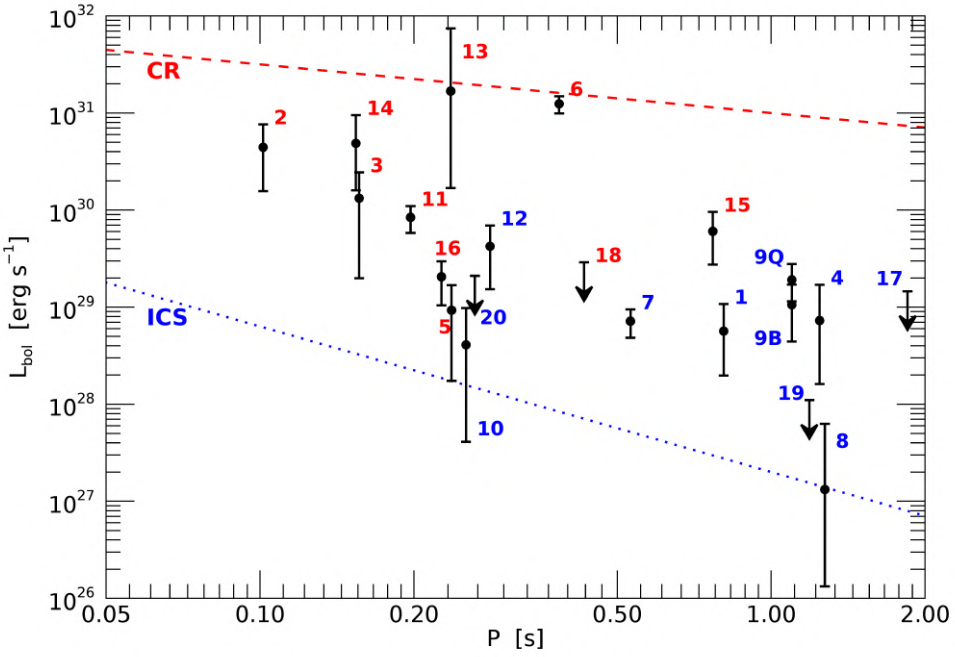

Figure 8.10: Bolometric luminosity of polar cap emission vs. rotation period. The lines represent the predicted thermal luminosities in case of CR (red dashed line, see Eq. 3.22) and ICS (blue dotted line, see Eq. 3.23) pair fronts. The theoretical lines are taken from Harding et al. [151] in the case of non-recycled pulsars. Pulsars labeled with blue numbers are expected to produce pairs only from ICS photons. The error bars on the bolometric luminosity are computed taking into account both the uncertainties of the blackbody fit and those on the distances. See Table 8.4 for details.

The bolometric luminosity inferred for large periods in the CR ($L_{\rm bol}^{\rm CR} \approx 10^{31}$ erg s^{-1} $P^{-1/2}$, see Eq. 3.22) and the ICS ($L_{\rm bol}^{\rm CR} \approx 2 \times 10^{27}$ erg s^{-1} $P^{-3/2}$, see Eq. 3.23) scenario, which should be considered as upper limits in the case of incomplete screening, are compared with the observed thermal luminosities of the pulsars in Figure 8.10. Although there is a general agreement between the data and the model predictions, I note that most of the pulsars for which only the ICS mechanism should operate (indicated in Figure 8.10 with blue numbers) have luminosities above the maximum predicted in this scenario. Therefore, some additional emission mechanism is expected. Nevertheless, no observed pulsar has a luminosity below the ICS line. This could reinforce the SCLF model, but it could also be a selection effect.

8.4.2 Polar cap heating in the PSG model

In the PSG model of Gil & Mitra [109], Gil et al. [111, 112, 113], presented in Section 3.4.2, the ions are trapped on the stellar surface when the surface temperature is below the critical value $T_{\rm i}$ defined in Eq. 3.13. As a consequence, a vacuum gap is formed above the polar cap region. Electrons are accelerated backward and bombard the polar cap surface, causing a thermal ejection of ions, which causes partial screening of the acceleration potential drop.

If the temperature is too high and/or the magnetic field too low, too much ions are emitted and no vacuum gap can form. In the opposite conditions a pure vacuum gap is formed. Since the surface heating is due to the flow of particles back-accelerated in the gap, a self-regulating thermostatic mechanism acts to keep the temperature at the value required by the PSG model to work. The temperatures observed in old pulsar spectra require surface fields of $B \sim 10^{14}$ G to operate in the PSG regime (see Eq. 3.10). This request is not implausible if we consider that, on the surface, the dipole approximation may be no longer valid and a multipole expansion is needed to describe the actual magnetic field. If this is true, the polar cap area should be squeezed in order to conserve the the magnetic flux: $A_{\rm PC} = b \times A_{\rm PC,d}$, where b is the ratio between the actual magnetic field at the surface and the canonical dipolar component at the polar cap (see Eq. 3.28), and $A_{\rm PC,d} = \pi R_{\rm PC}^2 \approx 0.1\ P^{-1}$ km^2 is the polar cap area in the dipole configuration.

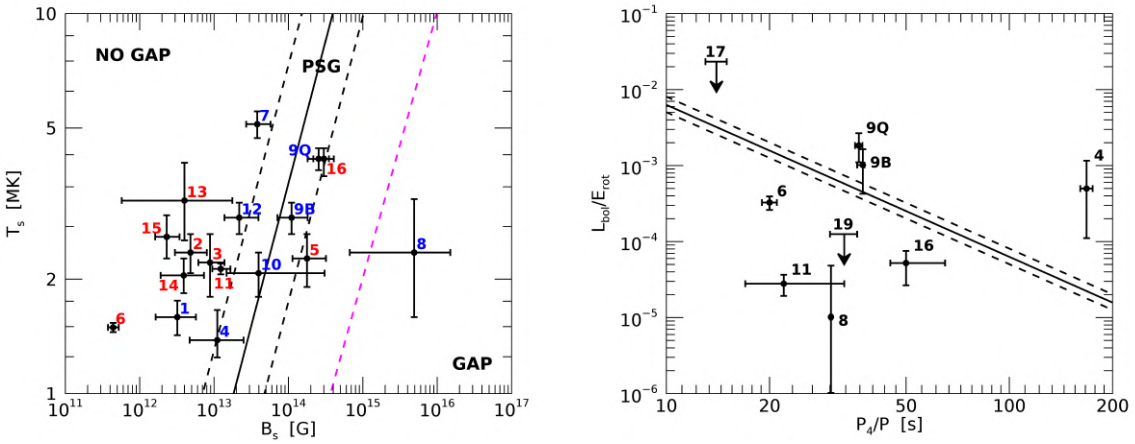

Figure 8.11: Left panel: Surface temperature vs. surface magnetic field required to form a partially screen gap. The theoretical line, indicated in the figure with a solid line and dashed lines to account for uncertainties, is Eq. 3.10 for $Z = 26$ [260], while the dashed magenta line refers to a hydrogen outer layer, see Eq. 3.8. For higher temperatures no gap can form, while for lower temperatures the gap is of pure vacuum. The data, numbered according to Table 8.4, are obtained as described in the text (red: CR photon pair production; blue: ICS photon pair production). Right panel: Thermal efficiency vs. circulation period of the drifting subpulses. The data, listed in Table 8.4, are taken from Weltevrede et al. [432], Gil et al. [114], Szary [391].

According to the PSG model, then, the polar cap should have magnetic fields $B_{\rm s} \sim 10^{14} - 10^{15}$ G and radii of $\sim$10 m to sustain a surface temperature in the range $1 - 5$ MK. Figure 8.11, left panel, shows the surface temperature $T_{\rm s}$ as a function of the magnetic field $B_{\rm s} = b^{-1} B_{\rm p}$, where $B_{\rm p}$ is the dipolar magnetic field, and $A_{\rm PC}$ is the observed emitting area inferred from the blackbody fit. The solid line represents the relation $T_{\rm crit} \approx 3.6$ MK $B_{14}^{3/4}$ (see Eq. 3.10 for iron ions), and the dashed lines account for theoretical uncertainties. Almost the totality of the pulsars that operate in the ICS regime (indicated in Figure 8.11, left panel, with blue numbers) are located within the dashed lines, meaning that a PSG has formed. On the contrary, the more energetic CR pulsars (red numbers) are located in the zone of no gap. Considering that CR photon production occurs at higher altitude than the ICS one ($h_{\rm CR} \approx 100$ m, $h_{\rm ICS} \approx 1 - 3$ m), the time spent to return on the surface ($\tau = 2h_{\rm CR}/c \approx 6 \times 10^{-7}$ s) is much longer than the time needed for the surface to cool down ($\tau_{\rm cool} \lesssim 10^{-8}$ s [111]). Gil et al. [113], Szary [391] argued that this could explain why the pulsars with CR pair production do not have to proper surface

conditions to partially screen the gap, that should be completely screened. This is at variance with the observed surface conditions, shown in Figure 8.11, left panel.

Another consequence of the PSG model is that the phenomenon of drifting subpulses observed in many radio pulsars (see Section 2.3.1) is naturally explained in terms of the $\mathbf{E} \times \mathbf{B}$ circulation of plasma filaments produced by vacuum discharges. Figure 8.11, right panel, shows with a solid line the relation between the thermal efficiency and the circulation period that PSG predicts in the quasi-equilibrium condition is verified ($L_{\rm bol}/\dot{E} \approx 0.63(P_4/P)^{-2}$, see Eq. 3.26). The data of the few pulsars that exhibit the subpulse-drifting phenomenon are also shown, that, however, disfavor this prediction of the PSG model.

Furthermore, note that if the outer layers of a neutron star consist of light elements, as in the case of a hydrogen atmosphere, the formation of PSG is not possible due to the low cohesive energy of the ions (see Eq. 3.8). The need for a hydrogen atmosphere as been demonstrated for PSR B0656+14, PSR B0943+10, PSR B0823+26 and PSR B0950+08 so far. In such a case, SCLF can be responsible for plasma generation and acceleration.

Chapter 9

Final remarks

In this PhD Thesis I considered some of the most recent models of X-ray thermal and nonthermal emission from neutron stars to explain the large variety of observed phenomena. Moreover, to extract the best possible information from the X-ray data, I implemented an analysis software that relies on the maximum likelihood (ML) method: given a certain model of how the counts are distributed on the detector, it estimates the most probable parameters that reproduce the observed data. I demonstrated that the ML method is particularly effective for dim sources, as most old pulsars are.

Subsequently, I modeled the X-ray spectra and pulse profiles extracted with the ML technique with realistic emission models, that account for the effects of the magnetic field on the surface temperature distribution and on the interaction between matter and radiation. I relied on an existing software that, given a set of stellar parameters, evaluates the emerging intensity of the radiation. Then, it collects and sums the contribution of surface elements which are in view at different rotation phases from a stationary observer. I adapted the software to the specific case of emission from small magnetic polar caps: from the computed emergent flux I fabricated synthetic phase-resolved spectra for a wide range of stellar parameters, as the surface temperature and magnetic field, and the pulsar orientation with respect to the observer.

I applied the methods described above to some old pulsars. PSR J0726−2612 is a slowly-rotating pulsars of 0.2 Myr that shows a hybrid behavior between different classes of neutron stars: it exhibits a single-peaked radio pulse profile, as the majority of the ordinary RPPs, but in the X-ray band it has a double-peaked pulse profile and a thermal spectrum that strongly resembles those of the radio-silent XDINSs [376].

I analyzed a deep *XMM-Newton* observation of PSR J0726−2612 and I found that its spectrum can be fitted by the sum of two blackbodies with $kT_1 \sim 74$ eV and $R_1 \sim 10.4$ km, $kT_2 \sim 140$ eV and $R_2 \sim 0.5$ km. This is in agreement with the expectation that middle-aged pulsars with strong magnetic fields have cooling emission with a nonuniform surface temperature, and a bolometric luminosity $L_{\rm bol} = (4.0^{+4.4}_{-1.0}) \times 10^{32}$ erg s^{-1} more intense than those of coeval RPPs with a lower magnetic field. In addition, the presence of a broad absorption line was required in the fit, and it was interpreted as a proton cyclotron feature with $E_0 \sim 390$ eV, consistently with the pulsar magnetic field intensity.

XMM-Newton data analysis also revealed that PSR J0726−2612 has an asymmetrical pulse profile and a high pulsed fraction that varies as a function of energy. I found that these characteristics cannot be reproduced without invoking magnetic beaming; moreover, magnetized atmosphere models naturally take into account the presence of two X-ray peaks and a single radio peak if the angles ξ and χ are similar. This geometry differs from that of two XDINSs

for which $\xi \sim 90^\circ$ and $\chi \sim 45^\circ$ have recently been estimated [143, 144]. Thus, the reason for the lack of radio emission from XDINSs could be simply an unfavorable viewing geometry, but more observations are needed to reduce the uncertainty in the radio and X-ray phase alignment and better constrain the geometry of PSR J0726−2612.

A second pulsar that showed inconsistencies between the predictions of X-ray and radio emission is the 5 Myr old PSR B0943+10. It is a mode-switching radio pulsar characterized by two emission modes with different radio and X-ray properties. Previous studies [161, 266], based on simple combinations of blackbody and power-law models, showed that its X-ray spectrum can be decomposed in a pulsed thermal plus an unpulsed nonthermal components, but had difficulties to reproduce the high observed pulsed fraction if, as derived from the radio data, PSR B0943+10 is a nearly aligned rotator seen pole-on [85, 42].

I reanalyzed all of the available X-ray observations of PSR B0943+10 with simultaneous radio coverage, modeling the emission from polar caps with thermal models more realistic than the blackbody. Replacing the blackbody with a model of thermal emission from an iron condensed surface, as it could be expected in the presence of strong multipolar components of the magnetic field, cannot solve these problems. Therefore, one has to invoke that in the blackbody and solid surface case, also the nonthermal emission is, to some extent, pulsed. Such a possibility is plausible, as shown by theoretical expectations and observations of other pulsars, and it is consistent with the current data of PSR B0943+10.

A good description of the PSR B0943+10 spectra and pulse profiles could be obtained using a magnetized hydrogen atmosphere model plus an unpulsed nonthermal component. In this case, it was possible to fit well the phase-resolved spectra of both modes, for several geometrical configurations consistent with the radio data. As first shown by Storch et al. [382] for this pulsar, the significant beaming of the emission predicted by magnetized atmosphere models gives rise to pulse profiles more consistent with the observed ones, and, as typically observed with atmosphere models, yields smaller temperatures and larger emission radii than those of blackbody fits ($kT \sim 90$ eV, $R \sim 260$ m, for the Q-mode; $kT \sim 80$ eV, $R \sim 170$ m, for the B-mode). I explored a few representative geometrical configurations derived from the radio data and found that for surface magnetic fields of the order of the dipole value derived from the timing parameters, the most-aligned configurations (i.e. $\xi = 5^\circ$ and $\chi = 3^\circ$) are favored.

I also studied the X-ray emission of other seven old and dim RPPs, of which four had controversial published results, and three were so far undetected. I found convincing evidence of thermal emission only in the phase-averaged spectrum of two of them, PSR B0114+58 and PSR J1154−6250, and a hint for a thermal pulsed spectrum in PSR B0628−28; the small emitting radii ($\sim$405 m, $\sim$82 m, and $\sim$100 m, respectively) indicate that for the three objects the thermal radiation comes from a hot spot on the stellar surface, most likely from the polar cap.

The spectra of PSR B0919+06 and PSR B1133+16 were fitted well by a single power law, and the addition of a thermal component was statistically not justified. Moreover, I found evidence for absorption lines at 220 eV and 440 eV in the spectrum of PSR B1133+16. If these lines are interpreted as cyclotron features due to protons they imply a magnetic field of a few 10^{13} G, higher than the dipole field inferred from the timing parameters of the pulsar ($B_{\rm d} = 2 \times 10^{12}$ G).

For what concerns the last two pulsars, PSR B0450−18 was detected in X-rays for the first time by EPIC with a 3.1σ of significance, while for PSR B1818−04 I conservatively evaluated a three sigma upper limit on the count rate. Then, adopting a standard absorbed power-law model, I derived the following nonthermal luminosities in the hard X-ray band: $L_{2-10} = 3.0^{+3.4}_{-1.2} \times 10^{28}$ erg s^{-1} (PSR B0450−18) and $L_{2-10} < 1.2 \times 10^{29}$ erg s^{-1} (PSR B1818−04). These values translate into an efficiency $\eta_{2-10} = 2 \times 10^{-5}$ and $\eta_{2-10} < 10^{-4}$, respectively, that are the

two lowest values (along with PSR J2043+2740 [32]) for old RPPs with $\tau_c > 1$ Myr.

Finally, I considered all the thermal emitters with ages $\gtrsim 0.1$ Myr reported in literature. By using the most updated spectral results and distance estimates, I compared their observed temperatures, radii and luminosities to the expectations of the current theoretical models for these objects. In particular, I found that the emitting area are generally in agreement with the polar cap regions evaluated in a dipole approximation, if the combined effects of geometry projections plus realistic thermal models (as the magnetic atmosphere) are taken into account.

The old pulsars can be subdivided into two classes, according to the principal mechanism of pair production in gap regions in the magnetosphere: pulsars with age $\lesssim 1$ Myr initiate the pair cascade by curvature radiation, while older pulsars can activate it only through the inverse-Compton scattering (ICS). There are two competing models about the location of the polar cap accelerators: right above the stellar surface (the partially screen gap, PSG, models), or some stellar radii above (the space charge limited flow, SCLF, models).

The observed bolometric luminosities of both classes are in general agreement with the scale relations expected by the SCLF models, even if most of the pulsars for which only the ICS mechanism should operate have luminosities above the maximum predicted in this scenario, suggesting that some other mechanism is operating. Instead, the predicted surface conditions of the PSG models are in disagreement with the observed quantities of the CR pulsars, and in agreement with those of the ICS pulsars only if they are inferred by a blackbody model fit. Moreover, I found that the bolometric luminosities of the few old pulsars that exhibit the subpulse drifting phenomenon do not follow the trend expected by the PSG model.

The results reported here underline the importance of exploiting the full spectral and timing information in the analysis of X-ray pulsars and the strong constraints posed on the models by the knowledge of the pulsar geometry, which unfortunately is not available for most pulsars. To further progress in this field it would be important to systematically analyze the X-ray data of all of the old pulsars with controversial published results with the ML technique, and secondly, to fit spectra and pulse profiles of thermal-emitting NSs, as PSR J0726$-$2612, the XDINSs and Calvera, with an autoconsistent model of a magnetized atmosphere.

Appendix A

Applications of the ML Software

In this chapter, I report the analysis of three X-ray sources I performed in collaboration with other working groups that have benefited from the ML technique. In fact, it applies not only to the pulsars, but to any point source, especially if it is dim and/or superimposed to another source. In the course of my PhD research activity, I analyzed the X-ray emission of a new flaring source, called J1806−27 and located in the galactic globular cluster NGC 6540 (Section A.1), and two ultraluminous X-ray sources (ULXs), accreting compact objects with X-ray luminosities above 10^{39} erg s^{-1} (Sections A.2 and A.3). All the three sources had a variable emission, alternating quiescent and flaring/outbursting states, and were almost overlapped with other sources. The detailed analysis and discussion of these sources can be found in Mereghetti et al. [267], Pintore et al. [315] and Pintore et al. [316].

A.1 Discovery of a peculiar flaring X-ray source in the globular cluster NGC 6540

In Mereghetti et al. [267], we report the discovery of J1806−27, a flaring X-ray source 7″ from the center of the globular cluster NGC 6540 obtained during the EXTraS project[1]. The source had a quiescent X-ray luminosity on the order of 10^{32} erg s^{-1} in the $0.5-10$ keV range (for a distance of NGC 6540 of 4 kpc) and showed a flare lasting about 300 s. During the flare, the X-ray luminosity increased by more than a factor 40, with a total emitted energy of $\sim 10^{36}$ erg. These properties, as well as *Hubble Space Telescope* photometry of the possible optical counterparts, suggest the identification with a chromospherically active binary in the cluster. However, the flare luminosity is significantly higher than what is commonly observed in stellar flares of such a short duration, leaving open the possibility of other interpretations (e.g., some form of flaring magnetar-like emission from a neutron star, or a peculiar outburst from a compact object).

I used the ML technique to extract the spectra of J1806−27 during the flare. The spectra obtained with the pn (130 ± 14 net counts) and with the sum of the two MOS (122 ± 13 net counts) were fitted simultaneously. An absorbed power law gave a good fit with $\Gamma = 1.7 \pm 0.2$, $N_{\rm H} = (6 \pm 2) \times 10^{21}$ cm^{-2}, and $F_{0.5-10} = 2.7 \times 10^{-12}$ erg s^{-1} cm^{-2}. Acceptable fits were obtained also with other single component models: blackbody, thermal bremsstrahlung, thermal plasma emission, multi blackbody disk emission.

[1] A project devoted to a systematic search for variability in archival data of the *XMM-Newton* satellite, see http://www.extras-fp7.eu/

With the ML method it was possible to extract also the spectra of J1806−27 during the quiescent emission, i.e. from the whole observation excluding the time interval of the flare. This yielded exposure times of 6.5 ks in the pn and 8.8 ks in the MOS (100 ± 20 and 86 ± 15 source counts, respectively). To avoid contamination from a nearby persistent source (at only 18″ from J1806−27), I included it in the ML model and extracted simultaneously the spectra of the two sources. In the spectral fits of J1806−27, I fixed the absorption at the values derived from the spectrum of the flare with the corresponding model. I found a quiescent source flux slightly smaller than 10^{-13} erg s^{-1} cm^{-2} and, although the uncertainties are large, some evidence that the spectrum during the quiescent period is softer than that of the flaring emission.

A.2 A new ULX in the galaxy NGC 5907

In Pintore et al. [315], we report on the serendipitous discovery of a new transient in NGC 5907, a galaxy distant 17.1 Mpc, at a peak luminosity of 6.4×10^{39} erg s^{-1}. The source was undetected in previous *Chandra* and *Swift*/XRT observations. We analyzed three recent *Chandra* and *XMM-Newton* observations, as well as all the available *Swift*/XRT observations performed between 2017 August and 2018 March. The transient entered the ULX regime in less than two weeks and its outburst was still on-going at the end of 2018 February. The $0.3 - 10$ keV spectrum is consistent with a single multicolour blackbody disc ($kT \sim 1.5$ keV). The source might be a $\sim 30\ M_{\odot}$ black hole accreting at the Eddington limit. However, although we did not find evidence of pulsations, we cannot rule out the possibility that this ULX hosts an accreting NS.

The galaxy NGC 5907 hosts a large population of X-ray sources, with the brightest being the pulsating ULX NGC 5907 X-1. Our source, thus called ULX-2, is only at $\sim$28″ from ULX-1. The analysis presented in the paper was performed with traditional methods because, at the time of observations, ULX-1 was in quiescence and hence not contaminating the ULX-2 emission. On the other hand, I double-checked all the available *XMM-Newton* observations of ULX-1 before 2017 August and, through the ML analysis, I found hints for the presence of ULX-2 only during the observation of 6 November 2013. I extracted 62 ± 18 counts in the pn camera in the energy range $0.3 - 10$ keV, and adopting the spectral model discussed above, I found a flux $F_{0.3-10} \sim 8 \times 10^{-15}$ erg s^{-1} cm^{-2}, a factor 0.05 lower than the source flux in the ULX regime.

A.3 A census of the ULX population in the galaxy NGC 7456

In Pintore et al. [316], submitted, we present a detailed analysis of all the ULXs hosted in the galaxy NGC 7456, 16 Mpc distant. We found that ULX-1 and ULX-2 are bright objects ($6 - 10 \times 10^{39}$ erg s^{-1}): they can be suitably described by a two-thermal component model as often seen in ULX. ULX-1 is a very peculiar source that shows also extreme variability on short-term timescales. The other sources (ULX-3 and ULX-4) are instead transient ULXs, with flux changes of at least an order of magnitude. In addition, we discovered a new ULX (ULX-5) with a luminosity of $\sim 10^{39}$ erg s^{-1} and hard power-law spectral shape, which nature is still unclear. We discuss the properties of all the ULXs in NGC 7456 through a scenario of super-Eddington accretion onto stellar mass compact objects. In particular, although no pulsations were detected, we cannot rule-out that all sources host neutron stars.

I used the ML technique to analyze the field containing ULX-2 and a second source, only $\sim$ 15″ apart. The EPIC spectrum of ULX-2 is well described by an absorbed multicolour blackbody disc plus blackbody model, and I estimated a flux $F_{0.3-10} = (2.8 \pm 0.1) \times 10^{-13}$

erg s^{-1} cm^{-2}, corresponding to a luminosity of $(8.5 \pm 0.2) \times 10^{39}$ erg s^{-1}. Subsequently, I estimated that the second source is very soft (there are 341 ± 39 pn-counts in $0.3 - 2$ keV, and < 60 pn-counts in $2 - 10$ keV) and carries about $5 - 10\%$ of the ULX-2 flux. In fact, it can be modeled by a single absorbed power law with $\Gamma = 3.3^{+2.4}_{-1.2}$ and $N_{\rm H} = (1.9^{+0.4}_{-1.9}) \times 10^{21}$ cm^{-2}. I estimated $F_{0.3-10} = (1.7^{+2.8}_{-0.6}) \times 10^{-14}$ erg s^{-1} cm^{-2}. Assuming the source is in NGC 7456, this corresponds to a luminosity of $\sim 2 \times 10^{38}$ erg s^{-1}, which is well below the ULX luminosity threshold and consistent with the Eddington limit of a NS.

Appendix B

Tables on pulsar properties

In this chapter, I report useful tables with information I used in the Thesis, especially in the figures of Chapters 3 and 8.

B.1 X-ray RPPs

Pulsar Name	P	$\dot{P}$	$\dot{E}$	τ_c	$B_{\rm s}$	DM	d	Spectrum and
PSR	s	s s^{-1}	erg s^{-1}	yrs	G	pc cm^{-3}	kpc	Reference
J0108−1431	0.808	7.70×10^{-17}	5.8×10^{30}	1.7×10^{8}	2.5×10^{11}	2.38(19)	$0.21^{+0.09}_{-0.05}$ P	PL+BB [15]
B0114+58	0.101	5.85×10^{-15}	2.2×10^{35}	2.8×10^{5}	7.8×10^{11}	49.42068(59)	1.77 D	BB [356]
J0205+6449	0.066	1.94×10^{-13}	2.7×10^{37}	5.4×10^{3}	3.6×10^{12}	140.7(3)	3.2 A	PL [375]
B0355+54	0.156	4.39×10^{-15}	4.5×10^{34}	5.6×10^{5}	8.4×10^{11}	57.142(3)	$1.0^{+0.2}_{-0.1}$ P	PL+BB [212]
B0450−18	0.549	5.75×10^{-15}	1.4×10^{33}	1.5×10^{6}	1.8×10^{12}	39.903(3)	$0.4^{+0.2}_{-0.1}$ P	PL This work
B0531+21	0.033	4.21×10^{-13}	4.5×10^{38}	1.3×10^{3}	3.8×10^{12}	56.77118(24)	2.0 ± 0.5 O	PL [29]
J0537−6910	0.016	5.18×10^{-14}	4.9×10^{38}	4.9×10^{3}	9.2×10^{11}	...	50 ± 5 O	PL [193]
J0538+2817	0.143	3.67×10^{-15}	4.9×10^{34}	6.2×10^{5}	7.3×10^{11}	39.57(1)	1.3 ± 0.2 P	BB [255]
B0540−69	0.051	4.79×10^{-13}	1.5×10^{38}	1.7×10^{3}	5.0×10^{12}	146.5(2)	50 ± 5 O	PL [271]
B0540+23	0.246	1.54×10^{-14}	4.1×10^{34}	2.5×10^{5}	2.0×10^{12}	77.7026(10)	1.56 D	PL [336]
B0628−28	1.244	7.12×10^{-15}	1.5×10^{32}	2.8×10^{6}	3.0×10^{12}	34.425(1)	$0.32^{+0.05}_{-0.04}$ P	PL+BB [356]
J0631+1036	0.288	1.05×10^{-13}	1.7×10^{35}	4.4×10^{4}	5.5×10^{12}	125.36(1)	2.1 D	PL [411]
J0633+1746	0.237	1.10×10^{-14}	3.3×10^{34}	3.4×10^{5}	1.6×10^{12}	2.89(2)	$0.25^{+0.23}_{-0.08}$ P	PL+2BB [79]
B0656+14	0.385	5.49×10^{-14}	3.8×10^{34}	1.1×10^{5}	4.7×10^{12}	13.94(9)	0.28 ± 0.03 P	PL+2BB [79]
J0726−2612	3.442	2.93×10^{-13}	2.8×10^{32}	1.9×10^{5}	3.2×10^{13}	69.4(4)	1 O	2BB [358]
J0729−1448	0.252	1.13×10^{-13}	2.8×10^{35}	3.5×10^{4}	5.4×10^{12}	91.7(2)	2.68 D	PL [203]
B0823+26	0.531	1.71×10^{-15}	4.5×10^{32}	4.9×10^{6}	9.6×10^{11}	19.47633(18)	$0.32^{+0.08}_{-0.05}$ P	2BB [163]
B0833−45	0.089	1.25×10^{-13}	6.9×10^{36}	1.1×10^{4}	3.4×10^{12}	67.97(2)	0.28 ± 0.02 P	PL+BB [305]
B0834+06	1.274	6.80×10^{-15}	1.3×10^{32}	3.0×10^{6}	3.0×10^{12}	12.864(4)	0.19 D	BB [114]
J0855−4644	0.065	7.26×10^{-15}	1.1×10^{36}	1.4×10^{5}	6.9×10^{11}	236.4(1)	0.75 A	PL [3]
B0906−49	0.107	1.52×10^{-14}	4.9×10^{35}	1.1×10^{5}	1.3×10^{12}	180.37(5)	$1.0^{+1.7}_{-0.7}$ P	PL [203]
B0919+06	0.431	1.37×10^{-14}	6.8×10^{33}	5.0×10^{5}	2.5×10^{12}	27.2986(5)	$1.1^{+0.2}_{-0.1}$ P	PL [356]
B0943+10	1.098	3.49×10^{-15}	1.0×10^{32}	5.0×10^{6}	2.0×10^{12}	15.31845(90)	0.89 D	PL+BB [357]
B0950+08	0.253	2.30×10^{-16}	5.6×10^{32}	1.8×10^{7}	2.4×10^{11}	2.96927(8)	0.261 ± 0.005 P	PL+BB [449]
J1016−5857	0.107	8.08×10^{-14}	2.6×10^{36}	2.1×10^{4}	3.0×10^{12}	394.48(9)	3.16 D	PL [200]

Continued on next page

Table B.1 – continued from previous page

Pulsar Name PSR	P s	$\dot{P}$ s s^{-1}	$\dot{E}$ erg s^{-1}	τ_c yrs	B_s G	DM pc cm^{-3}	d kpc	Spectrum and Reference
J1028−5819	0.091	1.61×10^{-14}	8.3×10^{35}	9.0×10^{4}	1.2×10^{12}	96.525(2)	1.42 D	PL [203]
B1046−58	0.124	9.63×10^{-14}	2.0×10^{36}	2.0×10^{4}	3.5×10^{12}	128.679(4)	$2.9^{+1.2}_{-0.7}$ P	PL [122]
B1055−52	0.197	5.83×10^{-15}	3.0×10^{34}	5.3×10^{5}	1.1×10^{12}	29.69(1)	0.35 A	PL+2BB [79]
J1101−6101	0.063	8.60×10^{-15}	1.4×10^{36}	1.2×10^{5}	7.4×10^{11}	...	7 ± 1 A	PL [300]
J1105−6107	0.063	1.58×10^{-14}	2.5×10^{36}	6.3×10^{4}	1.0×10^{12}	271.24(1)	2.36 D	PL [132]
J1112−6103	0.065	3.15×10^{-14}	4.5×10^{36}	3.3×10^{4}	1.4×10^{12}	599.1(7)	4.5 D	PL [336]
J1119−6127	0.408	4.02×10^{-12}	2.3×10^{36}	1.6×10^{3}	4.1×10^{13}	704.8(2)	8.4 A	PL+BB [367]
J1124−5916	0.135	7.53×10^{-13}	1.2×10^{37}	2.9×10^{3}	1.0×10^{13}	330(2)	5^{+3}_{-2} P	PL [182]
B1133+16	1.188	3.73×10^{-15}	8.8×10^{31}	5.0×10^{6}	2.1×10^{12}	4.84066(34)	0.35 ± 0.02 P	PL [356]
J1154−6250	0.282	5.59×10^{-16}	9.8×10^{32}	8.0×10^{6}	4.0×10^{11}	74(6)	1.36 D	BB [188]
B1221−63	0.216	4.95×10^{-15}	1.9×10^{34}	6.9×10^{5}	1.1×10^{12}	97.686(4)	4 ± 2 P	PL [336]
J1301−6310	0.664	5.64×10^{-14}	7.6×10^{33}	1.9×10^{5}	6.2×10^{12}	86.1(12)	1.46 D	PL [336]
B1338−62	0.193	2.53×10^{-13}	1.4×10^{36}	1.2×10^{4}	7.1×10^{12}	719.65(5)	12.6 D	PL [336]
J1357−6429	0.166	3.60×10^{-13}	3.1×10^{36}	7.3×10^{3}	7.8×10^{12}	128.5(7)	3.1 D	PL+BB [61]
J1400−6325	0.031	3.89×10^{-14}	5.1×10^{37}	1.3×10^{4}	1.1×10^{12}	563(4)	7 A	PL [353]
J1420−6048	0.068	8.32×10^{-14}	1.0×10^{37}	1.3×10^{4}	2.4×10^{12}	360.15(6)	5.63 D	PL [360]
B1451−68	0.263	9.83×10^{-17}	2.1×10^{32}	4.2×10^{7}	1.6×10^{11}	8.639(7)	$0.43^{+0.06}_{-0.05}$ D	PL [325]
J1509−5850	0.089	9.17×10^{-15}	5.2×10^{35}	1.5×10^{5}	9.1×10^{11}	142.1(1)	3.37 D	PL [183]
B1509−58	0.151	1.53×10^{-12}	1.8×10^{37}	1.6×10^{3}	1.5×10^{13}	252.5(3)	$4.4^{+1.3}_{-0.8}$ P	PL [27]
J1524−5625	0.078	3.90×10^{-14}	3.2×10^{36}	3.2×10^{4}	1.8×10^{12}	152.2(1)	3.38 D	PL [203]
J1531−5610	0.084	1.37×10^{-14}	9.1×10^{35}	9.7×10^{4}	1.1×10^{12}	110.41(3)	2.84 D	PL [203]
J1617−5055	0.069	1.35×10^{-13}	1.6×10^{37}	8.1×10^{3}	3.1×10^{12}	467(5)	4.74 D	PL [201]
J1640−4631	0.206	9.76×10^{-13}	4.4×10^{36}	3.4×10^{3}	1.4×10^{13}	...	12.75 ± 0.75 A	PL [131]
J1702−4128	0.182	5.23×10^{-14}	3.4×10^{35}	5.5×10^{4}	3.1×10^{12}	367.1(7)	3.97 D	PL [203]
B1706−44	0.102	9.30×10^{-14}	3.4×10^{36}	1.8×10^{4}	3.1×10^{12}	75.68(3)	$2.6^{+0.5}_{-0.6}$ P	PL+BB [256]
J1718−3718	3.379	1.61×10^{-12}	1.6×10^{33}	3.3×10^{4}	7.5×10^{13}	371.1(17)	3.92 D	BB [459]
J1718−3825	0.075	1.32×10^{-14}	1.2×10^{36}	8.9×10^{4}	1.0×10^{12}	247.46(6)	3.49 D	PL [203]
B1719−37	0.236	1.09×10^{-14}	3.3×10^{34}	3.5×10^{5}	1.6×10^{12}	99.49(3)	2.48 D	BB [293]
J1732−3131	0.197	2.80×10^{-14}	1.5×10^{35}	1.1×10^{5}	2.4×10^{12}	15.44(32)	0.64 D	PL [349]
J1734−3333	1.169	2.28×10^{-12}	5.6×10^{34}	8.1×10^{3}	5.2×10^{13}	578(9)	4.46 D	BB [291]
J1740+1000	0.154	2.15×10^{-14}	2.3×10^{35}	1.1×10^{5}	1.8×10^{12}	23.897(25)	1.23 D	PL+2BB [202]
J1741−2054	0.414	1.70×10^{-14}	9.5×10^{33}	3.9×10^{5}	2.7×10^{12}	4.7(1)	$0.27^{+0.08}_{-0.00}$ D	PL+BB [250]
J1747−2809	0.052	1.56×10^{-13}	4.3×10^{37}	5.3×10^{3}	2.9×10^{12}	1133(3)	8.5 A	PL [323]
J1747−2958	0.099	6.13×10^{-14}	2.5×10^{36}	2.5×10^{4}	2.5×10^{12}	101.5(16)	2.52 D	PL [95]
B1757−24	0.125	1.28×10^{-13}	2.6×10^{36}	1.6×10^{4}	4.0×10^{12}	291.55(5)	5 A	PL [207]
B1800−21	0.134	1.34×10^{-13}	2.2×10^{36}	1.6×10^{4}	4.3×10^{12}	233.99(5)	$4.4^{+0.5}_{-0.6}$ P	PL [200]
J1809−1917	0.083	2.55×10^{-14}	1.8×10^{36}	5.1×10^{4}	1.5×10^{12}	197.1(4)	3.27 D	PL [198]
J1811−1925	0.065	4.40×10^{-14}	6.4×10^{36}	2.3×10^{4}	1.7×10^{12}	...	5.0 ± 1.5 A	PL [359]
J1813−1749	0.045	1.27×10^{-13}	5.6×10^{37}	5.6×10^{3}	2.4×10^{12}	...	8.5 ± 3.5 A	PL [157]
J1819−1458	4.263	5.63×10^{-13}	2.9×10^{32}	1.2×10^{5}	5.0×10^{13}	196(4)	3.3 D	BB [274]
B1822−09	0.769	5.25×10^{-14}	4.6×10^{33}	2.3×10^{5}	6.4×10^{12}	19.3833(9)	$0.3^{+0.7}_{-0.2}$ P	2BB [162]
B1822−14	0.279	2.27×10^{-14}	4.1×10^{34}	1.9×10^{5}	2.5×10^{12}	352.23(4)	4.44 D	BB [49]
B1823−13	0.101	7.53×10^{-14}	2.8×10^{36}	2.1×10^{4}	2.8×10^{12}	231(10)	3.61 D	PL [306]
B1830−08	0.085	9.17×10^{-15}	5.8×10^{35}	1.5×10^{5}	8.9×10^{11}	410.95(10)	4.5 ± 0.5 P	PL [204]
J1833−1034	0.062	2.02×10^{-13}	3.4×10^{37}	4.8×10^{3}	3.6×10^{12}	169.5(1)	4.1 ± 0.3 P	PL [254]

Continued on next page

Table B.1 – continued from previous page

Pulsar Name PSR	P s	$\dot{P}$ s s^{-1}	$\dot{E}$ erg s^{-1}	τ_c yrs	B_s G	DM pc cm^{-3}	d kpc	Spectrum and Reference
J1838−0655	0.070	4.93×10^{-14}	5.5×10^{36}	2.3×10^{4}	1.9×10^{12}	...	6.6 ± 0.9 A	PL [124]
J1846−0258	0.327	7.11×10^{-12}	8.1×10^{36}	7.3×10^{2}	4.9×10^{13}	...	$5.8^{+0.5}_{-0.4}$ P	PL [158]
J1849−0001	0.039	1.42×10^{-14}	9.8×10^{36}	4.3×10^{4}	7.5×10^{11}	...	7.0 ± 2.1 A	PL [129]
B1853+01	0.267	2.08×10^{-13}	4.3×10^{35}	2.0×10^{4}	7.5×10^{12}	96.74(12)	3.3 A	PL [313]
J1856+0245	0.081	6.21×10^{-14}	4.6×10^{36}	2.1×10^{4}	2.3×10^{12}	623.5(2)	6.32 D	PL [362]
J1907+0602	0.107	8.68×10^{-14}	2.8×10^{36}	1.9×10^{4}	3.1×10^{12}	82.1(11)	2.37 A	PL [2]
B1916+14	1.181	2.12×10^{-13}	5.1×10^{33}	8.8×10^{4}	1.6×10^{13}	27.202(17)	1.3 D	BB [460]
J1930+1852	0.137	7.51×10^{-13}	1.2×10^{37}	2.9×10^{3}	1.0×10^{13}	308(4)	7^{+3}_{-2} P	PL [55]
B1929+10	0.227	1.16×10^{-15}	3.9×10^{33}	3.1×10^{6}	5.2×10^{11}	3.18321(16)	$0.31^{+0.09}_{-0.06}$ P	PL+BB [276]
B1951+32	0.040	5.84×10^{-15}	3.7×10^{36}	1.1×10^{5}	4.9×10^{11}	45.006(19)	3 ± 2 P	PL [28]
J2021+3651	0.104	9.57×10^{-14}	3.4×10^{36}	1.7×10^{4}	3.2×10^{12}	367.5(10)	10^{+2}_{-4} A	PL [167]
J2022+3842	0.049	8.61×10^{-14}	3.0×10^{37}	8.9×10^{3}	2.1×10^{12}	429.1(5)	10 A	PL [13]
J2043+2740	0.096	1.27×10^{-15}	5.6×10^{34}	1.2×10^{6}	3.5×10^{11}	21.02064(15)	1.48 D	PL [32]
B2224+65	0.683	9.66×10^{-15}	1.2×10^{33}	1.1×10^{6}	2.6×10^{12}	36.44362(51)	1 A	PL [184]
J2229+6114	0.052	7.83×10^{-14}	2.2×10^{37}	1.1×10^{4}	2.0×10^{12}	204.97(2)	3 A	PL [141]
B2334+61	0.495	1.93×10^{-13}	6.3×10^{34}	4.1×10^{4}	9.9×10^{12}	58.41(15)	$3.1^{+0.2}_{-2.4}$ A	BB [257]

Table B.1: Properties of the 86 known X-ray isolated pulsars. The distance measure methods are: A, association; D, dispersion measure; P, parallax; O, other; see the corresponding reference.

B.2 Nonthermal X-ray RPPs

Pulsar Name PSR	N_H 10^{22} cm^{-2}	Γ	PL Norm	F_{2-10} erg s^{-1} cm^{-2}	L_{2-10} erg s^{-1}	$\log \eta_{2-10}$	Spectrum and Reference
J0108−1431	$0.021^{+0.017}_{-0.012}$	$2.45^{+0.33}_{-0.27}$	$(3.6 \pm 0.4) \times 10^{-6}$	$(4.8 \pm 0.6) \times 10^{-15}$	$(2.5 \pm 0.3) \times 10^{28}$	−2.4	PL+BB [15]
J0205+6449	0.34 ± 0.01	1.67 ± 0.03	$(1.4 \pm 0.7) \times 10^{-4}$	$(5.9 \pm 3.1) \times 10^{-13}$	$(7.2 \pm 3.7) \times 10^{32}$	−4.6	PL [375]
B0355+54	6.1	$1.45^{+0.21}_{-0.24}$	$(5.1 \pm 1.6) \times 10^{-6}$	$(3.1 \pm 1.0) \times 10^{-14}$	$(3.7 \pm 1.2) \times 10^{30}$	−4.1	PL+BB [212]
B0450−18	0.12	2.5	$(1.3 \pm 0.4) \times 10^{-6}$	$(1.6 \pm 0.5) \times 10^{-15}$	$(3.0 \pm 0.9) \times 10^{28}$	−4.7	PL This work
B0531+21	0.345 ± 0.002	1.63 ± 0.07	$(4.9 \pm 2.0) \times 10^{-1}$	$(2.2 \pm 0.9) \times 10^{-9}$	$(1.1 \pm 0.4) \times 10^{36}$	−2.6	PL [29]
J0537−6910	0.95 ± 0.07	1.8 ± 0.1	$(3.4 \pm 1.9) \times 10^{-3}$	$(1.2 \pm 0.7) \times 10^{-11}$	$(3.5 \pm 2.0) \times 10^{36}$	−2.1	PL [193]
B0540−69	0.46	1.92 ± 0.11	$(4.8 \pm 2.8) \times 10^{-4}$	$(1.4 \pm 0.8) \times 10^{-12}$	$(4.2 \pm 2.4) \times 10^{35}$	−2.5	PL [271]
B0540+23	0.24	1.7	$(2.0 \pm 0.5) \times 10^{-6}$	$(8.4 \pm 2.2) \times 10^{-15}$	$(2.4 \pm 0.6) \times 10^{30}$	−4.2	PL [336]
B0628−28	0.1	2.95 ± 0.06	$(1.44 \pm 0.05) \times 10^{-5}$	$(9.8 \pm 0.3) \times 10^{-15}$	$(1.21 \pm 0.04) \times 10^{29}$	−3.1	PL+BB [356]
J0631+1036	$0.2^{+0.2}_{-0.1}$	$2.30^{+0.38}_{-0.30}$	$(6.9 \pm 3.7) \times 10^{-5}$	$(1.1 \pm 0.6) \times 10^{-13}$	$(6.1 \pm 3.3) \times 10^{31}$	−3.5	PL [411]
J0633+1746	0.0107	1.7 ± 0.1	$(6.7 \pm 0.7) \times 10^{-5}$	$(2.7 \pm 0.3) \times 10^{-13}$	$(2.0 \pm 0.2) \times 10^{30}$	−4.2	PL+2BB [79]
B0656+14	0.043 ± 0.002	2.1 ± 0.3	$(4.3^{+0.6}_{-1.5}) \times 10^{-5}$	$(9.6^{+1.3}_{-3.3}) \times 10^{-14}$	$(9.0^{+1.3}_{-3.1}) \times 10^{29}$	−4.6	PL+2BB [79]
J0729−1448	0.28	1.5	$(1.8 \pm 0.5) \times 10^{-6}$	$(1.0 \pm 0.3) \times 10^{-14}$	$(8.7 \pm 2.5) \times 10^{30}$	−4.5	PL [203]
B0833−45	0.022 ± 0.003	2.7 ± 0.4	$(1.1 \pm 0.1) \times 10^{-3}$	$(1.02 \pm 0.10) \times 10^{-12}$	$(9.6 \pm 0.9) \times 10^{30}$	−5.9	PL+BB [305]
J0855−4644	$0.64^{+0.13}_{-0.11}$	$1.24^{+0.09}_{-0.10}$	$(3.0^{+0.3}_{-0.6}) \times 10^{-5}$	$(2.6^{+0.3}_{-0.5}) \times 10^{-13}$	$(1.8^{+0.2}_{-0.3}) \times 10^{31}$	−4.8	PL [3]
B0906−49	0.56	1.5	$(8.2 \pm 3.1) \times 10^{-7}$	$(4.6 \pm 1.7) \times 10^{-15}$	$(5.5 \pm 2.1) \times 10^{29}$	−6.0	PL [203]
B0919+06	0.08	3.1 ± 0.2	$(3.6 \pm 0.4) \times 10^{-6}$	$(2.0 \pm 0.2) \times 10^{-15}$	$(2.9 \pm 0.3) \times 10^{29}$	−4.4	PL [356]

Continued on next page

Table B.2 – continued from previous page

Pulsar Name PSR	$N_{\rm H}$ 10^{22} cm^{-2}	Γ	PL Norm	F_{2-10} erg s^{-1} cm^{-2}	L_{2-10} erg s^{-1}	$\log \eta_{2-10}$	Spectrum and Reference
B0943+10 (Q)	0.043	$2.6^{+0.2}_{-0.1}$	$(2.9^{+0.4}_{-0.5}) \times 10^{-6}$	$(3.2^{+0.4}_{-0.5}) \times 10^{-15}$	$(3.0^{+0.4}_{-0.5}) \times 10^{29}$	-2.5	PL+BB [357]
B0943+10 (B)	0.043	$2.2^{+0.2}_{-0.3}$	$(1.0 \pm 0.3) \times 10^{-6}$	$(1.9 \pm 0.6) \times 10^{-15}$	$(1.8 \pm 0.5) \times 10^{29}$	-2.8	PL+BB [357]
B0950+08	0.033 ± 0.022	1.75 ± 0.15	$(1.5 \pm 0.1) \times 10^{-5}$	$(5.7 \pm 0.4) \times 10^{-14}$	$(4.6 \pm 0.3) \times 10^{29}$	-3.1	PL+BB [449]
J1016−5857	1.2	1.5 ± 0.4	$(6.8 \pm 2.7) \times 10^{-6}$	$(3.8 \pm 1.5) \times 10^{-14}$	$(4.6 \pm 1.8) \times 10^{31}$	-4.8	PL [200]
J1028−5819	0.3	1.5	$(7.3 \pm 1.3) \times 10^{-6}$	$(4.1 \pm 0.7) \times 10^{-14}$	$(9.8 \pm 1.8) \times 10^{30}$	-4.9	PL [203]
B1046−58	$0.9^{+0.4}_{-0.2}$	$1.7^{+0.4}_{-0.2}$	$(1.6 \pm 0.8) \times 10^{-5}$	$(6.4 \pm 3.2) \times 10^{-14}$	$(6.5 \pm 3.3) \times 10^{31}$	-4.5	PL [122]
B1055−52	0.027 ± 0.002	1.7 ± 0.1	$(1.9^{+0.3}_{-0.2}) \times 10^{-5}$	$(7.8^{+1.2}_{-0.8}) \times 10^{-14}$	$(1.1 \pm 0.1) \times 10^{30}$	-4.4	PL+2BB [79]
J1101−6101	1.0 ± 0.2	1.1 ± 0.2	$(5.6 \pm 0.6) \times 10^{-5}$	$(6.1 \pm 0.6) \times 10^{-13}$	$(3.6 \pm 0.4) \times 10^{33}$	-2.6	PL [300]
J1105−6107	0.7 ± 0.2	1.8 ± 0.4	$(1.8 \pm 0.2) \times 10^{-4}$	$(6.4 \pm 0.7) \times 10^{-13}$	$(4.3 \pm 0.5) \times 10^{32}$	-3.8	PL [132]
J1112−6103	$1.2^{+1.1}_{-1.0}$	1.5 ± 0.7	$(1.3^{+2.3}_{-0.8}) \times 10^{-5}$	$(7.3^{+12.9}_{-4.5}) \times 10^{-14}$	$(1.8^{+3.1}_{-1.1}) \times 10^{32}$	-4.4	PL [336]
J1119−6127	$1.8^{+1.5}_{-0.6}$	$1.9^{+1.1}_{-0.9}$	$(1.5^{+2.3}_{-0.9}) \times 10^{-5}$	$(4.5^{+6.9}_{-2.7}) \times 10^{-14}$	$(3.8^{+5.8}_{-2.3}) \times 10^{32}$	-3.8	PL+BB [367]
J1124−5916	0.31 ± 0.04	1.6 ± 0.1	$(2.2 \pm 1.1) \times 10^{-5}$	$(1.1 \pm 0.5) \times 10^{-13}$	$(3.2 \pm 1.6) \times 10^{32}$	-4.6	PL [182]
B1133+16	0.015	2.9 ± 0.2	$(2.9 \pm 0.2) \times 10^{-6}$	$(2.1 \pm 0.1) \times 10^{-15}$	$(3.1 \pm 0.2) \times 10^{28}$	-3.5	PL [356]
B1221−63	0.3	1.7	$(2.6 \pm 0.8) \times 10^{-6}$	$(1.0 \pm 0.3) \times 10^{-14}$	$(2.0 \pm 0.6) \times 10^{31}$	-3.0	PL [336]
J1301−6310	< 0.39	$3.4^{+0.8}_{-0.6}$	$(3.2 \pm 0.7) \times 10^{-6}$	$(1.2 \pm 0.3) \times 10^{-15}$	$(3.2 \pm 0.7) \times 10^{29}$	-4.4	PL [336]
B1338−62	4 ± 3	1.1 ± 0.7	$(1.5^{+2.1}_{-1.0}) \times 10^{-6}$	$(1.6^{+2.3}_{-1.1}) \times 10^{-14}$	$(3.1^{+4.3}_{-2.1}) \times 10^{32}$	-3.7	PL [336]
J1357−6429	$0.47^{+0.36}_{-0.28}$	$1.72^{+0.55}_{-0.63}$	$(9.8^{+9.1}_{-5.8}) \times 10^{-6}$	$(3.9^{+3.6}_{-2.3}) \times 10^{-14}$	$(4.5^{+4.1}_{-2.6}) \times 10^{31}$	-4.8	PL+BB [61]
J1400−6325	2.09 ± 0.12	1.22 ± 0.15	$(2.2 \pm 0.6) \times 10^{-4}$	$(1.9 \pm 0.5) \times 10^{-12}$	$(1.1 \pm 0.3) \times 10^{34}$	-3.6	PL [353]
J1420−6048	2.2	1.6 ± 0.4	$(9.8 \pm 5.0) \times 10^{-4}$	$(4.7 \pm 2.4) \times 10^{-12}$	$(1.8 \pm 0.9) \times 10^{34}$	-2.8	PL [360]
B1451−68	0.026	1.7 ± 0.2	$(6.6 \pm 0.9) \times 10^{-6}$	$(2.7 \pm 0.4) \times 10^{-14}$	$(6.0 \pm 0.8) \times 10^{29}$	-2.6	PL [325]
J1509−5850	$0.80^{+0.23}_{-0.21}$	$1.0^{+0.2}_{-0.3}$	$(5.1 \pm 1.6) \times 10^{-6}$	$(6.5 \pm 2.1) \times 10^{-14}$	$(8.9 \pm 2.8) \times 10^{31}$	-3.8	PL [183]
B1509−58	0.95 ± 0.03	1.19 ± 0.04	$(2.9 \pm 0.2) \times 10^{-3}$	$(2.7 \pm 0.2) \times 10^{-11}$	$(6.2 \pm 0.5) \times 10^{34}$	-2.4	PL [27]
J1524−5625	0.47	1.5	$(2.7 \pm 1.2) \times 10^{-6}$	$(1.5 \pm 0.6) \times 10^{-14}$	$(2.1 \pm 0.9) \times 10^{31}$	-5.2	PL [203]
J1531−5610	0.34	1.5	$(6.2 \pm 4.1) \times 10^{-6}$	$(3.4 \pm 2.3) \times 10^{-14}$	$(3.3 \pm 2.2) \times 10^{31}$	-4.4	PL [203]
J1617−5055	3.45 ± 0.14	1.14 ± 0.06	$(3.5^{+0.7}_{-0.5}) \times 10^{-4}$	$(3.6^{+0.7}_{-0.5}) \times 10^{-12}$	$(9.6 \pm 1.3) \times 10^{33}$	-3.2	PL [201]
J1640−4631	18 ± 6	$1.3^{+0.9}_{-0.5}$	$(2.3 \pm 0.5) \times 10^{-5}$	$(1.8 \pm 0.4) \times 10^{-13}$	$(3.5 \pm 0.8) \times 10^{33}$	-3.1	PL [131]
J1702−4128	1.13	1.5	$(4.9 \pm 3.7) \times 10^{-6}$	$(2.7 \pm 2.1) \times 10^{-14}$	$(5.2 \pm 4.0) \times 10^{31}$	-3.8	PL [203]
B1706−44	$0.45^{+0.07}_{-0.04}$	$1.49^{+0.09}_{-0.08}$	$(2.8 \pm 1.0) \times 10^{-5}$	$(1.6^{+1.2}_{-0.6}) \times 10^{-13}$	$(1.3^{+0.9}_{-0.5}) \times 10^{32}$	-4.4	PL+BB [256]
J1718−3825	0.76	1.5	$(9.0 \pm 2.3) \times 10^{-6}$	$(5.0 \pm 1.3) \times 10^{-14}$	$(7.3 \pm 1.8) \times 10^{31}$	-4.2	PL [203]
J1732−3131	0.046	1.5	$(8.3 \pm 3.3) \times 10^{-6}$	$(4.7 \pm 1.9) \times 10^{-14}$	$(2.3 \pm 0.9) \times 10^{30}$	-4.8	PL [349]
J1740+1000	$0.097^{+0.015}_{-0.013}$	1.6 ± 0.6	$(2.3 \pm 0.3) \times 10^{-6}$	$(1.1 \pm 0.1) \times 10^{-14}$	$(2.0 \pm 0.3) \times 10^{30}$	-5.1	PL+2BB [202]
J1741−2054	0.121 ± 0.001	2.68 ± 0.04	$(1.13 \pm 0.03) \times 10^{-4}$	$(1.11 \pm 0.03) \times 10^{-13}$	$(9.6 \pm 0.2) \times 10^{29}$	-4.0	PL+BB [250]
J1747−2809	$13.9^{+1.3}_{-1.2}$	1.93 ± 0.18	$(2.0 \pm 0.2) \times 10^{-3}$	$(5.7 \pm 0.6) \times 10^{-12}$	$(5.0 \pm 0.5) \times 10^{34}$	-2.9	PL [323]
J1747−2958	2.7 ± 0.1	1.80 ± 0.08	$(2.2 \pm 1.3) \times 10^{-3}$	$(7.6 \pm 4.5) \times 10^{-12}$	$(5.8 \pm 3.4) \times 10^{33}$	-2.6	PL [95]
B1757−24	3.5	$1.6^{+0.6}_{-0.5}$	$(1.1 \pm 0.6) \times 10^{-4}$	$(5.4 \pm 3.1) \times 10^{-13}$	$(1.6 \pm 0.9) \times 10^{33}$	-3.2	PL [207]
B1800−21	1.38	1.4 ± 0.6	$(3.8 \pm 2.2) \times 10^{-5}$	$(2.5 \pm 1.4) \times 10^{-13}$	$(5.9 \pm 3.3) \times 10^{32}$	-3.6	PL [200]
J1809−1917	0.7	1.23 ± 0.62	$(2.8 \pm 2.2) \times 10^{-6}$	$(2.4 \pm 1.9) \times 10^{-14}$	$(3.1 \pm 2.4) \times 10^{31}$	-4.8	PL [198]
J1811−1925	$2.22^{+0.78}_{-0.57}$	$0.97^{+0.39}_{-0.32}$	$(1.87 \pm 0.08) \times 10^{-4}$	$(2.5 \pm 0.1) \times 10^{-12}$	$(7.5 \pm 0.3) \times 10^{33}$	-2.9	PL [359]
J1813−1749	$9.80^{+0.07}_{-1.10}$	1.3 ± 0.3	$(1.7 \pm 0.4) \times 10^{-4}$	$(1.3 \pm 0.3) \times 10^{-12}$	$(1.1 \pm 0.3) \times 10^{34}$	-3.7	PL [157]
B1823−13	0.7	$1.98^{+0.40}_{-0.36}$	$(7.0 \pm 4.2) \times 10^{-6}$	$(1.9 \pm 1.1) \times 10^{-14}$	$(2.9 \pm 1.8) \times 10^{31}$	-5.0	PL [306]
B1830−08	3.9 ± 1.9	2.3 ± 0.8	$(1.8^{+9.0}_{-0.8}) \times 10^{-4}$	$(3.0^{+15.0}_{-1.3}) \times 10^{-13}$	$(7.2^{+36.2}_{-3.2}) \times 10^{32}$	-2.9	PL [204]
J1833−1034	$2.24^{+0.09}_{-0.10}$	$1.47^{+0.05}_{-0.06}$	$(7.7 \pm 0.6) \times 10^{-4}$	$(4.5 \pm 0.4) \times 10^{-12}$	$(9.1 \pm 0.7) \times 10^{33}$	-3.6	PL [254]
J1838−0655	$4.5^{+0.7}_{-0.8}$	0.5 ± 0.2	$(2.9 \pm 0.3) \times 10^{-4}$	$(8.8 \pm 0.9) \times 10^{-12}$	$(4.6 \pm 0.5) \times 10^{34}$	-2.1	PL [124]
J1846−0258	3.96	1.39 ± 0.04	$(1.1 \pm 0.4) \times 10^{-3}$	$(7.1 \pm 2.8) \times 10^{-12}$	$(2.9 \pm 1.1) \times 10^{34}$	-2.5	PL [158]

Continued on next page

Table B.2 – continued from previous page

Pulsar Name PSR	$N_{\rm H}$ 10^{22} cm^{-2}	Γ	PL Norm	F_{2-10} erg s^{-1} cm^{-2}	L_{2-10} erg s^{-1}	$\log \eta_{2-10}$	Spectrum and Reference
J1849−0001	4.3 ± 0.6	1.1 ± 0.2	$(3.5 \pm 0.3) \times 10^{-4}$	$(3.8 \pm 0.3) \times 10^{-12}$	$(2.2 \pm 0.2) \times 10^{34}$	−2.6	PL [129]
B1853+01	5	1.28 ± 0.36	$(9.6 \pm 4.2) \times 10^{-6}$	$(7.7 \pm 3.4) \times 10^{-14}$	$(1.0 \pm 0.4) \times 10^{32}$	−3.6	PL [313]
J1856+0245	4	1.5	$(1.5^{+0.4}_{-1.4}) \times 10^{-5}$	$(8.3^{+2.5}_{-7.9}) \times 10^{-14}$	$(4.0^{+1.2}_{-3.8}) \times 10^{32}$	−4.1	PL [362]
J1907+0602	$1.8^{+1.3}_{-0.9}$	$0.9^{+0.6}_{-0.4}$	$(2.9^{+0.5}_{-1.2}) \times 10^{-5}$	$(4.4^{+0.7}_{-1.8}) \times 10^{-13}$	$(3.0^{+0.5}_{-1.2}) \times 10^{32}$	−4.0	PL [2]
J1930+1852	1.6	$1.35^{+0.06}_{-0.10}$	$(2.6 \pm 1.4) \times 10^{-4}$	$(1.9 \pm 1.0) \times 10^{-12}$	$(1.1 \pm 0.6) \times 10^{34}$	−3.0	PL [55]
B1929+10	< 0.040	$1.73^{+0.46}_{-0.66}$	$(1.6^{+1.7}_{-0.3}) \times 10^{-5}$	$(6.4^{+6.8}_{-1.1}) \times 10^{-14}$	$(7.3^{+7.8}_{-1.3}) \times 10^{29}$	−3.7	PL+BB [276]
B1951+32	0.3	1.74 ± 0.03	$(4.9 \pm 2.0) \times 10^{-4}$	$(1.9 \pm 0.8) \times 10^{-12}$	$(2.0 \pm 0.8) \times 10^{33}$	−3.3	PL [28]
J2021+3651	$0.78^{+0.17}_{-0.14}$	$1.70^{+0.23}_{-0.15}$	$(1.9 \pm 0.8) \times 10^{-4}$	$(7.8 \pm 3.3) \times 10^{-13}$	$(9.3 \pm 4.0) \times 10^{33}$	−2.6	PL [167]
J2022+3842	$2.32^{+0.29}_{-0.26}$	$0.93^{+0.10}_{-0.09}$	$(4.5^{+0.8}_{-0.7}) \times 10^{-5}$	$(6.5^{+1.2}_{-1.0}) \times 10^{-13}$	$(7.8 \pm 1.2) \times 10^{33}$	−3.6	PL [13]
J2043+2740	< 0.02	$3.1^{+1.1}_{-0.6}$	$(3.6 \pm 1.9) \times 10^{-6}$	$(2.0 \pm 1.1) \times 10^{-15}$	$(5.4 \pm 2.8) \times 10^{29}$	−5.0	PL [32]
B2224+65	$0.25^{+0.10}_{-0.07}$	$2.2^{+0.2}_{-0.3}$	$(8.3 \pm 1.6) \times 10^{-6}$	$(1.6 \pm 0.3) \times 10^{-14}$	$(1.9^{+0.5}_{-0.4}) \times 10^{30}$	−2.8	PL [184]
J2229+6114	0.63 ± 0.13	0.99 ± 0.27	$(3.7 \pm 1.9) \times 10^{-5}$	$(4.9 \pm 2.5) \times 10^{-13}$	$(5.3 \pm 2.7) \times 10^{32}$	−4.6	PL [141]

Table B.2: Nonthermal emission properties of the 72 sampled RPPs.

Bibliography

[1] Abdo, A. A., Ackermann, M., Ajello, M., et al. 2010, ApJL, 725, L73. doi: 10.1088/2041-8205/725/1/L73

[2] —. 2010, ApJ, 711, 64. doi: 10.1088/0004-637X/711/1/64

[3] Acero, F., Gallant, Y., Ballet, J., Renaud, M., & Terrier, R. 2013, A&A, 551, A7. doi: 10.1051/0004-6361/201220799

[4] Aguilera, D. N., Pons, J. A., & Miralles, J. A. 2008, A&A, 486, 255. doi: 10.1051/0004-6361:20078786

[5] —. 2008, ApJL, 673, L167. doi: 10.1086/527547

[6] Alford, M. G. & Schwenzer, K. 2014, ApJ, 781, 26. doi: 10.1088/0004-637X/781/1/26

[7] Alfvén, H. & Herlofson, N. 1950, PhRv, 78, 616. doi: 10.1103/PhysRev.78.616

[8] Allafort, A., Baldini, L., Ballet, J., et al. 2013, ApJL, 777, L2. doi: 10.1088/2041-8205/777/1/L2

[9] Allen, M. P. & Horvath, J. E. 2004, ApJ, 616, 346. doi: 10.1086/424836

[10] Antoniadis, J., Freire, P. C. C., Wex, N., et al. 2013, Science, 340, 448. doi: 10.1126/science.1233232

[11] Arons, J. & Scharlemann, E. T. 1979, ApJ, 231, 854. doi: 10.1086/157250

[12] Arras, P., Cumming, A., & Thompson, C. 2004, ApJL, 608, L49. doi: 10.1086/422337

[13] Arumugasamy, P., Pavlov, G. G., & Kargaltsev, O. 2014, ApJ, 790, 103. doi: 10.1088/0004-637X/790/2/103

[14] Arumugasamy, P., Kargaltsev, O., Posselt, B., Pavlov, G. G., & Hare, J. 2018, ApJ, 869, 97. doi: 10.3847/1538-4357/aaec69

[15] Arumugasamy, P. & Mitra, D. 2019, MNRAS, 489, 4589. doi: 10.1093/mnras/stz2299

[16] Ashworth, Jr., W. B. 1980, JHA, 11, 1. doi: 10.1177/002182868001100102

[17] Atwood, W. B., Abdo, A. A., Ackermann, M., et al. 2009, ApJ, 697, 1071. doi: 10.1088/0004-637X/697/2/1071

[18] Baade, W. 1942, ApJ, 96, 188. doi: 10.1086/144446

[19] Baade, W. & Zwicky, F. 1934, Proc. Nat. Acad. Sci., 20, 259. doi: 10.1073/pnas.20.5.259

[20] Backer, D. C. 1970, Nature, 228, 752. doi: 10.1038/228752a0

[21] —. 1973, ApJ, 182, 245. doi: 10.1086/152134

[22] Bak, P., Tang, C., & Wiesenfeld, K. 1987, PhRvL, 59, 381. doi: 10.1103/PhysRevLett.59.381

[23] Baldo, M. & Schulze, H.-J. 2007, PhRvC, 75, 025802. doi: 10.1103/PhysRevC.75.025802

[24] Baring, M. G. & Harding, A. K. 1998, ApJL, 507, L55. doi: 10.1086/311679

[25] —. 2001, ApJ, 547, 929. doi: 10.1086/318390

[26] Basu, R., Paul, A., & Mitra, D. 2019, MNRAS, 486, 5216. doi: 10.1093/mnras/stz1225

[27] Becker, W. 2009, in Astrophysics and Space Science Library, ed. W. Becker, Vol. 357, 91. doi: 10.1007/978-3-540-76965-1_6

[28] Becker, W. & Truemper, J. 1996, A&AS, 120, 69

[29] —. 1997, A&A, 326, 682. arXiv: astro-ph/9708169

[30] Becker, W., Trümper, J., & Ögelman, H. 1993, in Isolated Pulsars, ed. K. A. van Riper, R. I. Epstein, & C. Ho, 104

[31] Becker, W., Jessner, A., Kramer, M., Testa, V., & Howaldt, C. 2005, ApJ, 633, 367. doi: 10.1086/462399

[32] Becker, W., Weisskopf, M. C., Tennant, A. F., et al. 2004, ApJ, 615, 908. doi: 10.1086/424498

[33] Beloborodov, A. M. 2002, ApJL, 566, L85. doi: 10.1086/339511

[34] Beloborodov, A. M. & Li, X. 2016, ApJ, 833, 261. doi: 10.3847/1538-4357/833/2/261

[35] Bernardini, F., Israel, G. L., Dall'Osso, S., et al. 2009, A&A, 498, 195. doi: 10.1051/0004-6361/200810779

[36] Bethe, H. A. 2014, Supernova Theory (World Scientific Publishing Co. Pte. Ltd.), 147–157

[37] Bhattacharya, D., Wijers, R. A. M. J., Hartman, J. W., & Verbunt, F. 1992, A&A, 254, 198

[38] Bhattacharya, S., Heinke, C. O., Chugunov, A. I., et al. 2017, MNRAS, 472, 3706. doi: 10.1093/mnras/stx2241

[39] Biggs, J. D. 1992, ApJ, 394, 574. doi: 10.1086/171608

[40] Bignami, G. F. & Caraveo, P. A. 1996, ARA&A, 34, 331. doi: 10.1146/annurev.astro.34.1.331

[41] Bignami, G. F., Caraveo, P. A., De Luca, A., & Mereghetti, S. 2003, Nature, 423, 725. doi: 10.1038/nature01703

[42] Bilous, A. V. 2018, A&A, 616, A119. doi: 10.1051/0004-6361/201732106

[43] Bilous, A. V., Kondratiev, V. I., Kramer, M., et al. 2016, A&A, 591, A134. doi: 10.1051/0004-6361/201527702

[44] Blaskiewicz, M., Cordes, J. M., & Wasserman, I. 1991, ApJ, 370, 643. doi: 10.1086/169850

[45] Bogdanov, S. 2013, ApJ, 762, 96. doi: 10.1088/0004-637X/762/2/96

[46] —. 2014, ApJ, 790, 94. doi: 10.1088/0004-637X/790/2/94

[47] Bogdanov, S. & Grindlay, J. E. 2009, ApJ, 703, 1557. doi: 10.1088/0004-637X/703/2/1557

[48] Bogdanov, S., Grindlay, J. E., Heinke, C. O., et al. 2006, ApJ, 646, 1104. doi: 10.1086/505133

[49] Bogdanov, S., Ng, C. Y., & Kaspi, V. M. 2014, ApJL, 792, L36. doi: 10.1088/2041-8205/792/2/L36

[50] Bowyer, S., Byram, E. T., Chubb, T. A., & Friedman, H. 1964, Nature, 201, 1307. doi: 10.1038/2011307a0

[51] Brinkmann, W. 1980, A&A, 82, 352

[52] Brisken, W. F., Benson, J. M., Goss, W. M., & Thorsett, S. E. 2002, ApJ, 571, 906. doi: 10.1086/340098

[53] Burbidge, G. 1957, ASPL, 7, 257

[54] Burgay, M., Joshi, B. C., D'Amico, N., et al. 2006, MNRAS, 368, 283. doi: 10.1111/j.1365-2966.2006.10100.x

[55] Camilo, F., Lorimer, D. R., Bhat, N. D. R., et al. 2002, ApJL, 574, L71. doi: 10.1086/342351

[56] Camilo, F., Reynolds, J., Johnston, S., et al. 2007, ApJL, 659, L37. doi: 10.1086/516630

[57] Camilo, F., Reynolds, J., Johnston, S., Halpern, J. P., & Ransom, S. M. 2008, ApJ, 679, 681. doi: 10.1086/587054

[58] Caraveo, P. A. 2014, ARA&A, 52, 211. doi: 10.1146/annurev-astro-081913-035948

[59] Chadwick, J. 1932, Proc. Roy. Soc., A, 136, 692. doi: 10.1098/rspa.1932.0112

[60] Chandrasekhar, S. 1935, MNRAS, 95, 226. doi: 10.1093/mnras/95.3.226

[61] Chang, C., Pavlov, G. G., Kargaltsev, O., & Shibanov, Y. A. 2012, ApJ, 744, 81. doi: 10.1088/0004-637X/744/2/81

[62] Chang, P. & Bildsten, L. 2003, ApJ, 585, 464. doi: 10.1086/345551

[63] Chang, P., Arras, P., & Bildsten, L. 2004, ApJL, 616, L147. doi: 10.1086/426789

[64] Chatterjee, S., Brisken, W. F., Vlemmings, W. H. T., et al. 2009, ApJ, 698, 250. doi: 10.1088/0004-637X/698/1/250

[65] Cheng, K. S., Ho, C., & Ruderman, M. 1986, ApJ, 300, 500. doi: 10.1086/163829

[66] —. 1986, ApJ, 300, 522. doi: 10.1086/163830

[67] Chiang, J. & Romani, R. W. 1994, ApJ, 436, 754. doi: 10.1086/174949

[68] Clark, C. J., Pletsch, H. J., Wu, J., et al. 2016, ApJL, 832, L15. doi: 10.3847/2041-8205/832/1/L15

[69] Cocke, W. J., Disney, M. J., & Westerlund, B. E. 1969, Nature, 222, 359. doi: 10.1038/222359a0

[70] Colpi, M., Geppert, U., & Page, D. 2000, ApJL, 529, L29. doi: 10.1086/312448

[71] Cordes, J. M. 1978, ApJ, 222, 1006. doi: 10.1086/156218

[72] Cordes, J. M. & Lazio, T. J. W. 2002, ArXiv e-prints. arXiv: astro-ph/0207156

[73] Coti Zelati, F., Rea, N., Pons, J. A., Campana, S., & Esposito, P. 2018, MNRAS, 474, 961. doi: 10.1093/mnras/stx2679

[74] Cromartie, H. T., Fonseca, E., Ransom, S. M., et al. 2019, ArXiv e-prints. arXiv: 1904.06759

[75] Cumming, A., Arras, P., & Zweibel, E. 2004, ApJ, 609, 999. doi: 10.1086/421324

[76] Cummings, J. R., Burrows, D., Campana, S., et al. 2011, ATel, 3488, 1

[77] Daugherty, J. K. & Harding, A. K. 1982, ApJ, 252, 337. doi: 10.1086/159561

[78] De Luca, A. 2017, in Journal of Physics Conference Series, ed. G. Pavlov, J. Pons, S. P.S., & D. Yakovlev, Vol. 932, 012006. doi: 10.1088/1742-6596/932/1/012006

[79] De Luca, A., Caraveo, P. A., Mereghetti, S., Negroni, M., & Bignami, G. F. 2005, ApJ, 623, 1051. doi: 10.1086/428567

[80] Degenaar, N. & Suleimanov, V. F. 2018, in Astrophysics and Space Science Library, ed. L. Rezzolla, P. Pizzochero, D. I. Jones, N. Rea, & I. Vidaña, Vol. 457, 185. doi: 10.1007/978-3-319-97616-7_5

[81] Degenaar, N., Ballantyne, D. R., Belloni, T., et al. 2018, SSRv, 214, 15. doi: 10.1007/s11214-017-0448-3

[82] Deller, A. T., Tingay, S. J., Bailes, M., & Reynolds, J. E. 2009, ApJ, 701, 1243. doi: 10.1088/0004-637X/701/2/1243

[83] Demorest, P. B., Pennucci, T., Ransom, S. M., Roberts, M. S. E., & Hessels, J. W. T. 2010, Nature, 467, 1081. doi: 10.1038/nature09466

[84] den Herder, J. W., Brinkman, A. C., Kahn, S. M., et al. 2001, A&A, 365, L7. doi: 10.1051/0004-6361:20000058

[85] Deshpande, A. A. & Rankin, J. M. 2001, MNRAS, 322, 438. doi: 10.1046/j.1365-8711.2001.04079.x

[86] —. 1999, ApJ, 524, 1008. doi: 10.1086/307862

[87] Ding, D., Rios, A., Dussan, H., et al. 2016, PhRvC, 94, 025802. doi: 10.1103/PhysRevC.94.025802

[88] Duncan, R. C. & Thompson, C. 1992, ApJL, 392, L9. doi: 10.1086/186413

[89] Espinoza, C. M., Lyne, A. G., Kramer, M., Manchester, R. N., & Kaspi, V. M. 2011, ApJL, 741, L13. doi: 10.1088/2041-8205/741/1/L13

[90] Espinoza, C. M., Lyne, A. G., & Stappers, B. W. 2017, MNRAS, 466, 147. doi: 10.1093/mnras/stw3081

[91] Espinoza, C. M. 2018, in IAU Symposium, Vol. 337, Pulsar Astrophysics the Next Fifty Years, ed. P. Weltevrede, B. B. P. Perera, L. L. Preston, & S. Sanidas, 221–224. doi: 10.1017/S1743921317008535

[92] Ferdman, R. D., Archibald, R. F., & Kaspi, V. M. 2015, ApJ, 812, 95. doi: 10.1088/0004-637X/812/2/95

[93] Fichtel, C. E., Hartman, R. C., Kniffen, D. A., et al. 1975, ApJ, 198, 163. doi: 10.1086/153590

[94] Fonseca, E., Pennucci, T. T., Ellis, J. A., et al. 2016, ApJ, 832, 167. doi: 10.3847/0004-637X/832/2/167

[95] Gaensler, B. M., van der Swaluw, E., Camilo, F., et al. 2004, ApJ, 616, 383. doi: 10.1086/424906

[96] Gaensler, B. M. & Slane, P. O. 2006, ARA&A, 44, 17. doi: 10.1146/annurev.astro.44.051905.092528

[97] Gamow, G. & Schoenberg, M. 1941, PhRv, 59, 539. doi: 10.1103/PhysRev.59.539

[98] Gangadhara, R. T. & Gupta, Y. 2001, ApJ, 555, 31. doi: 10.1086/321439

[99] Gavriil, F. P., Kaspi, V. M., & Woods, P. M. 2002, Nature, 419, 142. doi: 10.1038/nature01011

[100] Gavriil, F. P., Gonzalez, M. E., Gotthelf, E. V., et al. 2008, Science, 319, 1802. doi: 10.1126/science.1153465

[101] Geppert, U. & Rheinhardt, M. 2002, A&A, 392, 1015. doi: 10.1051/0004-6361:20020978

[102] Geppert, U., Rheinhardt, M., & Gil, J. 2003, A&A, 412, L33. doi: 10.1051/0004-6361:20034605

[103] Geppert, U., Küker, M., & Page, D. 2004, A&A, 426, 267. doi: 10.1051/0004-6361:20040455

[104] —. 2006, A&A, 457, 937. doi: 10.1051/0004-6361:20054696

[105] Geppert, U., Gil, J., & Melikidze, G. 2013, MNRAS, 435, 3262. doi: 10.1093/mnras/stt1527

[106] Ghizzardi, S. 2002, In flight calibration of the PSF for the PN camera, XMM-SOC-CAL-TN-0029. http://www.cosmos.esa.int/web/xmm-newton/calibration-documentation

[107] Giacconi, R., Gursky, H., Kellogg, E., Schreier, E., & Tananbaum, H. 1971, ApJL, 167, L67. doi: 10.1086/180762

[108] Giacconi, R., Murray, S., Gursky, H., et al. 1972, ApJ, 178, 281. doi: 10.1086/151790

[109] Gil, J. & Mitra, D. 2001, ApJ, 550, 383. doi: 10.1086/319714

[110] Gil, J., Gronkowski, P., & Rudnicki, W. 1984, A&A, 132, 312

[111] Gil, J., Melikidze, G., & Geppert, U. 2003, A&A, 407, 315. doi: 10.1051/0004-6361:20030854

[112] Gil, J., Melikidze, G., & Zhang, B. 2006, ApJ, 650, 1048. doi: 10.1086/506982

[113] —. 2006, A&A, 457, L5. doi: 10.1051/0004-6361:20065228

[114] Gil, J., Haberl, F., Melikidze, G., et al. 2008, ApJ, 686, 497. doi: 10.1086/590657

[115] Gil, J. A. & Kijak, J. 1993, A&A, 273, 563

[116] Ginzburg, V. L. 1970, The propagation of electromagnetic waves in plasmas (Pergamon Press)

[117] Gold, T. 1968, Nature, 218, 731. doi: 10.1038/218731a0

[118] —. 1969, Nature, 221, 25. doi: 10.1038/221025a0

[119] Goldreich, P. & Julian, W. H. 1969, ApJ, 157, 869. doi: 10.1086/150119

[120] Goldreich, P. & Reisenegger, A. 1992, ApJ, 395, 250. doi: 10.1086/171646

[121] Gonzalez, D. & Reisenegger, A. 2010, A&A, 522, A16. doi: 10.1051/0004-6361/201015084

[122] Gonzalez, M. E., Kaspi, V. M., Pivovaroff, M. J., & Gaensler, B. M. 2006, ApJ, 652, 569. doi: 10.1086/507125

[123] González Caniulef, D., Zane, S., Taverna, R., Turolla, R., & Wu, K. 2016, MNRAS, 459, 3585. doi: 10.1093/mnras/stw804

[124] Gotthelf, E. V. & Halpern, J. P. 2008, ApJ, 681, 515. doi: 10.1086/588779

[125] —. 2009, ApJL, 695, L35. doi: 10.1088/0004-637X/695/1/L35

[126] Gotthelf, E. V., Vasisht, G., Boylan-Kolchin, M., & Torii, K. 2000, ApJL, 542, L37. doi: 10.1086/312923

[127] Gotthelf, E. V., Halpern, J. P., & Seward, F. D. 2005, ApJ, 627, 390. doi: 10.1086/430300

[128] Gotthelf, E. V., Perna, R., & Halpern, J. P. 2010, ApJ, 724, 1316. doi: 10.1088/0004-637X/724/2/1316

[129] Gotthelf, E. V., Halpern, J. P., Terrier, R., & Mattana, F. 2011, ApJL, 729, L16. doi: 10.1088/2041-8205/729/2/L16

[130] Gotthelf, E. V., Halpern, J. P., & Alford, J. 2013, ApJ, 765, 58. doi: 10.1088/0004-637X/765/1/58

[131] Gotthelf, E. V., Tomsick, J. A., Halpern, J. P., et al. 2014, ApJ, 788, 155. doi: 10.1088/0004-637X/788/2/155

[132] Gotthelf, E. V. & Kaspi, V. M. 1998, ApJL, 497, L29. doi: 10.1086/311266

[133] Göğüş, E., Lin, L., Kaneko, Y., et al. 2016, ApJL, 829, L25. doi: 10.3847/2041-8205/829/2/L25

[134] Greenstein, G. & Hartke, G. J. 1983, ApJ, 271, 283. doi: 10.1086/161195

[135] Gudmundsson, E. H., Pethick, C. J., & Epstein, R. I. 1982, ApJL, 259, L19. doi: 10.1086/183840

[136] —. 1983, ApJ, 272, 286. doi: 10.1086/161292

[137] Haberl, F. 2007, ApSS, 308, 181. doi: 10.1007/s10509-007-9342-x

[138] Haberl, F., Motch, C., Zavlin, V. E., et al. 2004, A&A, 424, 635. doi: 10.1051/0004-6361:20040440

[139] Halpern, J. P. & Gotthelf, E. V. 2010, ApJ, 709, 436. doi: 10.1088/0004-637X/709/1/436

[140] —. 2015, ApJ, 812, 61. doi: 10.1088/0004-637X/812/1/61

[141] Halpern, J. P., Gotthelf, E. V., Camilo, F., Collins, B., & Helfand, D. J. 2002, in Astronomical Society of the Pacific Conference Series, Vol. 271, Neutron Stars in Supernova Remnants, ed. P. O. Slane & B. M. Gaensler, 199

[142] Halpern, J. P., Bogdanov, S., & Gotthelf, E. V. 2013, ApJ, 778, 120. doi: 10.1088/0004-637X/778/2/120

[143] Hambaryan, V., Suleimanov, V., Schwope, A. D., et al. 2011, A&A, 534, A74. doi: 10.1051/0004-6361/201117548

[144] Hambaryan, V., Suleimanov, V., Haberl, F., et al. 2017, A&A, 601, A108. doi: 10.1051/0004-6361/201630368

[145] Hamil, O., Stone, J. R., Urbanec, M., & Urbancová, G. 2015, PhRvD, 91, 063007. doi: 10.1103/PhysRevD.91.063007

[146] Hamil, O., Stone, N. J., & Stone, J. R. 2016, PhRvD, 94, 063012. doi: 10.1103/PhysRevD.94.063012

[147] Harding, A. K. 2007, ArXiv e-prints. arXiv: 0710.3517

[148] Harding, A. K. & Muslimov, A. G. 1998, ApJ, 508, 328. doi: 10.1086/306394

[149] —. 2001, ApJ, 556, 987. doi: 10.1086/321589

[150] —. 2002, ApJ, 568, 862. doi: 10.1086/338985

[151] Harding, A. K., Muslimov, A. G., & Zhang, B. 2002, ApJ, 576, 366. doi: 10.1086/341633

[152] Harding, A. K. 2013, JASS, 30, 145. doi: 10.5140/JASS.2013.30.3.145

[153] Harding, A. K., Contopoulos, I., & Kazanas, D. 1999, ApJL, 525, L125. doi: 10.1086/312339

[154] He, C., Ng, C.-Y., & Kaspi, V. M. 2013, ApJ, 768, 64. doi: 10.1088/0004-637X/768/1/64

[155] Heger, A., Fryer, C. L., Woosley, S. E., Langer, N., & Hartmann, D. H. 2003, ApJ, 591, 288. doi: 10.1086/375341

[156] Heinke, C. O., Rybicki, G. B., Narayan, R., & Grindlay, J. E. 2006, ApJ, 644, 1090. doi: 10.1086/503701

[157] Helfand, D. J., Gotthelf, E. V., Halpern, J. P., et al. 2007, ApJ, 665, 1297. doi: 10.1086/519734

[158] Helfand, D. J., Collins, B. F., & Gotthelf, E. V. 2003, ApJ, 582, 783. doi: 10.1086/344725

[159] Henriksen, R. N., Reinhardt, M., & Aschenbach, B. 1973, A&A, 28, 47

[160] Herfindal, J. L. & Rankin, J. M. 2007, MNRAS, 380, 430. doi: 10.1111/j.1365-2966.2007.12089.x

[161] Hermsen, W., Hessels, J. W. T., Kuiper, L., et al. 2013, Science, 339, 436. doi: 10.1126/science.1230960

[162] Hermsen, W., Kuiper, L., Hessels, J. W. T., et al. 2017, MNRAS, 466, 1688. doi: 10.1093/mnras/stw3135

[163] Hermsen, W., Kuiper, L., Basu, R., et al. 2018, MNRAS, 480, 3655. doi: 10.1093/mnras/sty2075

[164] Hernquist, L. 1985, MNRAS, 213, 313. doi: 10.1093/mnras/213.2.313

[165] Hernquist, L. & Applegate, J. H. 1984, ApJ, 287, 244. doi: 10.1086/162683

[166] Herold, H. 1979, PhRvD, 19, 2868. doi: 10.1103/PhysRevD.19.2868

[167] Hessels, J. W. T., Roberts, M. S. E., Ransom, S. M., et al. 2004, ApJ, 612, 389. doi: 10.1086/422408

[168] Hewish, A., Bell, S. J., Pilkington, J. D. H., Scott, P. F., & Collins, R. A. 1968, Nature, 217, 709. doi: 10.1038/217709a0

[169] Heyl, J. S. & Kulkarni, S. R. 1998, ApJL, 506, L61. doi: 10.1086/311628

[170] Hibschman, J. A. & Arons, J. 2001, ApJ, 546, 382. doi: 10.1086/318224

[171] Ho, W. C. G. 2007, MNRAS, 380, 71. doi: 10.1111/j.1365-2966.2007.12043.x

[172] Ho, W. C. G. 2014, in IAU Symposium, Vol. 302, Magnetic Fields throughout Stellar Evolution, ed. P. Petit, M. Jardine, & H. C. Spruit, 435–438. doi: 10.1017/S1743921314002683

[173] Ho, W. C. G. & Lai, D. 2003, in Astronomical Society of the Pacific Conference Series, Vol. 288, Stellar Atmosphere Modeling, ed. I. Hubeny, D. Mihalas, & K. Werner, 621

[174] Ho, W. C. G., Potekhin, A. Y., & Chabrier, G. 2008, ApJS, 178, 102. doi: 10.1086/589238

[175] Ho, W. C. G., Elshamouty, K. G., Heinke, C. O., & Potekhin, A. Y. 2015, PhRvC, 91, 015806. doi: 10.1103/PhysRevC.91.015806

[176] Ho, W. C. G. 2011, MNRAS, 414, 2567. doi: 10.1111/j.1365-2966.2011.18576.x

[177] Ho, W. C. G. & Lai, D. 2003, MNRAS, 338, 233. doi: 10.1046/j.1365-8711.2003.06047.x

[178] Hobbs, G., Lyne, A. G., Kramer, M., Martin, C. E., & Jordan, C. 2004, MNRAS, 353, 1311. doi: 10.1111/j.1365-2966.2004.08157.x

[179] Hobbs, G., Lorimer, D. R., Lyne, A. G., & Kramer, M. 2005, MNRAS, 360, 974. doi: 10.1111/j.1365-2966.2005.09087.x

[180] Hollerbach, R. & Rüdiger, G. 2002, MNRAS, 337, 216. doi: 10.1046/j.1365-8711.2002.05905.x

[181] —. 2004, MNRAS, 347, 1273. doi: 10.1111/j.1365-2966.2004.07307.x

[182] Hughes, J. P., Slane, P. O., Park, S., Roming, P. W. A., & Burrows, D. N. 2003, ApJL, 591, L139. doi: 10.1086/377072

[183] Hui, C. Y. & Becker, W. 2007, A&A, 470, 965. doi: 10.1051/0004-6361:20077628

[184] Hui, C. Y., Huang, R. H. H., Trepl, L., et al. 2012, ApJ, 747, 74. doi: 10.1088/0004-637X/747/1/74

[185] Ibrahim, A. I., Safi-Harb, S., Swank, J. H., et al. 2002, ApJ, 574, L51. doi: 10.1086/342366

[186] Ibrahim, A. I., Swank, J. H., & Parke, W. 2003, ApJ, 584, L17. doi: 10.1086/345774

[187] Igoshev, A. P., Popov, S. B., & Turolla, R. 2014, Astr. Nachr., 335, 262. doi: 10.1002/asna.201312029

[188] Igoshev, A. P., Tsygankov, S. S., Rigoselli, M., et al. 2018, ApJ, 865, 116. doi: 10.3847/1538-4357/aadd93

[189] Israel, G. L., Esposito, P., Rea, N., et al. 2010, MNRAS, 408, 1387. doi: 10.1111/j.1365-2966.2010.17001.x

[190] Jansen, F., Lumb, D., Altieri, B., et al. 2001, A&A, 365, L1. doi: 10.1051/0004-6361:20000036

[191] Jones, D. I. 2012, MNRAS, 420, 2325. doi: 10.1111/j.1365-2966.2011.20238.x

[192] Jones, P. B. 1976, ApSS, 45, 369. doi: 10.1007/BF00642671

[193] Kaaret, P., Marshall, H. L., Aldcroft, T. L., et al. 2001, ApJ, 546, 1159. doi: 10.1086/318287

[194] Kalberla, P. M. W., Burton, W. B., Hartmann, D., et al. 2005, A&A, 440, 775. doi: 10.1051/0004-6361:20041864

[195] Kaminker, A. D., Kaurov, A. A., Potekhin, A. Y., & Yakovlev, D. G. 2014, MNRAS, 442, 3484. doi: 10.1093/mnras/stu1102

[196] Kaplan, D. L. 2008, in Astrophysics of Compact Objects, ed. Y.-F. Yuan, X.-D. Li, & D. Lai, Vol. 968, 129–136. doi: 10.1063/1.2840384

[197] Kaplan, D. L., Kamble, A., van Kerkwijk, M. H., & Ho, W. C. G. 2011, ApJ, 736, 117. doi: 10.1088/0004-637X/736/2/117

[198] Kargaltsev, O. & Pavlov, G. G. 2007, ApJ, 670, 655. doi: 10.1086/521814

[199] Kargaltsev, O., Pavlov, G. G., & Garmire, G. P. 2006, ApJ, 636, 406. doi: 10.1086/497897

[200] —. 2007, ApJ, 660, 1413. doi: 10.1086/513312

[201] Kargaltsev, O., Pavlov, G. G., & Wong, J. A. 2009, ApJ, 690, 891. doi: 10.1088/0004-637X/690/1/891

[202] Kargaltsev, O., Durant, M., Misanovic, Z., & Pavlov, G. G. 2012, Science, 337, 946. doi: 10.1126/science.1221378

[203] Kargaltsev, O., Durant, M., Pavlov, G. G., & Garmire, G. 2012, ApJS, 201, 37. doi: 10.1088/0067-0049/201/2/37

[204] Kargaltsev, O., Schmitt, B. M., Pavlov, G. G., & Misanovic, Z. 2012, ApJ, 745, 99. doi: 10.1088/0004-637X/745/1/99

[205] Kaspi, V. M. 2010, PNAS, 107, 7147. doi: 10.1073/pnas.1000812107

[206] Kaspi, V. M. & Beloborodov, A. M. 2017, ARA&A, 55, 261. doi: 10.1146/annurev-astro-081915-023329

[207] Kaspi, V. M., Gotthelf, E. V., Gaensler, B. M., & Lyutikov, M. 2001, ApJL, 562, L163. doi: 10.1086/324757

[208] Kaspi, V. M., Gavriil, F. P., Woods, P. M., et al. 2003, ApJL, 588, L93. doi: 10.1086/375683

[209] Kaspi, V. M., Roberts, M. S. E., & Harding, A. K. 2006, Isolated neutron stars, Vol. 39 (Cambridge University Press), 279–339

[210] Keane, E. F. & Kramer, M. 2008, MNRAS, 391, 2009. doi: 10.1111/j.1365-2966.2008.14045.x

[211] Keane, E. F., Kramer, M., Lyne, A. G., Stappers, B. W., & McLaughlin, M. A. 2011, MNRAS, 415, 3065. doi: 10.1111/j.1365-2966.2011.18917.x

[212] Klingler, N., Rangelov, B., Kargaltsev, O., et al. 2016, ApJ, 833, 253. doi: 10.3847/1538-4357/833/2/253

[213] Komesaroff, M. M. 1970, Nature, 225, 612. doi: 10.1038/225612a0

[214] Kondratiev, V. I., McLaughlin, M. A., Lorimer, D. R., et al. 2009, ApJ, 702, 692. doi: 10.1088/0004-637X/702/1/692

[215] Kramer, M. 1994, A&AS, 107, 527

[216] Kramer, M., Bell, J. F., Manchester, R. N., et al. 2003, MNRAS, 342, 1299. doi: 10.1046/j.1365-8711.2003.06637.x

[217] Kramer, M., Karastergiou, A., Gupta, Y., et al. 2003, A&A, 407, 655. doi: 10.1051/0004-6361:20030842

[218] Kramer, M., Lyne, A. G., O'Brien, J. T., Jordan, C. A., & Lorimer, D. R. 2006, Science, 312, 549. doi: 10.1126/science.1124060

[219] Krishnamohan, S. & Downs, G. S. 1983, ApJ, 265, 372. doi: 10.1086/160682

[220] Kuijpers, J. M. E. 2009, in Astrophysics and Space Science Library, ed. W. Becker, Vol. 357, 543. doi: 10.1007/978-3-540-76965-1_20

[221] Kumar, H. S. & Safi-Harb, S. 2008, ApJL, 678, L43. doi: 10.1086/588284

[222] Kurkela, A., Fraga, E. S., Schaffner-Bielich, J., & Vuorinen, A. 2014, ApJ, 789, 127. doi: 10.1088/0004-637X/789/2/127

[223] Kuz'min, A. D. & Wu, X. 1992, ApSS, 190, 209. doi: 10.1007/BF00644848

[224] Lai, D. 2001, RvMP, 73, 629. doi: 10.1103/RevModPhys.73.629

[225] Lai, D. & Ho, W. C. 2003, PhRvL, 91, 071101. doi: 10.1103/PhysRevLett.91.071101

[226] Lai, D. & Ho, W. C. G. 2003, ApJ, 588, 962. doi: 10.1086/374334

[227] Lai, D. & Salpeter, E. E. 1997, ApJ, 491, 270. doi: 10.1086/304937

[228] Landau, L. D. 1932, Phys. Zs. Sowjet, 1, 285

[229] Large, M. I., Vaughan, A. E., & Mills, B. Y. 1968, Nature, 220, 340. doi: 10.1038/220340a0

[230] Latham, C., Mitra, D., & Rankin, J. 2012, MNRAS, 427, 180. doi: 10.1111/j.1365-2966.2012.21985.x

[231] Lattimer, J. M. & Prakash, M. 2001, ApJ, 550, 426. doi: 10.1086/319702

[232] —. 2016, PhRp, 621, 127. doi: 10.1016/j.physrep.2015.12.005

[233] Lattimer, J. M., Pethick, C. J., Prakash, M., & Haensel, P. 1991, PhRvL, 66, 2701. doi: 10.1103/PhysRevLett.66.2701

[234] Li, Z., Falanga, M., Chen, L., Qu, J., & Xu, R. 2017, ApJ, 845, 8. doi: 10.3847/1538-4357/aa7d0b

[235] Livingstone, M. A. & Kaspi, V. M. 2011, ApJ, 742, 31. doi: 10.1088/0004-637X/742/1/31

[236] Livingstone, M. A., Kaspi, V. M., Gotthelf, E. V., & Kuiper, L. 2006, ApJ, 647, 1286. doi: 10.1086/505570

[237] Livingstone, M. A., Ng, C. Y., Kaspi, V. M., Gavriil, F. P., & Gotthelf, E. V. 2011, ApJ, 730, 66. doi: 10.1088/0004-637X/730/2/66

[238] Lopez, M., Otte, N., Rissi, M., et al. 2009, ArXiv e-prints. arXiv: 0907.0832

[239] Lorimer, D. R. & Kramer, M. 2004, Handbook of Pulsar Astronomy (Cambridge University Press)

[240] Lyne, A., Hobbs, G., Kramer, M., Stairs, I., & Stappers, B. 2010, Science, 329, 408. doi: 10.1126/science.1186683

[241] Lyne, A. G. & Manchester, R. N. 1988, MNRAS, 234, 477. doi: 10.1093/mnras/234.3.477

[242] Lyne, A. G., Jordan, C. A., Graham-Smith, F., et al. 2015, MNRAS, 446, 857. doi: 10.1093/mnras/stu2118

[243] Malofeev, V. M., Malov, O. I., & Shchegoleva, N. V. 2000, ARep, 44, 436. doi: 10.1134/1.163868

[244] Malofeev, V. M., Malov, O. I., Teplykh, D. A., Tyul'Bashev, S. A., & Tyul'Basheva, G. E. 2005, ARep, 49, 242. doi: 10.1134/1.1882782

[245] Malofeev, V. M., Malov, O. I., Teplykh, D. A., et al. 2006, ATel, 798

[246] Manchester, R. N. 2017, JApA, 38, 42. doi: 10.1007/s12036-017-9469-2

[247] Manchester, R. N. & Taylor, J. H. 1977, Pulsars (W. H. Freeman)

[248] Manchester, R. N., Lyne, A. G., Taylor, J. H., et al. 1978, MNRAS, 185, 409. doi: 10.1093/mnras/185.2.409

[249] Manchester, R. N., Hobbs, G. B., Teoh, A., & Hobbs, M. 2005, VizieR Online Data Catalog, 7245. http://www.atnf.csiro.au/research/pulsar/psrcat/

[250] Marelli, M., Belfiore, A., Saz Parkinson, P., et al. 2014, ApJ, 790, 51. doi: 10.1088/0004-637X/790/1/51

[251] Margueron, J., Sagawa, H., & Hagino, K. 2008, PhRvC, 77, 054309. doi: 10.1103/PhysRevC.77.054309

[252] Maron, O., Kijak, J., Kramer, M., & Wielebinski, R. 2000, A&AS, 147, 195. doi: 10.1051/aas:2000298

[253] Mason, K. O., Breeveld, A., Much, R., et al. 2001, A&A, 365, L36. doi: 10.1051/0004-6361:20000044

[254] Matheson, H. & Safi-Harb, S. 2010, ApJ, 724, 572. doi: 10.1088/0004-637X/724/1/572

[255] McGowan, K. E., Kennea, J. A., Zane, S., et al. 2003, ApJ, 591, 380. doi: 10.1086/375332

[256] McGowan, K. E., Zane, S., Cropper, M., et al. 2004, ApJ, 600, 343. doi: 10.1086/379787

[257] McGowan, K. E., Zane, S., Cropper, M., Vestrand, W. T., & Ho, C. 2006, ApJ, 639, 377. doi: 10.1086/497327

[258] McLaughlin, M. A., Lyne, A. G., Lorimer, D. R., et al. 2006, Nature, 439, 817. doi: 10.1038/nature04440

[259] McLaughlin, M. A., Lyne, A. G., Keane, E. F., et al. 2009, MNRAS, 400, 1431. doi: 10.1111/j.1365-2966.2009.15584.x

[260] Medin, Z. & Lai, D. 2007, MNRAS, 382, 1833. doi: 10.1111/j.1365-2966.2007.12492.x

[261] —. 2006, PhRvA, 74, 062508. doi: 10.1103/PhysRevA.74.062508

[262] Melrose, D. 2004, in IAU Symposium, Vol. 218, Young Neutron Stars and Their Environments, ed. F. Camilo & B. M. Gaensler, 349

[263] Mereghetti, S. & Rigoselli, M. 2017, JApA, 38, 54. doi: 10.1007/s12036-017-9464-7

[264] Mereghetti, S., Tiengo, A., Esposito, P., & Turolla, R. 2013, MNRAS, 435, 2568. doi: 10.1093/mnras/stt1472

[265] Mereghetti, S., Pons, J. A., & Melatos, A. 2015, SSRv, 191, 315. doi: 10.1007/s11214-015-0146-y

[266] Mereghetti, S., Kuiper, L., Tiengo, A., et al. 2016, ApJ, 831, 21. doi: 10.3847/0004-637X/831/1/21

[267] Mereghetti, S., De Luca, A., Salvetti, D., et al. 2018, A&A, 616, A36. doi: 10.1051/0004-6361/201833086

[268] Mészáros, P. 1992, High-energy radiation from magnetized neutron stars. (University of Chicago Press)

[269] Michel, F. C. 1969, ApJ, 157, 1183. doi: 10.1086/150146

[270] Mignani, R. P. 2012, in Astronomical Society of the Pacific Conference Series, ed. W. Lewandowski, O. Maron, & J. Kijak, Vol. 466, 3

[271] Mignani, R. P., Pulone, L., Iannicola, G., et al. 2005, A&A, 431, 659. doi: 10.1051/0004-6361:20041781

[272] Mignani, R. P., Zane, S., Turolla, R., et al. 2011, A&A, 530, A39. doi: 10.1051/0004-6361/201016362

[273] Mignani, R. P., De Luca, A., Zharikov, S., et al. 2019, MNRAS, 486, 5716. doi: 10.1093/mnras/stz1195

[274] Miller, J. J., McLaughlin, M. A., Rea, N., et al. 2013, ApJ, 776, 104. doi: 10.1088/0004-637X/776/2/104

[275] Minkowski, R. 1942, ApJ, 96, 199. doi: 10.1086/144447

[276] Misanovic, Z., Pavlov, G. G., & Garmire, G. P. 2008, ApJ, 685, 1129. doi: 10.1086/590949

[277] Mitra, D. & Deshpande, A. A. 1999, A&A, 346, 906. arXiv: astro-ph/9904336

[278] Mitra, D., Gil, J., & Melikidze, G. I. 2009, ApJL, 696, L141. doi: 10.1088/0004-637X/696/2/L141

[279] Mitra, D. & Rankin, J. M. 2002, ApJ, 577, 322. doi: 10.1086/342136

[280] —. 2011, ApJ, 727, 92. doi: 10.1088/0004-637X/727/2/92

[281] Morello, V., Keane, E. F., Enoto, T., et al. 2019, ArXiv e-prints. arXiv: 1910.04124

[282] Mori, K. & Ho, W. C. G. 2007, MNRAS, 377, 905. doi: 10.1111/j.1365-2966.2007.11663.x

[283] Mori, K. & Heyl, J. S. 2007, MNRAS, 376, 895. doi: 10.1111/j.1365-2966.2007.11485.x

[284] Morrison, P., Olbert, S., & Rossi, B. 1954, PhRv, 94, 440. doi: 10.1103/PhysRev.94.440

[285] Muslimov, A. G. & Tsygan, A. I. 1992, MNRAS, 255, 61. doi: 10.1093/mnras/255.1.61

[286] Narayan, R. & Vivekanand, M. 1982, A&A, 113, L3

[287] Nather, R. E., Warner, B., & Macfarlane, M. 1969, Nature, 221, 527. doi: 10.1038/221527a0

[288] Ng, C. Y. & Kaspi, V. M. 2011, in American Institute of Physics Conference Series, ed. E. Göğüş, T. Belloni, & Ü. Ertan, Vol. 1379, 60–69. doi: 10.1063/1.3629486

[289] Nobili, L., Turolla, R., & Zane, S. 2008, MNRAS, 386, 1527. doi: 10.1111/j.1365-2966.2008.13125.x

[290] —. 2008, MNRAS, 389, 989. doi: 10.1111/j.1365-2966.2008.13627.x

[291] Olausen, S. A., Zhu, W. W., Vogel, J. K., et al. 2013, ApJ, 764, 1. doi: 10.1088/0004-637X/764/1/1

[292] Oort, J. H. & Walraven, T. 1956, BAIN, 12, 285

[293] Oosterbroek, T., Kennea, J., Much, R., & Córdova, F. A. 2004, NuPhS, 132, 636. doi: 10.1016/j.nuclphysbps.2004.04.111

[294] Oppenheimer, J. R. & Volkoff, G. M. 1939, PhRv, 55, 374. doi: 10.1103/PhysRev.55.374

[295] Pacini, F. 1967, Nature, 216, 567. doi: 10.1038/216567a0

[296] —. 1968, Nature, 219, 145. doi: 10.1038/219145a0

[297] Page, D. 1995, ApJ, 442, 273. doi: 10.1086/175439

[298] Page, D. & Sarmiento, A. 1996, ApJ, 473, 1067. doi: 10.1086/178216

[299] Page, D., Prakash, M., Lattimer, J. M., & Steiner, A. W. 2011, PhRvL, 106, 081101. doi: 10.1103/PhysRevLett.106.081101

[300] Pavan, L., Bordas, P., Pühlhofer, G., et al. 2014, A&A, 562, A122. doi: 10.1051/0004-6361/201322588

[301] Pavlov, G. G. & Luna, G. J. M. 2009, ApJ, 703, 910. doi: 10.1088/0004-637X/703/1/910

[302] Pavlov, G. G. & Meszaros, P. 1993, ApJ, 416, 752. doi: 10.1086/173274

[303] Pavlov, G. G., Shibanov, Y. A., Ventura, J., & Zavlin, V. E. 1994, A&A, 289, 837

[304] Pavlov, G. G., Shibanov, Y. A., Zavlin, V. E., & Meyer, R. D. 1995, in NATO Advanced Science Institutes (ASI) Series C, ed. M. A. Alpar, U. Kiziloglu, & J. van Paradijs, Vol. 450, 71

[305] Pavlov, G. G., Zavlin, V. E., Sanwal, D., Burwitz, V., & Garmire, G. P. 2001, ApJL, 552, L129. doi: 10.1086/320342

[306] Pavlov, G. G., Kargaltsev, O., & Brisken, W. F. 2008, ApJ, 675, 683. doi: 10.1086/525842

[307] Pavlov, G. G. & Potekhin, A. Y. 1995, ApJ, 450, 883. doi: 10.1086/176192

[308] Pearson, J. M., Chamel, N., Potekhin, A. Y., et al. 2018, MNRAS, 481, 2994. doi: 10.1093/mnras/sty2413

[309] Pechenick, K. R., Ftaclas, C., & Cohen, J. M. 1983, ApJ, 274, 846. doi: 10.1086/161498

[310] Pérez-Azorín, J. F., Miralles, J. A., & Pons, J. A. 2005, A&A, 433, 275. doi: 10.1051/0004-6361:20041612

[311] Pérez-Azorín, J. F., Miralles, J. A., & Pons, J. A. 2006, A&A, 451, 1009. doi: 10.1051/0004-6361:20054403

[312] Peterson, L. E. & Jacobson, A. S. 1966, ApJ, 145, 962. doi: 10.1086/148848

[313] Petre, R., Kuntz, K. D., & Shelton, R. L. 2002, ApJ, 579, 404. doi: 10.1086/342672

[314] Philippov, A., Tchekhovskoy, A., & Li, J. G. 2014, MNRAS, 441, 1879. doi: 10.1093/mnras/stu591

[315] Pintore, F., Belfiore, A., Novara, G., et al. 2018, MNRAS, 477, L90. doi: 10.1093/mnrasl/sly048

[316] Pintore, F., Marelli, M., Salvaterra, R., et al. 2020, ApJ, under review

[317] Pires, A. M., Schwope, A. D., Haberl, F., et al. 2019, A&A, 623, A73. doi: 10.1051/0004-6361/201834801

[318] Pizzochero, P. M., Antonelli, M., Haskell, B., & Seveso, S. 2017, Nature, 1, 0134. doi: 10.1038/s41550-017-0134

[319] Pons, J. A., Link, B., Miralles, J. A., & Geppert, U. 2007, PhRvL, 98, 071101. doi: 10.1103/PhysRevLett.98.071101

[320] Pons, J. A., Miralles, J. A., & Geppert, U. 2009, A&A, 496, 207. doi: 10.1051/0004-6361:200811229

[321] Popov, S. B., Colpi, M., Prokhorov, M. E., Treves, A., & Turolla, R. 2003, A&A, 406, 111. doi: 10.1051/0004-6361:20030680

[322] Popov, S. B., Turolla, R., Prokhorov, M. E., Colpi, M., & Treves, A. 2005, ApSS, 299, 117. doi: 10.1007/s10509-005-5160-1

[323] Porquet, D., Decourchelle, A., & Warwick, R. S. 2003, A&A, 401, 197. doi: 10.1051/0004-6361:20021670

[324] Posselt, B., Arumugasamy, P., Pavlov, G. G., et al. 2012, ApJ, 761, 117. doi: 10.1088/0004-637X/761/2/117

[325] Posselt, B., Pavlov, G. G., Manchester, R. N., Kargaltsev, O., & Garmire, G. P. 2012, ApJ, 749, 146. doi: 10.1088/0004-637X/749/2/146

[326] Possenti, A., Cerutti, R., Colpi, M., & Mereghetti, S. 2002, A&A, 387, 993. doi: 10.1051/0004-6361:20020472

[327] Potekhin, A. Y. 2010, A&A, 518, A24. doi: 10.1051/0004-6361/201014781

[328] Potekhin, A. Y. & Chabrier, G. 2003, ApJ, 585, 955. doi: 10.1086/346150

[329] —. 2004, ApJ, 600, 317. doi: 10.1086/379807

[330] —. 2013, A&A, 550, A43. doi: 10.1051/0004-6361/201220082

[331] —. 2018, A&A, 609, A74. doi: 10.1051/0004-6361/201731866

[332] Potekhin, A. Y., Suleimanov, V. F., van Adelsberg, M., & Werner, K. 2012, A&A, 546, A121. doi: 10.1051/0004-6361/201219747

[333] Potekhin, A. Y., Chabrier, G., & Ho, W. C. G. 2014, A&A, 572, A69. doi: 10.1051/0004-6361/201424619

[334] Potekhin, A. Y., Ho, W. C. G., & Chabrier, G. 2016, ArXiv e-prints. arXiv: 1605.01281

[335] Potekhin, A. Y., Chabrier, G., & Shibanov, Y. A. 1999, PhRvE, 60, 2193. doi: 10.1103/PhysRevE.60.2193

[336] Prinz, T. & Becker, W. 2015, ArXiv e-prints. arXiv: 1511.07713

[337] Proszynski, M. 1979, A&A, 79, 8

[338] Pynzar', A. V. 2017, ARep, 61, 417. doi: 10.1134/S1063772917050031

[339] Radhakrishnan, V. & Cooke, D. J. 1969, ApL, 3, 225

[340] Radhakrishnan, V. & Rankin, J. M. 1990, ApJ, 352, 258. doi: 10.1086/168531

[341] Rankin, J. M. 1983, ApJ, 274, 333. doi: 10.1086/161450

[342] —. 1983, ApJ, 274, 359. doi: 10.1086/161451

[343] —. 1986, ApJ, 301, 901. doi: 10.1086/163955

[344] —. 1990, ApJ, 352, 247. doi: 10.1086/168530

[345] —. 1993, ApJ, 405, 285. doi: 10.1086/172361

[346] —. 1993, ApJS, 85, 145. doi: 10.1086/191758

[347] Rankin, J. M., Rodriguez, C., & Wright, G. A. E. 2006, MNRAS, 370, 673. doi: 10.1111/j.1365-2966.2006.10512.x

[348] Rankin, J. M. & Suleymanova, S. A. 2006, A&A, 453, 679. doi: 10.1051/0004-6361:20054140

[349] Ray, P. S., Kerr, M., Parent, D., et al. 2011, ApJS, 194, 17. doi: 10.1088/0067-0049/194/2/17

[350] Rea, N., Israel, G. L., & Stella, L. 2004, NuPhS, 132, 554. doi: 10.1016/j.nuclphysbps.2004.04.093

[351] Rea, N., Israel, G. L., Turolla, R., et al. 2009, MNRAS, 396, 2419. doi: 10.1111/j.1365-2966.2009.14920.x

[352] Rea, N., McLaughlin, M. A., Gaensler, B. M., et al. 2009, ApJL, 703, L41. doi: 10.1088/0004-637X/703/1/L41

[353] Renaud, M., Marandon, V., Gotthelf, E. V., et al. 2010, ApJ, 716, 663. doi: 10.1088/0004-637X/716/1/663

[354] Rho, J. & Petre, R. 1997, ApJ, 484, 828. doi: 10.1086/304350

[355] Richards, D. W. & Comella, J. M. 1969, Nature, 222, 551. doi: 10.1038/222551a0

[356] Rigoselli, M. & Mereghetti, S. 2018, A&A, 615, A73. doi: 10.1051/0004-6361/201732408

[357] Rigoselli, M., Mereghetti, S., Turolla, R., et al. 2019, ApJ, 872, 15. doi: 10.3847/1538-4357/aafac7

[358] Rigoselli, M., Mereghetti, S., Suleimanov, V., et al. 2019, A&A, 627, A69. doi: 10.1051/0004-6361/201935485

[359] Roberts, M. S. E., Tam, C. R., Kaspi, V. M., et al. 2003, ApJ, 588, 992. doi: 10.1086/374266

[360] Roberts, M. S. E., Romani, R. W., & Johnston, S. 2001, ApJL, 561, L187. doi: 10.1086/324752

[361] Romani, R. W. 1987, ApJ, 313, 718. doi: 10.1086/165010

[362] Rousseau, R., Grondin, M. H., Van Etten, A., et al. 2012, A&A, 544, A3. doi: 10.1051/0004-6361/201118685

[363] Roy, J., Gupta, Y., & Lewandowski, W. 2012, MNRAS, 424, 2213. doi: 10.1111/j.1365-2966.2012.21380.x

[364] Ruderman, M. 1971, PhRvL, 27, 1306. doi: 10.1103/PhysRevLett.27.1306

[365] Ruderman, M. A. & Sutherland, P. G. 1975, ApJ, 196, 51. doi: 10.1086/153393

[366] Rutledge, R. E., Fox, D. B., & Shevchuk, A. H. 2008, ApJ, 672, 1137. doi: 10.1086/522667

[367] Safi-Harb, S. & Kumar, H. S. 2008, ApJ, 684, 532. doi: 10.1086/590359

[368] Seward, F. D. & Wang, Z.-R. 1988, ApJ, 332, 199. doi: 10.1086/166646

[369] Shabaltas, N. & Lai, D. 2012, ApJ, 748, 148. doi: 10.1088/0004-637X/748/2/148

[370] Shapiro, I. I. 1964, PhRvL, 13, 789. doi: 10.1103/PhysRevLett.13.789

[371] Shapiro, S. L. & Teukolsky, S. A. 1983, Black Holes, White Dwarfs, and Neutron Stars (John Wiley & Sons)

[372] Shibanov, I. A., Zavlin, V. E., Pavlov, G. G., & Ventura, J. 1992, A&A, 266, 313

[373] Shklovsky, I. S. 1967, ApJL, 148, L1. doi: 10.1086/180001

[374] Skrzypczak, A., Basu, R., Mitra, D., et al. 2018, ApJ, 854, 162. doi: 10.3847/1538-4357/aaa758

[375] Slane, P., Helfand, D. J., van der Swaluw, E., & Murray, S. S. 2004, ApJ, 616, 403. doi: 10.1086/424814

[376] Speagle, J. S., Kaplan, D. L., & van Kerkwijk, M. H. 2011, ApJ, 743, 183. doi: 10.1088/0004-637X/743/2/183

[377] Spiewak, R., Kaplan, D. L., Archibald, A., et al. 2016, ApJ, 822, 37. doi: 10.3847/0004-637X/822/1/37

[378] Spitkovsky, A. 2006, ApJL, 648, L51. doi: 10.1086/507518

[379] Staelin, D. H. & Reifenstein, Edward C., I. 1968, Science, 162, 1481. doi: 10.1126/science.162.3861.1481

[380] Steiner, A. W., Heinke, C. O., Bogdanov, S., et al. 2018, MNRAS, 476, 421. doi: 10.1093/mnras/sty215

[381] Stokes, G. H., Taylor, J. H., Welsberg, J. M., & Dewey, R. J. 1985, Nature, 317, 787. doi: 10.1038/317787a0

[382] Storch, N. I., Ho, W. C. G., Lai, D., Bogdanov, S., & Heinke, C. O. 2014, ApJL, 789, L27. doi: 10.1088/2041-8205/789/2/L27

[383] Strohmayer, T. E. & Ibrahim, A. I. 2000, ApJL, 537, L111. doi: 10.1086/312769

[384] Strüder, L. et al. 2001, A&A, 365, L18. doi: 10.1051/0004-6361:20000066

[385] Sturner, S. J., Dermer, C. D., & Michel, F. C. 1995, ApJ, 445, 736. doi: 10.1086/175736

[386] Sturrock, P. A. 1971, ApJ, 164, 529. doi: 10.1086/150865

[387] Suleimanov, V., Potekhin, A. Y., & Werner, K. 2009, A&A, 500, 891. doi: 10.1051/0004-6361/200912121

[388] Suleimanov, V., Hambaryan, V., Potekhin, A. Y., et al. 2010, A&A, 522, A111. doi: 10.1051/0004-6361/200913641

[389] Suleimanova, S. A. & Izvekova, V. A. 1984, SvA, 28, 32

[390] Swanenburg, B. N., Bennett, K., Bignami, G. F., et al. 1981, ApJL, 243, L69. doi: 10.1086/183445

[391] Szary, A. 2013, PhD thesis, University of Zielona Góra. http://ui.adsabs.harvard.edu/abs/2013arXiv1304.4203S/abstract

[392] Szary, A., Gil, J., Zhang, B., et al. 2017, ApJ, 835, 178. doi: 10.3847/1538-4357/835/2/178

[393] Tan, C. M., Bassa, C. G., Cooper, S., et al. 2018, ApJ, 866, 54. doi: 10.3847/1538-4357/aade88

[394] Tananbaum, H., Gursky, H., Kellogg, E. M., et al. 1972, ApJL, 174, L143. doi: 10.1086/180968

[395] Tauris, T. M. & Manchester, R. N. 1998, MNRAS, 298, 625. doi: 10.1046/j.1365-8711.1998.01369.x

[396] Tavani, M., Barbiellini, G., Argan, A., et al. 2009, A&A, 502, 995. doi: 10.1051/0004-6361/200810527

[397] Taverna, R. 2015, PhD thesis, Università degli Studi di Padova. http://paduaresearch.cab.unipd.it/9146/

[398] Taverna, R., Turolla, R., Gonzalez Caniulef, D., et al. 2015, MNRAS, 454, 3254. doi: 10.1093/mnras/stv2168

[399] Taylor, J. H. & Cordes, J. M. 1993, ApJ, 411, 674. doi: 10.1086/172870

[400] Tendulkar, S. P., Cameron, P. B., & Kulkarni, S. R. 2012, ApJ, 761, 76. doi: 10.1088/0004-637X/761/1/76

[401] Tepedelenlıoğlu, E. & Ögelman, H. 2005, ApJL, 630, L57. doi: 10.1086/444360

[402] Tetzlaff, N., Eisenbeiss, T., Neuhäuser, R., & Hohle, M. M. 2011, MNRAS, 417, 617. doi: 10.1111/j.1365-2966.2011.19302.x

[403] The Fermi-LAT collaboration. 2019, ArXiv e-prints. arXiv: 1902.10045

[404] Thompson, C., Lyutikov, M., & Kulkarni, S. R. 2002, ApJ, 574, 332. doi: 10.1086/340586

[405] —. 2002, ApJ, 574, 332. doi: 10.1086/340586

[406] Thompson, C. & Duncan, R. C. 1995, MNRAS, 275, 255. doi: 10.1093/mnras/275.2.255

[407] —. 1996, ApJ, 473, 322. doi: 10.1086/178147

[408] Thompson, D. J. 2001, in American Institute of Physics Conference Series, ed. F. A. Aharonian & H. J. Völk, Vol. 558, 103–114. doi: 10.1063/1.1370784

[409] Thorsett, S. E. 1991, ApJ, 377, 263. doi: 10.1086/170355

[410] Tiengo, A. & Mereghetti, S. 2007, ApJL, 657, L101. doi: 10.1086/513143

[411] Torii, K., Saito, Y., Nagase, F., et al. 2001, ApJL, 551, L151. doi: 10.1086/320016

[412] Turbiner, A. V. & López Vieyra, J. C. 2006, PhRp, 424, 309. doi: 10.1016/j.physrep.2005.11.002

[413] Turner, M. J. L. et al. 2001, A&A, 365, L27. doi: 10.1051/0004-6361:20000087

[414] Turolla, R. 2009, in Astrophysics and Space Science Library, ed. W. Becker, Vol. 357, 141. doi: 10.1007/978-3-540-76965-1_7

[415] Turolla, R. & Nobili, L. 2013, ApJ, 768, 147. doi: 10.1088/0004-637X/768/2/147

[416] Turolla, R., Zane, S., & Watts, A. L. 2015, RPPh, 78, 116901. doi: 10.1088/0034-4885/78/11/116901

[417] Turolla, R., Zane, S., & Drake, J. J. 2004, ApJ, 603, 265. doi: 10.1086/379113

[418] Usov, V. V. & Melrose, D. B. 1995, AuJPh, 48, 571. doi: 10.1071/PH950571

[419] van Adelsberg, M. & Lai, D. 2006, MNRAS, 373, 1495. doi: 10.1111/j.1365-2966.2006.11098.x

[420] van Adelsberg, M., Lai, D., Potekhin, A. Y., & Arras, P. 2005, ApJ, 628, 902. doi: 10.1086/430871

[421] van Riper, K. A. 1982, ApJ, 257, 793. doi: 10.1086/160032

[422] Verbiest, J. P. W., Weisberg, J. M., Chael, A. A., Lee, K. J., & Lorimer, D. R. 2012, ApJ, 755, 39. doi: 10.1088/0004-637X/755/1/39

[423] Viganó, D. 2013, PhD thesis, Universitat d'Alacant. http://ui.adsabs.harvard.edu/abs/2013PhDT.....7V/abstract

[424] Viganò, D. & Pons, J. A. 2012, MNRAS, 425, 2487. doi: 10.1111/j.1365-2966.2012.21679.x

[425] Viganò, D., Rea, N., Pons, J. A., et al. 2013, MNRAS, 434, 123. doi: 10.1093/mnras/stt1008

[426] Viganò, D., Perna, R., Rea, N., & Pons, J. A. 2014, MNRAS, 443, 31. doi: 10.1093/mnras/stu1109

[427] Wahl, H. M., Orfeo, D. J., Rankin, J. M., & Weisberg, J. M. 2016, MNRAS, 461, 3740. doi: 10.1093/mnras/stw1589

[428] Walter, F. M., Eisenbeiß, T., Lattimer, J. M., et al. 2010, ApJ, 724, 669. doi: 10.1088/0004-637X/724/1/669

[429] Wang, N., Manchester, R. N., & Johnston, S. 2007, MNRAS, 377, 1383. doi: 10.1111/j.1365-2966.2007.11703.x

[430] Wang, W.-Y., Feng, Y., Lai, X.-Y., et al. 2018, RAA, 18, 082. doi: 10.1088/1674-4527/18/7/82

[431] Wang, W., Lu, J., Tong, H., et al. 2017, ApJ, 837, 81. doi: 10.3847/1538-4357/aa5e52

[432] Weltevrede, P., Edwards, R. T., & Stappers, B. W. 2006, A&A, 445, 243. doi: 10.1051/0004-6361:20053088

[433] Weltevrede, P., Johnston, S., & Espinoza, C. M. 2011, MNRAS, 411, 1917. doi: 10.1111/j.1365-2966.2010.17821.x

[434] Wilms, J., Allen, A., & McCray, R. 2000, ApJ, 542, 914. doi: 10.1086/317016

[435] Wilson, J. R. 1980, in Ninth Texas Symposium on Relativistic Astrophysics, Vol. 336, 358–365. doi: 10.1111/j.1749-6632.1980.tb15943.x

[436] Woods, P. M., Kaspi, V. M., Thompson, C., et al. 2004, ApJ, 605, 378. doi: 10.1086/382233

[437] Wright, G. & Weltevrede, P. 2017, MNRAS, 464, 2597. doi: 10.1093/mnras/stw2498

[438] Yakovlev, D. G., Haensel, P., Baym, G., & Pethick, C. 2013, PhyU, 56, 289. doi: 10.3367/UFNe.0183.201303f.0307

[439] Yao, J. M., Manchester, R. N., & Wang, N. 2017, ApJ, 835, 29. doi: 10.3847/1538-4357/835/1/29

[440] Yoneyama, T., Hayashida, K., Nakajima, H., & Matsumoto, H. 2019, PASJ, 71, 17. doi: 10.1093/pasj/psy135

[441] Young, N. J., Stappers, B. W., Weltevrede, P., Lyne, A. G., & Kramer, M. 2012, MNRAS, 427, 114. doi: 10.1111/j.1365-2966.2012.21934.x

[442] Zane, S. & Turolla, R. 2006, MNRAS, 366, 727. doi: 10.1111/j.1365-2966.2005.09784.x

[443] Zane, S., Turolla, R., Stella, L., & Treves, A. 2001, ApJ, 560, 384. doi: 10.1086/322360

[444] Zane, S., Cropper, M., Turolla, R., et al. 2005, ApJ, 627, 397. doi: 10.1086/430138

[445] Zane, S., Haberl, F., Israel, G. L., et al. 2011, MNRAS, 410, 2428. doi: 10.1111/j.1365-2966.2010.17619.x

[446] Zavlin, V. E. 2006, ApJ, 638, 951. doi: 10.1086/449308

[447] Zavlin, V. E. 2009, in Astrophysics and Space Science Library, ed. W. Becker, Vol. 357, 181. doi: 10.1007/978-3-540-76965-1_9

[448] Zavlin, V. E. & Pavlov, G. G. 2002, in Neutron Stars, Pulsars, and Supernova Remnants, ed. W. Becker, H. Lesch, & J. Trümper, 263

[449] Zavlin, V. E. & Pavlov, G. G. 2004, ApJ, 616, 452. doi: 10.1086/424894

[450] Zavlin, V. E., Pavlov, G. G., Shibanov, Y. A., & Ventura, J. 1995, A&A, 297, 441

[451] Zavlin, V. E., Pavlov, G. G., & Shibanov, Y. A. 1996, A&A, 315, 141. arXiv: astro-ph/9604072

[452] Zavlin, V. E., Pavlov, G. G., Sanwal, D., & Trümper, J. 2000, ApJL, 540, L25. doi: 10.1086/312866

[453] Zeldovich, Y. B. & Guseynov, O. H. 1966, ApJ, 144, 840. doi: 10.1086/148672

[454] Zhang, B., Sanwal, D., & Pavlov, G. G. 2005, ApJL, 624, L109. doi: 10.1086/430522

[455] Zhang, B. & Harding, A. K. 2000, ApJ, 532, 1150. doi: 10.1086/308598

[456] —. 2000, ApJL, 535, L51. doi: 10.1086/312694

[457] Zharikov, S. & Mignani, R. P. 2013, MNRAS, 435, 2227. doi: 10.1093/mnras/stt1439

[458] Zharikov, S. V., Shibanov, Y. A., Mennickent, R. E., & Komarova, V. N. 2008, A&A, 479, 793. doi: 10.1051/0004-6361:20077728

[459] Zhu, W. W., Kaspi, V. M., McLaughlin, M. A., et al. 2011, ApJ, 734, 44. doi: 10.1088/0004-637X/734/1/44

[460] Zhu, W., Kaspi, V. M., Gonzalez, M. E., & Lyne, A. G. 2009, ApJ, 704, 1321. doi: 10.1088/0004-637X/704/2/1321

Acknowledgments

First and foremost I would like to thank my PhD supervisor Sandro Mereghetti, for his constant guidance, attentive help and constructive criticism. I can truly say that none of this work would have been possible without him. I would like to thank him also for the complete confidence he showed in me, and for encouraging me to pursue the research in the astrophysical field.

I would like to thank the reviewers Nanda Rea and Sergey Popov, for the enthusiastic feedback to this research work, and for constructive suggestions. A special thanks to Roberto Turolla, for his advice and support, and to Sasha Potekhin and Valery Suleimanov, for their willingness to compute any requested model in a few days, and to carefully read some extracts of this work.

Un grazie di cuore...

A tutto il gruppo INAF IASF-Milano, per avermi accolta e accudita fin dalla tesi magistrale. Grazie per i pranzi in mensa e fuori, per le pause caffè, per le astrosieste, per le feste di Natale, e per molto altro. Un particolare ringraziamento va a Fabio, molto più che un collega di ufficio, ma un amico, un compagno di sushi e un padrone di casa in Sardegna molto ospitale.

A tutto il gruppo di Astrofisica di Bicocca, per l'affetto dimostratomi nonostante la mia presenza sporadica. Grazie per i pranzi in "auletta" con l'immancabile HQ Trivia, e soprattutto per la bellissima esperienza del Meet Me Tonight, in cui ho imparato a rapportarmi con il grande pubblico e a comunicare la mia passione per l'Astrofisica anche senza voce. Per questa esperienza voglio in particolare ringraziare Tullia, colonna portante e guida spirituale di tutti noi.

A tutti i giovani (e meno giovani) astrofisici che ho incontrato alle diverse scuole e conferenze, per avermi fatta sentire in famiglia, per la competenza e l'entusiasmo ma anche per i momenti più ludici (karaoke!) e riflessivi.

Ai miei compagni di università ora sparsi in giro per il globo, per aver reso 5 anni di università ed esami una bellissima esperienza e palestra di vita, e per accompagnarmi tuttora nelle scelte importanti. In particolare un enorme grazie alle mie due amiche Sara e Vale, per essere così diverse fra voi ma così simili a me e per darmi sempre un giudizio sincero.

Ai miei amici, che conosco da sempre o che ho coltivato negli ultimi anni, che mi regalano momenti spensierati ma anche forza e motivazione poiché inseguono, ognuno a modo proprio, il lavoro dei sogni. Un grazie speciale va a Martina, per essere una presenza costante nella mia vita quando tutto attorno a me cambia.

Ai miei genitori, la mia forza, che mi hanno ispirata fin da piccola a coltivare le mie passioni e a credere in me stessa, e che mi hanno supportata in tutto con amore e orgoglio. Indubbiamente mi hanno resa quello che sono.

A Dario, per essere tutto ciò che ho elencato finora e molto di più. Ci auguro di affrontare le nuove sfide che verranno con lo stesso spirito che abbiamo avuto fino ad ora.

Michela